Repository Istituzionale dei Prodotti della Ricerca del Politecnico di Bari

Expermental and analytical study of thermographic techniques for stress analysis and materials characterization

This is a PhD Thesis

Original Citation:
Expermental and analytical study of thermographic techniques for stress analysis and materials characterization / Di Carolo, Francesca. - ELETTRONICO. - (2021). [10.60576/poliba/iris/di-carolo-francesca_phd2021]

Availability:
This version is available at http://hdl.handle.net/11589/226758 since: 2021-06-09

Published version
Politecnico di Bari
DOI:10.60576/poliba/iris/di-carolo-francesca_phd2021

Terms of use:
Altro tipo di accesso

(Article begins on next page)

27 April 2024

Politecnico di Bari

Department of Mechanics, Mathematics and Management

MECHANICAL AND MANAGEMENT ENGINEERING
Ph.D. Program

SSD: ING-IND/14–Mechanical design and machine construction

Final Dissertation

EXPERIMENTAL AND ANALYTICAL STUDY OF THERMOGRAPHIC TECHNIQUES FOR STRESS ANALYSIS AND MATERIALS CHARACTERIZATION

By
Di Carolo Francesca:

____

Referees:
Prof. G. Arcidiacono
Prof. L.A. Felipe Sese

Supervisor:
Prof. U. Galietti

Coordinator of Ph.D Program:

Prof. G. P. Demelio

________________ *firma*

Course n°33, 01/11/2017-31/03/2021

Alla mia famiglia

Index

INTRODUCTION

The mechanical designer is often called upon to solve problems of components and even very complex structures subjected to both static and dynamic loads; in this framework, the capability to quantify in a reliable and not invasive way the mechanical and physical characteristics of materials and components is fundamental.

Despite nowadays the availability of Finite Element Method modelling Multiphysics software allows to reduce time and costs, experimental mechanics plays a key role in the design process as any modelling to be used requires a validation that only the experimental measurement of the calculated quantities can provide.

In this respect, the development and optimization of increasingly efficient techniques for stress analysis and material characterization is a topic of strong engineering interest.

The Infra-Red (IR) Thermography is the basis of a family of such the techniques, precisely thermographic techniques, which over recent years attracted the attention of both the academic and industrial sector thanks to the peculiarities that make them competitive with other characterization techniques (such as strain gauges, X-ray, photoelasticity, classical destructive tests etc...), which, even if well established, have limits of practical application or instrumentation costs or the quality and quantity of the information acquired.

All thermographic techniques share the fact that they are full-field, non-destructive, superficial and do not require direct contact with the component or structure, furthermore the transparency properties of some materials at certain wavelengths of the IR emission also allow application in contexts of extreme environmental conditions that require shielding.

The potential fields and methods of use of thermographic techniques are different, the versatility of these techniques lies in the possibility of using the temperature signal as a sentinel of physical phenomena that depend on the characteristics under study. Thus, for example the thermoelastic effect can be exploited to measure the stress field by calibrating the thermal response or the thermal transient rate can be related to the material thermal proprieties or the heating due to heat dissipation can identify an area prone to plasticization.

In order to interpret a thermal signal and identify the analytical relation that link it to a phenomenon or quantity to be evaluated, it is essential to understand the underlying physical principles. The analytical description of these phenomena allows the optimization and development of techniques and procedures through a simulation-based approach which must however be validated by experiments.

The motivation behind this research study is the important impact in the academic and industrial fields that the implementation of innovative thermographic techniques can have. Hence the need to investigate the application potential offered in the field of experimental mechanics.

The main goal is to explore this potential through the study, development, optimization, and validation of IR thermography-based procedures for the characterization of materials, aiming at increasingly accuracy, reliability, and precision.

In particular, the study was focused on four main promising application, which are: 1)The evaluation of the superficial stress field of components and structures by means of the Thermoelastic Stress Analysis (TSA), 2) The identification of residual stress exploiting the mean load effect on the Thermoelastic signal, 3) the fracture mechanics characterization of components, which included the combination of TSA equations with the linear elastic theory to find the Stress Intensity Factor and the identification of the locally plasticized area around the crack tip through the interpretation of the thermal dissipation footprint, 4) The temperature measurement in aerospace applications implementing the dual color technique, that is a free-emissivity temperature measurement technique suitable to characterize the spaceships Thermal Protection System performance in extreme environmental conditions during atmospheric re-entry tests.

Even if different levels have been reached, in relation to the point of maturity of the application itself, each of them was addressed with a systematic approach which saw a first phase of study of the state of the art on the solutions proposed for the particular problem with an examination of their validity, limits and potential; the analysis therefore focused on the physical principles underlying all the phenomena involved (with particular attention to heat transfers and including sources of noise), aiming at an analytical description of the system that was as close to reality as possible and identifying particular cases of interest that allow simplifications of the most complex relation.

Once defined the analytical relations between the observed phenomena and the thermal response, the model validation involved the planning and implementation of experimental campaigns on sample specimens whose response can be known or measurable with an alternative validated comparison technique. In this phase was important to identify the main variables acting on the system.

It was not a one-way path, but an iterative process in which experimental detection can provide evidence of relationships and phenomena that should be involved in the analytical description, until reaching the desired goal of a stable and precise prediction.

In this regard, a further step was to propose a Robust Design-like approach to optimize the measurement performances of thermographic techniques.

In fact, even if the availability of complex analytical models linking signal and measurement gives the chance to assess the capability of an experimental technique to obtain the required measurement with the available sensors, the complexity of relations and the effect of random noise variables make the implementation of statistical methods a useful tool to study the applicability of the technique.

The structure of the present thesis has been designed to allow the reader to follow the same evolution of steps above described.

Chapter 1 gives a brief introduction to the IR thermography with a description of its main features, the physical principles on which it is based and the hardware solutions that make its application possible (the IR thermal cameras).

Chapter 2 provides a detailed description of the four considered application, in particular, for each one the theory on the techniques applied to the state of the art is reported, highlighting the limits of validity, simplifications and development prospects.

Chapter 3 introduces the Robust-Design approach implemented to realize the statistical optimization of thermographic techniques measurement performance.

Next follow the chapters dedicated to individual case studies and in which the innovative contributions that this work has produced are described: in Chapter 4 the development of a general model for TSA and its applications in the evaluation of the superficial stress field and in detecting biaxial residual stress, in Chapter 5 the application of a Robust Design approach to improve TSA stress and residual stress measurement performances, in Chapter 6 the experimental study of novel fracture mechanics characterization procedures based on thermal signal analysis and in Chapter 7 The Dual Color applicability studies for materials associated to different classes of emissivity from low to high temperatures typical of aerospace re-entry.

CHAPTER 1.

INFRARED THERMOGRAPHY FOR MECHANICAL APPLICATIONS

The use of thermal methods in experimental mechanics have grown faster and faster in the last 50 years, hand in hand with the technological development of infrared (IR) systems.

The first civil application of IR radiometry dates to the 1950s, when the first devices were able to provide a "thermogram", that is a thermal map of an immobile object at a constant temperature following an exposure time of at least 10 minutes. It was only in the 1960s that the first thermal imaging cameras began to be sold in the United States, which, although very heavy and bulky, were able to provide a qualitative real-time temperature map[1].

The development of high-sensitive and high-speed thermal imaging cameras has made possible their use in the most varied fields, allowing the solution of problems involving (sometimes even very small) energy transfer, which cannot be easily demonstrated with other methods.

The discovery of IR radiations is attributed to Herschel in the late 1800 [2]. He was studying the heat passing through the telescopes filters to protect his eyes when observing sunlight and accidentally discovered that color temperatures rose from purple to red and that the temperature was even higher beyond the red band, where no radiation was visible.

Herschel's experience was a milestone, as for the first time it was possible to demonstrate the existence of a form of light that cannot be seen by the human eye.

The practical implication of Herschel's discovery is the development of radiometry, which is the measurement of the electromagnetic radiation emitted by a surface in order to know its temperature.

Pyrometers and radiometric thermal cameras are the devices designed for this purpose; the former provide the precise value of a single-point temperature while thermal cameras develop thermal maps, providing two-dimensional images of the irradiation measurement.

In the first part of this chapter a brief overview of the physical principles at the base of the working of an IR system will be given.

The second part will be dedicated to the description of the measurement systems and hardware technologies that carry out the acquisition of the infrared signal and its transformation into a temperature value, i.e. IR sensors.

1.1. Physical Principle Behind IR Thermography

1.1.1. The Spectrum of the Electromagnetic Radiation

Radiometry and thermographic techniques are based on the physical phenomenon of thermal radiation.

Any object that is at a temperature above 0 kelvin, regardless of the medium in which it is located, emits electromagnetic radiation, and receives it from surrounding objects.

When two or more objects, having different temperatures, see each other in a medium that is sufficiently transparent to radiation, this transfer of thermal energy occurs at the speed of light (given as well known by the product of the wavelength for frequency $c = \lambda \cdot \upsilon$) and does not require any direct contact between the exchangers. Of course, the medium too, except for empty space, takes an active part in the radiation exchange, as it too emits and absorbs the radiant energy, albeit to an extent that may be more or less negligible.

Thermal radiation affects any aggregate of solid, liquid or gaseous material, but the behaviour varies depending on whether the aggregate is gaseous or condensed (liquid or solid). Gases and aeriforms emit a striped spectrum consisting of a discrete number of wavelengths, and the absorption spectrum is of the same type; moreover, their emission is of the volumetric type. For solids and liquids, on the other hand, a continuous spectrum is generally found; the radiation emitted by the internal molecules is mostly absorbed by the adjacent ones, so the radiation that comes from a solid or liquid body is only that emitted by the molecules that are within the distance of 1µm from the exposed surface.

The atoms and molecules making up any aggregate of material are equipped with electrons which, if accelerated, emit electromagnetic waves that also propagate in a vacuum carrying energy. The discovery of this phenomenon is by J.C. Maxwell, who first hypothesized that electric and magnetic fields originate from the acceleration of electrical charges or from the temporal variation of electric currents.

After these findings, Planck[3] proposed the radiant body model which is formed by a large number of harmonic oscillators generating electromagnetic waves of all possible frequencies. The radiating matter does not emit radiant energy continuously but discontinuously, in discrete packets or quanta. Maxwell suggested that electromagnetic radiation can be considered as the propagation of a series of energy packets, called photons, characterized by a quantum of energy inversely proportional to the wavelength:

$$\boldsymbol{e} = \frac{\boldsymbol{h} \cdot \boldsymbol{c}}{\boldsymbol{\lambda}}\ [J] \qquad \text{Eq 1}$$

Where h=6.625·10^{-34} $J·s$ is the Planck's constant, c=2,998·10^{8} m/s is the speed of light and λ (measured in µm) is the wavelength.

It is possible to distinguish different kind of electro-magnetic radiations, which differs in wavelengths. Radio waves, microwaves, infrared radiation, visible radiation, ultraviolet radiation, X rays and γ rays are all forms of the same physical phenomenon and they are all governed by the same physical laws.

The transmission of heat by radiation occurs through the thermal electromagnetic radiation.

The emitted electromagnetic radiation is proportional to the temperature, which, in turn, is related to the agitation level of the body atomic and subatomic particles.

Solids and liquids emit radiations at all wavelengths but with un unequal distribution of energy among them and not uniformly in all direction; for temperatures below 500°C (the range of natural and technological process), the higher intensities are concentrated mostly in the infrared range. For this reason, the infrared band is often known as the thermal region of the electromagnetic spectrum. The infrared is characterized by radiation with a wavelength between 0.78 µm and 1000 µm.

The IR imaging is based on a small range of the IR spectrum which is commonly split into further regions. There is no single way to identify ranges and classify the infrared bands [1][4][5], here is a division by applications.

Table 1 InfraRed spectral ranges and their applicatios

Range	Wavelength	Applications
Near Infrared	from 0.78 μm to 1.5 μm	• Laboratory research • Analysis of ancient paintings by infrared reflectography
Mid Infrared	from 1.5 μm to 6 μm	also known as the first atmospheric window • detectors and optical materials at low cost • possibility of cooling the sensors working in this range of wavelengths with Peltier batteries allows for a reduction in costs and dimensions of the thermal imaging camera
Far Infrared	from 6 μm to 15 μm	also known as the second atmospheric window, is widely used due to its excellent transparency to the atmosphere and the availability of microbolometric FPA sensors that do not require cooling systems and are less sensitive to solar reflections.
Extreme Infrared	from 15 μm to 1000 μm	It is used only in the astronomical sector

1.1.2. Radiative heat transfer

The energy transfer through thermal radiation implies the emission of the radiation from a surface and its incidence on another.

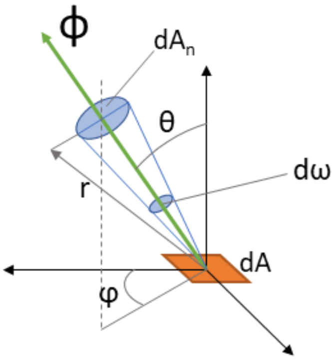

Figure 1 Emitted radiation in the polar coordinates system r, θ, φ

Considering a surface element dA (Figure 1), the rate at which the emitted flux ϕ_e is emitted at the wavelength λ in the direction identified by the angles θ and φ is the spectral radiance L, which is the ratio of ϕ to the surface element subtended by the solid angle dω and immediately surrounding the flux direction per unit of wavelength interval [1]:

$$I_{\lambda,e}(\lambda,\theta,\varphi) = \frac{d^3\Phi_e}{dA \cdot cos\,\theta \cdot d\omega \cdot d\lambda}\ [W \cdot m^{-2} \cdot sr^{-1} \cdot \mu m^{-1}] \qquad \text{Eq 2}$$

Similarly, the incident spectral radiance is defined as the ratio of the incident flux Φ_i for the wavelength interval $d\lambda$ from the direction identified by the angles θ and φ to the projected surface element subtended by the solid angle $d\omega$ and immediately surrounding the flux:

$$I_{\lambda,i}(\lambda,\theta,\phi) = \frac{d^3\Phi_i}{dA \cdot cos\,\theta \cdot d\omega \cdot d\lambda}\ [W \cdot m^{-2} \cdot sr^{-1} \cdot \mu m^{-1}] \qquad \text{Eq 3}$$

The spectral emissive power is defined as the spectral radiant power at the wavelength λ incident on a surface from all directions in the hemispheric space above the surface considered:

$$E(\lambda) = \frac{d\phi(\lambda)}{dA}\ [W \cdot m^{-2} \cdot \mu m^{-1}] \qquad \text{Eq 4}$$

It is called spectral because it is still a function of λ and it is hemispherical because it is integrated with respect to a hypothetical hemisphere. The total hemispherical emissive power is E:

$$E = \int_0^\infty E(\lambda)\ d\lambda\ [W \cdot m^{-2}] \qquad \text{Eq 5}$$

where total means that the integration is with respect to the wavelength.

1.1.3. Blackbody absorber and emitter of radiant energy

One of the main concepts of the physics of thermal radiation is that of the black body. The black body is an ideal body that acts as a perfect emitter and absorber of radiation.

The blackbodies totally absorb the incident radiation, regardless of the direction and wavelength.

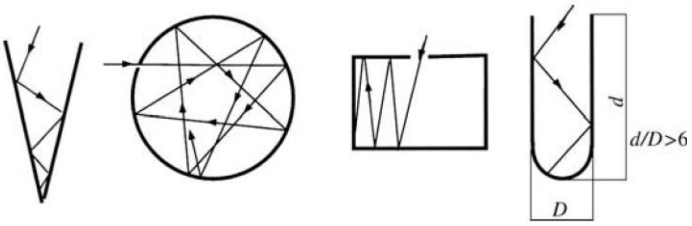

Figure 2 examples of black body cavities

In nature black bodies do not exist, however the definition allows to write the laws governing the phenomenon of radiation in a relatively simple form to study the radiative behaviour of real bodies.

In practice, it is possible to create systems that approximate even up to 99% the blackbody behaviour, through the use of hollow bodies with cylindrical or conical geometry coated with highly absorbent material, provided with a small opening and kept at a constant temperature through a thermostatic bath. The radiation entering the cavity, undergoes multiple reflections and is almost completely absorbed before being able to exit, reproducing the black body behaviour. Four different models of black bodies are showed in Figure 2[6].

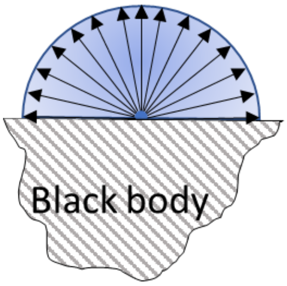

Figure 3 black body diffused emission.

The power irradiated by black body is uniform in all directions and it is the maximum radiance that can be emitted by any other body for a given temperature and wavelength.

The spectral radiance irradiated by a black body per unit surface and per unit of solid angle is given by an analytical relation known as Planck's law:

$$E_{b\lambda}(T,\lambda) = \frac{2 \cdot \pi \cdot c^2}{\lambda^5 \cdot \left(e^{\frac{h \cdot c}{k \cdot \lambda \cdot T}} - 1\right)} \; [W \cdot m^{-2} \cdot sr^{-1} \cdot \mu m^{-1}] \qquad \text{Eq 6}$$

The constants in Eq 6 are:

- $c = 2{,}998 \cdot 10^8 \; [m/s]$, speed of light
- $h = 6{,}625 \cdot 10^{-34} \; [J \cdot s]$, Planck’s constant
- $k = 1{,}3805 \cdot 10^{-23} \; [J/K]$, Boltzmann’s constant

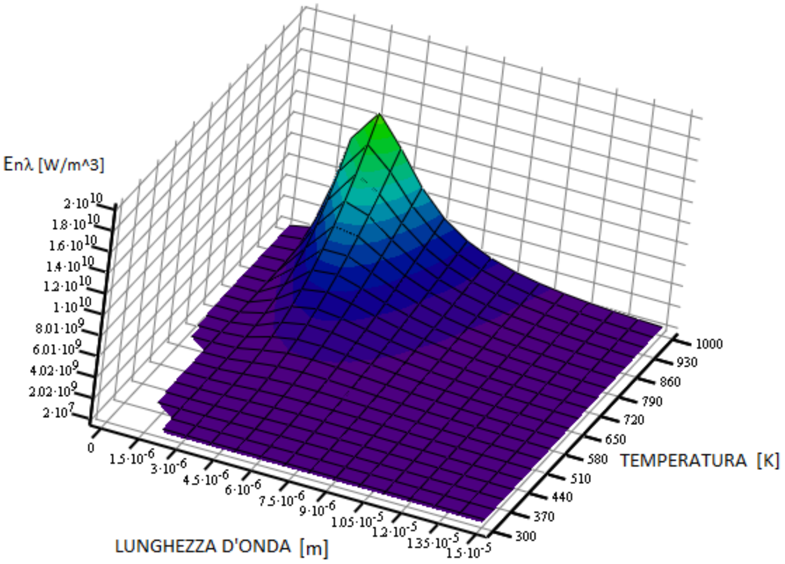

Figure 4 Planck's Law for the calculation of the spectral radiance as function of wavelength and temperature.

In Figure 4 the surface describing the spectral radiance as function of wavelength and temperature shows how $E_{b\lambda}$ increases with temperature (due to the correlation between body temperature and infrared radiation explained in paragraph 1.1.1. Furthermore, for each temperature value $E_{b\lambda}$ presents a maximum point function of the wavelength. In fact, although the black body is a source of radiation whose energy is not concentrated in any region of the electromagnetic spectrum, at each temperature it has a wavelength at which the emitted radiation has a maximum. In Figure 5 it is possible to see how the maximum moves towards smaller values of λ as the temperature increases.

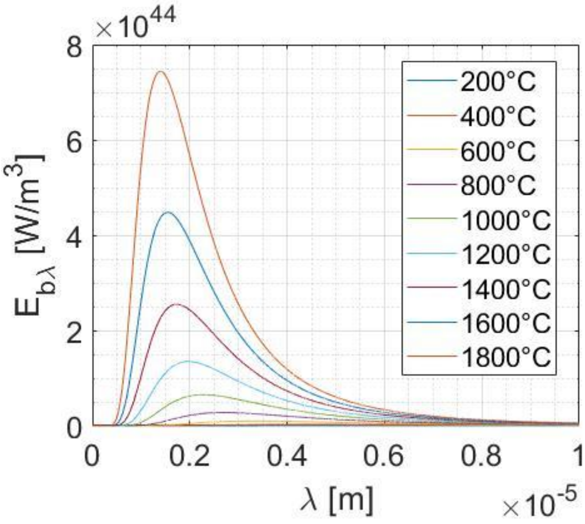

Figure 5 Planck's Law for the calculation of the spectral radiance as function of wavelength.

It is therefore possible to identify the locus of the maxima of curves at constant temperature by deriving:

$$\left.\frac{\partial\, E_{b\lambda}(\lambda,T)}{\partial\lambda}\right|_{T=cost} = 0 \qquad \text{Eq 7}$$

From which we obtain:

$$\lambda_{max}\cdot T = 2897.8\,\mu m\cdot K \qquad \text{Eq 8}$$

The relation in Eq 8 is known as Wien's displacement Law and establishes a simple correspondence between the black body temperature and the wavelength at the maximum of emission.

Thus, for example, a black body that is at a temperature of 5200 K, will have its radiation peak at 0.6 µm, which is located approximately in the center of the visible spectrum. In this case, which can therefore be considered the one with the most visible emission, only 40% of the total radiation emitted falls in the visible area while 6% is found in the ultraviolet and the remaining part in the infrared. An object at an ambient temperature of 290 K will present its maximum at a wavelength of about 10 µm.

The radiation emitted by bodies is produced by the rotational and vibrational motions of the atomic and subatomic particles of which they are made. Since there is a great variety of these particles, radiation at different frequencies is emitted, and since the heat flow sensors are unable to perceive the radiation relative to a single wavelength; it is therefore more useful to evaluate the power irradiated by the black body in a spectral band.

The black body emission in the spectral band (λ_1, λ_2) for a given temperature is the fraction $E_b(\lambda_1, \lambda_2)$ obtained by integrating Planck's law:

$$E_{b,\lambda_1-\lambda_2}(\lambda_1,\lambda_2,T) = \int_{\lambda_1}^{\lambda_2} \frac{2\cdot\pi\cdot c^2}{\lambda^5\cdot\left(e^{\frac{h\cdot c}{k\cdot\lambda\cdot T}}-1\right)}\,d\lambda \qquad \text{Eq 9}$$

Integrating Eq 9 between 0 and ∞ we obtain the black body total emission:

$$E_b(\mathrm{T}) = \int_0^{\infty} \frac{2\cdot\pi\cdot c^2}{\lambda^5\cdot\left(e^{\frac{h\cdot c}{k\cdot\lambda\cdot T}}-1\right)}\,d\lambda = B\cdot T^4 \qquad \text{Eq 10}$$

whose final solution is known as the Stefan-Boltzmann's Law, and therefore the constant $B\ = 5.679\cdot 10^{-8}\ [W/m^2\ K^4]$ takes its name.

1.1.4. Radiation Laws for Real Surfaces

In nature there are not real surfaces that behave as a blackbody; real surfaces cannot absorb all the incident radiation, which is in part absorbed, in part reflected and in part transmitted.

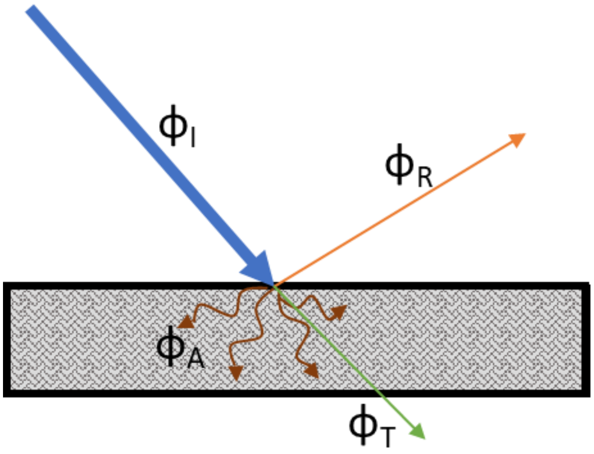

Figure 6 Incident flux of thermal radiation

If the incident flux of thermal radiation ϕ_I (amount of heat per time) falls on the surface of an object with a certain thickness, then it will be split into three parts, being absorbed, reflected, and transmitted.

The amount of the flux fractions absorbed (ϕ_A), reflected (ϕ_R) and transmitted (ϕ_T) depend on the wavelengths, orientation, and temperature of the incident radiation and on the surface characteristics, such as roughness and cleanliness.

The incident flux is the sum of these three contributions:

$$\Phi_I = \Phi_R + \Phi_A + \Phi_T \; [W] \qquad \text{Eq 11}$$

Dividing the flow balance by ϕ_I, we obtain:

$$1 = \rho + \alpha + \tau \qquad \text{Eq 12}$$

where ρ, a and τ are respectively the reflection, absorption, and transmission coefficients. These coefficients not only depend on the nature of the body, but also on its thickness and temperature and on wavelength and incidence direction of the radiation.

Thus, a black body is characterized by $\rho=\tau=0$, while a completely opaque body is characterized by $\tau=0$.

The absorption of radiant energy within a body follows an exponential trend:

$$\Phi(x) = \Phi(0)e^{-\alpha x}[W] \qquad \text{Eq 13}$$

Where $\Phi(0)$ represents the incident flux on the surface and $\Phi(x)$ its value after crossing the depth x. The absorption constant α depends on the material and has the unit of m^{-1}.

Unlike the black body, the behaviour of real surfaces as emitters not only depends on their temperature but also on their nature and conformation.

For a given temperature, this involves a jagged distribution of emission energy which does not follow the Planck's Law. The black body is the capable of emitting the greatest flux of radiation per unit of area at the same temperature and can be used as a reference to describe the behaviour as an emitter of any real surface.

To describe the radiant energy spectral distribution emitted by a real surface we use the definition of its radiative properties, which in addition to the absorption, reflection and transmission coefficients also include the emissivity ε.

The emissivity is expressed as the ratio of the radiation emitted by a surface to the radiation emitted by the blackbody; thus, it is dimensionless, and it ranges from 0 to 1.

The emissivity depends on several parameters, including:

- type of material
- state of the surface (roughness); mechanical processing or chemical can lead to an important variation in emissivity (for example, a high not-oriented roughness increases the emissivity and makes it less sensitive to variations in the emission angle)
- geometry of the object
- temperature of the surface
- wavelength of the emitted radiation
- emission angle

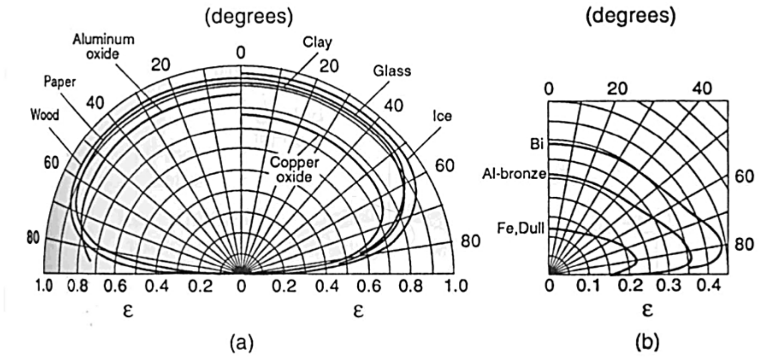

Figure 7 emissivity of metals as a function of the emission angle.

In general, metals have low emissivity which increases with temperature. As showed in Figure 7, emissivity of metals is low when the radiation is normal to the surface and increases with the angle reaching a peak between 70 ° and 80 °, then it tends to zero for the direction parallel to the surface (90 °).

Non-conductive materials show an opposite trend with high values for angles close to the normal and values that tend to zero for angles close to 90 °.

The spectral directional emissivity of a surface for given values of temperature, wavelength end emission angles is:

$$\varepsilon_\lambda(\lambda, T, \theta_{em}, \varphi_{em}) = \frac{E_\lambda(\lambda, T, \theta_{em}, \varphi_{em})}{E_{b\lambda}(\lambda, T)} \quad \text{Eq 14}$$

The thermal radiation phenomenon is a result of the energy balance between emitted energy and absorbed energy, so to determine its contribution in the heat exchange between two bodies it is necessary to know the properties of these bodies in terms of emission and absorption characteristics.

In this context, the Kirchoff law is of great importance; it establishes how to deduce the absorption properties of an opaque body from its emission proprieties, or vice versa. It states that the relationship between the emission and the absorption processes does not depend on the nature of the surface and that emissivity and absorption are linked by the relation:

$$\varepsilon(\lambda, \theta_{em}, \varphi_{em}) = \alpha(\lambda, \theta_{ab}, \varphi_{ab}) \quad \text{Eq 15}$$

The real surface emission in the spectral band (λ₁, λ₂) for a given temperature is the fraction *F*(λ₁, λ₂) obtained by integrating the emissivity corrected Planck's law:

$$E_{\lambda 1-\lambda 2}(\lambda_1, \lambda_2, T, \varepsilon, \theta_{em}, \varphi_{em}) = \int_{\lambda_1}^{\lambda_2} \varepsilon(\lambda, \theta_{em}, \varphi_{em}) \cdot \frac{2 \cdot \pi \cdot c^2}{\lambda^5 \cdot \left(e^{\frac{h \cdot c}{k \cdot \lambda \cdot T}} - 1\right)} d\lambda \qquad \text{Eq 16}$$

Integrating Eq 16 between 0 and ∞ we obtain the real surface total emission:

$$E(\mathrm{T}, \varepsilon,, \theta_{em}, \varphi_{em}) = \int_{0}^{\infty} \varepsilon(\lambda, \theta_{em}, \varphi_{em}) \cdot \frac{2 \cdot \pi \cdot c^2}{\lambda^5 \cdot \left(e^{\frac{h \cdot c}{k \cdot \lambda \cdot T}} - 1\right)} d\lambda \qquad \text{Eq 17}$$

The integration in Eq 17 can be very complex, due to the functional dependence of the emissivity on the temperature, wavelength and emission direction, which cannot always be determined; therefore, it is often convenient to apply some simplifications.

The first simplification is that of the diffusing surface, that is, the radiative properties are considered independent of the direction.

The second simplification consists in considering the emissivity independent of the wavelength, the bodies for which this simplification is valid are called gray bodies.

For a diffusing gray body, the emissivity in Eq 17 can be put out of the integral operator, and therefore becomes:

$$E_g(\mathrm{T}, \varepsilon) = \varepsilon \cdot \int_{0}^{\infty} \frac{2 \cdot \pi \cdot c^2}{\lambda^5 \cdot \left(e^{\frac{h \cdot c}{k \cdot \lambda \cdot T}} - 1\right)} d\lambda \qquad \text{Eq 18}$$

Substituting with Eq 10:

$$E_g(\mathrm{T}, \varepsilon) = \varepsilon \cdot B \cdot T^4 \qquad \text{Eq 19}$$

The gray body hypothesis can result quite restrictive if applied to the entire electromagnetic spectrum, but it can be less conditioning if applied to a narrow band of it; in this case the local gray body simplification is applied.

1.2. Infrared thermal imaging system

1.2.1. Thermographic measurements of real surfaces

To convert the radiant energy impinging the IR camera sensor into a temperature value, it is necessary to understand what exactly the radiant energy that reaches the sensor consists of.

The radiative energy globally emitted by the surface due to its thermal state depends on its emissivity and thus on the wavelength and temperature.

Moreover, the surface reflects part of the energy emitted by the surrounding environment. However, the dependence of the energy emitted by the fourth power of the temperature can be assumed valid also for real surfaces. This implies, especially at high temperatures and for high emissivity values, that the thermal contribution of the emitted energy is preponderant with respect to the reflection contribution. Therefore, for high emissivity values (greater than 0.8) or for high values of the surface temperature (compared to the surrounding environment), the contribution of reflected energy is minimal and can be neglected.

Outside these conditions it is difficult to distinguish the influence; to improve the accuracy of the measurement, it is preferable to shield the heat sources that cause reflection rather than try to quantify their value.

Another important aspect to consider is that the atmosphere interposed between the detection device and the target is not completely transparent to infrared radiation. In most cases the gases can be considered transparent to radiation; moreover, they absorb or emit in certain narrow bands of wavelength. Some gases, such as oxygen and nitrogen, with non-polar symmetrical molecular structure are transparent at low temperatures, while carbon dioxide and water vapor cannot be considered as such.

An accurate temperature measurement can only be obtained if the correct value of the transmissivity coefficient τ_a of the interposed medium is considered.

The air, which is generally an interposed medium in most measurement operations, is characterized by bands of good transparency called "atmospheric windows" and bands of absolute opacity, in which the absorption of radiation is high.

Two main atmospheric windows can be identified:

- The first atmospheric window, which extends from 0.46 µm to 5.6 µm, including the visible, near infrared and medium infrared bands; The lower infrared transparency is due to the presence in the air of some components such as carbon dioxide and water vapor.
- The second atmospheric window, between 7.5 µm and 14 µm, is entirely contained in the far infrared band; it has a transparency that reaches an average value of 80% and has no areas of opacity, making it more suitable for long distance measurements.
- The transparency of the air to radiation depends, as for all aggregates of matter, on the thickness; thus, it is preferable to reduce the air thickness, i.e. to reduce the distance between sensor and target.

1.2.2. Hardware description

The physical principles illustrated in paragraph 1.1 are the basis of the operation of the thermal imaging camera, which converts the incoming information from the radiative energy that hit the sensor into a bidimensional heat map of the observed surface.

The input to the infrared camera is the thermal energy radiated by the target and at the output are electronic signals. These signals are focused onto the detector by the optics and then amplified and transmitted to the apparatus that operates the video processing and provides the final bidimensional information on a screen.

The input signal is processed through the following path:

- pass through the optical scan module: lens, any filters and a mirrors chain which address the signal to a series of optical relays equipped with an opening unit and filters
- focusing on the detector that operates the signal conversion from optical to electronics
- amplification by the preamplifier and conversion into a 12 bit digital signal by the A/D converter
- Transmission to the Microprocessor through optical fibres

Figure 8 shows a simplified block diagram of an IR camera.

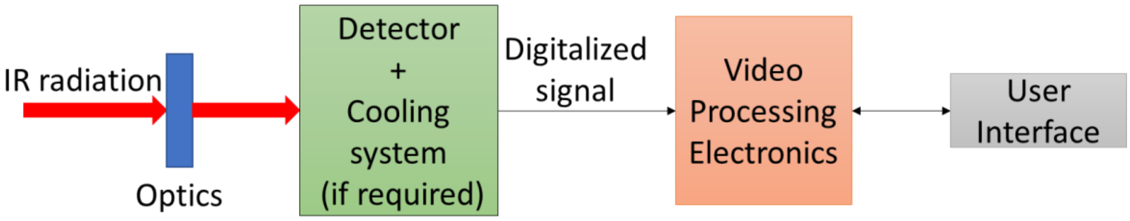

Figure 8 Simplified block diagram of an IR camera [7]

The IR cameras sensors are always protected by optics that shield them from the environment; moreover, in many applications the use of filters may be required, in order to reduce the radiation impinging the sensor for a given temperature value and shifting the sensor saturation to higher temperatures.

The optics and filters are transparent only at certain wavelengths. The exact amount of radiation that reaches the sensor depends not only on the transmissivity curve of all the interposed windows but also on the emission of the optic itself and the reflection effects due to the surrounding environment.

The materials mainly used are fluorocarbons such as silicon and germanium. These materials have good mechanical proprieties, they are not hygroscopic, and they can be formed into lens. Each material can be transparent in a certain infrared band and can be opaque in the remaining areas of the electromagnetic spectrum, so they must be selected for the desired range.

Some materials used in the construction of infrared optics are shown in Table 2 together with their cutting wavelength.

Table 2 Material for optics and their cutting wavelengths.

MATERIAL	**λ of cut approx. [μm]**
Germanium (Ge)	50
Silicon (Si)	40
Arsenic trisulfide (As_2S_3)	12
Irtran 2 (ZnS)	14
Sapphire	7
Irtran 1 (MgF)	8

1.2.3. Infrared detectors

Detectors are the main element of the infrared imaging system; their function is to acquire infrared radiation and turn it into an interpretable signal. In theory any physical property sensitive to temperature can be exploited.

The first infrared image system was created by Herschel in 1840; the system consisted of a liquid in a glass thermometer with a specially blackened bulb to absorb radiation. This crude monochromator used a thermometer as a detector to measure the distribution of energy in sunlight.

One of the first solution employed to obtain infrared images was the evaporograph developed in 1929 by Czerny. The evaporograph physical principle was the differential evaporation of a thin film of oil on a dark membrane, thus differences of reflectivity with visible light on the dark membrane allow the visualization of the infrared image.

Since then, the technologies used for detectors have evolved towards increasingly sophisticated devices, with high sensitivity and very high acquisition frequency. The detector in modern IR is a focal plane array (FPA), that is an array of micrometric size pixels made of various materials sensitive to IR wavelength.

The response curve of most detectors does not cover the full IR range. For this reason, detectors must be selected considering the IR range of the user's application.

To rate infrared detectors, it is possible to refer to the values of some characteristic parameters, such as:

The impedance, that is the intrinsic detector characteristic measured using Ohm's law:

$$Z = \frac{dV}{dI} \ [ohms] \qquad \text{Eq 20}$$

The responsivity, that is the transformation ratio of the incident optical flow *F*:

$$R_v = \frac{\partial V}{\partial F} \ [V \cdot W^{-1}] \qquad \text{Eq 21}$$

The Noise Equivalent Power (NEP), that is the amount of Power induced by an optical signal whose amplitude is equivalent to the intrinsic noise power. The related incident optical flow is cooled the noise equivalent flow FNEP.

The Noise Equivalent Temperature Difference (NETD), that is the change in temperature of a large blackbody in the observed scene, causing a change in the signal-to Noise ratio of unity in the output of the detector.

Detectivity, it is defined as the ratio:

$$D = \frac{1}{F_{NEP}} \, [W^{-1}] \qquad \text{Eq 22}$$

To compare the detectivity of different detectors, the detectivity D*, measured in W^{-1} cm $Hz^{1/2}$ is introduced by scaling D to the unit sensitive detector area and unit of bandwidth.

Figure 9 shows the spectral response for some infrared detectors families, the spectral atmospheric window is also plotted.

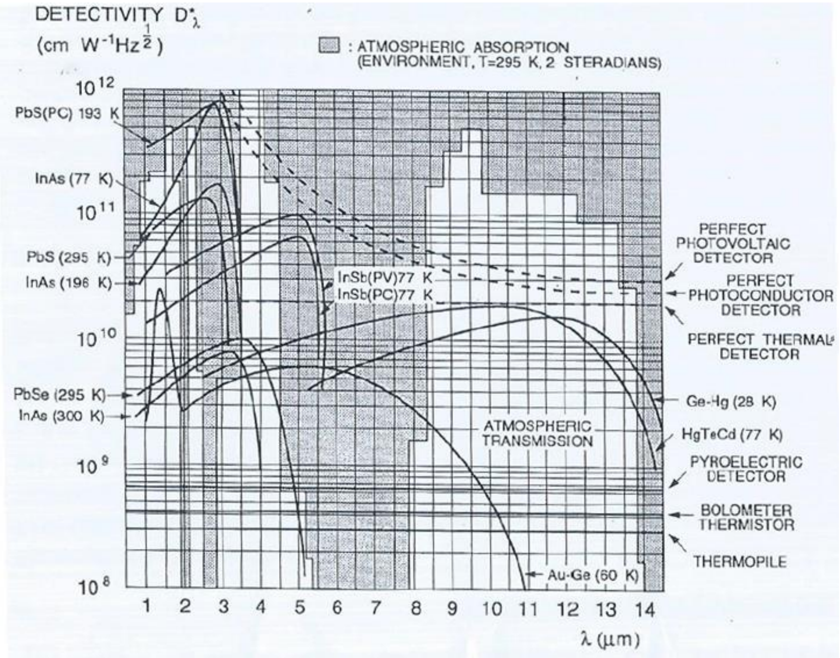

Figure 9 Spectral detectivity of infrared detectors. Atmospheric absorption bands are also included.

The first detectors classification divides the FPA into two main categories: thermal detectors and photonic detectors.

Thermal detectors consist of materials for which a particular physical property varies with temperature, in such a way to produce a measurable signal when the incident radiation heats their surface and the heating affects this property.

For this kind of detectors, the response is independent of the radiation wavelength.

The technologies that over the years have been used as thermal detectors are: Bolometers, thermopiles, Pneumatic detectors, Pyroelectric detectors and Liquid Crystals.

Modern IR cameras with thermal detector are commonly equipped with an uncooled microbolometer made of a metal or semiconductor material which operates according to non-quantum principles.

The main advantages of such devices are the low cost, the wide IR spectral response (limited only by the entry optics and the presence of any filter) and no cooling is required (allowing a compact camera design). The disadvantages include: a slow reaction to the incident radiation (~12ms), a small range of observable temperatures, a detectivity only about half as good as photonic detectors and an average quality of the images.

Photonic detectors are semiconductor whose free electrons states are affected by the incident radiation. When the incident photon heats the sensor, its energy releases an electron, augmenting the density of free electrons and thus increasing the detector electrical conductivity or its output voltage. The photonic detector response depends on the incident photon wavelengths since a given energy amount is needed to move electrons.

Photonic detectors response is faster that thermal devices since no temperature increase is required, They react to changes in IR levels with a constant response time on the order of 1μs. However, they require cooling, even up to cryogenic temperature using liquid nitrogen or small Stirling cycle refrigerator system.

The most common materials employed as photonic detectors are Si, InAs, InSb, HgCdTe, InGaAs, PtSi and layered GaAs/AlGaAs. These materials respond to IR by absorbing photons that elevate the material’s electrons to higher energy state, causing a change in conductivity, voltage or current. The sensitivity of these materials to IR increases when they are cooled to cryogenic temperatures.

There are three main Infrared Cameras technologies that employ photonic detectors, these are:

Systems equipped with point detectors (single pixel sensor) and mechanical scanning for image formation

Systems equipped with SPRITE detectors and mechanical scanning for image formation. The SPRITE (Signal Processing In The Element) was developed by the Royal Signals and Radar Establishment (UK)

Cameras using InfraRed Focal Plane Arrays (IRFPA), that involve an electronic scanning of the image.

IRFPAs constitute the technology used in modern thermal imaging cameras and their evolution is currently in a state of flux.

A detailed chronology of IRFPAs architecture development and the current state of art can be found in the work of Kinch [8].

CHAPTER 2.

MATERIALS AND COMPONENTS CHARACTERIZATION BY MEANS OF IR TECHINQUES

The use of thermographic techniques for the characterization of materials is a practice that in recent years is assuming an increasingly important role in the scenario of experimental mechanics.

Their potential is based on the possibility to exploit the thermal signal as sentinel of physical phenomena and use it together with the physical understanding of the system in order to characterize the variables of interest.

The reasons why IR thermography has found wide use and diffusion in various sectors and it is currently a method of great interest in the field of applied research are to be found among its exclusive features:

- It is a contactless remote sensing technique: measurements are performed at a distance and do not require direct contact with the target. This feature involves several advantages, including greater operator safety, greater accessibility, ability to monitor movable or rotating objects, no wires to connect and no need to make changes to the object to be measured to increase the resolution (such as the increase of holes and wires that would require thermocouples). Furthermore, the distance between heat source and detector allows to measure also very hot objects.
- It allows the elaboration of full-field surface temperature maps. The information provided by a thermographic acquisition is bi-dimensional, being the result of temperature measurements on multiple points of the surface under examination. The image thus obtained allows a quick diagnosis of the state of the surface,

providing a clear overview from which, it is possible to identify the critical and interesting points.

- It provides real-time information. Since the thermal radiation propagates at the speed of light and thank to the high technology and sophistication of the equipment available today, it manage to capture phenomena at very high frequencies kipping the characteristic time constants of measuring process very small, due to miniaturisation.
- The availability of portable IR cameras allows the in-situ testing of structures and component under their workloads and full-scale conditions.

The applications explored so far both in the academic and industrial sectors are different and each characterized by a different level of maturity. The possibilities of their improvement grow hand in hand with the new technologies that push towards ever more demanding and marketable solutions.

The current applications are manifold.

Thermography is widely used in non-destructive testing, to detect and characterize defects affecting components and structures; in this case the physical principle exploited is the different response to thermal excitation due to the differences in thermophysical behaviour between the sound area and the anomalies such as cracks, delamination, inclusions etc..

The response to thermal excitation can be also employed in order to characterize the thermo-physical proprieties of surfaces, such as their emissivity and diffusivity and to determine the nature of propagation of a heat flux in materials.

The source of excitation that involves a temperature variation can be not only thermal, but also mechanical: vibrations, acoustic waves or a simple mechanical load can be used.

In the latter case, the physical phenomenon that is exploited is the thermoelastic effect, i.e. the generation of small reversible temperature variations, following deformations in the elastic field. Such a relation allows to link the stress field to the thermal response and the technique is known as Thermoelastic Stress Analysis.

The thermoelastic stress analysis (TSA) is a well-established, non-contact technique used to assess the superficial stress field exploiting the thermoelastic effect, i.e. the generation of small and reversible temperature variations linked to the volume variation in components subjected to a dynamic load in the linear elastic range [9]

In recent years, the development of highly performing IR cameras allowed the large employment of the TSA in several applications. In particular, the advantages of being contactless, full field, totally safety for the component and not requiring substantial surface preparation make the TSA a valid tool for testing real components and validating finite element models (FEM) [10][12][13].

The applicability of such a technique has been demonstrated in stress measurement [10][14][15], residual stress measurement [16][17][18], fracture mechanics [13][19][20][21] and fatigue characterization [22][23][24].

The TSA deployment as stress measurement technique is consolidated and researcher validated calibration procedures aiming to obtain both a precise and accurate result [25][26].

The other large slice of applications involves the use of passive thermographic techniques, i.e. that do not require the action of an external source of excitation. This category includes all the process monitoring and radiometric measurements techniques.

In this work four particular applications have been identified for an in-depth study aimed at exploring their potential and limits, with the objective of developing them by proposing new and improved approaches.

The four applications are: 1)The evaluation of the superficial stress field of components and structures by means of the Thermoelastic Stress Analysis (TSA), 2) The identification of residual stress exploiting the mean load effect on the Thermoelastic signal, 3) the fracture mechanics characterization of components 4) The temperature measurement in aerospace applications implementing the free-emissivity dual color technique.

2.1. Thermoelastic Stress Analysis (TSA)

2.1.1. Historical Background

Figure 10[27] shows the thermoelectricity history as told by Harwood and Cummings [10] and Stanley [28].

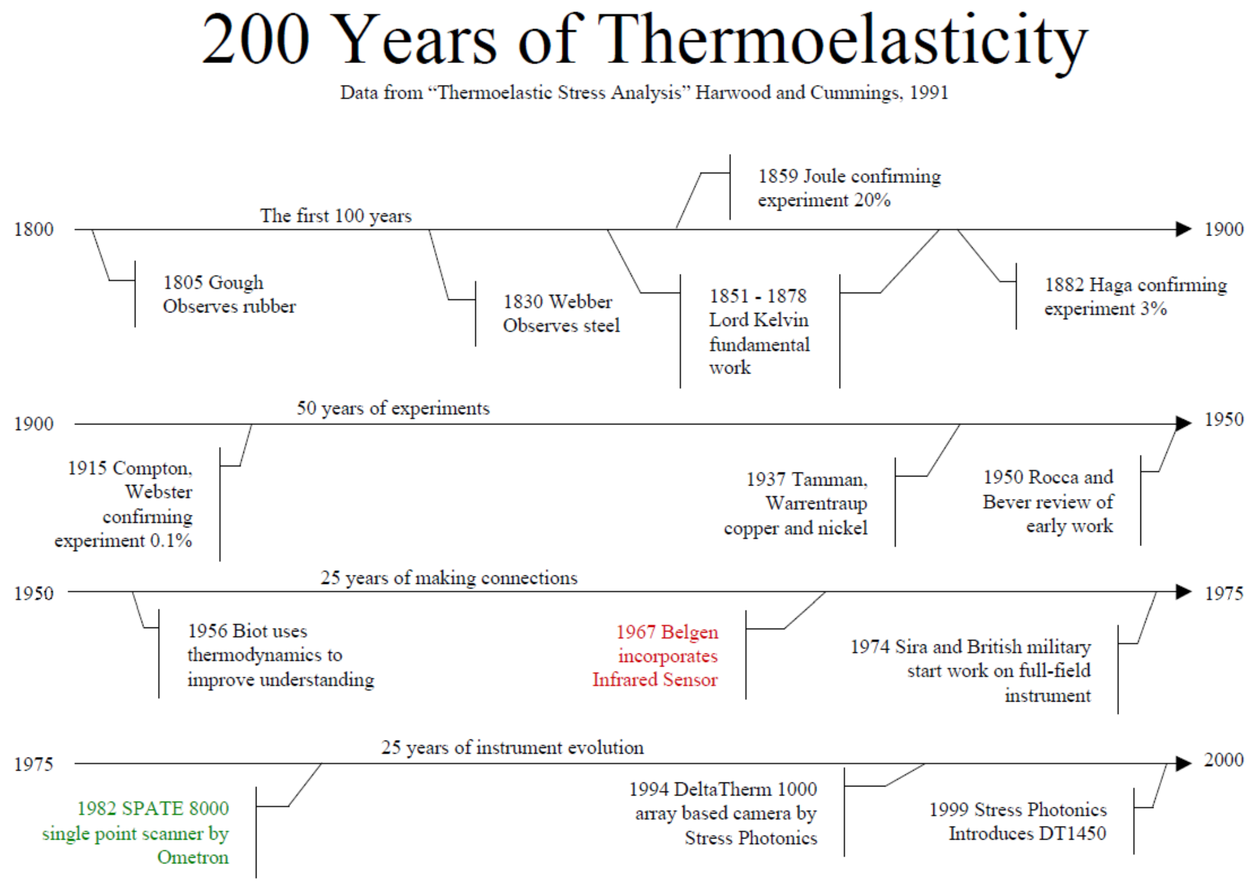

Figure 10 the thermoelectricity history as told by Harwood and Cummings [27]

The succession of discoveries that led to the development of TSA began in 1805, when for the first time Gough, intent on experiments with strands of natural rubber, noted the cause-effect relationship between the application of a load and temperature variation[29].

The first observation of the thermoelastic effect on metals is attributed to Weber, who in the 1830 during experiments on vibrating metallic wires noticed a gradual variation of the fundamental frequency in the face of a sudden change of tension [30]. He attributed this gradual transient effect to the temperature variation that followed the change in tension, however, he did not elaborate on an explanation of the observed effect.

The study of the thermoelastic effect was started in 1851 by Lord Kelvin, who first developed the thermodynamic theory for isotropic solids subjected to a generic stress field [31][32]. Since then, many researchers have been working on validating Lord Kelvin's theory, including Joule[33][34][35].

In 1915 Compton and Webster developed a high precision temperature measurement system which measured the resistance variations induced in a piano string directly connected to the Wheatstone's bridge. Such an experiment was able to validate the predictions of Lord Kelvin's theory with a mean deviation of 0.1%[36].

The thermoelastic theory was further refined in subsequent years by Biot [9], who in the 1956 first proposed the classical TSA equation currently used in most applications.

In 1967 Belgen took a fundamental step for thermoelastic stress analysis, proposing for the first time the combination of TSA and thermography. Belgen's paper [37] presented a new method of determining the stresses in structural components using infrared radiometer measurements, however thermography was not yet a easily usable technology at the time and his work did not lead to the development of a commercial radiometer for full-field stress measurement.

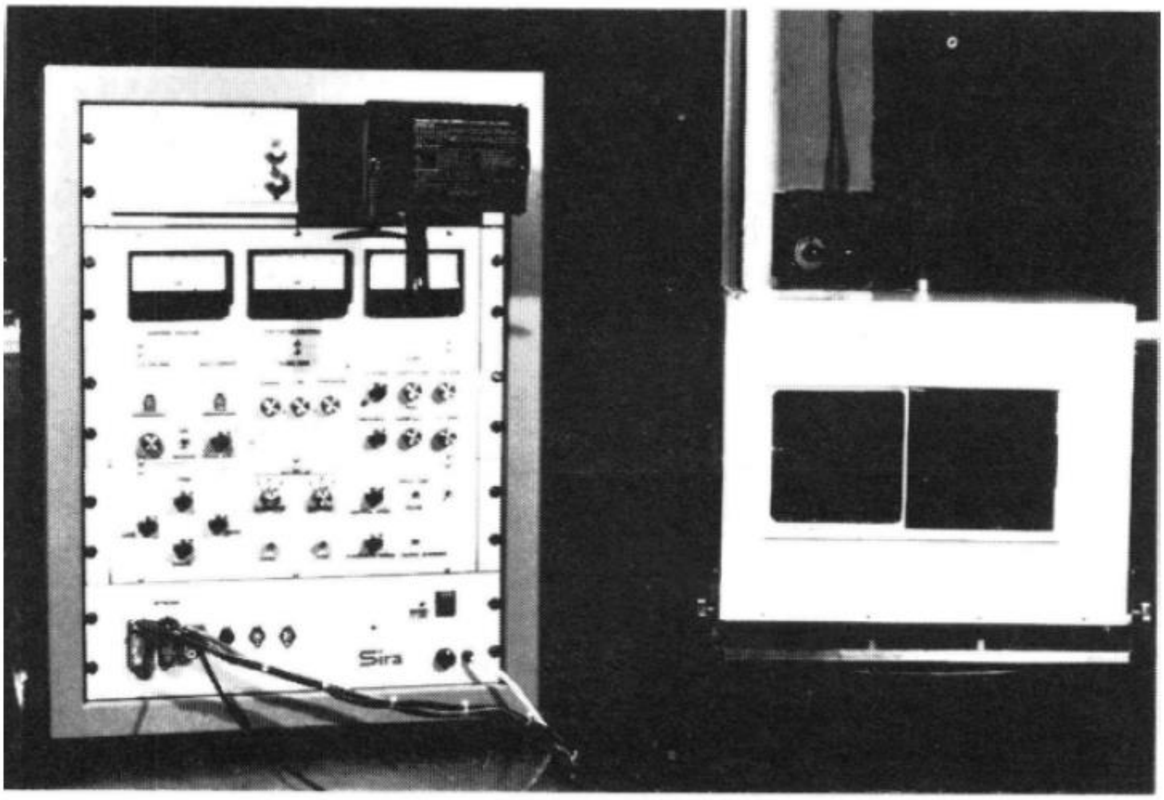

Figure 11 SPATE 8000 equipment

One of the most important milestones in the development of technology for thermoelastic stress analysis was reached in 1974, when Sira Ldt, commissioned by the Admiralty

Research Establishment, started to work on the SPATE (Stress Pattern Analysis by measurement of Thermal Emission) prototype.

The SPATE system was equipped with a single photon detector, but it was able to provide full-field stress maps by analysing the thermal signal of surfaces through a chain of motorized mirrors that performed the scan.

With both a public and private funds, the evolution of the SPATE technology continued. In the 1982 the first industrial commercial product was released with the name SPATE 8000, and in the 1987 the improved version, the SPATE 9000 was presented.

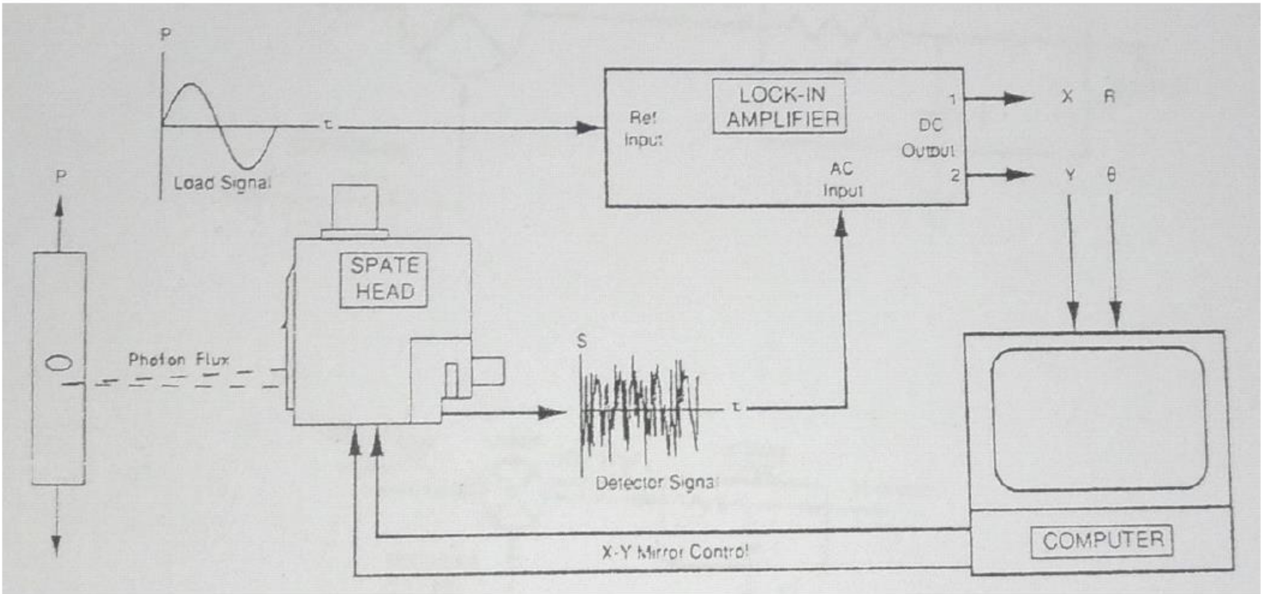

Figure 12 SPATE 9000 block diagram system

In 1994 Stress Photonics introduced a fast-imaging array-based instrument. The implementation of the infrared FPA shortened the time to produce a high quality full-field image to under a minute. The product launched on the market was the DELTATHERM (Figure 13), which in its latest versions is currently industrially employed to evaluate the surface distribution of stress in engineering components.

DELTATHERM® 1350, 1450, 1550

Full-field Thermoelastic Stress Measurement System

The DELTATHERM, by Stress Photonics, is a unique IR differential thermography system suited to Thermoelastic Stress Analysis (TSA) and Thermal Nondestructive Evaluation (TNDE). By coupling special high-speed image processing electronics with a high-performance infrared array detector, it is now possible to image stresses in ***just seconds!***

Applications

- *Thermoelastic Stress Analysis*
- *Lock-In Thermography*
- *Standard Thermography*
- *Forced-diffusion Thermography*
- *Coating Tolerant Thermography*
- *Fracture Mechanics*
- *Crack and Flaw Detection*
- *Structural Integrity Assessment*
- *Composite Material Damage Evolution*
- *Composite Material Fatigue Life Prediction*

Figure 13 DeltaTherm equipment.

From 1994 to today, the technology of detectors has rapidly evolved to make commercial devices with high performance such as modern cooled thermal imaging cameras equipped with photonic FPA (described in paragraph 1.2.3). Currently the TSA analysis is carried out using these devices and the data processing is entrusted to lock in analysis algorithms. On the market there are software compatible with the data acquired by thermal cameras that carry out such analyses. In this study the TSA work was conducted by using IR cooled cameras produced by FLIR® and the commercial software IRTA®.

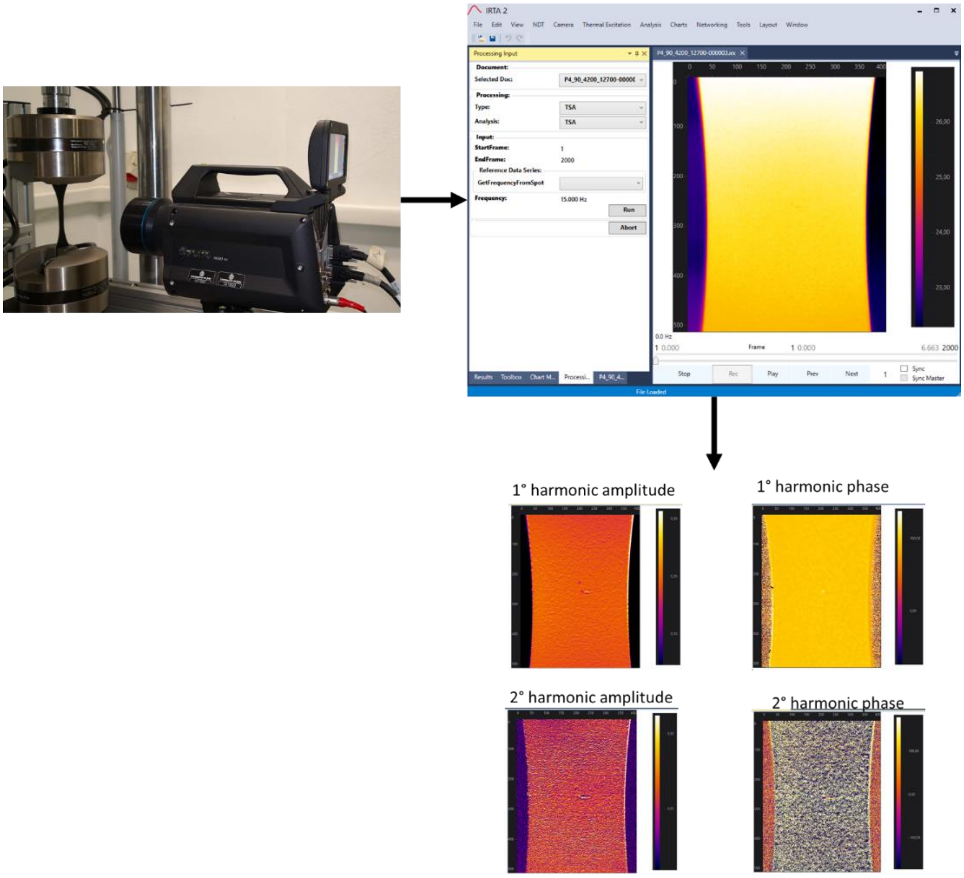

Figure 14 Modern TSA equipment and data flow

2.1.2. Thermoelastic classical theory

The demonstration of the classical equation describing the relationship between stress variation and the related thermoelastic temperature variation starts from the thermodynamic laws [14].

The first and second thermodynamic laws for a reversible process can be written as:

$$du = \delta q + \delta w \qquad \text{Eq 23}$$

and

$$\begin{gathered} ds = \frac{\delta q}{T} \geq \frac{(\delta q)_{reversible}}{T} \\ (ds)_{reversible} = \frac{(\delta q)_{reversible}}{T} \end{gathered} \qquad \text{Eq 24}$$

Where *u* is the internal energy, *w* and *q* are the work and the heat respectively exchanged between the considered system and the external environment and *s* is the entropy.

From the virtual work principle in the case of a continuum in equilibrium under quasi-static and small (compared to the system dimensions) deformations, it derives:

$$\delta w = \frac{\sigma_{ij} d\varepsilon_{ij}}{\rho}$$
$$\text{with } i,j = 1-3 \qquad \text{Eq 25}$$

Where σ_{ij} and ε_{ij} are respectively the stress and strain tensor and ρ is the material density.

Combining Eq 23 with Eq 24 and Eq 25 for local reversible changes it derives:

$$du = Tds + \frac{\sigma_{ij} d\varepsilon_{ij}}{\rho} \qquad \text{Eq 26}$$

The Helmholtz thermodynamic potential is defined in its differential form as:

$$H = du - Tds - sdT \qquad \text{Eq 27}$$

Substituting Eq 26 into Eq 27 gives:

$$H = \frac{\sigma_{ij} d\varepsilon_{ij}}{\rho} - sdT \qquad \text{Eq 28}$$

The state of an elastic solid is defined by two state variables, such as the temperature *T* and the strain tensor $\overline{\varepsilon}$ or *T* and the stress tensor $\overline{\sigma}$ (according to the linear strain-stress-temperature relationship). Any state function, such as the Helmholtz thermodynamic potential *H* and the entropy *s*, can be written as:

$$H = H(\varepsilon_{ij}, T)$$
$$s = s(\varepsilon_{ij}, T) \qquad \text{Eq 29}$$

And

$$dH = \left(\frac{\partial H}{\partial \varepsilon_{ij}}\right)_T d\varepsilon_{ij} + \left(\frac{\partial H}{\partial T}\right)_{\varepsilon_{ij}} dT$$

$$ds = \left(\frac{\partial s}{\partial \varepsilon_{ij}}\right)_T d\varepsilon_{ij} + \left(\frac{\partial s}{\partial T}\right)_{\varepsilon_{ij}} dT$$

Eq 30

From the comparison between Eq 28 and Eq 30:

$$\sigma_{ij} = \rho \frac{\partial H}{\partial \varepsilon_{ij}}$$

$$s = -\frac{\partial H}{\partial T}$$

Eq 31

The definition of specific heat per unit mass at zero strain can be written as:

$$C_\varepsilon = \left(\frac{\partial q}{\partial T}\right)_{\varepsilon_{ij}} = \left(\frac{T ds}{\partial T}\right)_{\varepsilon_{ij}} = T\left(\frac{ds}{\partial T}\right)_{\varepsilon_{ij}} = -T\left(\frac{\partial^2 H}{\partial T^2}\right)_{\varepsilon_{ij}}$$ Eq 32

Combining Eq 31 and Eq 32 with Eq 30, gives:

$$ds = -\frac{\partial^2 H}{\partial \varepsilon_{ij} \partial T} d\varepsilon_{ij} - \left(\frac{\partial^2 H}{\partial T^2}\right)_{\varepsilon_{ij}} dT$$ Eq 33

And after few mathematical steps:

$$ds = \frac{\delta q}{T} = -\frac{1}{\rho}\frac{\partial \sigma_{ij}}{\partial T} d\varepsilon_{ij} + C_\varepsilon \frac{dT}{T}$$ Eq 34

Integrating Eq 34 and setting at the starting conditions $\varepsilon_{ij}=\varepsilon_{ij0}$ and $T=T_0$, the following relationship was determined by Biot[9]:

$$\rho C_\varepsilon \Delta T = T_0 \frac{\partial \sigma_{ij}}{\partial T} \Delta\varepsilon_{ij} - \delta q$$ Eq 35

The constitutive Law for a solid with linear elastic behaviour is:

$$\sigma_{ij} = 2\mu\varepsilon_{ij} + (\lambda\varepsilon_{kk} - \beta\Delta T)\delta_{ij} \qquad \text{Eq 36}$$

where ΔT is the temperature difference respect to the reference T_0, ε_{kk} is the first strain invariant, δ_{ij} is the Kronecker delta (δ_{ij}=1 if $i=j$, δ_{ij}=0 if $i \neq j$), μ and λ are the Lamè constants:

$$\mu = \frac{E}{2(1+\nu)}, \qquad \lambda = \frac{\nu E}{(1+\nu)(1-2\nu)} \qquad \text{Eq 37}$$

and β is given by:

$$\beta = (3\lambda + 2\mu)\alpha \qquad \text{Eq 38}$$

with α linear thermal expansion coefficient.

Assuming that the Lamè elastic parameters are independent of temperature (i.e. neglecting the dependence on temperature of thermal and mechanical characteristics of the material), the derivative respect to the temperature of Eq 36 becomes:

$$\frac{\partial\sigma_{ij}}{\partial T} = -\beta\delta_{ij} \qquad \text{Eq 39}$$

Under adiabatic condition (hypothesis verified by applying a periodic dynamical load with a frequency high enough to neglect diffusion effects), substituting Eq 39, Eq 37 and Eq 38 into Eq 35 gives:

$$\Delta T = -\frac{E\alpha T_0}{\rho C_\varepsilon(1-2\nu)}\Delta\varepsilon_{kk} \qquad \text{Eq 40}$$

From Eq 36, Eq 37 and Eq 38 it derives:

$$\Delta\varepsilon_{kk} = \frac{1-2\nu}{E}\left(\Delta\sigma_{kk} + \frac{3E\alpha\Delta T}{1-2\nu}\right) \qquad \text{Eq 41}$$

Substituting Eq 41 into Eq 40 gives:

$$\Delta T = -\frac{\alpha T}{\rho C_\varepsilon}\left(\Delta\sigma_{kk} + \frac{3E\alpha\Delta T}{1-2\nu}\right) \qquad \text{Eq 42}$$

Where σ_{kk} represents the first stress invariant and $\Delta\sigma_{kk}$.its variation.

From Eq 42 it derives:

$$\Delta\sigma_{kk} = -\frac{\Delta T}{\alpha}\left(\frac{\rho C_\varepsilon}{T_0} + \frac{3E\alpha^2}{1-2\nu}\right) \qquad \text{Eq 43}$$

By applying relationship between the specific heat at constant pressure and the specific heat at constant deformation:

$$C_p - C_\varepsilon = \frac{3\alpha^2 E T_0}{\rho(1-2\nu)} \qquad \text{Eq 44}$$

Eq 43 becomes:

$$\frac{\Delta T}{T_0} = -\frac{\alpha}{\rho C_p}\Delta\sigma_{kk} \qquad \text{Eq 45}$$

The thermoelastic constant is defined as the quantity:

$$K = \frac{\alpha}{\rho C_p} \qquad \text{Eq 46}$$

Eq 45 is the TSA basic equation, and it is valid in adiabatic condition for homogeneous isotropic bodies undergoing elastic deformation and with the assumption of mechanical characteristics of the material independent of the temperature.

One of the main issues concerning the TSA is that the proportionality gives information about the first scalar invariant of the stress tensor, but it is not possible to get information about the stress component and their orientation. Over the years several researchers have tried to tackle this problem by proposing different stress separation techniques, based on the combination of TSA with other non-destructive experimental techniques. A common combination is simultaneous thermo- and photo- elasticity analyses [39].

2.1.3. Experimental measurement of the Thermoelastic Temperature variation

The TSA is based on the measurement of temperature variations of the order of 0.001 °C [14] that occur when a material is subject to an elastic strain variations.

The measurement of such the small temperature variation requires the use of IR camera with high sensitivity and high resolution. Before modern cooled IR cameras came on the market, the TSA was performed by differential infrared thermal cameras (such as the SPATE and DeltaTherm systems described in paragraph 2.1.1).

The detector of these cameras is an IR photon detector and it is sensitive to the photon flux received in its operation range of IR wavelength. The IR energy received is then converted into a voltage and further processed by the system (paragraph 1.2.2).

As demonstrated in paragraph 1.1.4, the relation between the measured photon flux and the temperature of the emitting body can be approximated by adopting the grey body hypothesis (Eq 19).

It follows by differentiation that the flux change, resulting from a small change in the surface temperature, ΔT, is given by [15]:

$$\Delta E \approx \Delta E_g = 4\varepsilon B T_0^3 \Delta T \qquad \text{Eq 47}$$

Combining Eq 47 with Eq 45 and Eq 46 gives:

$$\Delta E \approx -4\varepsilon B T_0^4 K \Delta\sigma_{kk} \qquad \text{Eq 48}$$

If the flux change ***ΔE*** is recorded by a linear detecting system, the signal *S* will be proportional to the change in temperature ΔT:

$$S = (-4R\varepsilon B T_0^4 K)\Delta\sigma_{kk} \qquad \text{Eq 49}$$

Where *R* is the detector response factor, which is determined by the manufacturer of the system.

The bracketed term in Eq 49 is the inverse of a constant of proportionality which is referred to as calibration factor A and it is dependent on the detector material. By including A in Eq 49 the familiar form of the TSA equation is obtained:

$$AS = \Delta\sigma_{kk} \qquad \text{Eq 50}$$

2.1.4. Classical Calibration methods

For quantitative stress analysis it is important to employ accurate value of the calibration factor.

If the signal is available in the form of calibrated temperature value, the calibration proportional factor is the thermoelastic parameter K.

When the analysis starts from the uncalibrated signal, the calibration factor to determine is A.

The calibration possibilities are the following [40][41]:

1) To calibrate from the radiometric properties of the detector, the systema variables and known values for the thermal and mechanical proprieties of the material.
2) To calibrate experimentally measuring deformation and applying the linear elastic relation to get the stress.
3) To calibrate experimentally using a specimen with simple geometry and a known stress distribution.

The first method requires the accurate knowledge of the material proprieties and the detector characteristics and can be very susceptible to errors[40].

The main advantage of the second method is that it can be used on the actual component, but its accuracy depends on the accuracy of the experimental method used for strain measurements and on the knowledge of the elastic proprieties of the material.

The third calibration method requires separate calibration experiments, but the sources of error are reduced at the minimum if the samples are manufactured and the test are performed with high accuracy.

2.1.5. The higher order theory

In adiabatic conditions and neglecting the dependence of thermo-mechanical proprieties from temperature, the thermoelastic signal is proportional to the sum of the principal stresses[9][10]. If this dependence is not neglected, the thermoelastic signal is affected also by the mean load.

This result has been first observed by Belgen [42] and widely demonstrated both analytically and experimentally by Machin et al.[43], Dunn et al.[44] and Wong et al. through the revised higher order theory [45][46].

Wong et al. [37][42][43][44][45][46] demonstrated and experimentally validated this result and highlighted the potential to employ the TSA for the residual stress evaluation [16][17][46][47][48][49].

Wong's second order equation for the thermoelastic parameter evaluation is valid only for isotropic materials under monoaxial load. Potter and Graves [143]proposed a more general equation, valid for anisotropic materials.

The mean stress effect on the thermoelastic signal can be neglected for almost all the steels [14], but cannot be neglected for non-ferrous alloys, such aluminium and titanium alloys [14] [45][46][50][53].

If the elastic and thermal proprieties are temperature-dependent the derivation of the constitutive law gives:

$$\frac{\partial \sigma_{ij}}{\partial T} = 2\frac{\partial \mu}{\partial T}\varepsilon_{ij} + \left(\frac{\partial \lambda}{\partial T}\varepsilon_{kk} - \frac{\partial \beta}{\partial T}\Delta T - \beta\right)\delta_{ij} \qquad \text{Eq 51}$$

By substituting into Eq 34, yields [45][46]:

$$T\left[\left(-\beta - \frac{\partial \beta}{\partial T}\Delta T + \frac{\partial \lambda}{\partial T}\varepsilon_{kk}\right)\delta_{ij} + 2\frac{\partial \mu}{\partial T}\varepsilon_{ij}\right]d\varepsilon_{ij} - \rho_0 C_\epsilon dT = \delta q \qquad \text{Eq 52}$$

Assuming adiabatic conditions and writing Eq 52 in terms of principal strain ε_i [45][46]:

$$\rho_0 C_\epsilon \frac{dT}{T} = -\left(\beta + \frac{\partial\beta}{\partial T}\Delta T - \frac{\partial\lambda}{\partial T}\varepsilon_{kk}\right) d\varepsilon_{kk} + 2\frac{\partial\mu}{\partial T}\varepsilon_i d\varepsilon_i \qquad \text{Eq 53}$$

Substituting Eq 37 and Eq 38 in Eq 53, neglecting the high order terms and the term $(\partial\beta/\partial T)\Delta T$ and expressing in terms of principal stresses [45][46], it gives:

$$\rho C_\varepsilon \frac{dT}{T} = -\left[\alpha + \left(\frac{\upsilon}{E^2}\frac{\partial E}{\partial T} - \frac{1}{E}\frac{\partial\upsilon}{\partial T}\right)\sigma_{kk}\right] d\sigma_{kk} + \left[\frac{(1+\upsilon)}{E^2}\frac{\partial E}{\partial T} - \frac{1}{E}\frac{\partial\upsilon}{\partial T}\right]\sigma_i d\sigma_i \qquad \text{Eq 54}$$

To achieve adiabatic condition a cyclic load is usually applied, it is therefore interesting to simplify Eq 54 in the case of a one-dimensional stress that changes over time with a sinusoidal waveform. The uniaxial stress state can be expressed as [46]:

$$\begin{aligned} &\sigma_{11} = \sigma_m + \Delta\sigma\sin(\omega t), \quad \sigma_{22} = \sigma_{33} = 0 \\ &\frac{d\sigma_{11}}{dt} = \omega\Delta\sigma\cos(\omega t), \qquad \frac{d\sigma_{22}}{dt} = \frac{d\sigma_{33}}{dt} = 0 \end{aligned} \qquad \text{Eq 55}$$

where σ_m and σ_a represent the mean and the amplitude stresses respectively.

Substituting Eq 55 into Eq 54 and assuming $\frac{\partial v}{\partial T} \approx 0$ ([50][51]), the integration of Eq 54 gives:

$$\rho C_\varepsilon \frac{\Delta T}{T_0} = -\left(\alpha - \frac{1}{E^2}\frac{\partial E}{\partial T}\sigma_m\right)\Delta\sigma\sin\omega t - \frac{1}{4E^2}\frac{\partial E}{\partial T}(\Delta\sigma)^2\cos 2\omega t \qquad \text{Eq 56}$$

In Eq 56 it is clear how the mean stress effect is strictly related to the Young modulus variation with the temperature. Moreover, it is interesting as a part of the thermoelastic signal occurs at the twice of the loading frequency.

Following the approach already used by Patterson et al. [47], Palumbo et al. [25] Galietti et al. [17] and Di Carolo et al. [18] the Thermoelastic parameters *a* and *b* are defined as:

$$a = -\frac{\alpha}{\rho\cdot C_\varepsilon}, \quad b = \frac{1}{E^2\cdot\rho\cdot C_\varepsilon}\cdot\frac{\partial E}{\partial T} \qquad \text{Eq 57}$$

Typical TSA analysis are conducted with a lock-in amplifier, allowing to discriminate the amplitude of the signal at the same frequency of the load.

By focusing on the semi-amplitude of the temperature running at the same loading frequency ΔT_1 and substituting with Eq 57, one can describe the temperature variations as:

$$\frac{\Delta T_1}{T_0} = -\mathrm{a}\Delta\sigma + b\sigma_m\Delta\sigma \qquad \text{Eq 58}$$

If γ is the ratio between σ_m and σ_a, constant for each pixel for a fixed test, Eq 58 can be written as follow:

$$\frac{\Delta T_1}{T_0} = -\mathrm{a}\Delta\sigma + b\gamma\Delta\sigma^2 \qquad \text{Eq 59}$$

The constants *a* and *b* can be determined through literature, or experimentally, therefore in adiabatic condition, for homogeneous isotropic bodies subjected to elastic and uniaxial load with sinusoidal waveform, the stress can be evaluated by measuring the thermoelastic signal ΔT and solving:

$$a\Delta\sigma + b\gamma\Delta\sigma^2 - \frac{\Delta T}{T_0} = 0 \qquad \text{Eq 60}$$

2.1.6. Calibration procedure to correct the mean load effect

Palumbo et al. proposed a calibration procedure in order to experimentally evaluate the thermoelastic parameters a and b needed for the Stress calculation [25].

The procedure is based on the calibration against calculated stress.

The experiments involve the implementation of dynamical loading tests on samples with a known stress distribution.

Usually, dog bone samples with a monoaxial and uniform stress distribution in the useful section are employed.

In this case, if a one-dimensional sinusoidal stress is applied, Eq 24 allows to evaluate the semi-amplitude of the thermoelastic signal running at the same loading frequency.

Dividing Eq 24 by the amplitude of the load σ_{a1}, gives:

$$\frac{\Delta T_1}{T_0 \sigma_{a1}} = -a + b\sigma_{m1} \qquad \text{Eq 61}$$

The parameters *a* and *b* represent intercept and slope respectively of the linear relation expressed by Eq 66 and can be evaluated by fitting experimental data (Figure 15).

The calibration involves the following steps:

1. Acquisition with an IR camera of thermoelastic signal during sinusoidal loading tests on dog bone samples at different levels of mean load.
2. Lock-in analysis and calculation of the first harmonic amplitude ΔT_1 and reference temperature T_0.
3. Evaluation of the thermoelastic parameters *a* and *b* by fitting the experimental data Eq 66.

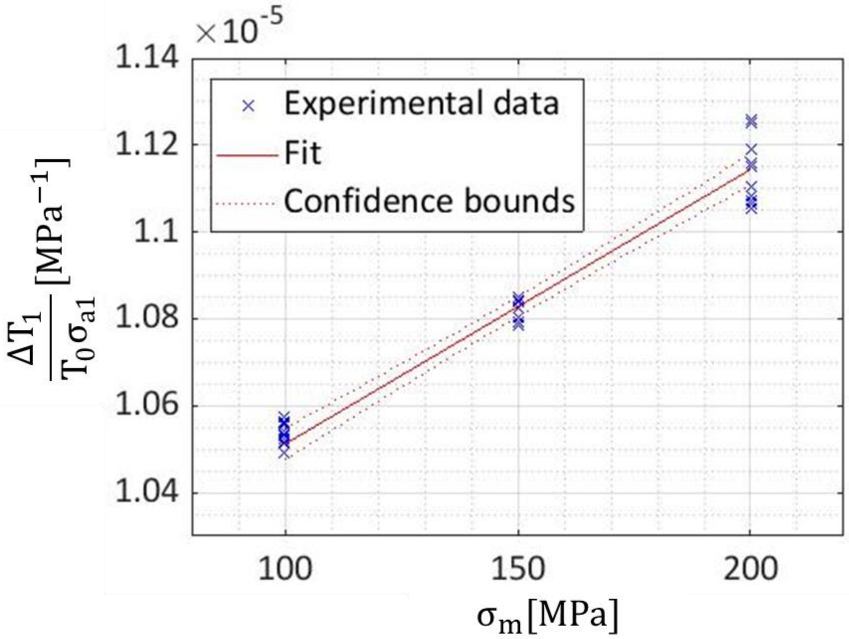

Figure 15 $\frac{\Delta T_1}{T_0 \sigma_{a1}}$ Vs σm. The thermoelastic parameters a and b represent the intercept and slope of the linear fitting.

2.1.7. The TSA higher order equation: validity, limitations, and potential

All the studies conducted until the last few years on the thermoelastic behaviour of materials, including the revised higher order theory on the thermoelastic effect, are based on several assumptions that limit the application of such theory to the cases of isotropic materials subjected to uniaxial residual stresses and uniaxial applied loads. These assumptions lead to some discrepancies in the description of the real thermoelastic behaviour of materials in presence of residual stresses.

In this work, by rewriting the general equation proposed by Potter and Graves in a matrixial form it was proposed an even more general equation, which could be employed in the thermoelastic response calculation for anisotropic materials subjected to multi-axial stress conditions. In particular, the equation proposed was employed to evaluate the effect of a bi-axial residual stress system on the thermoelastic signal.

Aim of this work is to propose a general model for Thermoelastic Stress Analysis that is able to provide the value of a thermoelastic signal as a function of either general biaxial applied load and general biaxial residual stress (or mean load) with different principal axes.

Moreover, the model provides the possibility to assess Thermoelastic signal for material with generic constitutive equations (i.e. isotropic/orthotropic/anisotropic behaviour) for homogeneous materials. The improvement lies in the fact that the proposed equation, valid under adiabatic and isentropic conditions, is for generalised homogeneous and anisotropic materials whatever the loading conditions are.

The thermoelastic signal has been evaluated through an equation whose demonstration derives from Wong's second order equation [45][46] and the more general equation presented by Potter and Graves [143]. The novelty of the proposed equation is given by the form of the same equation that is written using matrix products.

2.2. Residual Stress Analysis

2.2.1. Residual stress measurement techniques

Residual stress can be defined as those stresses that remain in a material or body after manufacture and processing in the absence of external forces or thermal gradients [52].

The origins of residual stresses in components can be mechanical, thermal or chemical. The assessment of the effective stress map of real components in the presence of residual stresses is of great importance together with their estimation in many industrial applications. This is the case, for instance, for mechanical components produced by means of the Additive Manufacturing process in which the residual stresses play a key role on the material stresses distribution, and then its mechanical behaviour.

Residual stress can be divided into three main types:

- type I includes the macrostresses that vary continuously over large distances (if the same order of the body dimensions)
- type II includes residual stresses which vary over the grain scale
- type III includes residual stresses which vary over the atomic scale

Among other factors, the selection of the residual stress measurement technique depends on the type of residual stress.

Other aspects that need to be considered, are the depth of measurement, the resolution and the component geometry and location (in situ or laboratory).

There are several techniques to measure residual stress that can be classified on the base of their effect on the component as destructive, semi-destructive e non-destructive.

The **destructive techniques** involve the structural damage of the sample and its dismissal from service. The principle at the base of such techniques is the local strain release which occurs at the edge of a cut. The relax deformation are elastic and the residual stress is evaluated by measuring strains and applying the linear elastic constitutive equation to get residual stresses. One of the main destructive techniques is the Curvature and Layer Removal. This technique is adopted on components with simple geometry, and it is based on the bending that occurs when a layer is removed from one side of a flat plate affected by residual stresses. The curvature depends on the original stress distribution present in the layer that has been removed and on the elastic properties of the material. After each layer removal, the curvature is measured and the distribution of stress in the original plate can then be deduced.

The **semi-destructive techniques** involve the removal of small quantities of material which generally does not compromise the structural integrity of the component. In this case the strain release principle is used as well.

The Hole Drilling is one of the most used semi-destructive techniques. It can be applied to a wide range of material and components and it is relatively cheap. Such the technique is carried out by drilling a small hole on the surface of the component and measuring the strain release with a special stain gauge rosette. The residual stresses are then evaluated using formulae and calculations derived from experimental and FEM [52]. Typical hole-drilling apparatus and strain gauge rosette are showed in Figure 16.

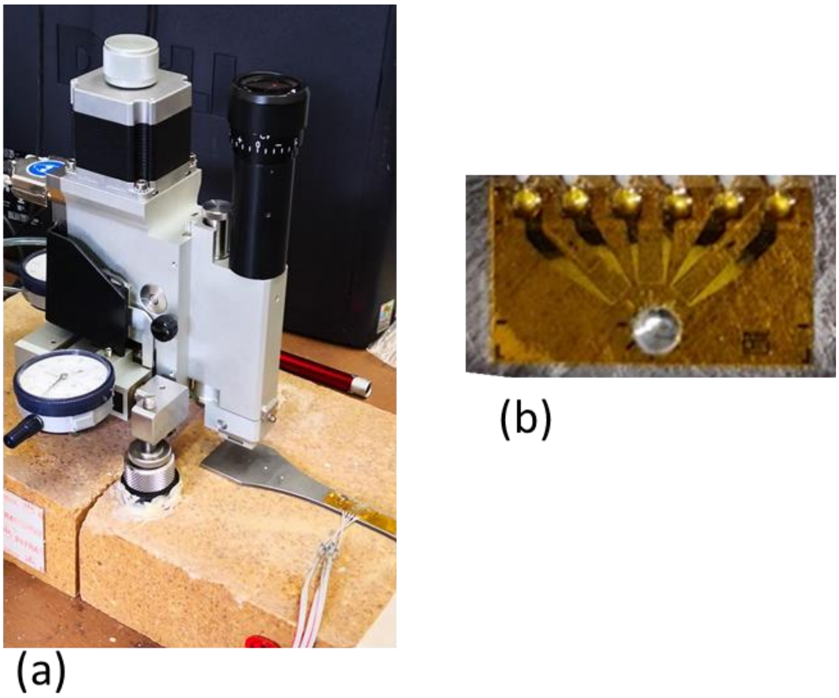

Figure 16 Typical hole-drilling apparatus (a) and strain gauge rosette (b)

Non-destructive techniques are the last category of residual stress measurement techniques. They do not cause any damage or modification to the component but generally require more expensive equipment.

These techniques work exploiting physical proprieties of materials and measure the effects of the residual stress on these priorities. The most common are:

- X-Ray diffraction, that relies on the elastic deformations within a polycrystalline material which cause changes in the spacing of the lattice planes from their stress-free value to a new value that corresponds to the magnitude of the applied stress. The measurement is performed irradiating the component with high energy X-rays that penetrate the surface. Some of the X-rays are diffracted by the crystal planes, according to Bragg's law, and a detector detects the angular positions where diffracted X-rays are located and records the intensity of these rays at that angular position. Residual stresses are evaluated from the location of the peaks. The disadvantage of this technique is the small penetration (few hundred microns)

- Synchrotrons or hard X-Rays. They work as described for X-rays, but with more intense beams of high energy that allow a much higher penetration depth, higher spatial resolution (limited only by the crystallite size) and three-dimensional maps of the strain distribution to millimetre depths.
- Neutron Diffraction like X-rays and synchrotrons relies on elastic deformations within a polycrystalline material that cause changes in the spacing of the lattice planes from their stress-free value. Measurements are carried out with a detector moving around the sample, locating the positions of high intensity diffracted beams. Neutrons have a very large penetration depths, which makes them capable of measuring at near surface depths of around 0.2 mm down to bulk measurements of up to 100 mm in aluminium or 25mm in steel [52].
- Magnetic methods are based on the effect of internal stresses on the ferromagnetic properties of steels and other ferromagnetic materials. The exploited effects are the magnetostriction and the consequent magnetoelastic effect. The method requires calibration of the magnetic parameter against known stress levels, and theoretical formulae are then used to interpolate and extrapolate the calibrations. The advantages of the magnetic methods are that they are non-destructive, cheap and very rapid and can measure biaxial stresses (up to ~6-10 mm). The disadvantage is the limited range of materials which can be examined and the inherent sensitivity to a variety of other microstructural features[52].
- Ultrasonic methods rely on the sensitivities of the velocity of ultrasound waves travelling through a solid to the presence of residual stresses. The measurement is performed considering the transit times, since the ultrasonic path length can be unknown. The resolution is not high because the changes in velocity are affected by the stress field over the entire ultrasonic path.
- The Raman method exploits the interaction of light with matter. The bonds between atoms vibrates if hit by Incident laser light. The scattered light reveals information about the sample's physical state and chemical structure. This

technique has a high spatial resolution and by using optical microscopy it is possible to select regions of interest just a few microns in size.

The Non-destructive techniques currently available do not offer an industrially attractive solution, since they are too much expensive or poor in resolution. On the other hand, all the techniques currently standardized and widely used as a reference are characterized destructive or semi-destructive techniques, which provide punctual information.

In this framework, the important contribution that the development of a full-field and non-intrusive technique such as that based on TSA could give is evident.

2.2.2. TSA Potential and limits in residual stress investigation

Eq 37 and Eq 47 show the possibility of measuring residual stress with the TSA.

The mean stress is due to all the stresses contributions which remain constant during the sinusoidal loading; it can be described by the sum of the applied mean load, the residual stress, the own weight of the structure and the stresses linked to bending moments on both in plane and out of plane direction. The latter two can generally be overlooked, thus Eq 56 can be written as[14][16][17][18]:

$$\rho C_\varepsilon \frac{\Delta T}{T_0} = -\left(\alpha - \frac{1}{E^2}\frac{\partial E}{\partial T}(\sigma_m + \sigma_r)\right)\Delta\sigma \sin \omega t - \frac{1}{4E^2}\frac{\partial E}{\partial T}\Delta\sigma^2 \cos 2\omega t \qquad \text{Eq 62}$$

The main limit of Wang equation is its validity restricted to uniaxial residual stresses directed as the applied load, in the most case the residual stresses are unknown, and o be defined the value of three variables should be found: the two principal stresses and the angle with respect to the considered reference system

So far, there have been two different approaches to evaluate residual stresses by means of the TSA. The first, proposed by Wong and et al. [14], considers residual stresses as a mean stress which remains constant during the dynamic load application. Several researchers followed this approach. Gyekenyesi et al. [53] demonstrated how to simultaneously obtain the stress amplitude and the mean stress from the first and second harmonics; the latter is approximately 2% of the first harmonic [54] and its measurements represent the main limitation of this technique. Patterson et al. [43] proposed an alternative technique based on a calibration procedure to directly relate the stress amplitude to the detector response, in such a way that the second harmonic evaluation is not necessary. In their work, Galietti et al. [17] proposed a calibration procedure and showed the applicability of this approach in the simple case of uniaxial load and assuming uniaxial residual stresses directed as the applied load.

The second approach has been proposed by Quinn et al. [49] [55], and it assumes that residual stresses associated to plastic deformation can be evaluated through TSA by determining the variation of the linear thermal expansion coefficient. This relation has been empirically proved but has the limit to neglect the second order effect.

In this work the potential of the TSA for the evaluation of the residual stress has been studied following the approach based on the mean stress effect on the thermoelastic signal. The novelty of the work lies into the application of the TSA general model, that provides the possibility to assess the thermoelastic signal for material with generic constitutive equations (i.e., isotropic/orthotropic/anisotropic behaviour) undergoing generally oriented bi-axial residual stress.

2.3. Fracture Mechanics

2.3.1. Analytical models for the elastic stress field around the crack tip

The residual life of a component depends on the material fracture strength and the stress field at the crack tip. The latter can be expressed by means of theoretical models parametrized respect to the SIF; in fact, for certain cracked configurations subjected to external forces, it is possible to derive closed-form expressions for the stresses in the body, assuming isotropic linear elastic material behaviour. Westergaard[56], Irwin [57], Sneddon [58], and Williams [59] were among the first to publish such solutions.

These solutions have the form[60]:

$$\sigma_{ij} = \frac{K}{\sqrt{2\pi r}} f_{ij}(\theta) + \sum_{n}^{\infty} A_n r^{\frac{n}{2}} g_{ij}^{(n)}(\theta) \qquad \text{Eq 63}$$

Where r and θ are coordinates in the polar referment system with the origin at the crack tip (Figure 17), f_{ij} and g_{ij} are dimensionless functions of θ and K is the SIF.

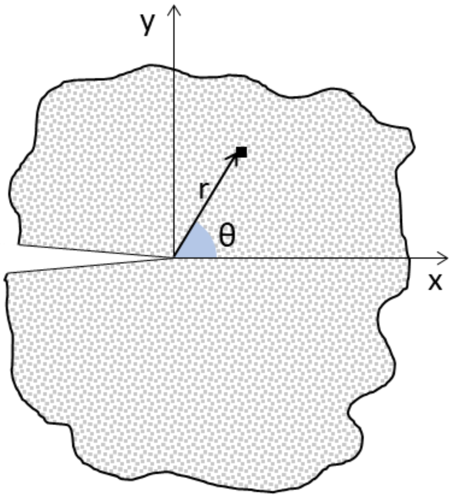

Figure 17 Polar referment system with the origin at the crack tip.

It is interesting to notice that Eq 63 describes a stress singularity, since stress is asymptotic to r = 0.

There are three modes of loading that a crack can experience (Figure 18):

1) Mode I: the principal load is applied normal to the crack plane, also known as opening mode, since it tends to open the crack.

2) Mode II: the load is in-plane shear and tends to slide one crack face with respect to the other.

3) Mode III: the load is out-of-plane shear.

A cracked body can be loaded in any one of these modes, or a combination of two or three modes. However, when the crack grows it tends to propagate on the plane normal to the main direction making mode I the prevailing mode.

The SIF and the function $f_{ij}(\theta)$ depend on the particular loading mode.

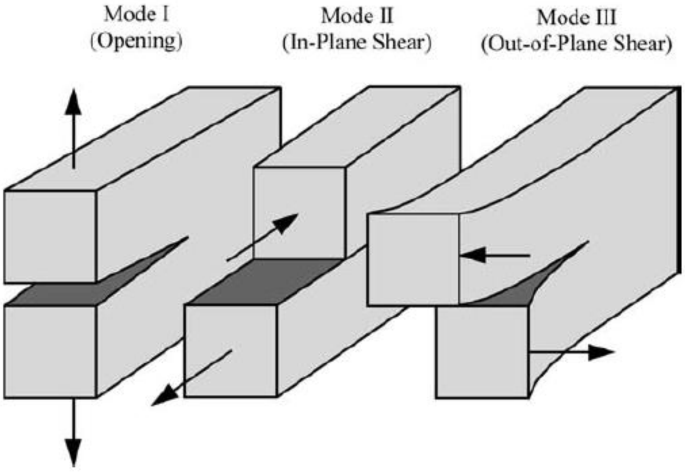

Figure 18 Crack opening modes [60]

The SIF can be evaluated by using the formula provided by the ASTM Standard E 647[61] or it can be experimentally found by fitting a theoretical model of the stress distribution at the crack tip with the stress field measured with experimental techniques.

In this work three theoretical models for the elastic stress distribution around the crack tip have been considered:

Westergaard's model Westergaard equations are among the first models to be proposed for the description of elastic stress field at the crack tip. This analytical model assumes a perfect elastic behavior for the material and does not consider the interaction at the elastic/plastic strain boundary.

Considering a polar coordinates system with its center at the crack tip, the Westergaard's equations which describe the stress field for mode I are the following[56]:

$$\sigma_{xx} = \frac{K_I}{\sqrt{2\pi r}} cos\frac{\theta}{2}\left(1 - sin\frac{\theta}{2} sin\frac{3\theta}{2}\right)$$
$$\sigma_{yy} = \frac{K_I}{\sqrt{2\pi r}} cos\frac{\theta}{2}\left(1 + sin\frac{\theta}{2} sin\frac{3\theta}{2}\right)$$

Eq 64

$$\tau_{xy} = \frac{K_I}{\sqrt{2\pi r}} cos\frac{\theta}{2} sin\frac{\theta}{2} sin\frac{3\theta}{2}$$

Where K_I represent the mode I stress intensity factor.

The principal stresses σ_1 and σ_2, can be obtained by applying Eq 64

$$\sigma_1, \sigma_2 = \frac{\sigma_x + \sigma_y}{2} \pm \sqrt{\left(\frac{\sigma_x - \sigma_y}{2}\right)^2 + \tau_{xy}^2} \qquad \text{Eq 65}$$

Substituting Eq 64in Eq 65, the principal stresses are:

$$\sigma_1 = \frac{K_I}{\sqrt{2\pi r}} \cos\frac{\theta}{2}\left[1 + sin\frac{\theta}{2}\right], \sigma_2 = \frac{K_I}{\sqrt{2\pi r}} \cos\frac{\theta}{2}\left[1 - sin\frac{\theta}{2}\right] \qquad \text{Eq 66}$$

Introducing the constitutive law, the same relation can be written in terms of horizontal and vertical displacement:

$$\begin{aligned} u &= \frac{K_I}{2G}\sqrt{\frac{r}{2\pi}} cos\frac{\theta}{2}\left(\kappa - 1 + 2sin^2\frac{\theta}{2}\right) \\ v &= \frac{K_I}{2G}\sqrt{\frac{r}{2\pi}} sin\frac{\theta}{2}\left(\kappa + 1 - 2cos^2\frac{\theta}{2}\right) \end{aligned} \qquad \text{Eq 67}$$

with $G = \frac{E}{2(1+\nu)}$ shear modulus ratio, and $\kappa = \frac{3-\nu}{1+\nu}$ for plane stress and $\kappa = 3 - 4\nu$ for plane strain.

Williams' model The model proposed by Williams describes the stress components as a function of a number of *n* terms in the series, whit *n* ranging from 1 to ∞. Generally, the approximation to the first two terms is used, nevertheless different works studied the improvement in the stress field description by using higher order terms[62][63].

Considering a polar coordinates system with its center at the crack tip, the first three terms of the Williams' series expansion describing the elastic stress field surrounding the crack for mode I are[59]:

$$\begin{aligned}
\sigma_x &= \frac{K_I}{\sqrt{2\pi r}} cos\frac{\theta}{2}\left(1 - sin\frac{\theta}{2} sin\frac{3\theta}{2}\right) + T + A_{I3}\sqrt{r}\cos\frac{\theta}{2}\left(1 + \sin^2\frac{\theta}{2}\right) + O(r) \\
\sigma_y &= \frac{K_I}{\sqrt{2\pi r}} cos\frac{\theta}{2}\left(1 + sin\frac{\theta}{2} sin\frac{3\theta}{2}\right) + A_{I3}\sqrt{r}\cos\frac{\theta}{2}\left(1 - \sin^2\frac{\theta}{2}\right) + O\left(r^{3/2}\right) \\
\tau_{xy} &= \frac{K_I}{\sqrt{2\pi r}} cos\frac{\theta}{2} sin\frac{\theta}{2} cos\frac{3\theta}{2} - A_{I3}\sqrt{r}\sin\frac{\theta}{2}\cos^2\frac{\theta}{2} + O(r)
\end{aligned} \tag{Eq 68}$$

Where *T* is the T-stress and *A_{I3}* the third term coefficient.

Introducing the constitutive law, the same relation can be written in terms of horizontal and vertical displacement:

$$\begin{aligned}
u &= \frac{1}{2G}\left\{K_I\sqrt{\frac{r}{2\pi}}\left[\left(k - \frac{1}{2}\right) cos\frac{\theta}{2} - \frac{1}{2} cos\frac{3\theta}{2}\right] - \frac{T}{4} r(k+1) cos\theta \right. \\
&\qquad \left. + A_{I3} r^2 \left[\left(k + \frac{1}{2}\right) cos\frac{3\theta}{2} - \frac{3}{2} cos\frac{\theta}{2}\right]\right\} \\
v &= \frac{1}{2G}\left\{K_I\sqrt{\frac{r}{2\pi}}\left[\left(k + \frac{1}{2}\right) sin\frac{\theta}{2} - \frac{1}{2} sin\frac{3\theta}{2}\right] - \frac{T}{4} r(k-3) sin\theta \right. \\
&\qquad \left. + A_{I3} r^2 \left[\left(k - \frac{1}{2}\right) sin\frac{3\theta}{2} - \frac{3}{2} sin\frac{\theta}{2}\right]\right\}
\end{aligned} \tag{Eq 69}$$

CJP model. The CJP model [64] is based on Muskhelishvili complex potential [65]. The improvement provided by the model is the incorporation of induced boundary stresses such as the effect of contact in the crack wake and the effect of compatibility-induced shear stresses at the interface of the elastic field with the local plasticized area surrounding the crack.

Experimental study showed the improved capability of prediction of a crack tip stress field model that incorporate the influence on the elastic stress field of any stresses induced by the plastically deformed area [66].

In the CJP model the elastic stress field is defined through five coefficients (*A*, *B*, *C*, *F* and *H*) and provides three different Stress Intensity Factors:

- K_f, the opening mode SIF, which characterize the forces perpendicular to the plane of the crack (mode I);

- *K_s* the shear SIF, which characterises shear stress in the plane of the crack induced by the compatibility at the interface between the plastic area and the surrounding elastic field;

- *K_r*, the retardation SIF, which characterizes the forces applied in the plane of the crack and counteracting the crack growth.

the equations can be written in terms of stress in a polar coordinate system as follow:

$$\sigma_x = -\frac{1}{2}(A-4B+8F)r^{-\frac{1}{2}}\cos\frac{\theta}{2} - \frac{1}{2}Br^{-\frac{1}{2}}cos\frac{5\theta}{2} - C \\ -\frac{1}{2}Fr^{-\frac{1}{2}}\left[\ln(r)\left(cos\frac{5\theta}{2}+3cos\frac{\theta}{2}\right)+\theta\left(sin\frac{5\theta}{2}+3sin\frac{\theta}{2}\right)\right] \\ +O\left(r^{\frac{1}{2}}\right)$$

$$\sigma_{\mathrm{y}} = \frac{1}{2}(A-4B+8F)r^{-\frac{1}{2}}\cos\frac{\theta}{2} + \frac{1}{2}Br^{-\frac{1}{2}}cos\frac{5\theta}{2} + H \\ +\frac{1}{2}Fr^{-\frac{1}{2}}\left[\ln(r)\left(cos\frac{5\theta}{2}-5cos\frac{\theta}{2}\right)+\theta\left(sin\frac{5\theta}{2}-5sin\frac{\theta}{2}\right)\right] \\ +O\left(r^{\frac{1}{2}}\right) \qquad \text{Eq 70}$$

$$\tau_{\mathrm{xy}} = -\frac{1}{2}r^{-\frac{1}{2}}\left(Asin\frac{\theta}{2}+Bsin\frac{5\theta}{2}\right) \; - Fr^{-\frac{1}{2}}sin\frac{\theta}{2}\left[\ln(r)\,cos\frac{3\theta}{2}+\theta sin\frac{5\theta}{2}\right]+O\left(r^{\frac{1}{2}}\right)$$

And in terms of displacements as:

$$2G(u+iv) = \kappa\left[-2(B+2F)z^{\frac{1}{2}}+4Fz^{\frac{1}{2}}-2Fz^{\frac{1}{2}}\ln(z)-\frac{C-H}{4}z\right] \\ -z\left[-(B+2F)\bar{z}^{-\frac{1}{2}}-F\bar{z}^{-\frac{1}{2}}\overline{\ln(z)}-\frac{C-H}{4}\right] \\ -\left[A\bar{z}^{\frac{1}{2}}+D\bar{z}^{\frac{1}{2}}\overline{\ln(z)}-2D\bar{z}^{\frac{1}{2}}+\frac{C+H}{2}\bar{z}\right] \qquad \text{Eq 71}$$

To guarantee an appropriate asymptotic behaviour of the stress along the crack flank, the assumption *D*+*F*=0 must be made in. Therefore, crack tip displacement fields are defined from the five coefficients: *A*, *B*, *C*, *F* and *H*. The coefficients are linked to three different stress intensity factors and the T-stress components through the following relations:

$$K_F = \lim_{r\to 0}\left[\sqrt{2\pi r}\left(\sigma_y + 2Fr^{-\frac{1}{2}}\ln r\right)\right] = \sqrt{\frac{\pi}{2}}(A - 3B - 8F)$$

$$K_S = \lim_{r\to 0}\left[\sqrt{2\pi r}\tau_{xy}\right] = \mp\sqrt{\frac{\pi}{2}}(A + B)$$

$$K_R = \lim_{r\to 0}\left[\sqrt{2\pi r}\sigma_x\right] = -(2\pi)^{\frac{3}{2}}F \qquad \text{Eq 72}$$

$$T_x = -C$$

$$T_y = -H$$

2.3.2. The plastic enclave at the crack tip

When a notched component undergoes cyclic stresses, even if these fall within the yielding limit of the material, it is possible that strong stress gradients are produced at the apex of the damage and that these may locally exceed the material yield stress forming a small plastic zone or ‘enclave’.

It has been shown how the local plasticity characterizing the area around the crack tip can affect the elastic strain field area due to the boundary interaction between the two zones [67]; in this contest, the characterization of the shape and size of the plastic zone around the crack tip has a key role in the in the description of the fracture behaviour of materials.

In a notched component subjected to a dynamical load it is possible to distinguish four main areas:

- The edges affected zone (the grey area in Figure 19). It is the area far enough away from the crack not to be affected by the singularity, but by the edge effect.

- The K-dominance elastic zone (the blue area in Figure 19). It is the area where the component is subjected to a purely linear-elastic strain and the stress distribution can be expressed by the SIF through the theoretical model described in paragraph 2.3.1

- The monotonic plastic zone (the yellow area in Figure 19). It is the area where the material experience during the half-period of growing load of the cycle an equivalent stress above the material yield strength, thus in this area inelastic phenomena take place and the plastic work occurs once per cycle.

- The cyclic plastic zone (the red area in Figure 19). It is the area where the material experiences a complete cycle of double reverse plasticity, thus in this area the plastic work occurs twice per cycle.

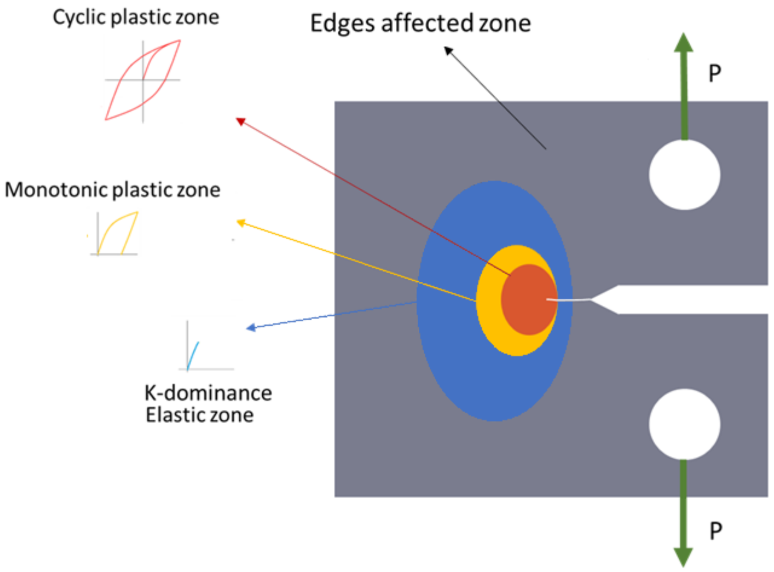

Figure 19 Deformation in a notched component subjected to a dynamical load.

The size and shape of the plastic zone can be guessed by applying two different approaches: The Irwin approach [68] and the strip yield model[69][70].

Both the approaches are based on simple correction to the linear elastic fracture mechanics and can only be trusted in the case of moderate crack tip yielding.

Irwin approach is based on the application of the elastic stress analysis in order to find the elastic/plastic boundary by imposing the yielding strength as limit.

Despite the availability of theoretical models mainly based on the linear elastic fracture mechanics allows to predict the plastic area, and thus the stress distribution, by means of FEM analysis, the need for experimental feedback remains for the validation of those models.

In several researches experimental techniques where employed in order to characterize the shape and size of the plastic zone [19][20][66][71][72][73][74][75][76]; These techniques include microhardness measurements, etching, optical interference, microstrain gauge and electron microscopy[76] and full field techniques such as synchrotron diffraction and tomography, digital image correlation (DIC), thermography and electron backscatter diffraction.

Among these, DIC and thermographic techniques showed great potential having the important feature of being full-field, easy to implement and requiring affordable equipment.

Both the techniques are widely used in fracture mechanics for the identification of stress/strain distribution and SIF [19][20][71][72][77][78][79][80].

In recent works these techniques have also been employed for the estimation of dissipated energy [73][74][75][76] and the plastic zone shape and size [76][66][19].

2.3.3. Crack growth rate: the Paris' Law

The common way of describing the fracture behaviour of cracked components is through the crack grow rate $\frac{da}{dN}$, with a crack length and N number of cycles. The Paris Law expresses the relationship between the crack grow rate and the range of the SIF when a dynamical load is applied[81]:

$$\frac{da}{dN} = C\Delta K^{m} \qquad \text{Eq 73}$$

Where C and n are constant coefficients, that unlike the ΔK and $\frac{da}{dN}$ are independent of the crack length but depend on environment, frequency, temperature and stress ratio.

The Paris Law coefficients are experimentally evaluated by the Law fitting with the values of $\frac{da}{dN}$ and ΔK at different number of cycles. Both the crack grow rate and the SIF range can be evaluated following Standards [61] and by applying experimental techniques. Among non-destructive methods the most used are microscopy, extensometry, ultrasound, X-ray and DIC [82][83][84][85][86][87][88].

IR was also employed in order to find these parameters, exploiting the information provided by the amplitude and phase of the first Fourier harmonic (as will be explained in paragraph 2.3.6) for the crack tip and the SIF evaluation[89].

2.3.4. Application of Digital Image Correlation to characterize fracture mechanics behaviour

The use of 2D Digital Image Correlation (DIC) in the study of fracture mechanics has been already addressed by several researcher [66][90][91][92][93][94].

DIC method has been employed to solve different problems related to the characterization of the crack tip stress field, such as the determination of fracture mechanics parameters, the evaluation of crack closure and its impact on crack driving force, the identification of the plastic zone ahead the crack tip, the evaluation of the Crack Opening Displacement (COD) and the crack tip location.

There are several advantages that make DIC methods attractive. It is a full-field technique, it has a high resolution and provides accurate result compared to conventional manual methods, and it requires easily available instrumentation (high-definition cameras and lighting system) and a simple set-up (Figure 20).

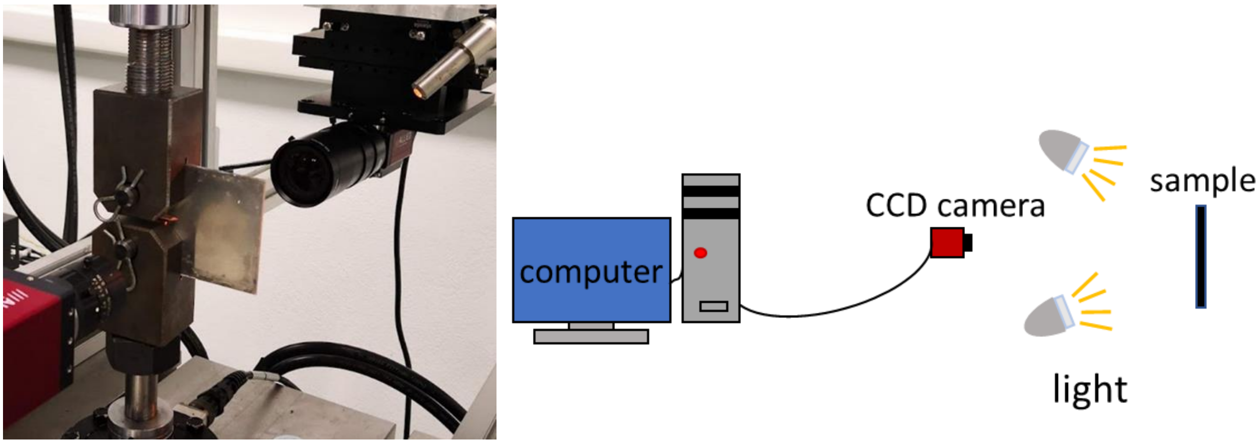

Figure 20 DIC set up

There are not limitations on materials. Usually, the samples must be prepared with the application of a speckle pattern on the surface, nevertheless there are materials whose natural pattern is enough to produce a suitable pattern.

The DIC is applied correlating 2 digital images taken from the sample before (reference image) and after the deformation (deformed image).

The random spackle allows to track small regions of at least 3x3 pixels (subset) with varies greyscales.

The data processing involves the mathematical mapping and cross-correlation of each subset throughout the reference and deformed images.

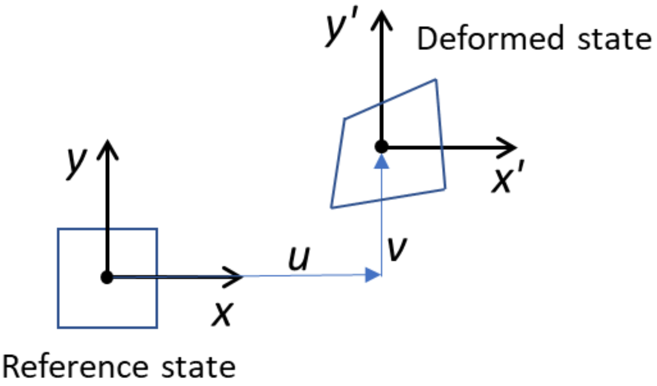

Figure 21Refernce and deformed state of a subset

Considering the point (x,y) in the reference image, it will be mapped in the deformed image onto a point (x’,y’) (Figure 21) as:

$$x' = x + u(x,y)$$
$$y' = y + u(x,y) \qquad \text{Eq 74}$$

Where *u* and *v* represent horizontal and vertical displacements of the centre of the subset respectively and can be expressed through the Taylor series as:

$$x' = x + u + \frac{\partial u}{\partial x}\Delta x + \frac{\partial u}{\partial y}\Delta y + \frac{1}{2}\frac{\partial^2 u}{\partial^2 x}\Delta x^2 + \frac{1}{2}\frac{\partial^2 u}{\partial^2 y}\Delta y^2 + \frac{\partial^2 u}{\partial x \partial y}\Delta x \Delta y$$
$$x' = y + v + \frac{\partial v}{\partial x}\Delta x + \frac{\partial v}{\partial y}\Delta y + \frac{1}{2}\frac{\partial^2 v}{\partial^2 x}\Delta x^2 + \frac{1}{2}\frac{\partial^2 v}{\partial^2 y}\Delta y^2 + \frac{\partial^2 v}{\partial x \partial y}\Delta x \Delta y \qquad \text{Eq 75}$$

Where Δx and Δy are the distances of the centre of the subset to the point (x,y).

The displacement fields are obtained from the minimization of the correlation coefficient C, which can be calculated as:

$$C = \frac{\sum_S [G(x,y) - H(x',y')]^2}{\sum_S G^2(x,y)} \qquad \text{Eq 76}$$

Where G and H are the grey scale light intensity of the points in the subset S. As an alternative, a Fast Fourier Transform (FFT) cross correlation can be used to compare the subsets.

The application of DIC to characterize the stress field around a growing crack can be performed comparing the image taken when the sample is unloaded (reference) with the image taken when the sample is loaded (deformed).

Figure 22 shows the displacements maps obtained from the DIC analysis on a cracked Compact Tensile sample in AA2024.

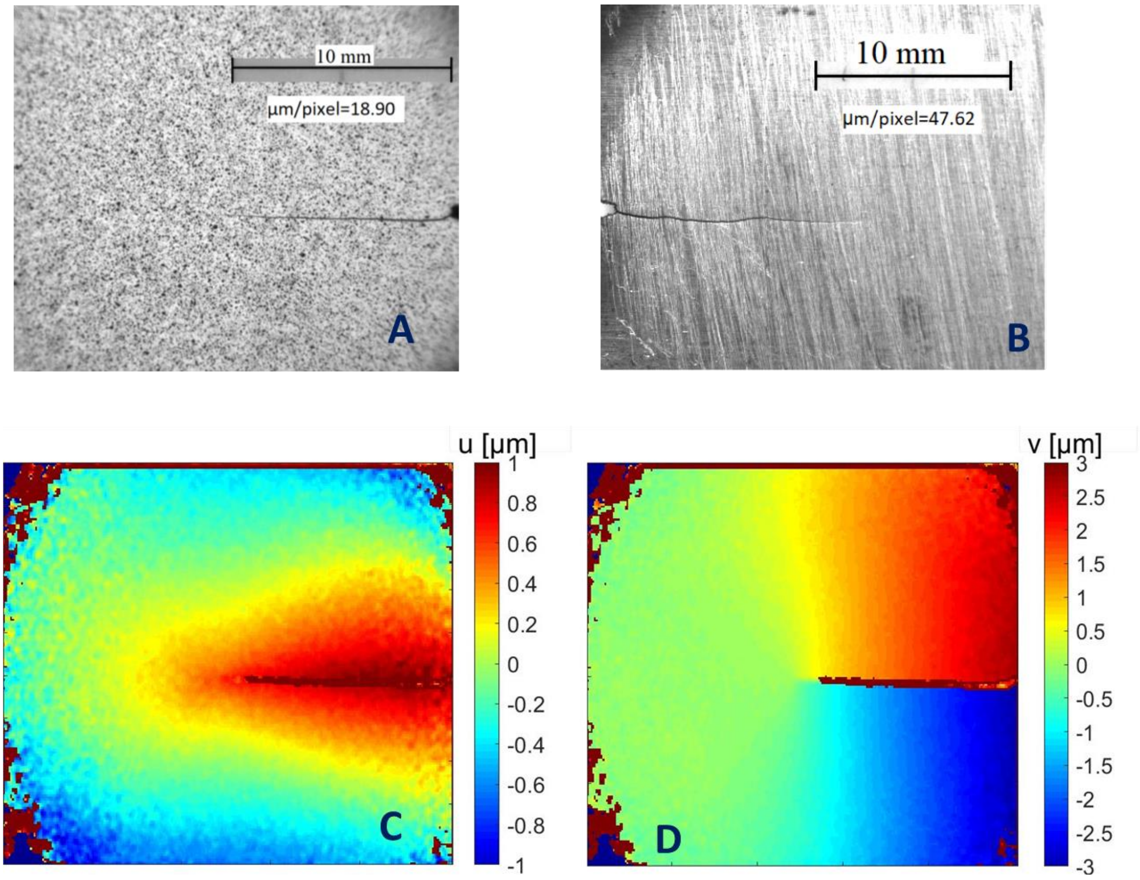

Figure 22 Image captures after 180000 loading cycles on the polished (B) and speckled (A) side in of a Compact Tensile sample in AA2024 and the Horizontal (C) and vertical (D) displacement fields measured by DIC. The applied load was 1000 N and the crack length is 12.33 mm.

The equivalent stress map can be obtained from the displacement field provided by the DIC work following two different methods[66].

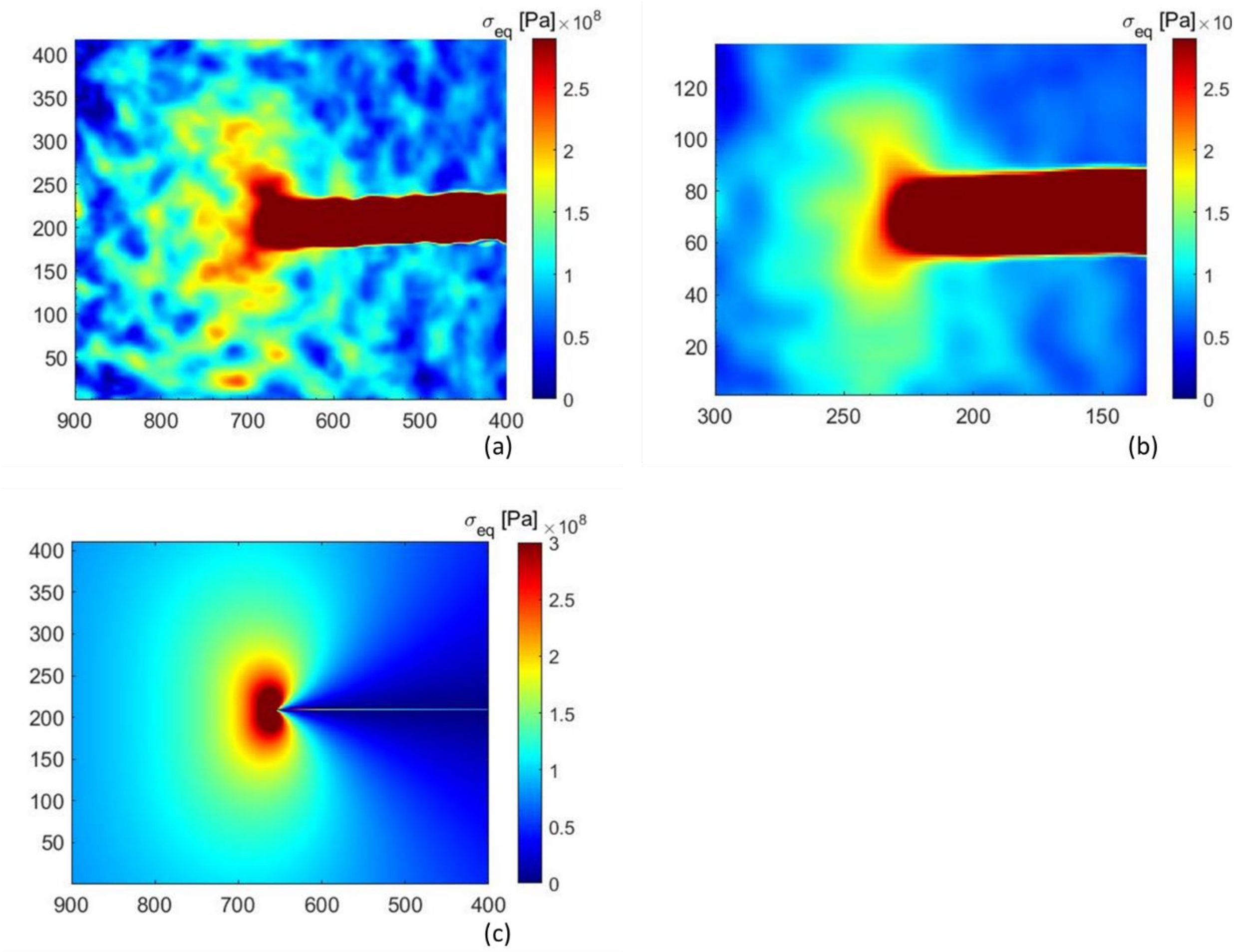

Figure 23 Equivalent stress maps obtained using the direct method with a subset of 3x3 pixels (a) and with a subset of 6x6 pixels and the equivalent stress map obtained using the indirect method (c)

The first method is the direct method, since it involves the direct derivation of strains form the experimental displacements and the application of the linear elastic relationship between strains and stress. Figure 23 shows how this method is affected by the high noise due to the operation of spatial derivation of experimental displacements; to reduce the noise it is possible to adopt a larger subset but giving up a better resolution.

The second method, or indirect method, is based on the evaluation of the fracture mechanics parameters that defines the theoretical models of stress distribution around the crack. This can be achieved by fitting the displacements data of a mesh of points in the elastic zone around the cack with the theoretical model. The quality of the results depends on the correctness theoretical model used; in Figure 23 (c) it is reported the Von Mises' equivalent stress map obtained by using the indirect method with the Westergaard model.

2.3.5. Stanley-Chan linear Interpolation method

Stanley-Chan linear interpolation method is based on the combination of the TSA basic equation (Eq 50) with the Westergaard's equations for the elastic stress field around the crack tip (Eq 69).

Stanley et al. [80] demonstrated an important relationship between *y*, the vertical distance of a line parallel to the crack line and the maximum signal in that line S_{max}.

Considering only the mode I, the combination of Eq 50 and Eq 64 gives:

$$S = \frac{\sqrt{2}\Delta K_I}{A\sqrt{\pi \frac{y}{sin\theta}}} cos\frac{\theta}{2} \qquad \text{Eq 77}$$

Where the radius *r* has been expressed a function of *y* and *θ* (Figure 17).

From Eq 77 it derives:

$$\frac{dS}{d\theta} = \frac{\Delta K_I}{A\sqrt{2\pi y sin\theta}} cos\frac{\theta}{2} \qquad \text{Eq 78}$$

Eq 78 is null for θ=60°, which is a point of maximum for the signal. Substituting in Eq 77, gives the relationship between S_{max} and y:

$$y = \left(\frac{3\sqrt{3}\Delta K_I^2}{4\pi A^2}\right)\frac{1}{S_{max}^2} \qquad \text{Eq 79}$$

Where y represents the vertical distance of a line parallel to the crack line and S_{max} is the maximum signal in that line, which occurs at θ=60°.

The Stanley method for the evaluation of the ΔK_I is based on the linear relation between y and $1/S^2_{max}$. In fact, once the constant A is known, ΔK_I can be obtained from the gradient of a graph of y versus $1/S^2_{max}$ as shown in Figure 24.

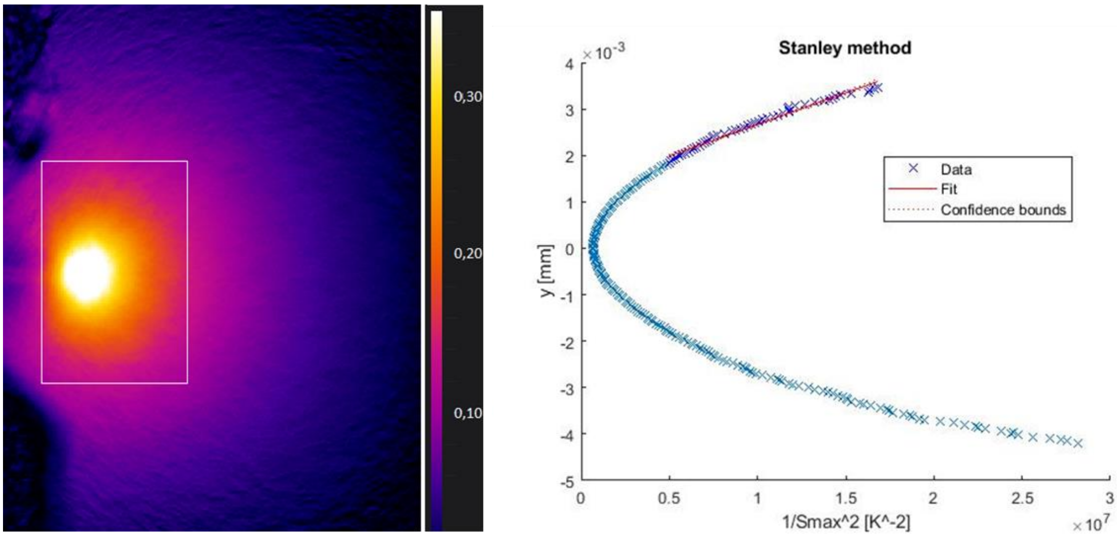

Figure 24 Appplication of the Stanley-Chan linear Interpolation method

2.3.6. Critical issues on the interpretation of the Thermoelastic response during a dynamical test

For a homogenous and isotropic material, the calibrated thermographic signal *T* during a cyclic test with a sinusoidal load, can be written in the time domain as [19]:

$$T(t) = T_0 + at + T_1 sin(\omega t + \Phi_1) + T_2 sin(2\omega t + \Phi_2) \qquad \text{Eq 80}$$

The first and the second term in Eq 80 represent respectively the mean temperature T_0 and its linear increase, defined through the coefficients *a* which depends on the physic characteristics and geometry of the component. This term is affected by the heat transfer (conduction in the specimen or convection and radiance to the environment).

The third term in Eq 80 represents the temperature variations induced by the thermoelastic effect; it varies at the same angular frequency as the load; and it is characterized by the amplitude T_1 and the phase Φ_1.

The amplitude T_1 is a direct indicator of the elastic strain field and its measurement, assuming known the thermoelastic constant *K* or the thermoelastic parameters *a* and *b*, provides the stress field around the crack.

The phase Φ_1 represents the delay between the load and the thermal response and under adiabatic conditions it is constant throughout the component. If the adiabatic condition is no longer respected, Φ_1 varies; this could be the case of high stress gradients, which lead to conduction effects [14][95]or heat generation due to local plasticity [96] [97].

The fourth term in Eq 80 represents the result of two effects both occurring at the twice of the loading frequency: the thermoelastic response due to the second order effect [14][25][46]and the temperature variation due to dissipation [98]; it is defined through the amplitude T_2 and the phase Φ_2.

When local plasticization effects occur, the thermoelastic component of the amplitude T_2 is at least one order of magnitude smaller than the second and therefore it can be neglected, in this case, the measured T_2 can be considered only related to the energy dissipation due to plasticization.

The potential of TSA in characterizing materials and components fracture behaviour lies on two different kind of information, namely the use of the first harmonic to assess the stress distribution near the crack tip and the interpretation of non-adiabatic phenomena on the thermoelastic signal to identify the dissipation related to the advancing damage.

As for the first type of application, the TSA gives the possibility to generate data of full-field temperature changes occurring at the tip during dynamical tests, providing a direct measurement of the cyclic strain in the elastic zone around the crack tip. Several researcher proved the capability of the TSA in calculating the fracture mechanics parameters such as the Stress Intensity Factor (SIF) and the Paris coefficients [20][78][79][80][99][100][101]. All the studies were characterized by the combination of thermoelastic data with theoretical models for the elastic stress field surrounding the crack.

The approach that is currently still widely used is that proposed by Stanley et al.[80] (as described in paragraph 2.3.5).

Other authors, including Diaz et al.[21], Zanganeh et al.[62] and Pitarresi et al.[63] employed the thermoelastic signal to evaluate the SIF by applying the over-deterministic least-square fitting (LSF) or the Multi-Point Over-Deterministic Method (MPODM).

All the cited works are based on the classical theory of TSA in which the changes of temperature are related to the changes of stresses through the thermoelastic constant for an isotropic material, in linear elastic conditions and under local adiabatic conditions, neglecting the higher order terms.

In this work a novel formulation has been developed, based on the TSA General model in order to improve the TSA fracture behaviour prediction in materials affected by the mean load effect.

The second ability of the TSA to provide information about the fracture behaviour of materials concerns the effect of dissipative phenomena that characterize the locally plasticized area.

The process of crack growth is affected by the energy dissipated at the notch/crack tip. In effect, in literature different analytical and numerical models [102][103][104] were proposed by researchers to describe as the plastic work affects the fatigue behaviour. Among the different approaches, those focusing their attention on energy dissipated in the plastic area proved a great potential in the evaluation of the crack growth behaviour [105][77]

In recent years, researchers focused their attention on energy-based approaches [82][106][107] The energy-based approach proposed firstly by Weertman [102], links the crack growth rate with the critical energy to create a unit surface area. Mazari et al., [104] starting from the Weertman's [102] and Klingbeil's [103] approaches, developed a new model in which a similar Paris Law model was obtained between the crack growth and the heat dissipated per cycle.

The main issue limiting the application of a fully-TSA based approach to identify the plastic zone is the absence of a validated and systematic criteria which allows to identify the plastic zone boundaries; in fact, the presence of periodic diffusivity phenomena (including the high stress gradient and the crack closure effect, that is the generation of hat when the opposing faces of a crack remain in contact during the loading, occurring at twice of the loading frequency) interferes with the thermal signal generated by the plasticization work. For this reason, the identification of the plastic zone boundaries cannot ignore the loading frequency effect.

In this work the TSA capability in detecting the plastic zone was studied by comparing its thermal footprint during dynamical tensile test with those predicted by a technique based on the combination of theoretical models with DIC experimental data.

2.4. Space aircraft Thermal Protection System (TPS) characterization

2.4.1. Temperature measurement to monitor re-entry tests in Plasma Wind Tunnel

Atmospheric reentry represents one of the most critical phases that must be faced by space aircraft. It is a process in which the spacecraft, which is located outside the atmosphere of a planet, is slowed down by the collision with the atmosphere. The main goal is a safe landing on the ground in order to ensure the conservation of the instruments and the survival of the astronauts.

The class of materials and structures employed to protect the internal environment of spacecraft and to ensure their integrity is that of Thermal Protection System (TPS) and their characterization is carried out in big facilities such as arc jet plasma wind tunnels (PWT)[108][109][110].

The tests conducted into a PWT facility allow qualification of the TPS which is subjected to thermal and mechanical stresses induced by the hypersonic jet in spite of the unavoidable intrinsic limitations when the complex flight physics phenomena are reproduced in ground test facilities [110].

The quantification of the temperature reached from the material during the tests represents a key factor to characterize the TPS.

When the PWT tests are performed, the TPS samples undergo strong spatial and temporal thermal stresses reaching very high temperatures, from 200°C up to 2500 °C. So techniques and tools able to achieve qualitative and quantitative information about the distribution of temperature over surfaces subjected to hypersonic plasma are needed [111].The implemented techniques should also be able to solve issues like the lack of knowledge of the TPS emissivity due both to the innovativeness of the used material and to the change of the chemical features during the ablation and erosion processes. In the last years, several techniques were developed to obtain high temperature value measurements as accurate and precise as possible. To monitor high temperatures and high-speed processes, intrusive techniques consisting of use of thermocouples, pressure sensors, gardon gauges and not intrusive techniques by means of spectroscopy, Infra-Red (IR) pyrometers and IR cameras [112]have been employed.

The use of thermocouples requires a direct contact with the test article material on which the temperature measurement is performed [112][113]. Moreover, the application involves the a priori knowledge of the points of interest and the achievement of very high temperatures (already above 600°C) could lead to long term and short-term drift [112]. Moreover, they can change the mechanical features of the test article and furthermore cannot always be used since usually are placed under the skin of the material surfaces.

The quantitative temperature measurements, using radiation techniques, are very tricky given the strong dependence of the surface radiation on the emissivity [1]. Indeed, the emission obtained by the Planck's Law [3] integration must be corrected with the factor ε (surface emissivity), that varies with the temperature as well as the wavelength and direction of radiation and depends on the state of the surface (in term of roughness, heat or mechanical treatment, etc.). The final measurement also depends on the IR system employed, which is characterized by its own spectral response and spectral band of detection [114] When operators perform measurements, it is assumed as object parameter a fixed value of emissivity which has to take into account all these effects; the apparent emissivity. In the Chrzanowski [115] work a theoretically demonstration of the importance of assuming a correct value for the apparent emissivity is described. This was experimentally proved by Riou et al. [116][117] which highlighted how the apparent emissivity depends on the spectral window and the temperature. Their experimental results demonstrated that a higher accuracy in temperature measurements can be reached by correctly calculating the apparent emissivity and that this effect is more evident at high temperatures.

In order to overcome problems in temperature evaluation due to emissivity determination, several solutions have been investigated, for example Maldague [1] proposes, among the others, black painting, thermal transfer imaging and multi-wavelength pyrometry.

In recent years, multispectral pyrometry has become a very popular technique [112][118][119][120][121][122] and several progresses have been made both in the construction of multichannel sensors and in the development of algorithms which allow to reach high accuracy. It is based on

However, for applications such as those related to the measurement of test articles in PWT, although pyrometry is usually used, it presents the limitation to give information over a limited number of target surface points due both to the intrinsic instrumentation features limitations and to the limited number of the optical accesses able to host pyrometers close to the test chamber. So in such a way to have a two dimensional temperature map of the surface material many of them should be used as well as many of test chamber optical accesses should be occupied in order to get a temperature map that is an interpolation of temperature measurement on a discrete number of points.

Black Painting over the surface is not a practicable way to know emissivity, both because the tested materials cannot be modified to maintain the ability to withstand high temperatures and because at high temperatures and in presence of plasma, painting would lose its features.

Zhang et al. [123] used a conceptual design for a multi-channel-system for multispectral thermography and demonstrated a relative uncertainty less than 10%, considering temperature in °C, over a large range of temperatures. The results are confirmed by experimental validation but only for static processes; the several spectral measurements have been performed with a rotary filter holder wheel and are relative to different times, even if the wheel switches quickly.

Meriaudeau [124] proposed a real time multispectral imaging system based on two CCD arrays equipped with different interferential filters on which the same radiation, separated by a beam splitter arrives to the IR detectors. CCD sensors work in a short band of the near infrared, so as inferable from Planck's radiation distribution, the technique is limited to high temperatures.

Mölleman [125] showed the potential of dual color thermography, using narrow pass band filters. He found that the technique is more sensitive in the middle wave (MW) region and underlined the importance of filters optimization.

Savino et al. [126] developed and validated up to 650°C an analytical model to determine the feasibility of the technique and how to find the best filters configurations. The results showed good application possibility using filters in the MW infrared region which is a good compromise between the validity of grey body hypothesis and the sensitivity of signals ratio. With the numerical analysis performed, using emissivity trend (at fixed temperature) provided by literature, it has been found an uncertainty less than 5% on the temperature measurement in MW.
This result is compatible with the analytical expression of the dual color uncertainty obtained by Reynolds [114] and with the parametric numerical analysis conducted by

Musto et al. [127] in which the uncertainty has been evaluated in function of emissivity trend, central filters wavelength and their distance.

2.4.2. TPS materials

TPS can be divided into two main categories:

- Ceramic Matrix Composites (CMCs)
- Ultra High Temperature ceramics (UHTCs)
- Cork based composites.

The CMCs are employed as reusable TPS[110][128][129][130][131][132][133] and are preferred when no change in the material geometry is a necessary requirement as well as no changes in the aerodynamic shape and profile of the spacecraft.

The Space Shuttle heatshield is the most famous example of reusable TPS based on carbon fiber composites in carbon matrix (C / C) and ceramic tiles[134].

The UHTCs are based on transition metal diborides such as ZrB2 and HfB2 and silicon carbide (SiC). During the atmospheric re-entry, this class of materials is subject to oxidation processes associate with the formation of oxide scales. Also CMCs are subject to oxidation processes and in both cases the physical stability depends on the environment conditions of pressure, partial oxygen pressure and temperature[128][135][136][137].

The Cork based composites are characterized by relatively low thermal conductivity values due to the honeycombed morphological structure of the cork.

The phenomenon of ablation that affects the heat shields during the re-entry phase has been the subject of studies since the 1960s[138][139].

The superficial temperature stabilization of the TPS during the thermal shock suffered when it reaches very high temperatures at very high heating rates is the result of the thermal dissipation in complex endothermic processes of chemical decomposition together with the production of pyrolytic gases, melting, sublimation, charring and evaporation[110].

During the ablation a carbonaceous char layer is formed, and if it shows a compact, uniform and mechanical stable structure, it can protect the inner layers of the material from the oxidation processes.

In this framework, advanced, non-intrusive and computational techniques have been (and still are) under development.

2.4.3. Dual color Thermography to overcame emissivity problem in re-entry tests

The radiance emitted by a surface, per unit solid angle and per unit projected area, is obtained from Eq 17 [114]:

$$E\left(T_{obj},\varepsilon_{obj}\right)=\int_0^{\infty}\varepsilon_{obj}\left(T_{obj},\lambda\right)\cdot\frac{C_1}{\lambda^5\cdot\left(e^{\frac{C_2}{\lambda\cdot Tobj}}-1\right)}d\lambda\left[\frac{W}{m^2\cdot sr}\right] \qquad \text{Eq 81}$$

where the surface emissivity ε_{obj} represents the ability of the material to radiate energy depending on many variables, like: kind of material, state of the surface (surface roughness, heat or mechanical treatments suffered etc..), geometry of the object, temperature, wavelength and angle of emission.

IR cameras convert the thermal radiation captured by the radiation sensor to a temperature value. However, to obtain information related to the investigated object temperature, it is necessary to take into account other contributions to the thermal radiation derived by surrounding environment and atmosphere.

Summarizing, the total radiant emittance impinging on the thermal camera sensor is composed by:

[1] The direct radiant emittance attenuated by the atmosphere, function of the thermal state of the surface and of the emissivity.

[2] The radiant emittance from the surrounding environment reflected by the object surface.

[3] The radiant emittance from the atmosphere between the IR camera and the object.

In this way, the total radiant emittance impinging the IR camera is:

$$E_{inc,\lambda}\left(T_{obj},\lambda,\varepsilon_{obj}\right)=\varepsilon_{obj}\left(T_{obj},\lambda\right)\cdot\tau_{atm}\cdot E_{bb\lambda}\left(T_{obj},\lambda\right)+\left(1-\varepsilon_{obj}\left(T_{obj},\lambda\right)\right)\cdot\tau_{atm}\cdot E_{bb\lambda}\left(T_{env},\lambda\right)+\left(1-\tau_{atm}\right)\cdot E_{atm\lambda}\left(T_{atm},\lambda\right)\left[\frac{\mathrm{W}}{\mathrm{m}^2}\right] \qquad \text{Eq 82}$$

If the IR camera operates in a wavelength range included in one of the so called “atmospheric window transparency”, the influence on the measurement of the atmospheric radiant emittance is negligible, since τ_{atm} is approximately equal to 1. Notice that a model subject to the hypersonic plasma is not well identified in the visible range since it is hidden from the shock wave emission due to the interaction between plasma and solid surface. Hence τ_{atm} in the visible range is very low and the emission from atmosphere, in the specific case, corresponding to the hypersonic plasma cannot be neglected. In the IR range the model is clearly visible and the only predominant emission comes from the model itself since the plasma emission is below the tolerance threshold of the detector [111]. Besides, when $T_{atm} << T_{obj}$ and $T_{env} << T_{obj}$, the 2nd and 3rd term in the second member of Eq 82 can be neglected. This is immediately achieved in a context like the Plasma Wind Tunnel test campaigns, where the time to reach hundreds of degrees is of the order of seconds. Moreover, the contributions of reflection coming from sunlight as well as the radiance from the intense radiation sources outside the field of view integrated in the spectral range of the detector are small enough to be neglected.

The thermosignal $G(T_{obj}, \varepsilon_{obj})$ can be evaluated by integrating the Planck's law for a real surface in the operating spectral range of the camera (λ' and λ'') and considering spectral response curve of the sensor $R_t(\lambda)$ and transmittance function for the optic $R_{ot}(\lambda)$, for the applied filter $F(\lambda)$ and for eventual attenuators $A(\lambda)$.

$$G(T_{obj}, \varepsilon_{obj}) = \int_{\lambda'}^{\lambda''} \varepsilon_{obj}(T_{obj}, \lambda) \cdot R_t(\lambda) \cdot R_{ot}(\lambda) \cdot F(\lambda) \cdot A(\lambda) \cdot \frac{C_1}{\lambda^5 \cdot \left(e^{\frac{C_2}{\lambda \cdot T_{obj}}} - 1\right)} d\lambda \left[\frac{\mathrm{W}}{\mathrm{m}^2 \cdot \mathrm{sr}}\right] \tag{Eq 83}$$

Integration of Eq 83 could be very complex due to temperature, wavelength and direction dependence of emissivity. Generally, in standard thermographic techniques some simplifications are used and emissivity is considered to be constant with wavelength (grey body assumption) and direction and most of the time also with temperature. The highest impact is given from the grey body assumption and this is a source of uncertainty on the temperature measurements.

The ratio principle representing the pivot of the dual color technique that is based on the ratio determination of two monochromatic radiations in two spectral wavelengths close enough to each other to consider valid the assumption of local grey body.

The ratio of the measured radiation intensity is indicated as Intensity of Radiation Ratio (*IRR*):

$$IRR\left(T_{obj},\varepsilon_{obj}\right)=\frac{\varepsilon_{obj}\left(T_{obj},\lambda_1\right)\cdot\frac{C_1}{{\lambda_1}^5\cdot\left(e^{\frac{C_2}{\lambda_1\cdot T_{obj}}}-1\right)}}{\varepsilon_{obj}\left(T_{obj},\lambda_2\right)\cdot\frac{C_1}{{\lambda_2}^5\cdot\left(e^{\frac{C_2}{\lambda_2\cdot T_{obj}}}-1\right)}} \qquad \text{Eq 84}$$

If the two wavelengths are close to each other, the $\varepsilon_{obj}(T_{obj},\lambda_1)=\varepsilon_{obj}(T_{obj},\lambda_2)$ approximation can be carried out in such a way to obtain the following:

$$IRR\left(T_{obj},\varepsilon_{obj}\right)=\frac{\frac{C_1}{{\lambda_1}^5\cdot\left(e^{\frac{C_2}{\lambda_1\cdot T_{obj}}}-1\right)}}{\frac{C_1}{{\lambda_2}^5\cdot\left(e^{\frac{C_2}{\lambda_2\cdot T_{obj}}}-1\right)}} \qquad \text{Eq 85}$$

usually, narrow band pass filters are used. If F_1 and F_2 are the transmittance curves of the two filters, the thermosignals which reaches the sensor (with a black body like source) when filters are applied are respectively:

$$G_{bb,1}(T)=\int_{\lambda'}^{\lambda''}R_t(\lambda)\cdot R_{ot}(\lambda)\cdot F_1(\lambda)\cdot\frac{C_1}{\lambda^5\cdot\left(e^{\frac{C_2}{\lambda\cdot T_{obj}}}-1\right)}d\lambda\left[\frac{\mathrm{W}}{\mathrm{m}^2\cdot\mathrm{sr}}\right] \qquad \text{Eq 86}$$

$$G_{bb,2}(T)=\int_{\lambda'}^{\lambda''}R_t(\lambda)\cdot R_{ot}(\lambda)\cdot F_2(\lambda)\cdot\frac{C_1}{\lambda^5\cdot\left(e^{\frac{C_2}{\lambda\cdot T_{obj}}}-1\right)}d\lambda\left[\frac{\mathrm{W}}{\mathrm{m}^2\cdot\mathrm{sr}}\right] \qquad \text{Eq 87}$$

Therefore, calibration curves can be obtained calculating the ratio of Eq 86 and Eq 87, $SR(T)=G_{bb,1}(T)/\ G_{bb,2}(T)$, which under grey-body hypothesis is a function of temperature only.

Generally, the information coming from IR cameras is not the filtered radiation values emitted by the target, but they are derived from software and hardware elaborations (amplification and A/D signal conversion). These values are directly proportional to the radiance and are usually indicated in IR cameras as Object Signal or Digital Level. Moreover, the optical system for the acquisition performed with two filters is the same, since the measurement is performed by switching filters that are supported by the inner camera wheel. So, the Field Of View (FOV) is the same in the two acquisitions through the two filters and is elided in the ratio of the signals acquired, Eq 84.

CHAPTER 3.

STATISTICAL TEST OPTIMIZATION

Despite the availability of an analytical model, the complexity of relations and the effect of random noise variables make the implementation of statistical methods a useful tool to study the applicability of the technique.

Due to the great number of both controllable and uncontrollable random variables affecting the results, an analytical approach, even if carried with detail, cannot include all these effects, and cannot provide results in an exhaustive and easy to interpret way as a statistical approach can do.

The analytical description gives information about interactions between parameters, but it cannot show their effect on the measured signal when random sources of noise are present.

Objective of the study is to provide operative directions for the TSA measurement, indicating best practices and expected measurement error ranges. This kind of problems can be addressed through the implementation of a probabilistic and statistic methods [142].

In fact, the robustness of an experimental measurement procedure can be improved in the first place through implementing statistical methods in simulation based on analytical model.

The aim of the robust design is to provide methods that allow to:

- minimize the number of experimental tests and
- simplify complex design support analyses
- minimize the sensitivity of the system/product to all the noise factors
- meet the quality requirements

This work proposes a Robust Design like approach [140][141] of the TSA measurement system by applying statistic on an analytical model simulating also the various types of errors that can be made on the process.

The aim of this chapter is to provide general notions on the analysis tool employed in a study based on the robust design-like approach.

3.1. Taguchi Robust design

3.1.1. System description

According to Taguchi[140][141], each product or process can be described through a block diagram, as shown in Figure 25

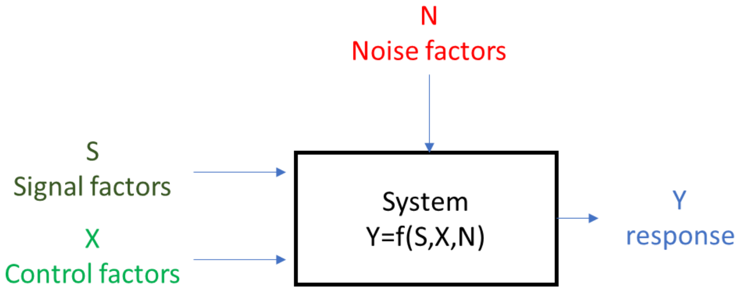

Figure 25 Definition of system in the Robust Design approach.

The system provides the output *Y*, the response to the signal factors S, (S_1, S_2,…,S_n) that are input to the system.

The ideal response of the system is Y_0 and it is represented by the functional relation:

$$Y_o = f(|S|) \qquad \text{Eq 88}$$

The real response *Y*, which stands for the quantitative measurement of the quality of the product/process, differs from Y_0 due to the effect of a certain number of parameters.

The input to the system can be classified into 3 main categories:

- Signal Factors (S): input parameters whose values can be selected by the operator to obtain the expected response.
- Noise Factors (N): Input variables that are not controlled by design choices and vary randomly. Among the noise factors there are environmental variables, tolerance variables, uncontrolled but known noise sources and uncontrolled and unknown noise sources.
- Control Factors (X): Input variables that are controlled by design choices.

Considering the different Factors, the real response can be represented by the following functional relation:

$$Y = f(|S|, |X|, |N|) \qquad \text{Eq 89}$$

For the same system it is possible to study a different kind of problems; for example, the TSA can be applied to measure stress but also to measure residual stresses. In the first case residual stress, if neglected or unknown, must be classified as noise factors, while in the second case their nominal value is a signal factor and their measurement is the output.

To achieve a robust design in terms of performances and response sensitivity to all the three input categories, the minimization of variables effect should be pursued, without trying to eliminate the causes them self. The designer cannot manage noise factors, but he can make response more stable by reducing the variance.

Therefore the designer will act on the control factors and in particular on those that do not involve a greater waste of resources, seeking the optimal combination of these that minimizes the dependence of the output on the Noise Factors.

The two main objectives are:

- to obtain a response Y as close as possible to the ideal response Y_0
- to minimize the intrinsic variation of Y with N

The first thing to do is to make Y tend to Y_0 by setting the Control Factors X in such a way to allow the system to have a response close to the target. The problem rises from the Noise Factors, which can affect the response making it not stable and sensitive to noise.

To minimize the response sensitivity to noise it is necessary to identify and choose among all the X possible configurations (which guarantee the target result) the one with the minimum variation in relation to N.

3.1.2. Analysis definition

For the implementation of the Robust Design, the System should be analysed in detail in order to identify:

- The quality characteristic (system response Y) to be optimized. This first step is fundamental and will affect the success in experimental design. Y should be a continuous variable with a monotonous trend which represents the observed phenomenon in the whole range considered. It has to be also easy to measure.

- Types of problem. The quality of a product or process can be associated with different quantitative criteria. For example, the quality of a component can be measured putting Y equal to the number of defects, thus it will be better as Y approaches zero, in this case the problem is of the ‘SMALLER THE BETTER’ type. If Y is instead set equal to the fatigue strength of a component, the higher this characteristic the better the product proprieties, in this case the problem is of the ‘LARGER THE BETTER’ type. In many cases it is not possible to take extreme values as reference, therefore the optimum objective is reaching a nominal value, in this case the problem is of the ‘NOMINAL THE BEST’ type.
- Signal Factors (S) and Control Factors (X) defining the respective values to the different variation level selected.
- Noise Factors (N). It is important at this stage to identify the noise factors and their range of variation in order to quantify their influence.

3.1.3. Selecting the experimental/simulation plan

The selection of the experimental or simulation plan to collect the data to carry out the statistical analysis depends on some characteristics of the system[140][141]:

- the number and levels of control factors
- the number and levels of noise factors
- the significance of possible interactions

One possibility is to perform a full factorial design, considering all the possible combination for the considered Factors and their levels and considering a certain number of measurement repetition (to consider the random noise effect in the analysis). This approach allows to get all possible information on the system under examination, but it could very hard to implement due to the high number of test required.

A loss of information can be tolerate compared to the test effort of a full factorial plan; for this reason, fractional factorial design is commonly used. The construction of such the plan can be very complex when a high number of Factors and levels are involved, therefore Standard Orthogonal Arrays can be used.

Taguchi Orthogonal Array (OA) design is a type of general fractional factorial design. It is a highly fractional orthogonal design that is based on a design matrix proposed by Dr. Genichi Taguchi and allows to consider a selected subset of combinations of multiple factors at multiple levels.

The standard matrix selection is based on the DOF of the problem, depending on the number of levels of control factors and on the number of influent interactions.

The matrix of the control factors combination can be indicated as the 'internal matrix',

If the study involves the simulation of the response, also the noise factors must be inserted in the plan through the construction of the 'external matrix'.

There are 3 common methods of evaluating the mean and variance of a product's response resulting from variations in many noise factors:

- Monte Carlo simulation
- Taylor series expansion
- Orthogonal array based simulation

In the Monte Carlo simulation a random number is generated to simulate a large number of testing conditions. The value of the response is computed for each condition and the mean and variance are then calculated. This can be very expensive, especially if there are many combinations of control factors.

In the Taylor expansion the mean response is estimated by setting each noise factor equal to its nominal value and the variance is evaluated through the sum of the derivatives of the response with respect to each noise factor multiplied for the respective variance. This formula can be applied only if correlations among noise factors are negligible, if not it becomes more complex and less accurate.

In the orthogonal array-based simulation for each noise factor three or two levels are considered[141]:

- 2 level: $\mu_i - \sigma_i$ and $\mu_i + \sigma_i$

- 3 level: $\mu_i - \sqrt{3/2} \cdot \sigma_i,\ \ \mu_i,\ \ \mu_i + \sqrt{3/2} \cdot \sigma_i$
- with μ_i and ${\sigma_i}^2$ mean and variance of the factor.

Then an orthogonal matrix is built assigning a combination of noise factors to each column and the response is evaluated. The mean and variance are then calculated (Figure 26).

			N_1	**1**	**1**	**…**		
			N_2	1	2			
			…	1	2			
			N_m	1	1		μ	σ
x_1	x_2	…	x_n					
1	1	1	1	y_{11}	..	y_{1j}	μ_1	σ_1
1	2	2	3					
…				y_{i1}	..	y_{ij}	μ_i	σ_i

Figure 26 Full factorial orthogonal matrix

3.1.4. Analysing Results

The 'ideal quality' of a product/process is achieved when every sample/run, every time it performs its function, in all the intended operative conditions and for its entire expected life provides the target performances, that is $Y=Y_0$, without harmful side effects[140].

The presence of Noise factors affects the response with random or systematic deviation respect to the ideal response Y_0. The greater is the difference $\Delta Y_0 = |Y - Y_0|$, the lower is the quality. Usually, the loss in quality implies an economic loss, for this reason the loss of quality is generally estimated in terms of economic loss.

Considering a single sample/run of the system on which the response measurement is carried out at a certain time (fixed the values of the signal factors), if Y is the value of the quality characteristic compared to the nominal one Y_0, the Quality Loss Function can be defined as follow:

$$Q = \frac{A_0}{\Delta Y_0^2}(Y - Y_0)^2 \qquad \text{Eq 90}$$

With $A_0 = Q(Y_0 + \Delta Y_0)$.

The ratio $K_q = \frac{A_0}{\Delta Y_0^2}$ is a constant and represents the economic loss.

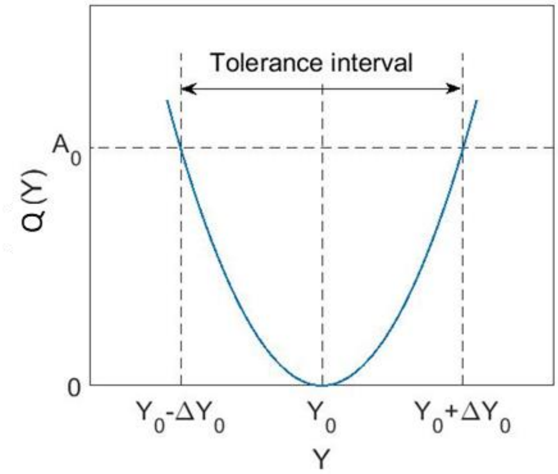

Figure 27 The quality of the product defined by means of the Quality Loss Function Q(Y).

This definition of non-quality therefore considers the uniformity of the characteristics of the product/process around the expected optimal value Y_0, not the conformity of these characteristics with the limits of the specifications. This quadratic representation of the loss function (Figure 27) has a minimum for $Y = Y_0$ and grows with ΔY_0. The points that fall outside the tolerance limit identify the functional limits of the system at which half of the systems are considered failures (customer tolerance).

Considering *n* experiments, the Mean Quality Loss Function becomes:

$$Q = K_q \left[(\mu - Y_0)^2 + \frac{n-1}{n} \sigma^2 \right] \qquad \text{Eq 91}$$

Where μ and σ^2 are the Mean and the variance of the quality characteristic *Y*:

$$\mu = \frac{1}{n} \sum_{j=1}^{n} Y_j$$

$$\sigma^2 = \frac{1}{n-1} \sum_{j=1}^{n} \left(Y_j - \mu \right)^2 \qquad \text{Eq 92}$$

The quality level of the individual experiments is measured by the Signal to Noise ratio (*SN ratio*), a quantity which is linked to the Quality Loss Function and is a function of the ratio between the Mean value and variance of a set of experiments:

$$SN = 10 \log_{10} \frac{\mu^2}{\sigma^2} \qquad \text{Eq 93}$$

The maximization of *SN* is equivalent to the Q*(Y)* minimization, that is, minimize the sensitivity of the system to the noise factors. The *SN* ratio is measured in dB and its definition implies a logarithmic transformation in order to extend the effective range of the quality characteristic. Furthermore, the additivity of the control factors effects is improved, and the variance results more stable and with improved Gaussian proprieties.

The type of problem defines which are the expressions for the Quality Loss Function and the SN ratio that have to be used in the analysis. There are three possible type of problem and are summarized in Table 3.

Table 3 Quality Loss Function and related SN ratio for typical problems

PROBLEM TYPE	QUALITY LOSS FUNCTIO	SN RATIO
NOMINAL THE BEST	$Q = K_q(Y - Y_0)^2$	$SN = 10 \log_{10} \frac{\mu^2}{\sigma^2}$
SMALLER THE BETTER	$Q = K_q Y^2$	$SN = -10 \log_{10} \left(\frac{1}{n} \sum_{j=1}^{n} Y_j^2 \right)$
LARGER THE BETTER	$Q = K_q \frac{1}{Y^2}$	$SN = -10 \log_{10} \left(\frac{1}{n} \sum_{j=1}^{n} \frac{1}{Y_j^2} \right)$

The contribution of the different factors to the overall mean can be evaluated by the Analysis of Means (AMOM), while the Analysis of Variance analyses the significance level of the effects of the individual factors end significative interactions. The results obtained from the ANOM and ANOVA analyses[142] indicates the relevant Factors to consider for the selection on the base of the maximum SN ratio and minimum Quality Loss Function.

CHAPTER 4.

DEVELOPMENT OF A TSA GENERAL MODEL AND ITS APPLICATIONS

In this work the TSA equation was proposed in a general formulation allowing to analytical simulate the thermoelastic response of a homogeneous material subjected to a generic linear elastic stress field in adiabatic conditions.

The proposed approach could represent a useful tool to obtain information about the residual stresses on real components subjected to actual loading conditions. The assessment of the effective stress map of real components in the presence of residual stresses is of great importance together with their estimation in many industrial applications. This is the case, for instance, for mechanical components produced by means of the Additive Manufacturing process in which the residual stresses play a key role on the material stresses distribution, and then its mechanical behaviour.

In the following paragraphs the mathematical steps which allowed to obtain the proposed formulation are described.

Such the model was then employed to describe effect of biaxial and generally oriented stress on the thermoelastic signal, following the representation proposed by Wang for the uniaxial case, that is considering the residual stress vector as an additive term to the mean load.

The developed analytical model was then used to study the technique sensitivity to the mechanical and physical characteristics of the material and to the presence of residual stress; the simulations were performed considering two non-ferrous alloys: the alluminum alloy AA6082 and the titanium alloy Ti 6Al 4V.

Furthermore, the proposed equation was used for evaluating the error made in neglecting the principal residual stresses in terms of modulus, sign and direction with respect to the applied amplitude and mean stresses. In particular, two approaches for calibrating the

TSA data were considered, based on the classical TSA equation [1,6] and the revised high order theory (mean stress effect) [19]. In both cases, the error was investigated as a function of the residual stresses.

Similar simulations with the proposed equation were used to carry out a statistical analysis with the aim to evaluate the minimum value of residual stresses which lead to significant and measurable variations in the thermoelastic signal for aluminium and titanium alloys.

4.1. TSA General model Analytical Development

Under isentropic and adiabatic condition and considering the material macroscopically homogeneous, the thermoelastic general equation obtained by Potter and Graves [143] can be written in tensorial form:

$$\rho C_\varepsilon \frac{dT}{T} = \left((\bar{\varepsilon}-\bar{\alpha}\Delta T)^T \frac{\partial \bar{\bar{C}}^T}{\partial T} - \bar{\alpha}^T \bar{\bar{C}}^T \right) d\bar{\varepsilon} \qquad \text{Eq 94}$$

In Eq 94, dT is the infinitesimal temperature difference due to the thermoelastic effect associated with the strain field $d\bar{\varepsilon}$.

$\bar{\varepsilon}$,$\bar{\alpha}$ and $\bar{\bar{C}}$ represent respectively the state of deformation in a point, the vector of the linear thermal expansion coefficients and the material stiffness matrix, and, expressed in the referment system xyz, are given by:

$$\bar{\varepsilon} = \begin{pmatrix} \varepsilon_{xx} \\ \varepsilon_{yy} \\ \varepsilon_{zz} \\ \gamma_{zx} \\ \gamma_{yz} \\ \gamma_{xy} \end{pmatrix} \qquad \bar{\alpha} = \begin{pmatrix} \alpha_{xx} \\ \alpha_{yy} \\ \alpha_{zz} \\ \alpha_{zx} \\ \alpha_{yz} \\ \alpha_{xy} \end{pmatrix}$$

$$\bar{\bar{C}} = \begin{pmatrix} C_{1111} & C_{1122} & C_{1133} & C_{1131} & C_{1123} & C_{1112} \\ C_{2211} & C_{2222} & C_{2233} & C_{2231} & C_{2223} & C_{2212} \\ C_{3311} & C_{3322} & C_{3333} & C_{3331} & C_{3323} & C_{3312} \\ C_{3111} & C_{3122} & C_{3133} & C_{3131} & C_{3123} & C_{3112} \\ C_{2311} & C_{2322} & C_{2333} & C_{2313} & C_{2323} & C_{2312} \\ C_{1211} & C_{1222} & C_{1233} & C_{1231} & C_{1223} & C_{1212} \end{pmatrix} \qquad \text{Eq 95}$$

In order to obtain Eq 94 the dependence of $\bar{\alpha}$ from temperature has been neglected. In fact, in most cases this term is negligible, being of the order of 10^{-9}K for $\Delta T \approx 10^{-2}$K and $\alpha \approx 10^{-7}$ K^{-1}.

The strain and the stress vectors are linked through the constitutive relation:

$$\bar{\varepsilon} = \bar{\bar{C}}^{-1}\bar{\sigma} + \bar{\alpha}\Delta T \qquad \text{Eq 96}$$

Substituting in Eq 94:

$$\rho c_\varepsilon T^{-1} dT = \left[\left(\bar{\bar{C}}^{-1}\bar{\sigma}\right)^T \frac{\partial \bar{\bar{C}}^T}{\partial T} - \bar{\alpha}^T \bar{\bar{C}}^T \right] \bar{\bar{C}}^{-1} d\bar{\sigma} \qquad \text{Eq 97}$$

Eq 97 describes the temperature variation due to the thermoelastic effect associated with the variation of the stress state $d\bar{\sigma}$, for a homogeneous material in adiabatic conditions. Eq 97 can therefore be applied to describe the thermoelastic behaviour in any load condition and for anisotropic materials.

It is possible to use Eq 97 to analyse some cases of practical interest.

If the stress vector components vary in phase with sinusoidal law one has:

$$\bar{\sigma} = \bar{\sigma}_M + \Delta\bar{\sigma}\, sin(\omega t), \qquad d\bar{\sigma} = \Delta\bar{\sigma}\, cos(\omega t)\, \omega dt \qquad \text{Eq 98}$$

where $\boldsymbol{\bar{\sigma}_M}$ and $\Delta\boldsymbol{\bar{\sigma}}$ are respectively the mean and the semi-amplitude vectors that can be expressed as vectors in the reference system as:

$$\Delta\bar{\sigma} = \begin{pmatrix} \Delta\sigma_{xx} \\ \Delta\sigma_{yy} \\ \Delta\sigma_{zz} \\ \Delta\sigma_{zx} \\ \Delta\sigma_{yz} \\ \Delta\sigma_{xy} \end{pmatrix} \qquad \bar{\sigma}_M = \begin{pmatrix} \sigma_{Mxx} \\ \sigma_{Myy} \\ \sigma_{Mzz} \\ \tau_{Mzx} \\ \tau_{Myz} \\ \tau_{Mxy} \end{pmatrix} \qquad \text{Eq 99}$$

Substituting Eq 98 into Eq 99:

$$\begin{aligned} \rho c_\varepsilon T^{-1} dT = {} & \left[\left(\bar{\bar{C}}^{-1}\bar{\sigma}_M\right)^T \frac{\partial \bar{\bar{C}}^T}{\partial T} - \bar{\alpha}^T \bar{\bar{C}}^T \right] \bar{\bar{C}}^{-1} \Delta\bar{\sigma}\, cos(\omega t)\, \omega dt \\ & + \frac{1}{2} \left[\left(\bar{\bar{C}}^{-1}\Delta\bar{\sigma}\right)^T \frac{\partial \bar{\bar{C}}^T}{\partial T} \right] \bar{\bar{C}}^{-1} \Delta\bar{\sigma}\, sin(2\omega t)\, \omega dt \end{aligned} \qquad \text{Eq 100}$$

Integrating between t_0=0 and t, with $T(t_0)$=T_0, Eq 100 became:

$$\rho c_\varepsilon {T_0}^{-1} \mathit{\Delta} T = \left[\left(\bar{\bar{C}}^{-1}\bar{\sigma}_M\right)^T \frac{\partial \bar{\bar{C}}^T}{\partial T} - \bar{\alpha}^T \bar{\bar{C}}^T \right] \bar{\bar{C}}^{-1}\Delta\bar{\sigma}\, sin(\omega t) + \frac{1}{4}\left[\left(\bar{\bar{C}}^{-1}\Delta\bar{\sigma}\right)^T \frac{\partial \bar{\bar{C}}^T}{\partial T}\right]\bar{\bar{C}}^{-1}\Delta\bar{\sigma}[1-cos(2\omega t)] \qquad \text{Eq 101}$$

In Eq 101, as well as in there are two terms: the first varies with the same frequency as the load and depends both on the amplitude of the stress and the mean stress; the second term has frequency twice the frequency of the load and depends only on the mean stress.

By focusing on the semi-amplitude of the temperature running at the same frequency as the applied load, one can describe the temperature variations as:

$$\rho c_\varepsilon {T_0}^{-1} \mathit{\Delta} T_1 = \left[\left(\bar{\bar{C}}^{-1}\bar{\sigma}_M\right)^T \frac{\partial \bar{\bar{C}}^T}{\partial T} - \bar{\alpha}^T \bar{\bar{C}}^T \right] \bar{\bar{C}}^{-1}\Delta\bar{\sigma} \qquad \text{Eq 102}$$

where the mean load vector $\bar{\sigma}_M$ represents all the stresses contributions which remain constant during the sinusoidal loading; it can be described by the sum of:

- the applied mean load, here considered proportional to $\Delta\bar{\sigma}$ for each pixel in a fixed test,
- the residual stress
- the own weight of the structure
- stresses linked to bending moments on both in plane and out of plane direction.

Considering the terms that add up to the mean load, both the own weight of the structure and the bending moments are usually negligible. Therefore, $\bar{\sigma}_M$ can be considered as the sum of the applied mean load and the residual stresses vector.

In this case, Eq 102 became:

$$\mathit{\Delta} T = (\rho C_\varepsilon)^{-1} T_0 \left[\left(\bar{\bar{C}}^{-1}\left(\bar{\sigma}_m + \bar{\bar{R}}\bar{\sigma}_r\right)\right)^T \frac{\partial \bar{\bar{C}}^T}{\partial T} - \bar{\alpha}^T \bar{\bar{C}}^T \right] \bar{\bar{C}}^{-1}\Delta\bar{\sigma} \qquad \text{Eq 103}$$

In Eq 103, the residual stress vector $\bar{\sigma}_r$ is expressed in the principal stress reference system, while the tensor $\bar{\bar{R}}$ is the rotation matrix that allows to write $\bar{\sigma}_r$ in the reference system used to write the equation.

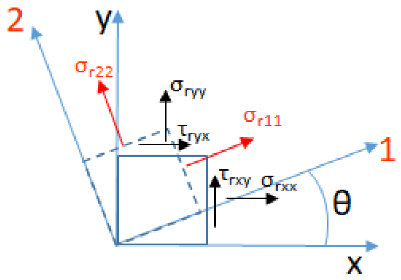

Figure 28 Residual stresses principal system and loading system.

Using Eq 103, it is also possible to evaluate the thermoelastic signal in the particular case of uniaxial stresses and isotropic material but with biaxial residual stresses, which is the case of main interest for practical applications.

Assuming $\bar{\sigma}_m$ and $\Delta\bar{\sigma}$ are uniaxial (σ_{mxx}, $\Delta\sigma_{xx}$), and considering the material isotropic and θ the angle between the residual stress principal system and the loading system, see Figure 28, Eq 103 became:

$$\Delta T = (\rho C_\varepsilon)^{-1} T_0 \left\{ \frac{1}{E^2}\frac{\partial E}{\partial T} \left[\sigma_{m_{xx}} + \sigma_{r11} \left[\cos^2\theta - \sin^2\theta \left(\nu - \frac{\partial \nu}{\partial T}\frac{E}{\frac{\partial E}{\partial T}} \right) \right] + \sigma_{r22} \left[\sin^2\theta - \cos^2\theta \left(\nu - \frac{\partial \nu}{\partial T}\frac{E}{\frac{\partial E}{\partial T}} \right) \right] \right] - \alpha \right\} \Delta\sigma_{xx} \qquad \text{Eq 104}$$

It is possible to assume $\frac{\partial \nu}{\partial T} \approx 0$ [50][51], therefore Eq 104 became:

$$\Delta T = (\rho C_\varepsilon)^{-1} T_0 \left\{ \frac{1}{E^2}\frac{\partial E}{\partial T} \left[\sigma_{mxx} + \sigma_{r11}[\cos^2\theta - \nu \sin^2\theta] + \sigma_{r22}[\sin^2\theta - \nu\cos^2\theta] \right] - \alpha \right\} \Delta\sigma_{xx} \qquad \text{Eq 105}$$

In this work, to consider the term linked to the residual stress, the parameter *c* has been defined as follows:

$$c = b\sigma_{r11}[(cos^2\theta - \nu\, sin^2\theta) + \gamma_r(sin^2\theta - \nu\, cos^2\theta)] \qquad \text{Eq 106}$$

with $\gamma_r = \sigma_{r22}/\sigma_{r11}$.

Substituting in Eq 105, it can be obtained that

$$\frac{\Delta T}{T_0} = (a + c)\Delta\sigma_{xx} + b\gamma\Delta\sigma_{xx}^2 \qquad \text{Eq 107}$$

Therefore, the stress can be evaluated by measuring the thermoelastic signal ΔT and solving

$$(a + c)\Delta\sigma_{xx} + b\gamma\Delta\sigma_{xx}^2 - \frac{\Delta T}{T_0} = 0 \qquad \text{Eq 108}$$

4.2. Study of TSA sensitivity to the material mechanical and physical characteristics and its potential in the evaluation of residual stress in non-ferrous metal

4.2.1. Introduction

The TSA general model was used to study the technique sensitivity to the mechanical and physical characteristics of the material and to the presence of residual stress.

This paragraph reports the simulation study carried out considering two non-ferrous alloys: the alluminum alloy AA6082 and the titanium alloy Ti 6Al 4V.

The simulations involved the employment of literature date for the material characteristics. The sensitivity to the mechanical and physical characteristics of the material was studied by imposing small variation of these characteristics around their reference values (±2%).

The thermoelastic signal sensitivity to the presence of residual stresses was studied by simulating several residual stress conditions, compatible with the mechanical strength of the materials.

By comparing the simulation results with TSA experimental results obtained for AA6082 samples, it was possible to evaluate a first raw estimation of the minimum value for residual stresses which can bring an experimentally detectable variation in the thermoelastic signal.

4.2.2. Methodology

Eq 103 was used in order to evaluate the TSA sensitivity to the variation of mechanical and physical characteristics of the material and to the presence of residual stresses. The analysis was conducted considering two materials: the Titanium alloy Ti 6Al 4V and the Alluminium alloy AA6082; both the alloys show a second order effect on the thermoelastic signal which can’t be neglected[14][25][45][46][53][54]

For each material a referment set of mechanical and physical characteristics was considered [45][50][144][145][146], as reported in Table 4.

The thermoelastic signal was calculated varying the mean load for a sinusoidal mono-axial loading condition; furthermore, it was calculated varying one by one the material characteristics with a variation of the 1% and of the 2% respect to the referment values. All the simulations were performed considering a peak-to-peak load amplitude σ_a of 110 MPa.

The residual stress effect was studied setting the referment set for the material characteristics and introducing in Eq 103 a non-null $\bar{\sigma}_r$ vector.

The proposed model was applied in the following cases:

- uniaxial residual stress, oriented as the load; stress was simulated of both traction (10, 25, 50 and 100 MPa) and compression (-10, -15, -50 and -100 MPa), with $\Delta\sigma$=55MPa.
- biaxial residual stress, oriented as the load; stress was simulated in the cases of traction-traction ($\sigma_{r1}= \sigma_{r2}$=100MPa), compression-compression ($\sigma_{r1}= \sigma_{r2}$=-100MPa) and traction-compression ($\sigma_{r1}=-\sigma_{r2}$=100MPa), with $\Delta\sigma$ =55MPa.
- biaxial residual stress, oriented as the load; stress was simulated varying the rotation angle of residual stress principal system in the cases of traction-traction ($\sigma_{r1}= \sigma_{r2}$=100MPa), compression-compression ($\sigma_{r1}= \sigma_{r2}$=-100MPa) and traction-compression ($\sigma_{r1}=-\sigma_{r2}$=100MPa), with $\Delta\sigma$ =55MPa and σ_m=100MPa.

All the simulations were performed with the assumptions of isotropic material and neglecting the term ∂v/∂T (it was experimentally proved that the Poisson modulus v is constant in the narrow temperature range covered by thermoelastic effect [51][52]).

Table 4 Refeernce set of mechanical and physical characteristics for the alloys Ti 6Al 4V and AA6082

Material	**ρ**	**Cp**	**Cε**[1]	**α**	**E**	**∂E/∂T**	**v**
	[Kg/dm^3]	[J/KgK]	[J/KgK]	K^{-1}	[GPa]	[MPa]	
Ti 6Al 4V	4.43	526.3	521.1	8.6E-6	114	-48	0.33.
AA6082	2.70	897.0	861.4	23.2E-6	69	-36	0.33

---

[1] The specific heat at constant strain was obtained by applying the relation $C_p - C_\varepsilon = \frac{2E\alpha^2 T_0}{\rho(1-\nu)}$

4.2.3. Experimental campaign

TSA experimental tests were conducted on dog bone specimens of AA 6082 obtained from a laminated sheet with the longitudinal direction inclined by 90 ° with respect to the rolling direction. The specimens state of supply is T6 (Figure 29).

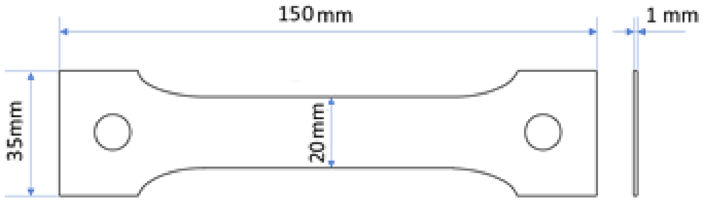

Figure 29 geometry of the specimens used in TSA tests.

All the tests have been performed on an MTS 100KN loading machine and TSA data were acquired with a cooled IR camera FLIR ax640 which is characterized by a NETD <25 mK and is equipped with a cooled 640x512 pixel InSb sensor.

The specimens were subjected to a monoaxial sinusoidal load. Three different load conditions were considered, characterized by the same peak-to-peak amplitude σ_a = $2\Delta\sigma$=110MPa and by three different values of the mean load: 120 180 and 240 MPa. The tests were performed with three different loading frequencies:13, 15 and 17 Hz. In Table 5 the experimental campaign parameters are reassumed.

Table 5 Test performed on the specimen in AA6082; peak-to-peak load amplitude, mean load, load frequency and number of repetitions for each measurement are reported.

σ_a [MPa]	σ_m [MPa]	f [Hz]	N°. rip.
110	120	13	3
110	180	13	3
110	240	13	3
110	120	15	3
110	180	15	3
110	240	15	3
110	120	17	3
110	180	17	3
110	240	17	3

The specimens were painted with opaque black paint to improve and standardize the emissivity of the surface and to avoid reflection.

Data processing was performed using the IRTA® software. For all the tests the ΔT value was obtained as the mean value of all the pixels of a rectangular area in the useful stretch of the specimen.

Figure 30 shows: (a) the surface temperature map captured in a generic instant of the test and (b) the surface map of ΔT obtained by applying the TSA technique.

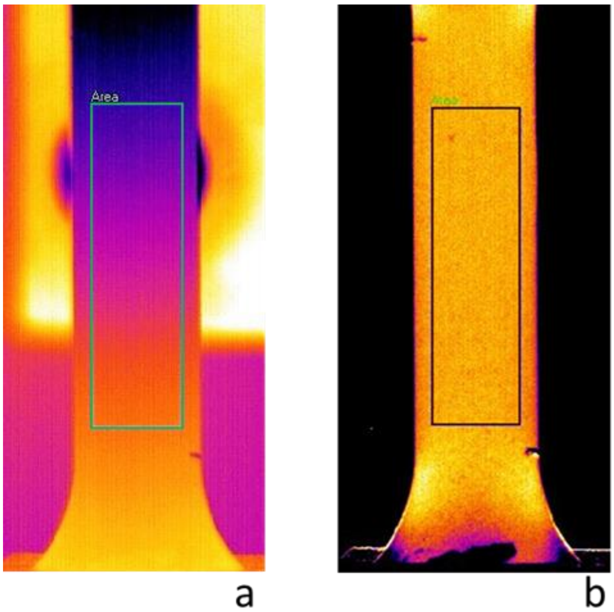

Figure 30 (a) the surface temperature map captured in a generic instant of the test and (b) the surface map of ΔT obtained by applying the TSA technique.

Experimental measurements were employed to find the confidence interval of the measurements. The confidence interval was then compared with the TSA sensitivity to the presence of residual stress obtained from the analytical simulation. The workflow is reassumed in Figure 31.

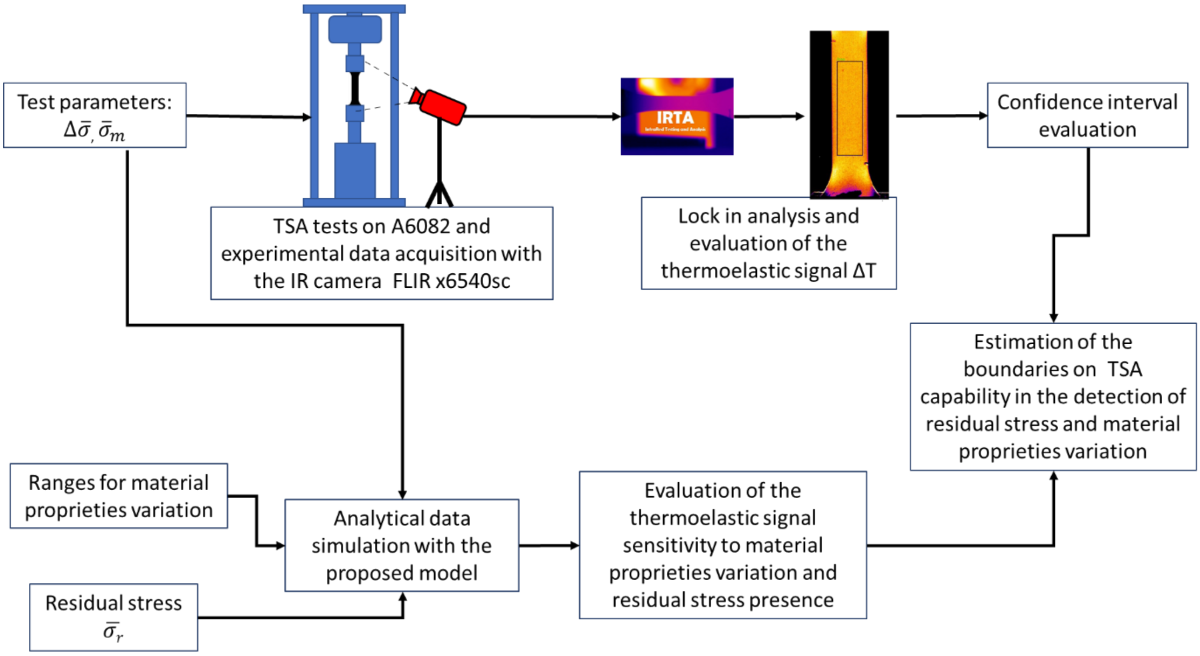

Figure 31 Activity workflow

4.2.4. Analytical study results and discussions

Figure 32 and Figure 33 show the results obtained from the analytical simulation of the variation of the mechanical and physical characteristics for the alloys AA6082 and Ti 6AL 4V respectively.

In particular, the thermoelastic signal is plotted as a function of the mean load; both materials show a slope variation with the variation of E and ∂E/T and an intercept variation with the variation of α, ρ and Cε.

For the Titanium alloy a variation of 2% on α, ρ and Cε corresponds to a variation of the thermoelastic signal of about 0.001 ° C which represents about 2% on the measurement, while for the Aluminum allloy it corresponds to a variation of about 0.003 ° C which represents about 2% of the measure. The influence of E and ∂E ∂T is negligible in both cases.

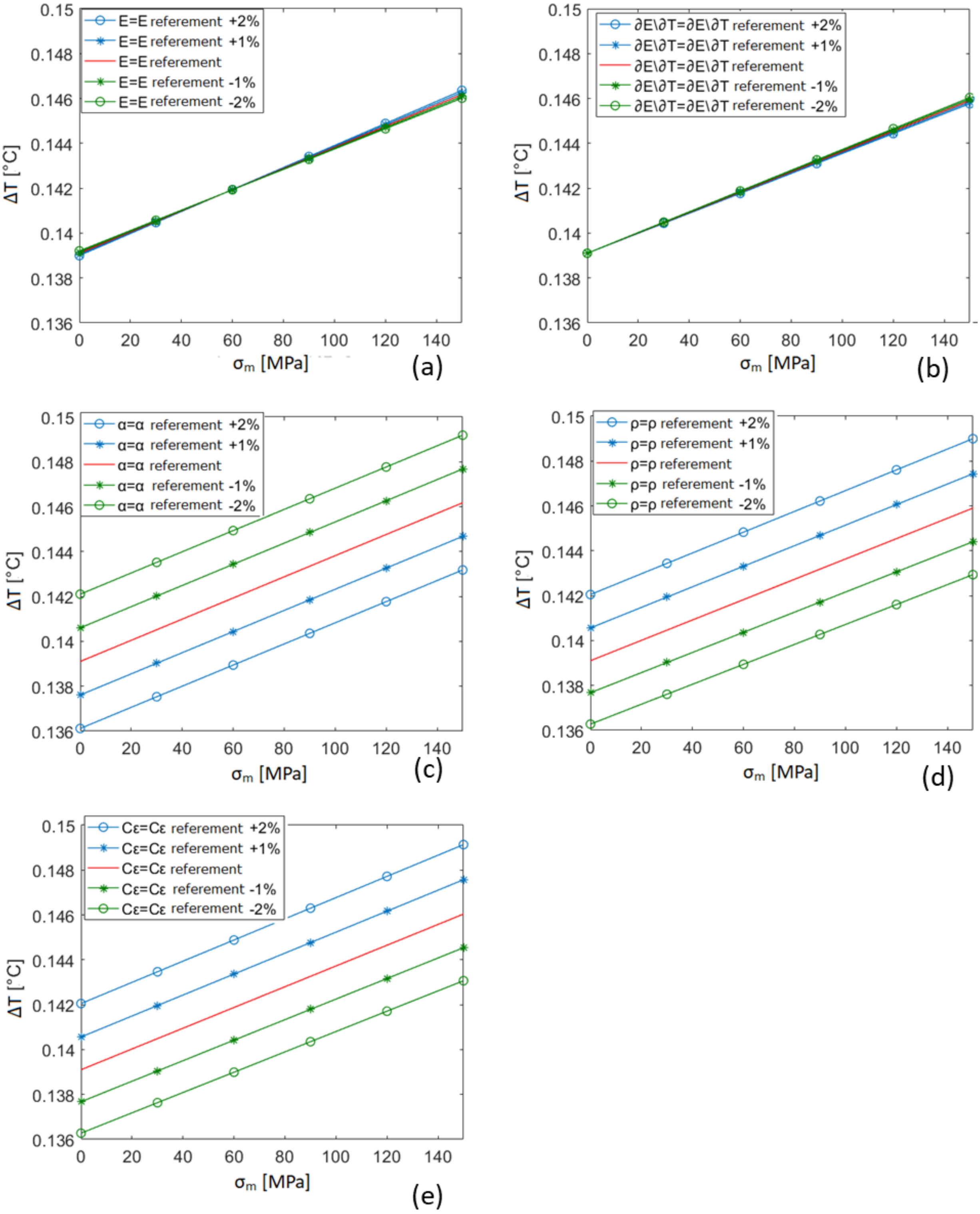

Figure 32 ΔT(σm) curves from the analytical simulation of the variation of the mechanical characteristics (a) E and (b) ∂E\∂T, and physical proprieties (c) α, (d) ρ and (e) Cε. for the alloy AA6082

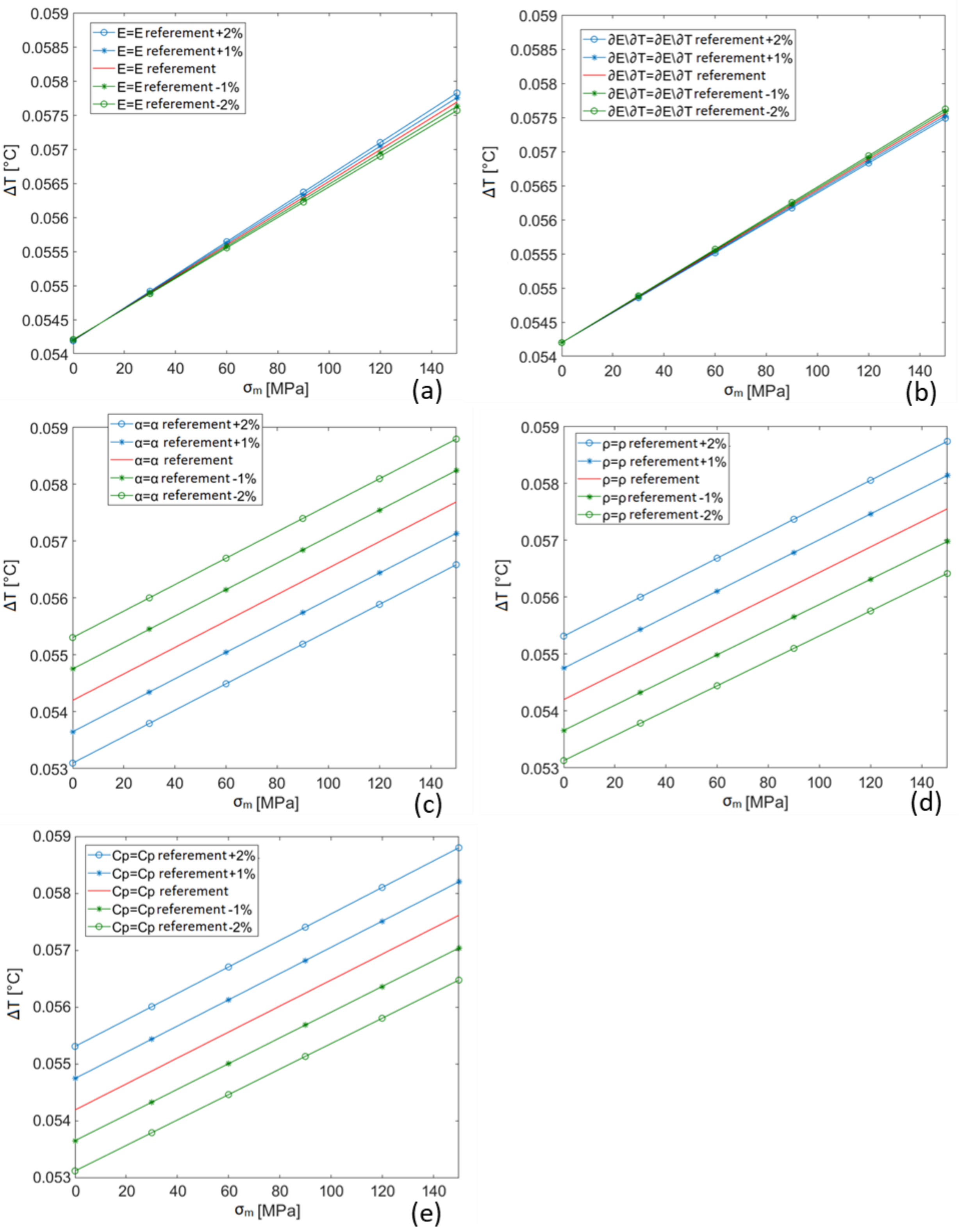

Figure 33 ΔT(σm) curves from the analytical simulation of the variation of the mechanical characteristics (a) E and (b) ∂E\∂T, and physical proprieties (c) α, (d) ρ and (e) Cε. for the alloy Ti 6Al 4V

The results obtained from the study of the presence of residual stress are reported in Figure 34 for the AA6082 and Figure 35 for the Ti 6AL 4V.

Considering the case of monoaxial residual stress, oriented as the load (Figure 34 a and Figure 35 a), for both the materials the presence of residual stress involves an intercept variation for the curve $\Delta T(\sigma_m)$ and a symmetric response to the residual stress direction inversion. For the Titanium alloy, the presence of residual stress with a modulus of 100MPa implies a thermoelastic signal variation of approximately 0.0023 ° C, or about 4% of the measurement; for the AA6082, on the other hand, with a residual stress of 100 MPa, a thermoelastic signal variation of 0.005 ° C is obtained, or 3.4% of the measurement.

Figure 34 b and Figure 35 b show how the presence of biaxial residual stress oriented as the load, can modify the intercept of the relation $\Delta T(\sigma m)$. In both cases the thermoelastic signal increases when σ_{r1} and σ_{r2} increase respectively as traction stress and compression stress.

Figure 34 c and Figure 35 c show how the orientation of a biaxial residual stress system respect to the loading direction can affect the thermoelastic signal. The traction-compression is the case with the higher variation. In the simulated loading condition, a residual stress system $\sigma r1=-\sigma r2=100MPa$ implies a variation of 0.013°C, or 8,84% of the measurement for the AA6082 and a variation of 0.007°C, or 12,17% of the measurement.

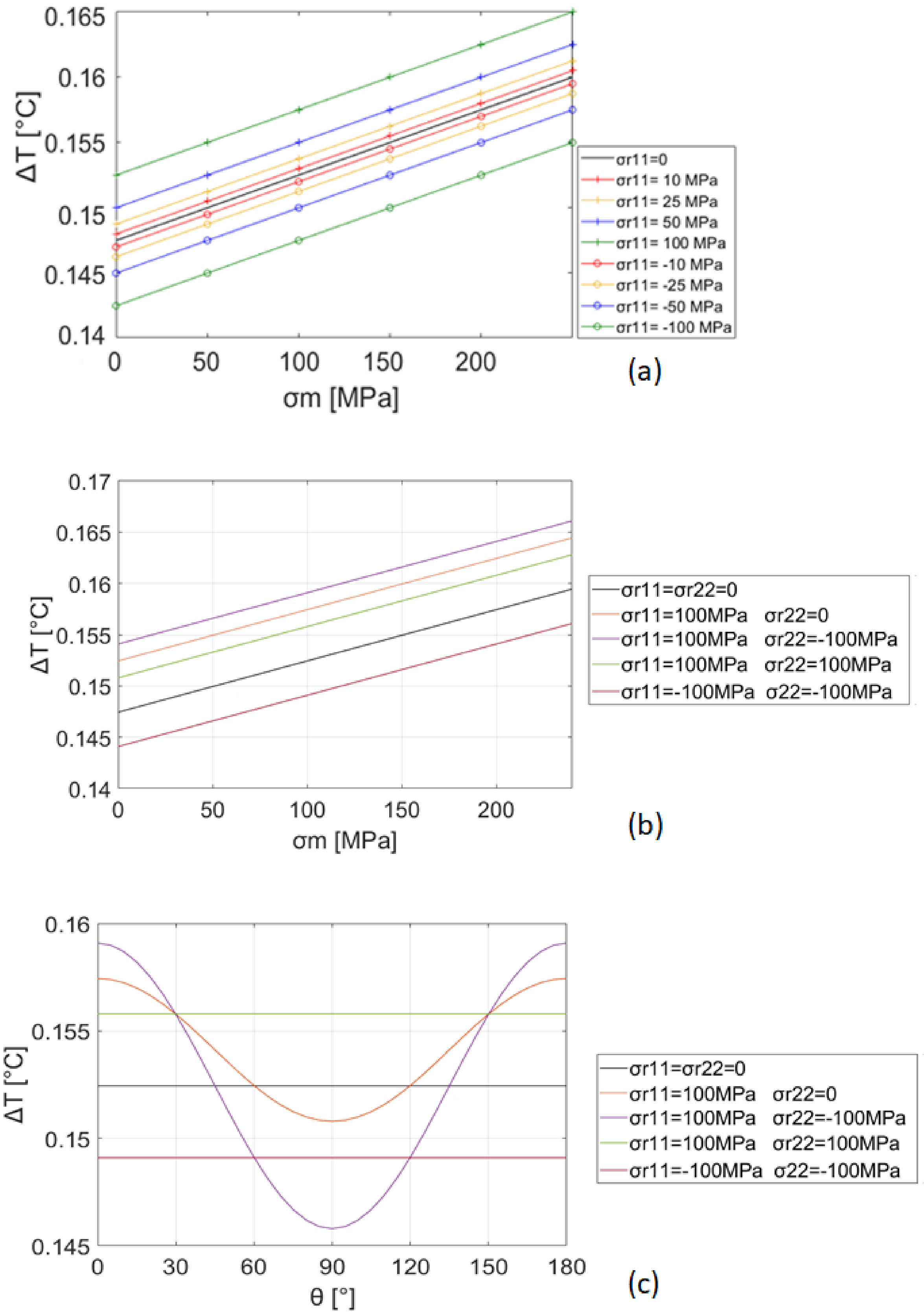

Figure 34 Results obtained from the analytical simulation of the presence of residual stress for the AA6082: ΔT(σm) curves for the cases of (a) uniaxial residual stress directed as the load and (b) biaxial residual stress directed as the load and ΔT(θ) curve for the case of biaxial residual stress with σm=100MPa. All the simulations were performed with Δσ=55MPa.

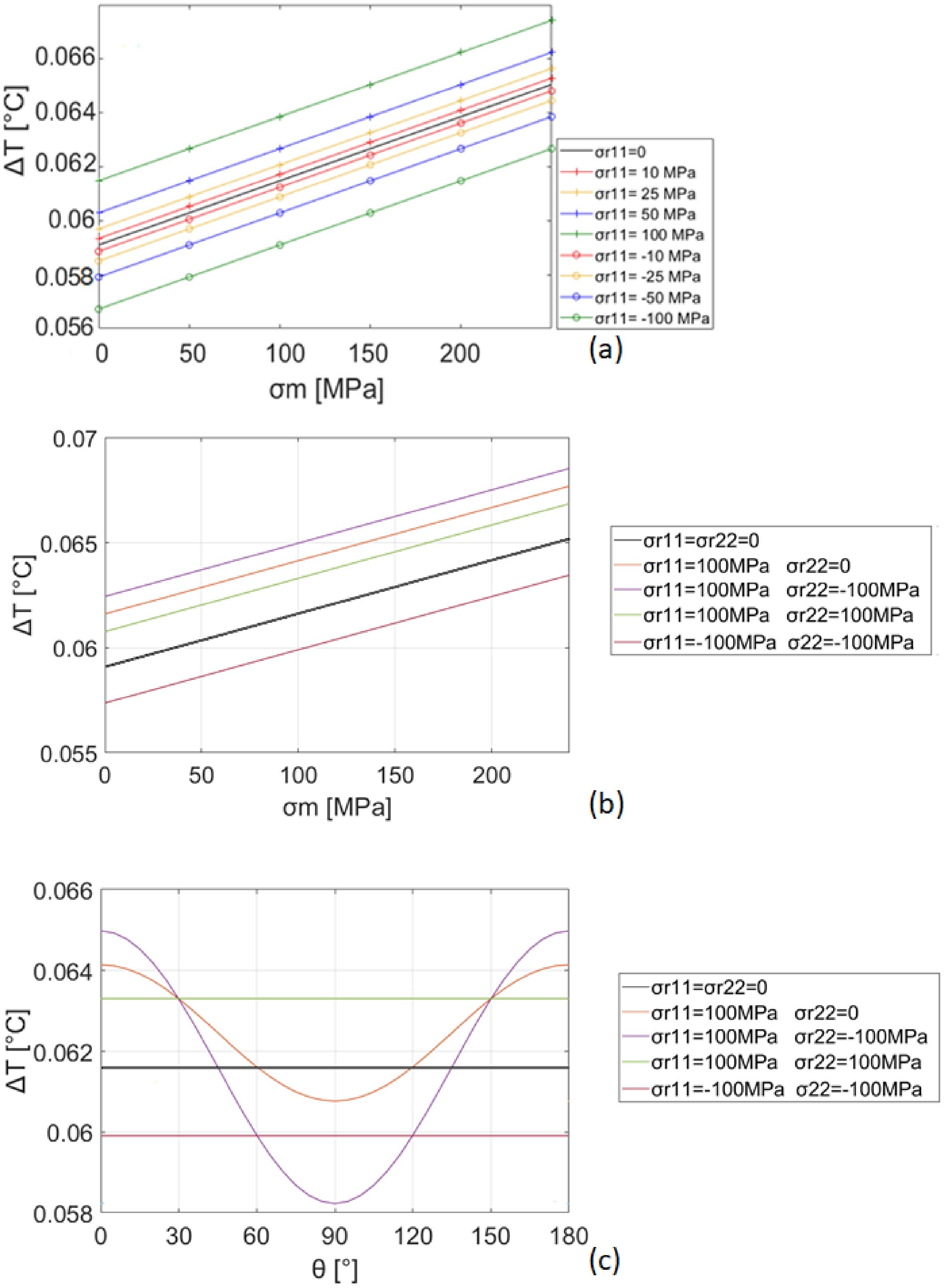

Figure 35 Results obtained from the analytical simulation of the presence of residual stress for the Ti 6Al 4V: ΔT(σm) curves for the cases of (a) uniaxial residual stress directed as the load and (b) biaxial residual stress directed as the load and ΔT(θ) curve for the case of biaxial residual stress with σm=100MPa. All the simulations were performed with Δσ=55MPa.

4.2.5. Comparison between experimental and analytical results

Figure 36 shows the comparison between the linear interpolation of the experimental data and those obtained from the analytical simulation for the AA6082.

The discrepancy between analytical and experimental results is in accordance with the sensitivity analysis. The values assumed for the more influent parameters (α, ρ, Cp) which affect the intercept of the curve, are probably incorrect.

Considering a confidence level of 95%, the confidence interval is ±0.0007°C, or 0.5% of the measurement. Assuming for the simulated measurements the same accuracy, it is possible to estimate the minimum residual stress value detectable with the TSA.

As a first approximation, the minimum residual stress value detectable with the TSA can be found as the minimum value which lead to a thermoelastic signal variation falling outside the confidence interval.

The equipment employed allows to detect a thermoelastic signal variation when the AA6082 presents at least a residual stress of 30 MPa (Figure 37).

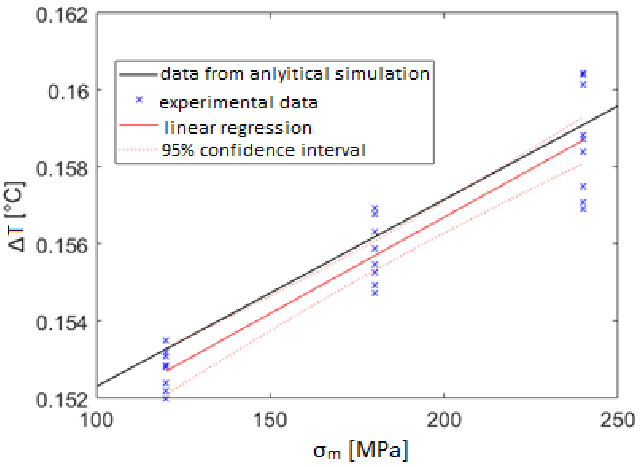

Figure 36 Comparison between the analytical ΔT(σm) curve and experimental data from TSA tests on AA6082

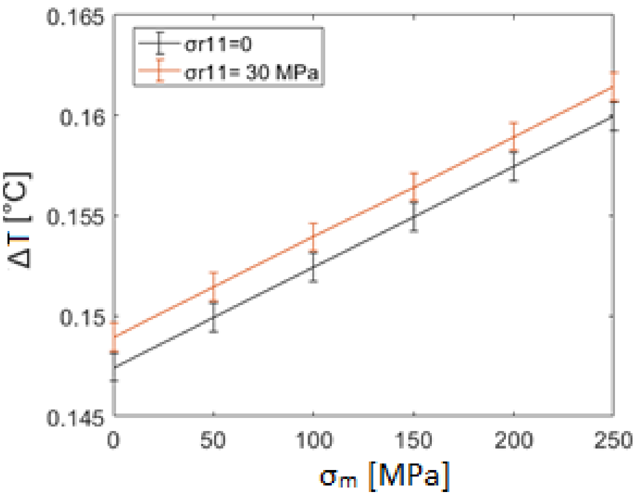

Figure 37 Analytical ΔT(σm) curve obtained for the AA6082 in the case of null residual stress and uniaxial residual stress directed as the load of 30MPa.

4.2.6. Conclusions

In this preliminary work a first analytical study was conducted in the simplified conditions of isotropic material and monoaxial loads to determine the sensitivity of the TSA to the variation of the mechanical and physical characteristics and to the presence of residual stresses.

The following considerations emerged from the study:

- The simulation showed how small variations of E and ∂E ∂T do not involve a variation of the experimentally detectable thermoelastic signal, while, as expected, variations of α, ρ and Cε of 2% involve a 2% variation on the measurement, then experimentally detectable.

- In the case of bi-axial residual stresses, the variation of the residual stress system orientation determines a strong variation of the thermoelastic signal. On one side, if neglected, this effect leads to an error in the measurement, on the other side it could be exploited, by applying appropriate procedures for residual stresses estimation.

- From the comparison with the experimental data, it was also possible to estimate the residual stresses measurable with the TSA. In the case of the AA6082 30MPa was found as the minimum threshold which produces significant variations in the thermoelastic signal.

The objective of this work was to verify the applicability of the general TSA equation for a known material, with a known and easily reproducible loading system. Since the proposed model has general validity, it will be necessary to continue the study by extending the analysis to more complex cases.

4.3. Statistical study of the Influence of Biaxial Residual Stress on Aluminium and Titanium

4.3.1. Introduction

The work presented in this paragraph is a statistical study applied to simulations of temperature measurement during TSA tests under different residual stress conditions.

Simulations were carried out generating synthetic thermal sequences affected by the Thermal Camera noise. Such the sequences were then processed with the same algorithm adopted for real acquisitions.

The application of a statistical approach was required due to the complexity of the equation and the random nature of the Noise. The aim was to determine the minimum value of residual stress which leads to a measurable variation in the thermoelastic signal for the considered materials.

4.3.2. Materials and Methods

Two different materials were used for simulating TSA data: Titanium alloy Ti-6Al-4V and Aluminium alloy AA6082; both alloys show a non-negligible second order effect on the thermoelastic signal [16][17][25][45][46][53][54]. In Table 4 are the values of the mechanical and thermo-physical properties of materials [45][50][144][145][146].

In each simulation, a reference temperature of 293 K was assumed. In order to simulate the real thermoelastic signal in different stress and residual stress conditions, Eq 103 was employed and the statistical analysis was carried out by considering a white gaussian noise. Experimental measurements were performed on a uniform temperature target (about 297 K), by using a cooled IR camera FLIR X6540sc (Flir System, Inc. Winstonville, OR, USA) with a frame rate of 200 Hz and an integration time of 0.596 ms, which are the settings used in TSA tests. The results demonstrated a standard deviation for the noise of 0.01 K (Figure 2) and, therefore, this was the value adopted in this study.

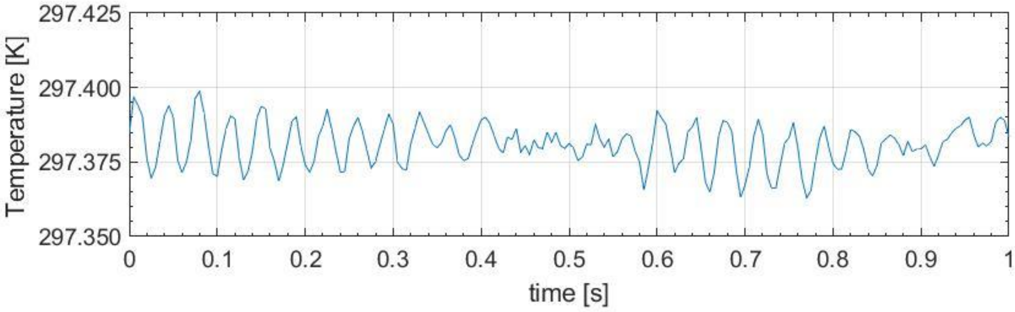

Figure 38 Sampling of a real signal using a cooled IR camera FLIR X6540sc.

4.3.3. Error Analysis in Stresses Evaluation neglecting Residual Stresses

In this paragraph, by using the proposed approach, the error made in stresses evaluation using TSA when the residual stresses are neglected, has been determined. In particular, the error was evaluated by considering two approaches for calibrating the TSA data: The one based on the classical TSA equation and the one based on the revised high order theory (mean stress effect). In both cases, the error was investigated as a function of the residual stresses.

By imposing a stress amplitude $\Delta\sigma_{xx}$ for fixed values of γ ($\sigma_{mxx}/\Delta\sigma_{xx}$), σ_{r1} and γ_r ($\sigma_{r22}/\sigma_{r11}$), the thermoelastic amplitude signal is

$$\frac{\Delta T}{T_0} = (a + b\sigma_{r1}[(cos^2(\theta) - \nu\, sin^2(\theta)) + \gamma_r(sin^2(\theta) - \nu\, cos^2(\theta))])\sigma_{axx} + b\gamma\Delta\sigma_{xx}^2 \qquad \text{Eq 109}$$

The classical thermoelastic equation provides the following relations between temperature and stress amplitude:

$$\frac{\Delta T}{T_0} = -K\Delta\sigma_{xx\mathrm{er(cl)}}, \qquad \text{Eq 110}$$

where $\Delta\sigma_{xx\mathrm{er(cl)}}$ is the stress amplitude evaluated by using such an approach. It is affected by the error related to neglected residual stresses.

By including Eq 157 in Eq 156 one can obtain

$$-K\Delta\sigma_{xx\mathrm{er(cl)}} = (a + b\sigma_{r1}[(cos^2(\theta) - \nu\, sin^2(\theta)) + \gamma_r(sin^2(\theta) - \nu\, cos^2(\theta))])\Delta\sigma_{xx} + b\gamma\Delta\sigma_{xx}^2. \qquad \text{Eq 111}$$

By writing the stress amplitude of the classic technique affected by error as the sum of the effective value and a real number $\Delta\sigma_{xxer(cl)} = \Delta\sigma_{xx} + \varepsilon_{cl}$, Eq 111 becomes

$$. \qquad -K(\Delta\sigma_{xx} + \varepsilon_{\mathrm{cl}}) = (a + b\sigma_{r1}[(cos^2(\theta) - \nu\, sin^2(\theta)) + \gamma_r(sin^2(\theta) - \nu\, cos^2(\theta))])\Delta\sigma_{xx} + b\gamma\Delta\sigma_{xx}^2 \qquad \text{Eq 112}$$

Hence, the error can be directly assessed by the following equation, when the ε turns into $\varepsilon_{\mathrm{cl}}$ for readability:

$$\varepsilon_{\mathrm{cl}} = -\frac{\Delta\sigma}{K}[(a + b\sigma_{r1}[(cos^2(\theta) - \nu\, sin^2(\theta)) + \gamma_r(sin^2(\theta) - \nu\, cos^2(\theta))] + K + b\gamma\Delta\sigma_{xx}^2)] \qquad \text{Eq 113}$$

This error can be also evaluated by taking into account the calibration procedure proposed by Galietti and Palumbo[17][17][25]. In this case, the thermoelastic signal was expressed as the polynomial sum of amplitude stress terms:

$$\frac{\Delta T}{T_0} = a\Delta\sigma_{xx\mathrm{er(Gal)}} + b\gamma\Delta\sigma_{xx\mathrm{er(Gal)}}^2, \qquad \text{Eq 114}$$

where the stress amplitude clearly contains the error. By expressing the latter as $\Delta\sigma_{xx\mathrm{er(Gal)}} = \Delta\sigma_{xx} + \varepsilon_{\mathrm{Gal}}$, and by substituting Eq 114 in Eq 109, it is possible to obtain

$$a(\Delta\sigma_{xx} + \varepsilon_{\mathrm{Gal}}) + b\gamma(\Delta\sigma_{xx} + \varepsilon_{\mathrm{Gal}})^2 = (a + b\sigma_{r1}[(cos^2(\theta) - \nu\, sin^2(\theta)) + \gamma_r(sin^2(\theta) - \nu\, cos^2(\theta))])\Delta\sigma_{xx} + b\gamma\Delta\sigma_{xx}^2. \qquad \text{Eq 115}$$

Finally, the error made by using the procedure $\varepsilon_{\mathrm{Gal}}$ is

$$\varepsilon_{\mathrm{Gal}} = \frac{-(2b\gamma\Delta\sigma_{xx} + a) \pm \sqrt{(2b\gamma\Delta\sigma_{xx} + a)^2 + 4b^2\gamma\sigma_{r1}[(cos^2(\theta) - \nu\, sin^2(\theta)) + \gamma_r(sin^2(\theta) - \nu\, cos^2(\theta))]}}{2b\gamma} \qquad \text{Eq 116}$$

When $\sigma_{r1} = 0$, the error is

$$\varepsilon_{\mathrm{Gal}} = \frac{-(2b\gamma\Delta\sigma_{xx}+a)\pm(2b\gamma\Delta\sigma_{xx}+a)}{2b\gamma}. \qquad \text{Eq 117}$$

Since ε_{Gal} has been defined as the error made by neglecting residual stresses, it has to be null in the case $\sigma_{r1} = 0$. Therefore, the only solution which has to be considered for evaluating the error using the technique in Reference [25], is the one with the negative sign of the radical term in Eq 116, being $-(2by\Delta\sigma_{xx} + a)$, a positive term. By considering the materials characteristics in Table 1, the parameter a has a negative value of order 10^{-10} for the AA60082 and 10^{-11} for the Ti6Al4V, while the product $2by\Delta\sigma_{xx}$ can be both positive or negative (depending on the loading system) and it has the order of 10^{-23} for the AA60082 and 10^{-24} for the Ti6Al4V. Therefore the term $-(2by\Delta\sigma_{xx} + a)$ always has a positive value.

Furthermore, in the manuscript the errors evaluated by using Equations (22) and (25) will be graphically shown and discussed.

4.3.4. TSA Capability in Evaluating Residual Stresses: Statistical Analysis

In this regard, two representative cases have been investigated as will be shown in the following section. In particular, the variation of the principal residual stress has been studied, by keeping the residual stress ratio y_r constant.

The simulation involved the following steps:

1. Signal amplitude calculation (Eq 103);
2. Signal temporal reconstruction, assuming a sampling frequency of 200 Hz;
3. Adding the gaussian noise according to the experimental value found with a cooled IR camera FLIR X6540sc, as described in the previous section; and
4. Performing a Fast Fourier Transform to obtain the amplitude of the signal.

The classical and the Palumbo et al. [25] approaches were then used to calculate the stress. A total of 1000 repetitions were performed for each approach in order to evaluate the mean and standard deviation values.

A statistical inference analysis allowed to carry out a hypothesis test and to calculate the probability of a second type error β that is to accept the null hypothesis when it is false [142]. In this study the null hypothesis is represented by the absence of residual stress, and the β-error is made when residual stresses are not null [142].

The second type error probability was calculated for each approach assuming a confidence interval of 95% and using 1 as samples dimension.

4.3.5. Results and Discussion

4.3.5.1. Effects of Biaxial Residual Stresses on TSA Signal

In this section the effect of the residual stresses on the thermoelastic signal (ΔT) has been investigated. To study this effect, Eq 103 has been considered, in which the thermoelastic signal is expressed as a function of the principal residual stresses and their direction with respect to the applied loads. In particular, to represent and compact all the data, the ratio between the residual stresses has been considered. In this way, the analyses have been performed at specific ratios between the principal residual stresses ($\gamma_r = \sigma_{r22}/\sigma_{r11}$): 1, 0, −1 and −2.

The material characteristics of the alloys used for the analysis were resumed in Table 4, while the load conditions are shown in Table 6. The amplitude and the mean load were selected considering the mechanical characteristics of the material and the yield strength in order to ensure the linear elastic conditions.

Table 6 Ranges of residual stress system modelled for AA6082 and Ti6Al4V alloys.

Material	**$\Delta\sigma_{xx}$ [MPa]**	**R**	**σ_{mxx} [MPa]**	**σ_{r11} [MPa]**	**γ_r [1]**	**θ [°]**
AA6082	60	0.1	73	From −100 to 100	From −2 to 1	From 0 to 360
Ti6Al4V	180	0.1	220	From −100 to 100	From −2 to 1	from 0 to 360

[1] The step increment of γ_r was 1 unit per test.

In Figure 39 and Figure 40, the thermoelastic signal is represented as a function of the two independent variables σ_{r11} and θ.

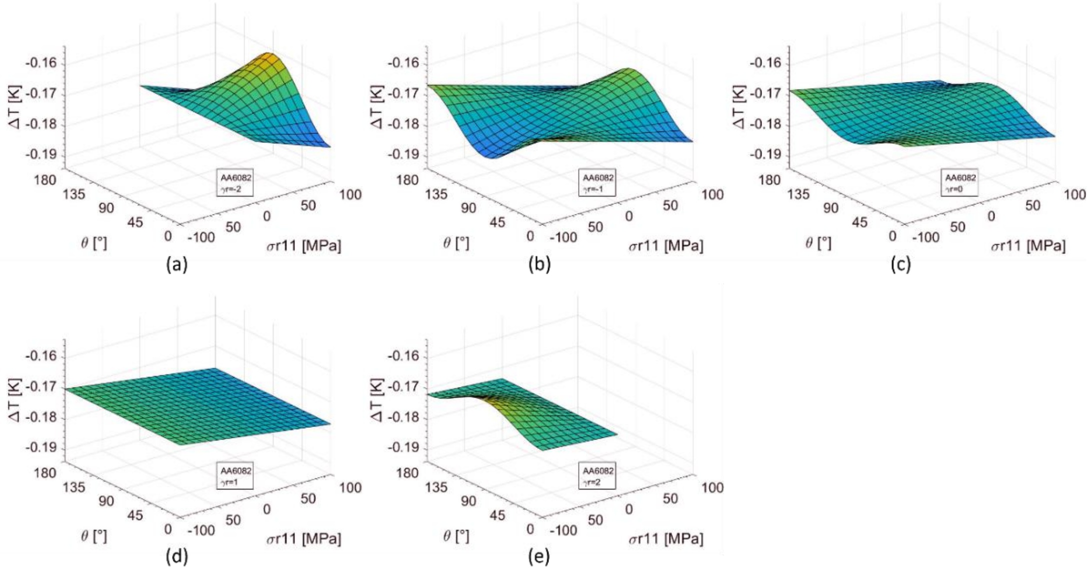

Figure 39 Thermoelastic signal as a function of the two independent variables σr11 and θ for the AA6082 alloy: (a) $\gamma_r = -2$ (b) $\gamma_r = -1$ (c) $\gamma_r = 0$ (d) $\gamma_r = -1$ (e) $\gamma_r = -2$.

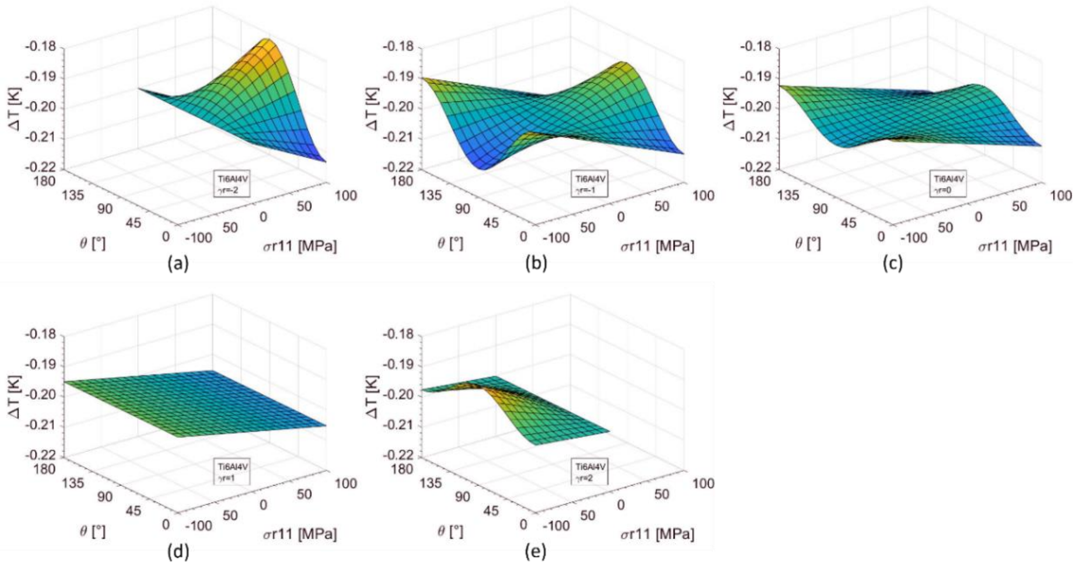

Figure 40 Thermoelastic signal as a function of the two independent variables σ_{r11} and θ for the Ti6Al4V alloy: (a) $\gamma_r = -2$ (b) $\gamma_r = -1$ (c) $\gamma_r = 0$ (d) $\gamma_r = -1$ (e) $\gamma_r = -2$.

The signal varies periodically with θ, with a period of 180°. The dependence of the signal on θ decreases, with ranging γ_r from −2 to 1. In particular, for $\gamma_r = 1$, there is no more an effect of θ on the thermoelastic signal.

Figure 41 shows the effect of the load amplitude on thermoelastic variations for three specific values of $\Delta\sigma_{xx}$. Clearly, the higher the stress the stronger is the effect of residual stresses affecting the signal. In fact, a higher value of the stresses ensures also a higher signal and therefore better detection capacity with equal noise.

As it is possible to observe in Figure 41, by fixing the value of θ and γr, the two alloys present the same trends in terms of temperature variations. Their different physical and mechanical properties determine a difference in the signal magnitude: At the same amplitude and mean stress, the AA6082 alloy responds with a signal which is higher than the Ti6Al4V alloy response. However, the possibility to apply higher stresses to the titanium alloy allows obtaining a signal of the same order and with a higher variability induced by the residual stresses.

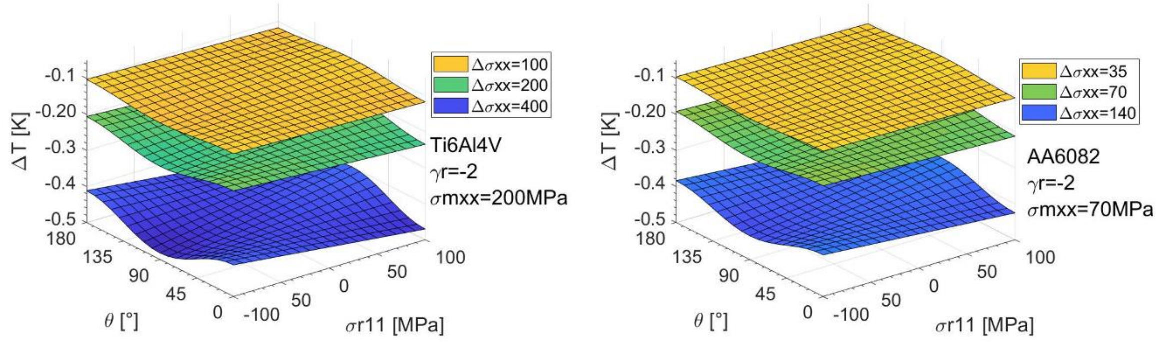

(a) (b)

Figure 41 Effect of the load amplitude on temperature variations for AA6082 (a) and Ti6Al4V (b) alloys.

Based on the trends resulted from the analysis presented in Figure 39 and Figure 40, two representative cases were selected for the following investigations. In both cases, $\Delta\sigma_{xx}$, γ and σ_{r11} are fixed. The first case represents a condition with the higher signal variation due to residual stresses with respect to the reference conditions (absence of residual stress, $\sigma_{r11} = 0$), with $\gamma_r = -2$ and $\theta = 90°$, while the second case represents a condition with a lower signal variation obtained by imposing $\gamma_r = 1$ and $\theta = 0°$. These cases will be deeply investigated in the next sections.

4.3.5.2. *Error Analysis: Results*

The error ε defined in paragraph 4.3.3 has been calculated for the two alloys in order to compare the error made in the evaluation of the stress amplitude (uniaxial and uniform applied stress) by using two different calibration approaches.

The imposed load conditions (Table 7) were the two case studies representative of high (γr = −2, θ = 90°) and low (γr = 1, θ = 0°) residual stresses effect, as just discussed in the previous section. Furthermore, the effects of the mean load and of the load amplitude were also investigated.

Table 7 Ranges of stress values used for modelling AA6082 and Ti6Al4V alloys.

Material	$\Delta\sigma_{xx}$ [MPa]	σ_{mxx} [MPa]	σ_{r11} [MPa]	Residual Stresses System
AA6082	35, 70	0, 70, 140	From 0 to 100	$\gamma_r = 1$ and $\theta = 0$ (low residual stresses effect) $\gamma_r = -2$ and $\theta = 90^\circ$ (high residual stresses effect)
Ti6Al4V	100, 200	0, 200, 400	From 0 to 100	$\gamma_r = 1$ and $\theta = 0$ (low residual stresses effect) $\gamma_r = -2$ and $\theta = 90^\circ$ (high residual stresses effect)

The simulations were performed by using the mechanical and physical characteristics in Table 4 and the stress values in Table 7.

As expected, the approach which leads to the minimum error is the calibration procedure proposed by Galietti et al. [17] which considers the mean stress effect (Figure 42 and Figure 43 c,d). Indeed, by increasing the mean stress, the error due to neglecting the residual stresses decrease, while the classical approach (Figure 42 and Figure 43a,b) presents an increasing error with the mean load. This effect is related to the analytical definition of the two terms that were modelled as additives.

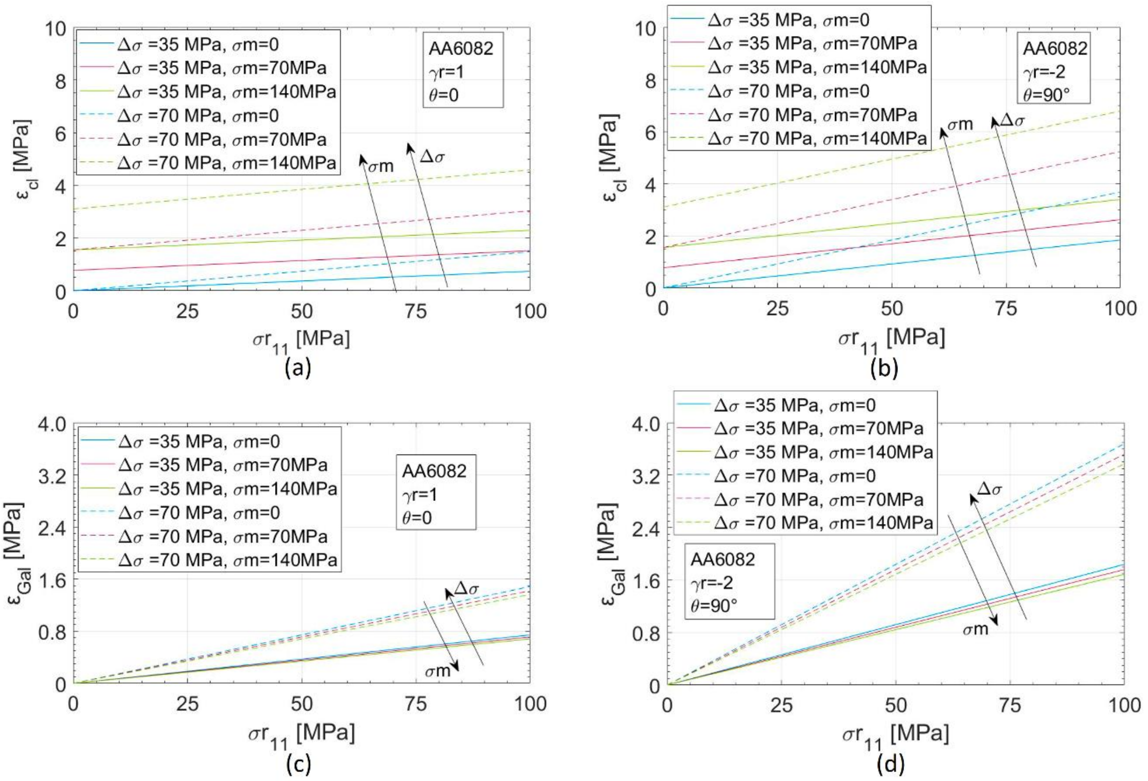

Figure 42 Parameter ε as function of σ_{r11} for the AA6082 alloy: (ε_{cl}) for the classical technique and (ε_{Gal}) for the method proposed in Reference [17] are compared for the case of (a) and (c) for low and (b) and (d) for high residual stresses effect.

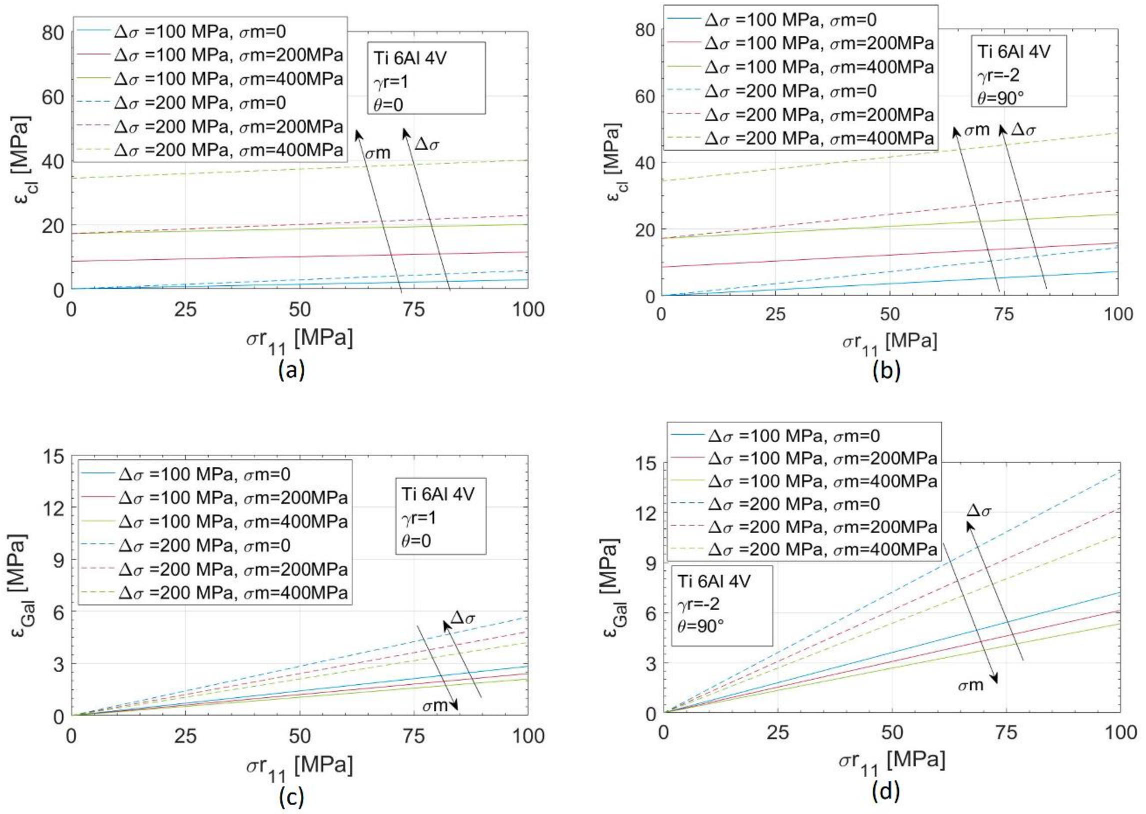

Figure 43 Parameter ε as function of σ_{r11} for the Ti6Al4V alloy: (ε_{cl}) for the classical technique and (ε_{Gal}) for the method proposed in Reference [17] are compared for the case of (a) and (c) for low and (b) and (d) for high residual stresses effect.

The two alloys present a similar behaviour, so for both materials the following considerations can be made:

1. The classical procedure presents the higher error.
2. In the case of higher residual stress influence ($\gamma_r = -2$, $\theta = 90°$), both the procedures give significant errors in stress amplitude evaluation, above 10%.
3. The error increases as the stress amplitude increases for both the approaches. It is more significant for the Galietti et al. [17] approach in which the effect of the mean stress is considered; and
4. the error always increases as the mean stress increases for the classic procedure while it decreases for the Galietti et al. [17] approach.

By resuming, the effect of neglecting residual stresses can involve significant errors in stresses evaluation by means of the TSA technique. However, when the modulus and directions of the residual stresses are known, the error in stress evaluation can be estimated by adopting the proposed approach.

4.3.5.3. Capability in Evaluating Residual Stresses: Results

In this section, the capability in residual stresses estimation will be investigated. In this regard, the second type error was evaluated as described in paragraph 4.3.3 for the two considered approaches.

In order to separate the effect of the mean stress from the residual stress influence, the second type error for the classical approach was calculated only for $\sigma_{mxx} = 0$ and for the same stress amplitude used in the error analysis. As expected, the results were equivalent to those obtained from the approach proposed by Galietti et al. [17] in the same stress conditions.

The stress conditions modelled to study the second type error made by using the method proposed by Galietti et al. [17] are reported in Table 7.

Figure 44 and Figure 45 show how the mean stress does not affect the minimum value of σ_{r11} for which β is null, while it varies significantly depending on the residual stress conditions and on the stress amplitude. Considering the case of a single TSA test and then of a single thermoelastic measurement, for the AA6082 alloy, this value is equal to 27 MPa if $\Delta\sigma_{xx}$ is 35 MPa and the residual stress condition is biaxial, with $\gamma_r = -2$ and $\theta = 0$ (Figure 44 b). If the residual stress system is uniaxial with $\theta = 0$, at least a σ_{r11} of 75 MPa is needed to have a discernible thermoelastic signal variation with the same $\Delta\sigma_{xx}$ (Figure 44 a).

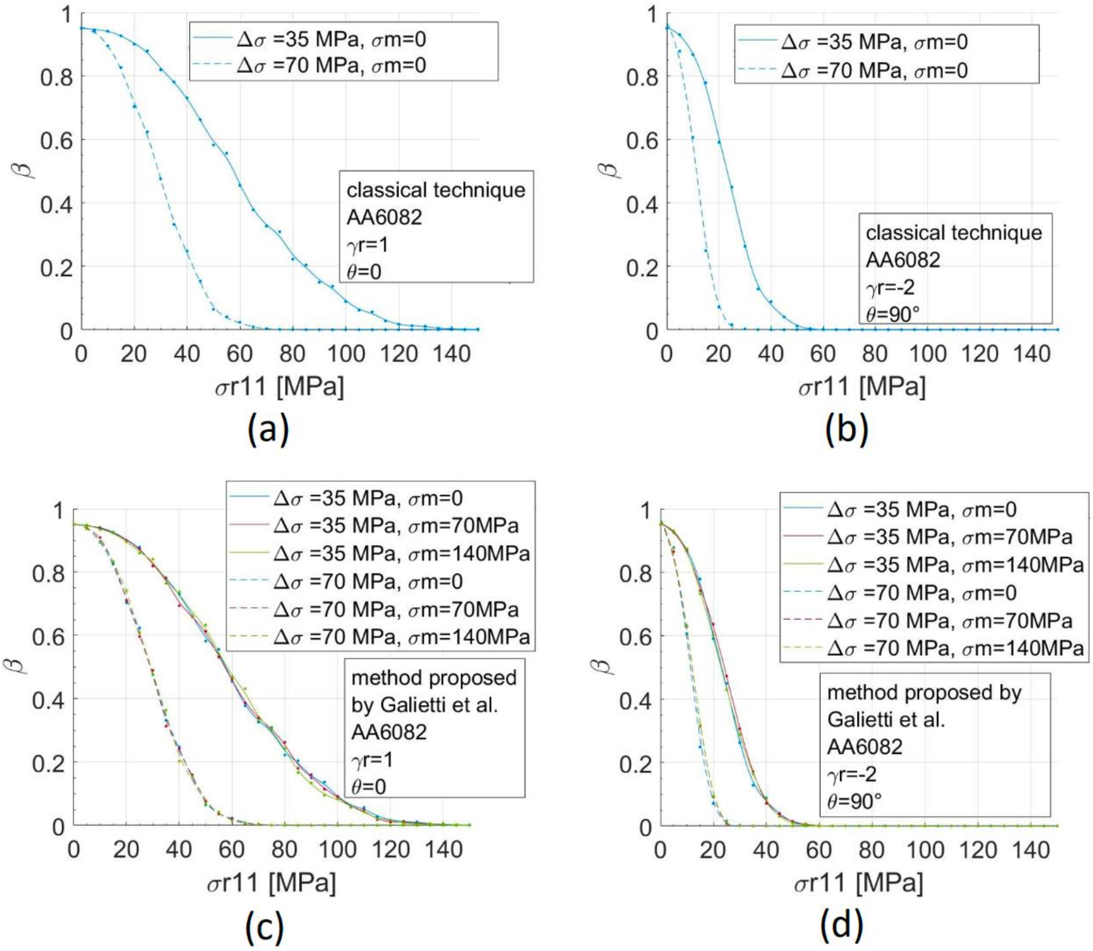

Figure 44 Second type error as function of σ_{r11} for the AA6082 alloy: The classical technique and the method proposed in Reference [17] are compered for the case of (a) and (c) for low and (b) and (d) for high residual stresses effect.

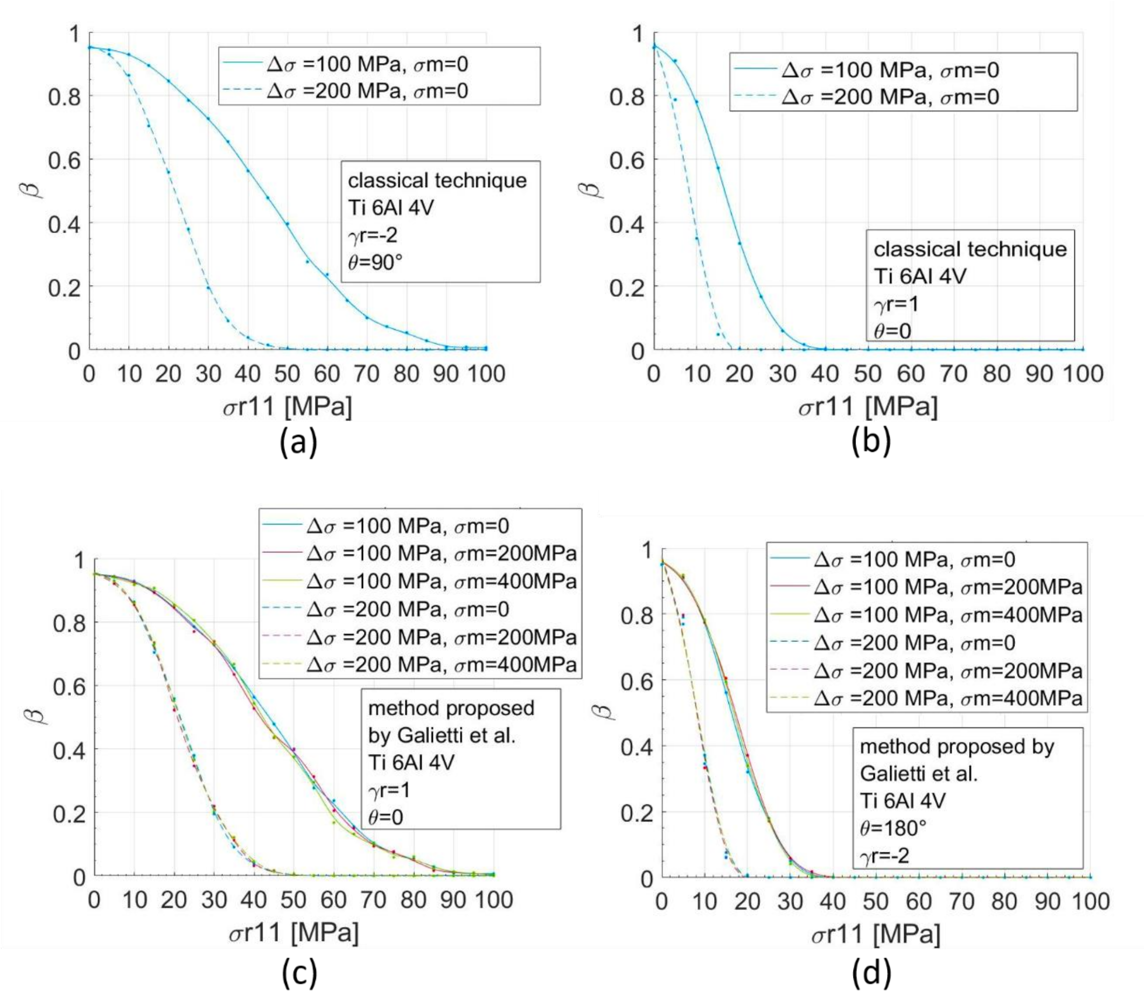

Figure 45 Second type error as function of σr_{11} for the Ti6Al4V alloy: The classical technique and the method proposed in Reference [17] are compered for the case of (a) and (c) for low and (b) and (d) for high residual stresses effect.

If $\Delta\sigma_{xx}$ is 70 MPa, the two discernible values of the amplitude stress become 65 and 150 MPa, respectively (Figure 44 a,b).

In the case of the alloy Ti6Al4V, the minimum σ_{r11} values are lower, in both the considered residual stress conditions (Figure 45). For the two considered cases, values of 20 MPa and 55 MPa were obtained, respectively, for $\Delta\sigma_{xx}$ = 100 MPa and values of 45 MPa and 100 MPa for $\Delta\sigma_{xx}$ = 200 MPa. It is important to underline that the better capability for titanium in evaluating the residual stresses is due to the possibility to apply higher loads.

4.3.6. Conclusions

In this work, a new equation for describing the thermoelastic behaviour of materials was proposed. In particular, the proposed equation allows to study the behaviour of homogeneous and non-isotropic materials undergoing any loading conditions and residual stresses. By using this equation, the error made by the two calibration approaches of thermoelastic stress analysis (TSA) data in presence of residual stresses has been investigated. Moreover, the minimum value of residual stresses leading to significant and measurable variations in the thermoelastic signal has been evaluated.

The main results obtained for uniaxial and uniform applied stresses, can be summarized as follows:

- the error in stress amplitude evaluation with TSA if the residual stresses are neglected depends on the modulus, direction and angle of the principal residual stresses with respect to the applied stresses. Significant errors (above 10%) can be made in stresses evaluation;
- this error depends also on the applied stresses (amplitude and mean) and on the considered material (thermo-physical and mechanical property); and
- in the same way, the capability of TSA in residual stresses evaluation depend on the considered material and on the modulus, direction and angle of the principal residual stresses with respect to the applied stresses.

4.4. Application of TSA general model for the study of the thermoelastic behaviour of a rolled AA2024

4.4.1. Introduction

In this work TSA experimental measurements were performed, and results were compared with the synthetical data obtained by applying the TSA general model. In particular, the analytical results (obtained considering reference material proprieties) were compared with the experimental TSA measurements performed on two AA2024 samples affected by biaxial residual stresses measured by a standard test method.

4.4.2. Materials and Methods

The experiments involved the implementation of dynamical tests on two samples with a known stress distribution. Thus, dog-bone AA2024 specimens with a monoaxial and uniform stress distribution in the useful section were employed (the geometry in Figure 46). The two tested samples were obtained from the same rolled sheet, but they were cut respectively at 0 ° and 90 ° respect to the rolling direction. The samples were painted with a black mat spray in order to enhance and uniform the surface emissivity.

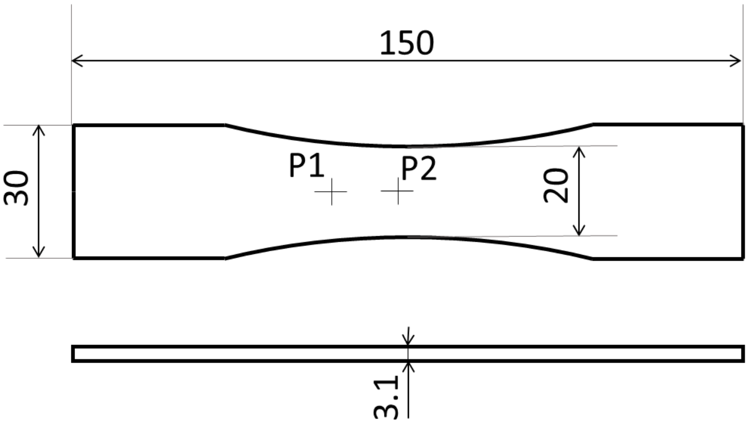

Figure 46 Sample geometry. P1 and P2 indicate the point where the residual stress was measured by using the hole drilling method.

TSA dynamical uniaxial tensile test with different level of amplitude (*ΔP*) and mean load P_m were carried out by using a loading frame MTS model 370 with a 25 kN of capacity. All the tests were performed with a frequency of the load of 15 Hz. In Table 2 the tests plan is reported.

Figure 47 Experimental set up

The thermal data were acquired by using the FLIR X6581 cooled IR camera. Figure 47 shows the experimental set-up.

Table 8 Tests plan

Loading conditions	F_a [N]	F_m [N]
1	1000	4200
2	2100	
3	3200	
4	4200	
5	1000	8500
6	2100	
7	3200	
8	4200	
9	1000	12700
10	2100	
11	3200	
12	4200	

Following the TSA tests, residual stress measurements were carried out on the samples with the semi-destructive hole drilling method. The residual stress measurement was performed in two different points in the useful of the samples (Figure 46), according to the standard [148].

The data processing consisted of:

1) Acquisition of the temperature signal by using an IR camera during the application of sinusoidal loading on dog bone samples with different levels of the mean load.

2) Lock-in analysis and assessment of the first harmonic amplitude ΔT_1 and reference temperature T_0.

3) Selection of a ROI (Region of Interest) in the gauge section of the sample and assessment of $\overline{\Delta T_1}$ and $\overline{T_0}$, the average values of ΔT_1 and T_0.

4) Normalization of $\overline{\Delta T_1}$ respect to the reference temperature and the stress amplitude:

$$S_{norm} = \frac{\overline{\Delta T_1}}{\overline{T_0}\Delta\sigma_{xx}} \quad \text{Eq 118}$$

with $\Delta\sigma_{xx}=\Delta P/A$, ratio between the amplitude of the load and sample cross section.

5) Evaluation of the intercept and slope of the curve S_{norm} vs σ_m, obtained by the linear fitting of the experimental data.

6) Measurement of the residual stress with the hole drilling method [148].

7) Calculation of the analytical curve S_{norm} vs σ_m (Eq 105), by using literature values for mechanical and physical characteristics.

4.4.3. Results and discussion

Figure 48 shows the experimental data fitting obtained as described in paragraph 4.4.2. In particular, the S_{norm} vs. σ_m curves are reported for the two samples (cut respectively at 0 ° and 90 ° respect to the rolling direction). Both samples present a not negligible dependence on the mean load and the linear fitting well describes the relationship, with R^2 values of 0.97 and 0.95 respectively. For the two specimens the fitted curves have very close slope values.

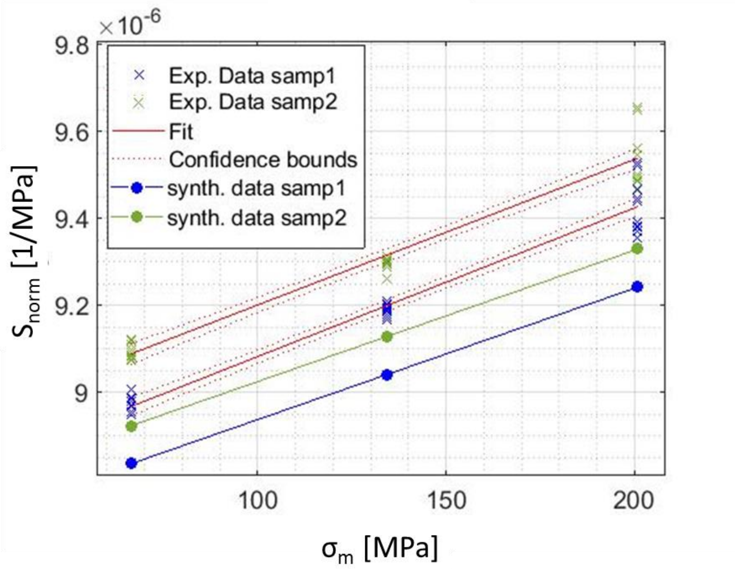

Figure 48 Snorm Vs σm curves. Both the experimental data linear regression with 95% confidence bounds and the synthetic curves are plotted.

In Table 9 and Table 10 the linear regression statistics are reported.

Table 9 linear regression statistic, sample 1

	Coefficients	*Standard error*	*lower 95%*	*upper 95%*
Intercept P1	8,74E-06	1,73E-08	8,71E-06	8,78E-06
Slope P1	3,42E-09	1,19E-10	3,18E-09	3,66E-09

Table 10 linear regression statistic, sample 2

	Coefficients	*Standard error*	*lower 95%*	*upper 95%*
Intercept P2	8,87E-06	1,93E-08	8,83E-06	8,91E-06
Slope P2	3,35E-09	1,33E-10	3,08E-09	3,62E-09

The slope depends only on the mechanical characteristics and on the product ρc_p (Eq 105), that are the same for both the samples.

If we assume the material characteristics reported in Table 4, it is possible to analytically evaluate the slope as:

$$b = -\frac{1}{E^2 \cdot \rho \cdot C_\varepsilon} \cdot \frac{\partial E}{\partial T} = 3.02 \cdot 10^{-9} \left[\frac{1}{MPa^2}\right] \qquad \text{Eq 119}$$

For both the samples the value follows outside the confidence interval. The percentage difference is of 11.7% and 9.7% respectively, and we can consider this discrepancy linked to the choice of the characteristics of the material used for the calculation.

On the contrary, the intercepts are significantly different. The intercept is a combination of the mechanical and physical characteristics of the material and the residual stress characteristics.

In Table 11 the residual stress measured with the hole drilling method are reported. It is important to notice that the sample residual stress condition follows in the case of bi-axial compression-compression.

For the comparison only the point P2 has been considered, since it is located in the ROI extracted for the TSA analysis. In Figure 4 the synthetic curves, obtained as described in paragraph 4.4.2 are also reported.

The values of intercept are reported in

Table 12. The percentage difference respect to the experimental values are 1.1% and 1.7% and also in this case we can deduce an error in the material characteristics employed in the calculation.

In accordance with the sensitivity indices evaluated, it is possible to deduce that the main effect is due to the error in the values of α and ρcε. Even if the intercept shows a better match, it could be due to the opposite effect of the two parameters.

Table 11 Residual stress measured with the hole drilling method.

	ε_a [μm/m]	ε_b [μm/m]	ε_c [μm/m]	σ_{r22} [N/mm^2]	σ_{r11} [N/mm^2]	θ [°]
S1 point2	9.787	9.279	9.047	-83.87	-79.21	79.77
S2 point2	2.973	4.793	6.38	-49.75	-29.93	-1.96

Table 12 Intercept and slope obtained for the synthetic curves S_{norm} Vs σ_m evaluated with the reference values for the material proprieties and with residual stress characteristics measured with the hole drilling method.

sample	***Intercept (analytical) [1/MPa]***	***Slope (analytical) [1/MPa^2]***
1	$8.64 \cdot 10^{-6}$	$3.02 \cdot 10^{-9}$
2	$8.72 \cdot 10^{-6}$	$3.02 \cdot 10^{-9}$

4.4.4. Conclusions

In this work an experimental validation of the TSA general model has been performed by comparing the experimental measurement with the synthetic data obtained considering reference material proprieties and residual stress characteristics measured with the standard hole drilling method.

The comparison lead to the following results:

- In accordance with the sensitivity analysis, there is a systematic error of the intercept and slope of the Snorm vs σm synthetic curves with respect to the experimental data due to the effect of materials physical proprieties on the thermoelastic stress analysis.
- The coincidence between the systematic errors for the two specimens, validates the model.
- The present study is a preliminary analysis which at the basis of a broader work which aims to explore the capability of TSA in residual stress assessment.

Future work will include:

- A wider experimental campaign for the validation of the model with samples with known stresses and residual stresses distributions (covering several cases and orientations) and known material proprieties.
- The development of procedures and algorithms for the measurement of residual stresses by means of TSA.

CHAPTER 5.

A ROBUST DESIGN-LIKE APPROACH TO IMPROVE TSA MEASUREMENT PERFORMANCE

Aim of the study is to provide operative directions for the TSA measurement, indicating best practices and expected measurement error ranges. This kind of problems can be addressed through the implementation of a probabilistic and statistic methods [142].

In the following paragraphs the Robust Design simulation approach developed will be illustrated and the study and results of two possible application will be discussed.

The first application performs a Robust Design like approach [140] [141] of the TSA measurement system by applying statistic on an analytical model simulating also the various types of errors that can be made on the process. A first study focused on the thermal signal; an ANOVA and an ANOM were performed to study the effect of the parameters describing the analytical relation between thermoelastic response and stresses in the presence of noise factors.

A second study was performed implementing a Robust Design approach to the stress measurement system. The main results are presented in terms of the effect of the various process parameters on the statistics of the measurement error and its range.

The second application focused on TSA optimization in measuring residual stress. The problem has been here studied by proposing a new procedure based on the realization of three measurements characterized by three different configurations for the set up. The procedure allows to write three equations in the three unknown values defining the residual stress system.

The objective was to identify the triad of values of the three loading characteristics which ensure the best performance in terms of quality and variance of the measurement.

5.1. Development of simulation-based Robust Design applied to measurement procedures

This paragraph presents the robust design simulation approach applied to measurement procedures.

Despite several authors already demonstrated its validity and potential, the application here proposed required the development of a dedicated approach to address the techniques and procedures optimization.

The objective was to identify the best set up conditions that can guarantee greater stability of the quality of the output when both the measured value and the different noise sources vary randomly.

Figure 49 shows the workflow implemented for the TSA measurement procedures robust design.

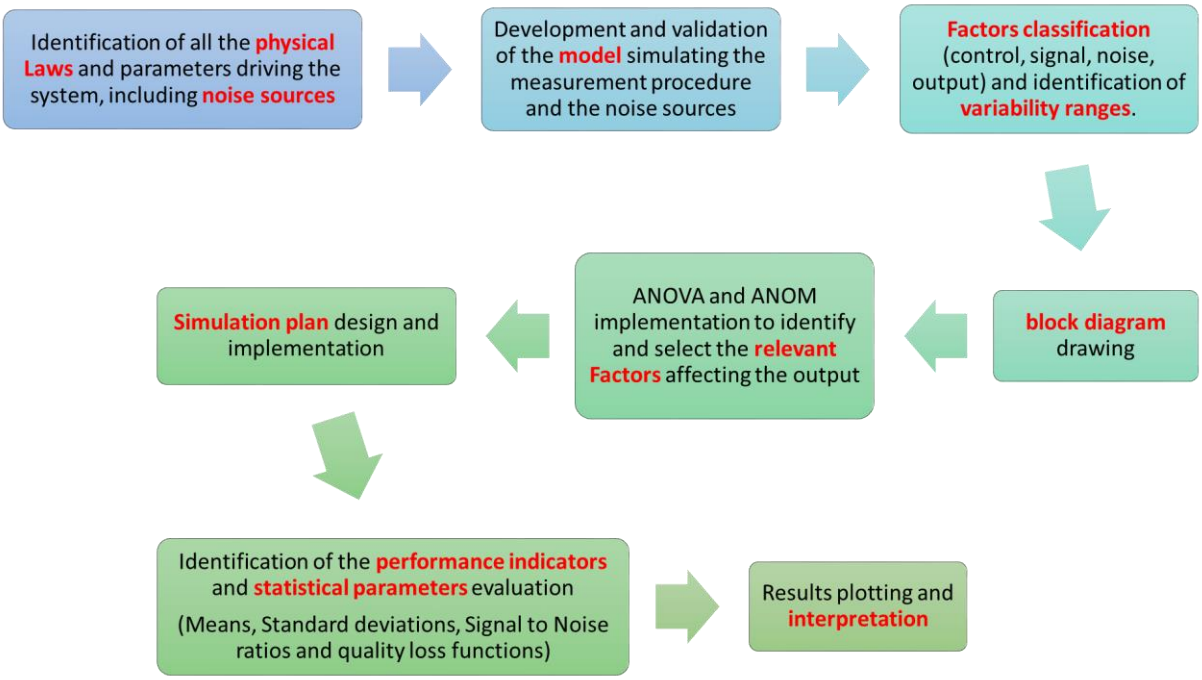

Figure 49 simulation robust design workflow

The first problem to address is the identification of all the actors and the related physical Laws that affect the system. The main issue of the analytical description is to obtain a faithful modelling that does not neglect any significant phenomena. Analytical solutions that describe cause and effect are not always available. For example, the noise of the IR camera, characterized by a random nature, cannot be described through a precise mathematical relationship. In these cases, the experimental experience can be of help, which allows us to associate a statistical model to the variable that can then be modelled while maintaining its random nature.

The experimental feedback is also important to check if any significative effect has been neglected.

The applications object of this study required the simulation of several steps: the first is the thermal signal from the component, the second is the thermal signal acquired and digitalized by the IR camera, the third is the procedure application and conversion or thermal signal/s into the quantity to measure.

In turn, the classification of parameters can also be tricky. The same variable involved in the problem can be signal factors, control factors, Noise factors or even output factors according to the aim of the analysis. For example, residual stresses can be noise factor when Δσ is assessed but the residual stress filed is unknown or neglected, while can be an output if they are the investigated variable.

In this study the factors ranges have been identified considering the material characteristics and the limits or simplicity of solution that characterize the procedure operating conditions.

The simulation plan is designed by building the internal and external matrix, as described in paragraph 3.1.3; the selection of the factors to vary can be supported by the ANOVA and the ANOM.

Once identified relevant factors (including sources of noise) and their levels the simulation plan can be implemented.

The output of each simulation run is the measured quantity, which being a variable, by itself is not representative of the system performance but needs to be compared with the nominal value.

The statistical analysis is then performed and interpretated as described in paragraph 3.1.4.

Test simulation analysis can be a powerful tool to design the best setup when a model is available. The possibility to use statistical tools allow an easy use also of very complex models providing information on both possible errors induced by neglected variables or underestimated variables (materials characteristics).

5.2. A Robust Design approach to improve TSA stress measurement performances on Ti6Al4V alloy

5.2.1. Introduction

The analytical solution expressed in Eq 103 allows to simulate the thermoelastic response once the material characteristics, the loading conditions and residual stresses are known.

The TSA capability in evaluating stresses and residual stresses is affected by several sources of errors whose effect is not easy to isolate and compensate due to the complex relationship between interdependent parameters.

In this framework a statistical approach applied through the test simulation analysis can lead to identify the more influent parameters or group of parameters and their effect, aiming to an optimized and robust measurement technique.

Considering a generic process, it can be defined by identifying its inputs and outputs. Inputs are distinguished in signal parameters, control parameters and noise parameters and are classified depending on the problem definition. For the same system it is possible to study a different kind of problems; for example, the TSA can be applied to measure stress but also to measure residual stresses. In the first case residual stress, if neglected or unknown, must be classified as noise factors, while in the second case their nominal value is a signal factor, and their measurement is the output.

Due to the great number of both controllable and uncontrollable random variables affecting the results, an analytical approach, even if carried with detail, cannot include all these effects and cannot provide results in an exhaustive and easy to interpret way as a statistical approach can do.

The analytical description gives information about interactions between parameters, but it cannot show their effect on the measured signal when random sources of noise are present.

5.2.2. Methodology

In this work the analytical model Eq 103 was used to perform full factorial plans of simulation in order to study the performance of the TSA.

First, preliminary ANOVA and ANOM were carried out to identify the main parameters and interactions affecting the measurement. The result was also compared with the analytical description to distinguish the effects hidden by noise factors from those which involve significant variations.

Then, the Robust design method was applied to optimize the measurement performance in stress measurement comparing three different calibration methods.

In Table 13, the analysis performed are listed and the parameter classifications are reported. The sources of noise considered in the study were: the IR camera Noise (TC Noise), the residual stress tensor (defined through the principal stress components and their orientation) and the material characteristics.

Table 13 Analysis performed and parameters classification.

Analysis	Input	Noise	Output
ANOVA and ANOM	• Material characteristics • Residual stress vector	• TC Noise	• p-values • Means
parameters design of the stress measurement methodology	• $\Delta\bar{\sigma}$	• TC Noise • $\bar{\bar{R}}\bar{\sigma}_r$ • Material characteristics variation	• $\Delta\sigma_{meas}$ • *SN* • *Q*

The parameters design aims to minimize the performance sensitivity to the various causes of variation and to ensure the minimal loss in quality of the response. The indicators are respectively the *Signal-to-Noise ratio* (*SN*) and the *Quality Loss Function* (*Q*) [141]. In the standard application of Robust Design, the quality loss function represents the loss in terms of costs which occurs once the product is operative; in this work it has been evaluated normalized respect to the costs K and it represents the deviation of the response from the correct value.

5.2.3. Material

The study was conducted considering the physical and mechanical characteristics of the alloy Ti6Al4V, whose thermoelastic behaviour is affected by the second order effect [45].

The material characteristics and their variability range were set based on literature values [45][50][144][145][146].

The amplitude and the mean load were selected considering the mechanical characteristics of the material and the yield strength to ensure the linear elastic conditions.

The residual stress vectors were selected considering both literature typical values and preliminary results from the analytical study of the thermoelastic behaviour of the Ti6Al4V alloy.

The study was carried out implementing a simulation plan which reflects the real operative conditions occurring in TSA measurements. The result is an unbalance representation of the loads and residual stress.

5.2.4. Effect of the main sources of error on the TSA measurement

The main parameters affecting the thermoelastic response were studied by performing an ANOVA and an ANOM on data generated with the analytical model.

To simulate the IR camera noise, a white gaussian noise of 0.01 K (experimentally determined on a typical Camera with an integration time of 2500μs [18]) was added to the response evaluated with Eq 103. and 5 repetitions were performed.

Eq 103 describes a complex relation between load and residual stress. This relation depends on the reciprocal configuration of the two tensors, in such a way that the same state of residual stress can determine an increase or a reduction of the signal according to the orientation and sign of the applied load.

In order to enhance the effect between load and residual stresses, the study was conducted considering two different cases for the applied load (mainly tensile and mainly compression). The residual stress characteristics are σ_{r11}, σ_{r22} and θ (Figure 28). The plan was built representing σ_{r22} through the difference between the principal component σ_{r11}-σ_{r22} to ensure a simulation plan including all the residual stress possible configuration, keeping $\sigma_{r11} > \sigma_{r22}$.

Thus, a significative simulation plan (Table 14 and
Table 15), containing all the configuration of statistical interest of residual stress, was designed considering:

- $\Delta\sigma_{11}$: 3 values for the first principal component of the semi-amplitude of the load. All the values selected represent a state of mainly tensile in the first case and mainly compression in the second case.
- γ_l: 3 values for the ratio between the principal components of the amplitude of the load. The selected values allow to simulate conditions of traction-

traction and traction-compression in the first case and of compression-compression in the second case.

- φ: 3 values for the angle between the principal loading system and the reference system.

- $k = \frac{\sigma_{m11}}{\Delta\sigma_{11}} = \frac{\sigma_{m22}}{\Delta\sigma_{22}}$: 3 values for the ratio between the mean load and the load and amplitude components, here considered constant in every direction of the amplitude tensor.

- σ_{r11}: 7 different values for the first principal component of the residual stress tensor; 3 for tensile, 3 for compression and one null.

- σ_{r11}-σ_{r22}: 3 for values for the difference between the principal component of the residual stress system.

- θ: 3 values for the angle between the principal residual stress system and the reference system.

- 2 different values for each material characteristic (Table 16).

Despite such a simulation plan includes both tensile and compression conditions for residual stresses, it is slightly unbalanced towards compression conditions. Furthermore, the two plans are not specular in loading, in particular the compression loading varies in a wider range and involves more critical conditions for the material. All these aspects make the simulation closer to real test conditions and affect the results which must be accordingly interpreted.

Table 14 Values for the load and residual stress characteristics of the traction case simulation plan

	val1	**val2**	**val3**	**val4**	**val5**	**val6**	**val7**
$\Delta\sigma_{11}$ [MPa]	100	150	200	-	-	-	-
γ_l	-0.5	0	1	-	-	-	-
φ	0	45	90	-	-	-	-
k	0	1	1.5	-	-	-	-
σ_{r11} [MPa]	-150	-100	-50	0	50	100	150
σ_{r11}-σ_{r22} [MPa]	0	100	150	-	-	-	-
θ	0	45	90	-	-	-	-

Table 15 Values for the load and residual stress characteristics of the compression case simulation plan.

	val1	**val2**	**val3**	**val4**	**val5**	**val6**	**val7**
$\Delta\sigma_{11}$ [MPa]	-100	-200	-300	-	-	-	-
γ_l	1	1.5	2	-	-	-	-
φ	0	45	90	-	-	-	-
k	0	1	1.5	-	-	-	-
σ_{r11} [MPa]	-150	-100	-50	0	50	100	150
σ_{r11}-σ_{r22} [MPa]	0	100	150	-	-	-	-
θ	0	45	90	-	-	-	-

Table 16 Values for material characteristics of both the traction and compression case simulation plan.

	Nominal value	**val1**	**val2**
a [1/K]	8.9E-6	8.6E-6	9.1E-6
E [GPa]	115	110	119
ρ [Kg/m^3]	4.471E3	4.429E3	4.512E3
C_ε[J/Kg K]	552	533	570
$\partial E/\partial T$ [MPa/K]	-48	-46	-50
a [1/K]	8.9E-6	8.6E-6	9.1E-6
E [GPa]	115	110	119

5.2.5. ANOVA and ANOM simulation workflow

Figure 3 shows the flow chart describing the simulation step to generate the data for the ANOVA.

For every combination a ΔT_{signal} was calculated by using Eq 103 and a synthetic data vector was generated considering a loading frequency of 17Hz and a time vector of 10 seconds with a sampling frequency of 200 Hz [18]. A white gaussian noise was also added. A lock-in analysis was then performed to obtain the $\Delta T_{measured}$. The observed response was calculated as the relative error:

$$Er = [(\Delta T_{nominal} - \Delta T_{measured})/\Delta T_{nominal}] \cdot 100 \qquad \text{Eq 120}$$

where $\Delta T_{nominal}$ is the amplitude of the thermal signal calculate with Equation 5 using the nominal values for the material characteristics (Table 16) and neglecting the presence of residual stress.

The ANOVA was performed on the data generated. The analysis considered as parameters both the controllable factors, i.e. the loading characteristics; and the error factors, i.e. the material characteristic variation and the residual stress system characteristics.

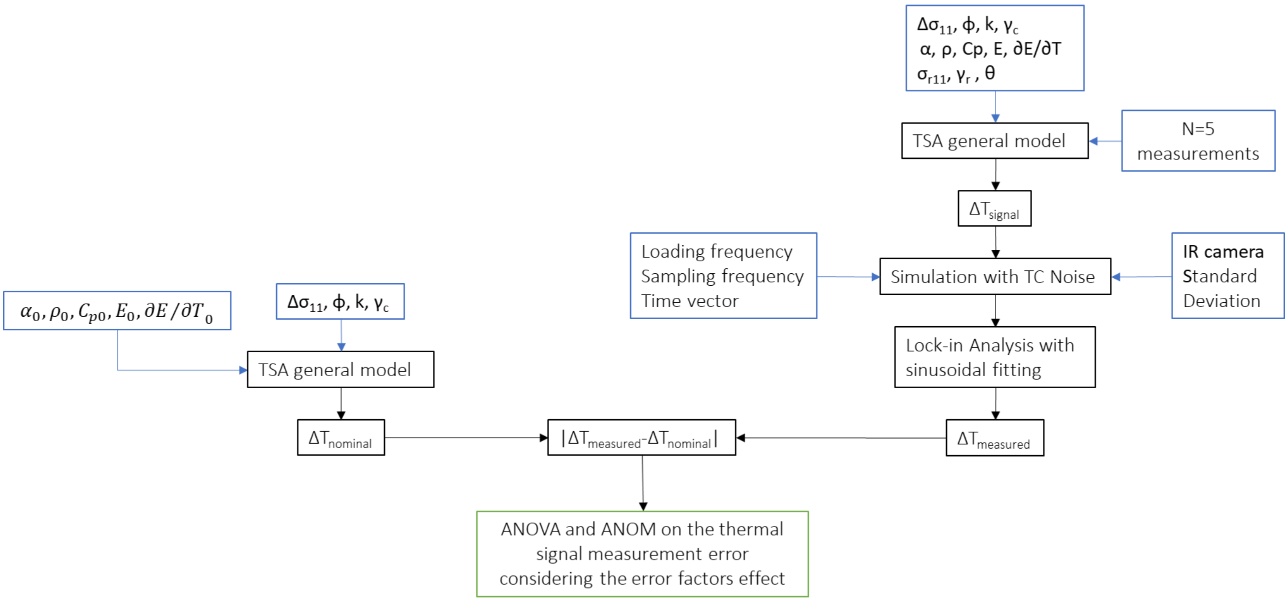

Figure 50 Workflow for the ANOVA and ANOM

The ANOM results provided an interval that allows to determine which of the error factor levels significantly influence the mean from the overall average. To be significant the mean has not to be contained in the interval formed between the lower decision line and the upper decision line (UDL and LDL) obtained adding and subtracting a measure of the sampling error around the statistic of interest, that is [149]:

$$\bar{X} \pm h_{c,nj} \cdot \sqrt{\frac{{S_p}^2 \cdot (N_l - 1)}{n_{tot}}} \qquad \text{Eq 121}$$

where $\bar{X}$ is the estimate overall mean response, N_l is the number of levels for each factor, nj is the number of measurements for the j-th level and S^2 is the pooled variance, which is the mean of the variances of each factor level ${S_p}^2 = \sum_{i=1}^{N_l} S_i^2 / N_l$.

$h_{c,Nj}$ is the critical value of Nelson's *h* statistic with N_l levels and nj equal observations for obtaining the 95% UDL and LDL. The $h_{c,Nj}$ values are obtained by interpolation from tables [149].

5.2.6. ANOVA and ANOM results and discussion

It is now possible to assess which would be the significant factors (and their interaction) given by an experimental campaign. More interesting is the information of which factors and/or their interaction that result to be NOT significant despite the model state their role, because of the level of noise generated by all noise factors.

The p-values calculated for the error factors in the two cases of traction and compression are reported in Table 17 and Table 18 respectively.

The results show what are the factors and interactions whose effect is covert by the sources of error, proving a p-value higher than 0.05 although the analytical model indicates their significance.
In both cases, all the material characteristics a, ρ, C_ε, $\partial E/\partial T$ and E and all the 3 characteristics of the residual stress system: σ_{r11}, $\Delta\sigma_{rp}$ and θ show p-value lower than 0.05, demonstrating significance on the relative error.
The influent 2-factors interactions common to both cases are the numbers *9, 10, 16, 19, 22, 24, 25, 27, 28, 29, 30, 31, 32, 36* in Tables 5 and 6.
The 2-factors interactions numbers *17, 18, 20* and *23* results significative only for the compression case. The parameter ρ varies in a range relatively smaller than other parameters, thus its interaction with the parameters which lead to a reduction of the amplitude of the thermal signal can be significative only in the second simulation plan

where the sum of the principal stress amplitude ranges from -200 to -900 MPa, rather than in the first simulation plan where it varies from 50 to 600 MPa.

For similar reasons, the 3-factors interactions numbers *74, 75, 77, 83* and *84* results significative only in the compression loading case.

The interaction *88* is significative only in the traction case when the component of the thermoelastic signal due to the imposed load is generally lower and the variation of θ has a higher effect.

As expected, many interactions result not significative, despite in Equation 6 they are directly connected to the temperature variation. The analytical model gives the exact relation between the parameters and the thermoelastic response but cannot give information about their effect on the measured signal which depends on all the noise factors.

Tensile case

Table 17 ANOVA results for the tensile case.

**a as expected from the analytical model, b should be significative from the analytical model, but covered by noise

	Source	Sum Sq.	d.f.	Mean Sq.	F	Prob>F	Significative (yes/no)	Note (a,b)**
1	**α**	5.7E+06	1	5.7E+06	5.3E+05	0.0E+00	Yes	a
2	**ρ**	6.9E+05	1	6.9E+05	6.4E+04	0.0E+00	Yes	a
3	**C_ε**	9.0E+06	1	9.0E+06	8.3E+05	0.0E+00	Yes	a
4	**E**	1.4E+05	1	1.4E+05	1.3E+04	0.0E+00	Yes	a
5	**∂E/∂T**	4.0E+04	1	4.0E+04	3.7E+03	0.0E+00	Yes	a
6	**σ_{r11}**	5.6E+06	6	9.3E+05	8.6E+04	0.0E+00	Yes	a
7	**$\Delta\sigma_{rp}$**	4.0E+05	2	2.0E+05	1.8E+04	0.0E+00	Yes	a
8	**θ**	4.2E+04	2	2.1E+04	1.9E+03	0.0E+00	Yes	a
9	**α * ρ**	5.0E+02	1	5.0E+02	4.6E+01	1.2E-11	Yes	a
10	**α * C_ε**	6.5E+03	1	6.5E+03	6.0E+02	2.1E-132	Yes	a
11	**α *E**	2.6E-01	1	2.6E-01	2.4E-02	8.8E-01	No	a
12	**α *∂E/∂T**	2.3E-04	1	2.3E-04	2.1E-05	1.0E+00	No	a
13	**α *sr11**	8.9E-01	6	1.5E-01	1.4E-02	1.0E+00	No	a
14	**α * $\Delta\sigma_{rp}$**	2.2E-01	2	1.1E-01	9.9E-03	9.9E-01	No	a
15	**α * θ**	1.3E-01	2	6.5E-02	6.0E-03	9.9E-01	No	a
16	**ρ * C_ε**	7.7E+02	1	7.7E+02	7.1E+01	3.0E-17	Yes	a
17	**ρ *E**	9.7E+00	1	9.7E+00	8.9E-01	3.4E-01	No	b
18	**ρ *∂E/∂T**	2.4E+00	1	2.4E+00	2.2E-01	6.4E-01	No	b
19	**ρ * σ_{r11}**	4.8E+02	6	8.0E+01	7.3E+00	7.4E-08	Yes	a
20	**ρ * $\Delta\sigma_{rp}$**	3.1E+01	2	1.5E+01	1.4E+00	2.4E-01	No	b
21	**ρ * θ**	2.5E+00	2	1.3E+00	1.2E-01	8.9E-01	No	b
22	**C_ε *E**	1.6E+02	1	1.6E+02	1.5E+01	1.2E-04	Yes	a
23	**C_ε *∂E/∂T**	4.8E+01	1	4.8E+01	4.5E+00	3.5E-02	No	b
24	**C_ε * σ_{r11}**	6.3E+03	6	1.0E+03	9.6E+01	3.1E-121	Yes	a
25	**C_ε * $\Delta\sigma_{rp}$**	4.2E+02	2	2.1E+02	2.0E+01	3.1E-09	Yes	a
26	**C_ε * θ**	5.0E+01	2	2.5E+01	2.3E+00	1.0E-01	No	b
27	**E*∂E/∂T**	2.5E+02	1	2.5E+02	2.3E+01	1.3E-06	Yes	a
28	**E* σ_{r11}**	3.4E+04	6	5.7E+03	5.2E+02	0.0E+00	Yes	a
29	**E* $\Delta\sigma_{rp}$**	2.4E+03	2	1.2E+03	1.1E+02	1.4E-48	Yes	a
30	**E* θ**	2.6E+02	2	1.3E+02	1.2E+01	6.4E-06	Yes	a
31	**∂E/∂T * σ_{r11}**	9.6E+03	6	1.6E+03	1.5E+02	6.8E-188	Yes	a
32	**∂E/∂T * $\Delta\sigma_{rp}$**	6.7E+02	2	3.4E+02	3.1E+01	3.3E-14	Yes	a
33	**∂E/∂T * θ**	7.5E+01	2	3.7E+01	3.4E+00	3.2E-02	No	b
34	**σ_{r11} * $\Delta\sigma_{rp}$**	9.6E-01	12	8.0E-02	7.4E-03	1.0E+00	No	b
35	**σ_{r11} * θ**	1.0E+00	12	8.5E-02	7.9E-03	1.0E+00	No	b
36	**$\Delta\sigma_{rp}$ * θ**	2.3E+04	4	5.8E+03	5.4E+02	0.0E+00	Yes	a
37	**α * ρ * C_ε**	6.7E-01	1	6.7E-01	6.2E-02	8.0E-01	No	b

38	$\alpha * \rho * E$	1.4E-02	1	1.4E-02	1.3E-03	9.7E-01	No	a
39	$\alpha * \rho * \partial E/\partial T$	4.1E-02	1	4.1E-02	3.8E-03	9.5E-01	No	a
40	$\alpha * \rho * \sigma_{r11}$	1.5E+00	6	2.5E-01	2.3E-02	1.0E+00	No	a
41	$\alpha * \rho * \Delta\sigma_{rp}$	9.3E-01	2	4.7E-01	4.3E-02	9.6E-01	No	a
42	$\alpha * \rho * \theta$	4.4E-02	2	2.2E-02	2.0E-03	1.0E+00	No	a
43	$\alpha * C_\varepsilon * E$	7.1E-02	1	7.1E-02	6.6E-03	9.4E-01	No	a
44	$\alpha * C_\varepsilon * \partial E/\partial T$	9.5E-02	1	9.5E-02	8.8E-03	9.3E-01	No	a
45	$\alpha * C_\varepsilon * \sigma_{r11}$	7.8E-01	6	1.3E-01	1.2E-02	1.0E+00	No	a
46	$\alpha * C_\varepsilon * \Delta\sigma_{rp}$	4.0E-02	2	2.0E-02	1.8E-03	1.0E+00	No	a
47	$\alpha * C_\varepsilon * \theta$	8.5E-03	2	4.3E-03	3.9E-04	1.0E+00	No	a
48	$\alpha * E * \partial E/\partial T$	2.9E-02	1	2.9E-02	2.7E-03	9.6E-01	No	a
49	$\alpha * E * \sigma_{r11}$	4.5E-01	6	7.5E-02	6.9E-03	1.0E+00	No	a
50	$\alpha * E * \Delta\sigma_{rp}$	2.4E-02	2	1.2E-02	1.1E-03	1.0E+00	No	a
51	$\alpha * E * \theta$	6.8E-01	2	3.4E-01	3.1E-02	9.7E-01	No	a
52	$\alpha * \partial E/\partial T * \sigma_{r11}$	6.7E-01	6	1.1E-01	1.0E-02	1.0E+00	No	a
53	$\alpha * \partial E/\partial T * \Delta\sigma_{rp}$	2.8E-02	2	1.4E-02	1.3E-03	1.0E+00	No	a
54	$\alpha * \partial E/\partial T * \theta$	1.6E-02	2	8.1E-03	7.5E-04	1.0E+00	No	a
55	$\alpha * sr11 * \Delta\sigma_{rp}$	6.8E-01	12	5.7E-02	5.2E-03	1.0E+00	No	a
56	$\alpha * \sigma_{r11} * \theta$	7.6E-01	12	6.3E-02	5.8E-03	1.0E+00	No	a
57	$\alpha * \Delta\sigma_{rp} * \theta$	1.7E-01	4	4.2E-02	3.9E-03	1.0E+00	No	a
58	$\rho * C_\varepsilon * E$	1.4E-02	1	1.4E-02	1.2E-03	9.7E-01	No	b
59	$\rho * C_\varepsilon * \partial E/\partial T$	1.2E-01	1	1.2E-01	1.1E-02	9.2E-01	No	b
60	$\rho * C_\varepsilon * \sigma_{r11}$	1.2E+00	6	2.1E-01	1.9E-02	1.0E+00	No	b
61	$\rho * C_\varepsilon * \Delta\sigma_{rp}$	4.7E-01	2	2.4E-01	2.2E-02	9.8E-01	No	b
62	$\rho * C_\varepsilon * \theta$	2.8E-02	2	1.4E-02	1.3E-03	1.0E+00	No	b
63	$\rho * E * \partial E/\partial T$	1.2E-01	1	1.2E-01	1.1E-02	9.2E-01	No	b
64	$\rho * E * \sigma_{r11}$	1.8E+00	6	3.0E-01	2.8E-02	1.0E+00	No	b
65	$\rho * E * \Delta\sigma_{rp}$	2.7E-01	2	1.4E-01	1.2E-02	9.9E-01	No	b
66	$\rho * E * \theta$	2.0E-02	2	1.0E-02	9.4E-04	1.0E+00	No	b
67	$\rho * \partial E/\partial T * \sigma_{r11}$	6.8E-01	6	1.1E-01	1.1E-02	1.0E+00	No	b
68	$\rho * \partial E/\partial T * \Delta\sigma_{rp}$	8.9E-02	2	4.4E-02	4.1E-03	1.0E+00	No	b
69	$\rho * \partial E/\partial T * \theta$	1.6E-01	2	7.8E-02	7.2E-03	9.9E-01	No	b
70	$\rho * \sigma_{r11} * \Delta\sigma_{rp}$	1.9E+00	12	1.6E-01	1.4E-02	1.0E+00	No	b
71	$\rho * \sigma_{r11} * \theta$	1.6E+00	12	1.3E-01	1.2E-02	1.0E+00	No	b
72	$\rho * \Delta\sigma_{rp} * \theta$	1.8E+00	4	4.5E-01	4.2E-02	1.0E+00	No	b
73	$C_\varepsilon * E * \partial E/\partial T$	1.5E-01	1	1.5E-01	1.4E-02	9.1E-01	No	b
74	$C_\varepsilon * E * \sigma_{r11}$	4.4E+01	6	7.3E+00	6.8E-01	6.7E-01	No	b
75	$C_\varepsilon * E * \Delta\sigma_{rp}$	1.9E+00	2	9.4E-01	8.6E-02	9.2E-01	No	b
76	$C_\varepsilon * E * \theta$	1.5E-01	2	7.3E-02	6.8E-03	9.9E-01	No	b
77	$C_\varepsilon * \partial E/\partial T * \sigma_{r11}$	1.0E+01	6	1.7E+00	1.6E-01	9.9E-01	No	b
78	$C_\varepsilon * \partial E/\partial T * \Delta\sigma_{rp}$	1.5E+00	2	7.3E-01	6.7E-02	9.3E-01	No	b

79	$C_\varepsilon * \partial E/\partial T * \theta$	2.1E-01	2	1.0E-01	9.6E-03	9.9E-01	No	b
80	$C_\varepsilon * \sigma_{r11} * \Delta\sigma_{rp}$	6.8E-01	12	5.7E-02	5.2E-03	1.0E+00	No	b
81	$C_\varepsilon * \sigma_{r11} * \theta$	2.0E+00	12	1.7E-01	1.5E-02	1.0E+00	No	b
82	$C_\varepsilon * \Delta\sigma_{rp} * \theta$	2.4E+01	4	6.0E+00	5.5E-01	7.0E-01	No	b
83	$E * \partial E/\partial T * \sigma_{r11}$	5.6E+01	6	9.3E+00	8.6E-01	5.3E-01	No	b
84	$E * \partial E/\partial T * \Delta\sigma_{rp}$	1.3E+00	2	6.7E-01	6.2E-02	9.4E-01	No	b
85	$E * \partial E/\partial T * \theta$	3.3E-01	2	1.6E-01	1.5E-02	9.9E-01	No	b
86	$E * \sigma_{r11} * \Delta\sigma_{rp}$	1.3E+00	12	1.1E-01	9.9E-03	1.0E+00	No	b
87	$E * \sigma_{r11} * \theta$	1.1E+00	12	8.8E-02	8.1E-03	1.0E+00	No	b
88	$E * \Delta\sigma_{rp} * \theta$	1.5E+02	4	3.8E+01	3.5E+00	7.3E-03	Yes	a
89	$\partial E/\partial T * \sigma_{r11} * \Delta\sigma_{rp}$	2.8E+00	12	2.4E-01	2.2E-02	1.0E+00	No	b
90	$\partial E/\partial T * \sigma_{r11} * \theta$	1.1E+00	12	9.3E-02	8.6E-03	1.0E+00	No	b
91	$\partial E/\partial T * \Delta\sigma_{rp} * \theta$	3.9E+01	4	9.9E+00	9.1E-01	4.6E-01	No	b
92	$\sigma_{r11} * \Delta\sigma_{rp} * \theta$	2.0E+00	24	8.4E-02	7.7E-03	1.0E+00	No	b
	Error	8.9E+06	816102	1.1E+01				
	Total	3.1E+07	816479					

Compression case

Table 18 ANOVA results for the compression case.

**a as expected from the analytical model, b should be significative from the analytical model, but covered by noise.

	Source	Sum Sq.	d.f.	Mean Sq.	F	Prob>F	Significative (yes/no)	Note (a,b)**
1	α	7.2E+06	1	7.2E+06	1.6E+07	0.0E+00	Yes	a
2	ρ	6.9E+05	1	6.9E+05	1.5E+06	0.0E+00	Yes	a
3	C_ε	9.0E+06	1	9.0E+06	1.9E+07	0.0E+00	Yes	a
4	E	2.1E+05	1	2.1E+05	4.6E+05	0.0E+00	Yes	a
5	$\partial E/\partial T$	5.9E+04	1	5.9E+04	1.3E+05	0.0E+00	Yes	a
6	σ_{r11}	7.0E+06	6	1.2E+06	2.5E+06	0.0E+00	Yes	a
7	$\Delta\sigma_{rp}$	7.1E+05	2	3.5E+05	7.7E+05	0.0E+00	Yes	a
8	θ	9.4E+02	2	4.7E+02	1.0E+03	0.0E+00	Yes	a
9	$\alpha * \rho$	6.3E+02	1	6.3E+02	1.4E+03	3.8E-297	Yes	a
10	$\alpha * C_\varepsilon$	8.1E+03	1	8.1E+03	1.8E+04	0.0E+00	Yes	a
11	$\alpha *E$	4.9E-06	1	4.9E-06	1.1E-05	1.0E+00	No	a
12	$\alpha *\partial E/\partial T$	4.5E-03	1	4.5E-03	9.7E-03	9.2E-01	No	a
13	α *sr11	5.5E-02	6	9.2E-03	2.0E-02	1.0E+00	No	a
14	$\alpha * \Delta\sigma_{rp}$	8.4E-04	2	4.2E-04	9.1E-04	1.0E+00	No	a
15	$\alpha * \theta$	1.0E-01	2	5.1E-02	1.1E-01	9.0E-01	No	a
16	$\rho * C_\varepsilon$	7.7E+02	1	7.7E+02	1.7E+03	0.0E+00	Yes	a
17	$\rho *E$	1.8E+01	1	1.8E+01	4.0E+01	2.8E-10	Yes	a
18	$\rho *\partial E/\partial T$	5.4E+00	1	5.4E+00	1.2E+01	6.2E-04	Yes	a
19	$\rho * \sigma_{r11}$	6.1E+02	6	1.0E+02	2.2E+02	3.1E-281	Yes	a
20	$\rho * \Delta\sigma_{rp}$	5.8E+01	2	2.9E+01	6.3E+01	3.3E-28	Yes	a
21	$\rho * \theta$	4.8E-02	2	2.4E-02	5.2E-02	9.5E-01	No	b
22	$C_\varepsilon *E$	2.4E+02	1	2.4E+02	5.1E+02	4.9E-113	Yes	a
23	$C_\varepsilon *\partial E/\partial T$	6.7E+01	1	6.7E+01	1.5E+02	1.4E-33	Yes	a
24	$C_\varepsilon * \sigma_{r11}$	7.9E+03	6	1.3E+03	2.9E+03	0.0E+00	Yes	a
25	$C_\varepsilon * \Delta\sigma_{rp}$	8.0E+02	2	4.0E+02	8.7E+02	0.0E+00	Yes	a
26	$C_\varepsilon * \theta$	1.2E+00	2	5.8E-01	1.2E+00	2.9E-01	No	b
27	$E*\partial E/\partial T$	3.7E+02	1	3.7E+02	8.0E+02	5.5E-175	Yes	a
28	$E* \sigma_{r11}$	4.3E+04	6	7.2E+03	1.6E+04	0.0E+00	Yes	a
29	$E* \Delta\sigma_{rp}$	4.4E+03	2	2.2E+03	4.7E+03	0.0E+00	Yes	a
30	$E* \theta$	6.3E+00	2	3.1E+00	6.8E+00	1.1E-03	Yes	a
31	$\partial E/\partial T * \sigma_{r11}$	1.2E+04	6	2.0E+03	4.4E+03	0.0E+00	Yes	a
32	$\partial E/\partial T * \Delta\sigma_{rp}$	1.2E+03	2	6.2E+02	1.3E+03	0.0E+00	Yes	a
33	$\partial E/\partial T * \theta$	1.7E+00	2	8.7E-01	1.9E+00	1.5E-01	No	b
34	$\sigma_{r11} * \Delta\sigma_{rp}$	1.4E-01	12	1.2E-02	2.5E-02	1.0E+00	No	b
35	$\sigma_{r11} * \theta$	1.4E-01	12	1.2E-02	2.5E-02	1.0E+00	No	b
36	$\Delta\sigma_{rp} * \theta$	5.3E+02	4	1.3E+02	2.9E+02	5.4E-249	Yes	a
37	$\alpha * \rho * C_\varepsilon$	6.5E-01	1	6.5E-01	1.4E+00	2.4E-01	No	b

38	$\alpha * \rho * E$	8.8E-04	1	8.8E-04	1.9E-03	9.7E-01	No	a
39	$\alpha * \rho * \partial E/\partial T$	4.0E-03	1	4.0E-03	8.6E-03	9.3E-01	No	a
40	$\alpha * \rho * \sigma_{r11}$	8.0E-02	6	1.3E-02	2.9E-02	1.0E+00	No	a
41	$\alpha * \rho * \Delta\sigma_{rp}$	7.1E-03	2	3.6E-03	7.7E-03	9.9E-01	No	a
42	$\alpha * \rho * \theta$	2.8E-02	2	1.4E-02	3.0E-02	9.7E-01	No	a
43	$\alpha * C_\varepsilon * E$	3.4E-03	1	3.4E-03	7.3E-03	9.3E-01	No	a
44	$\alpha * C_\varepsilon * \partial E/\partial T$	6.4E-03	1	6.4E-03	1.4E-02	9.1E-01	No	a
45	$\alpha * C_\varepsilon * \sigma_{r11}$	1.0E-01	6	1.7E-02	3.8E-02	1.0E+00	No	a
46	$\alpha * C_\varepsilon * \Delta\sigma_{rp}$	1.3E-02	2	6.7E-03	1.4E-02	9.9E-01	No	a
47	$\alpha * C_\varepsilon * \theta$	1.1E-02	2	5.5E-03	1.2E-02	9.9E-01	No	a
48	$\alpha * E * \partial E/\partial T$	4.7E-02	1	4.7E-02	1.0E-01	7.5E-01	No	a
49	$\alpha * E * \sigma_{r11}$	1.4E-02	6	2.3E-03	5.0E-03	1.0E+00	No	a
50	$\alpha * E * \Delta\sigma_{rp}$	4.5E-02	2	2.2E-02	4.9E-02	9.5E-01	No	a
51	$\alpha * E * \theta$	1.1E-02	2	5.4E-03	1.2E-02	9.9E-01	No	a
52	$\alpha * \partial E/\partial T * \sigma_{r11}$	6.4E-02	6	1.1E-02	2.3E-02	1.0E+00	No	a
53	$\alpha * \partial E/\partial T * \Delta\sigma_{rp}$	6.0E-03	2	3.0E-03	6.5E-03	9.9E-01	No	a
54	$\alpha * \partial E/\partial T * \theta$	1.9E-02	2	9.4E-03	2.0E-02	9.8E-01	No	a
55	$\alpha * sr11 * \Delta\sigma_{rp}$	1.8E-01	12	1.5E-02	3.3E-02	1.0E+00	No	a
56	$\alpha * \sigma_{r11} * \theta$	1.1E-01	12	9.0E-03	1.9E-02	1.0E+00	No	a
57	$\alpha * \Delta\sigma_{rp} * \theta$	1.2E-01	4	3.0E-02	6.6E-02	9.9E-01	No	a
58	$\rho * C_\varepsilon * E$	7.8E-03	1	7.8E-03	1.7E-02	9.0E-01	No	b
59	$\rho * C_\varepsilon * \partial E/\partial T$	1.7E-04	1	1.7E-04	3.6E-04	9.8E-01	No	b
60	$\rho * C_\varepsilon * \sigma_{r11}$	9.9E-01	6	1.6E-01	3.6E-01	9.1E-01	No	b
61	$\rho * C_\varepsilon * \Delta\sigma_{rp}$	7.1E-02	2	3.5E-02	7.6E-02	9.3E-01	No	b
62	$\rho * C_\varepsilon * \theta$	1.8E-02	2	9.0E-03	2.0E-02	9.8E-01	No	b
63	$\rho * E * \partial E/\partial T$	5.1E-02	1	5.1E-02	1.1E-01	7.4E-01	No	b
64	$\rho * E * \sigma_{r11}$	3.2E+00	6	5.3E-01	1.2E+00	3.3E-01	No	b
65	$\rho * E * \Delta\sigma_{rp}$	2.3E-01	2	1.1E-01	2.4E-01	7.8E-01	No	b
66	$\rho * E * \theta$	1.0E-05	2	5.1E-06	1.1E-05	1.0E+00	No	b
67	$\rho * \partial E/\partial T * \sigma_{r11}$	1.2E+00	6	2.1E-01	4.5E-01	8.5E-01	No	b
68	$\rho * \partial E/\partial T * \Delta\sigma_{rp}$	1.0E-01	2	5.2E-02	1.1E-01	8.9E-01	No	b
69	$\rho * \partial E/\partial T * \theta$	2.5E-02	2	1.2E-02	2.7E-02	9.7E-01	No	b
70	$\rho * \sigma_{r11} * \Delta\sigma_{rp}$	1.7E-01	12	1.4E-02	3.1E-02	1.0E+00	No	b
71	$\rho * \sigma_{r11} * \theta$	2.0E-01	12	1.6E-02	3.5E-02	1.0E+00	No	b
72	$\rho * \Delta\sigma_{rp} * \theta$	1.2E-01	4	2.9E-02	6.3E-02	9.9E-01	No	b
73	$C_\varepsilon * E * \partial E/\partial T$	5.3E-01	1	5.3E-01	1.1E+00	2.8E-01	No	b
74	$C_\varepsilon * E * \sigma_{r11}$	4.8E+01	6	8.0E+00	1.7E+01	3.0E-20	Yes	a
75	$C_\varepsilon * E * \Delta\sigma_{rp}$	4.5E+00	2	2.3E+00	4.9E+00	7.5E-03	Yes	a
76	$C_\varepsilon * E * \theta$	2.0E-02	2	9.9E-03	2.1E-02	9.8E-01	No	b
77	$C_\varepsilon * \partial E/\partial T * \sigma_{r11}$	1.4E+01	6	2.4E+00	5.2E+00	2.1E-05	Yes	a
78	$C_\varepsilon * \partial E/\partial T * \Delta\sigma_{rp}$	1.5E+00	2	7.5E-01	1.6E+00	2.0E-01	No	b

79	**C_{ε} *∂E/∂T * θ**	2.5E-02	2	1.3E-02	2.7E-02	9.7E-01	No	b
80	**C_{ε} * σ_{r11}* $\Delta\sigma_{rp}$**	1.2E-01	12	1.0E-02	2.2E-02	1.0E+00	No	b
81	**C_{ε} * σ_{r11}* θ**	2.0E-01	12	1.6E-02	3.5E-02	1.0E+00	No	b
82	**C_{ε} * $\Delta\sigma_{rp}$ * θ**	5.7E-01	4	1.4E-01	3.1E-01	8.7E-01	No	b
83	**E*∂E/∂T * σ_{r11}**	7.6E+01	6	1.3E+01	2.7E+01	8.3E-33	Yes	a
84	**E*∂E/∂T * $\Delta\sigma_{rp}$**	7.3E+00	2	3.7E+00	7.9E+00	3.6E-04	Yes	a
85	**E*∂E/∂T * θ**	3.9E-02	2	1.9E-02	4.2E-02	9.6E-01	No	b
86	**E* σ_{r11}* $\Delta\sigma_{rp}$**	9.3E-02	12	7.7E-03	1.7E-02	1.0E+00	No	b
87	**E* σ_{r11}* θ**	1.7E-01	12	1.4E-02	3.1E-02	1.0E+00	No	b
88	**E* $\Delta\sigma_{rp}$ * θ**	3.2E+00	4	8.0E-01	1.7E+00	1.4E-01	No	b
89	**∂E/∂T * σ_{r11}* $\Delta\sigma_{rp}$**	1.9E-01	12	1.6E-02	3.4E-02	1.0E+00	No	b
90	**∂E/∂T * σ_{r11}* θ**	5.9E-02	12	4.9E-03	1.1E-02	1.0E+00	No	b
91	**∂E/∂T * $\Delta\sigma_{rp}$ * θ**	5.8E-01	4	1.5E-01	3.2E-01	8.7E-01	No	b
92	**σ_{r11}* $\Delta\sigma_{rp}$ * θ**	4.7E-01	24	1.9E-02	4.2E-02	1.0E+00	No	b
	Error	3.8E+05	816102	4.6E-01				
	Total	2.5E+07	816479					

In Figure 51 the Means obtained for each level of the material characteristics for the traction case are plotted. Comparing the results with the overall average and the confidence interval (represented by the UDL and LDL) there is evidence of a significative difference in the mean of the TSA response with different levels of all the material characteristics. In particular α and C_ε variations result in a higher signal variation due both to their direct effect on the thermal signal and to the range selected for the simulation.

Figure 52 shows the group of Means which follow outside the UDL and the LDL lines for the residual stress tensor characteristics for the traction case. The graphical representation shows how the angle θ and induce significative variations but smaller than the variations induced by σ_{r11}.

Figure 53 and Figure 54 show the same trend for the compression case. Comparing the two cases it emerges that the overall error mean is higher in the compression case, characterized by more critical loading conditions and residual stress slightly unbalanced towards the same sign. Furthermore, this condition induces a higher influence of the amplitude of residual stresses but a lower effect of their orientation.

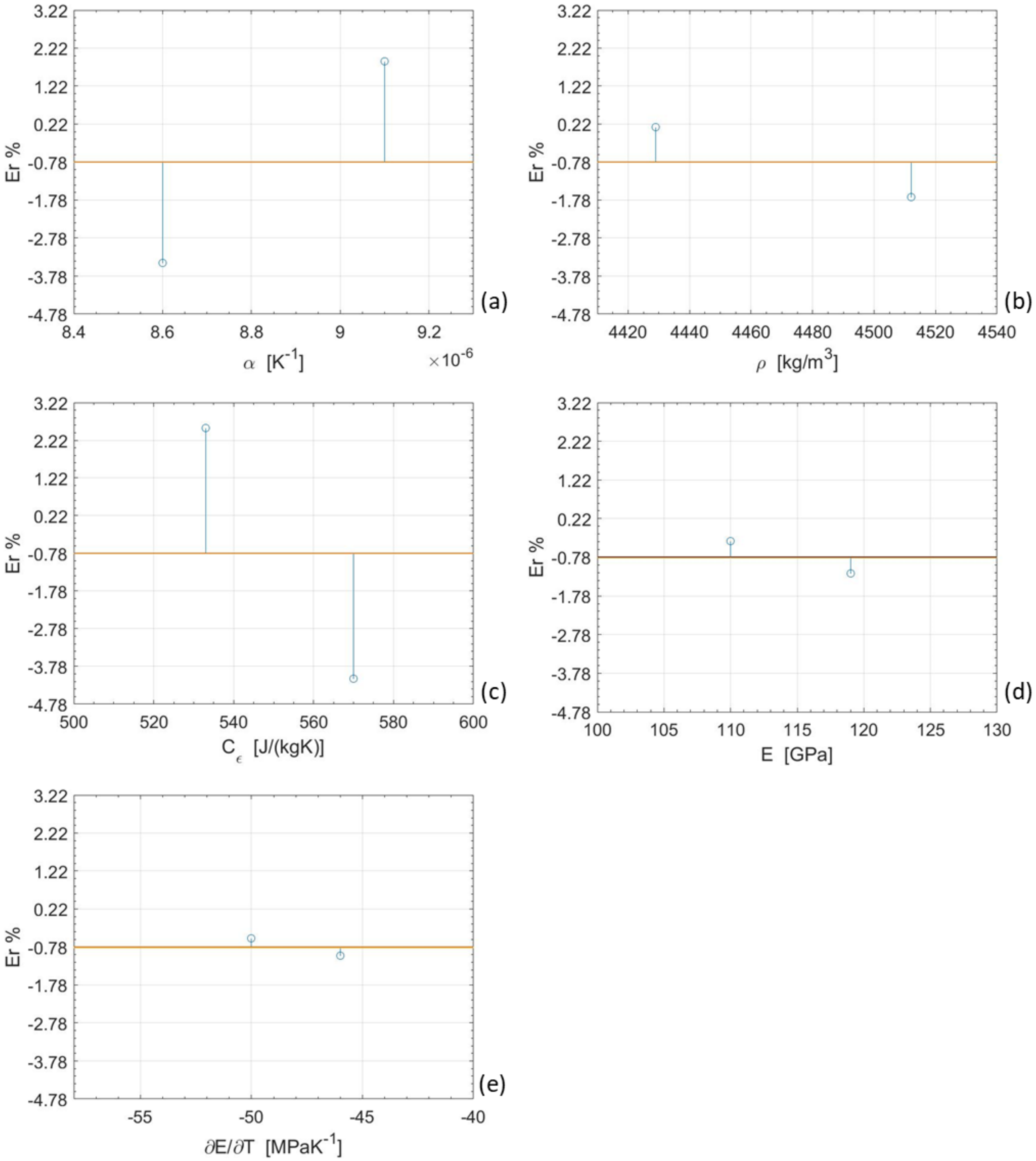

Figure 51 ANOM results for the tensile case. The Means (blue circles) and the UDL (orange line) and LDL (yellow line) are plotted for the different levels of the material characteristics (a) α, (b) ρ, (c) Cε, (d) E and (e) ∂E\∂T.

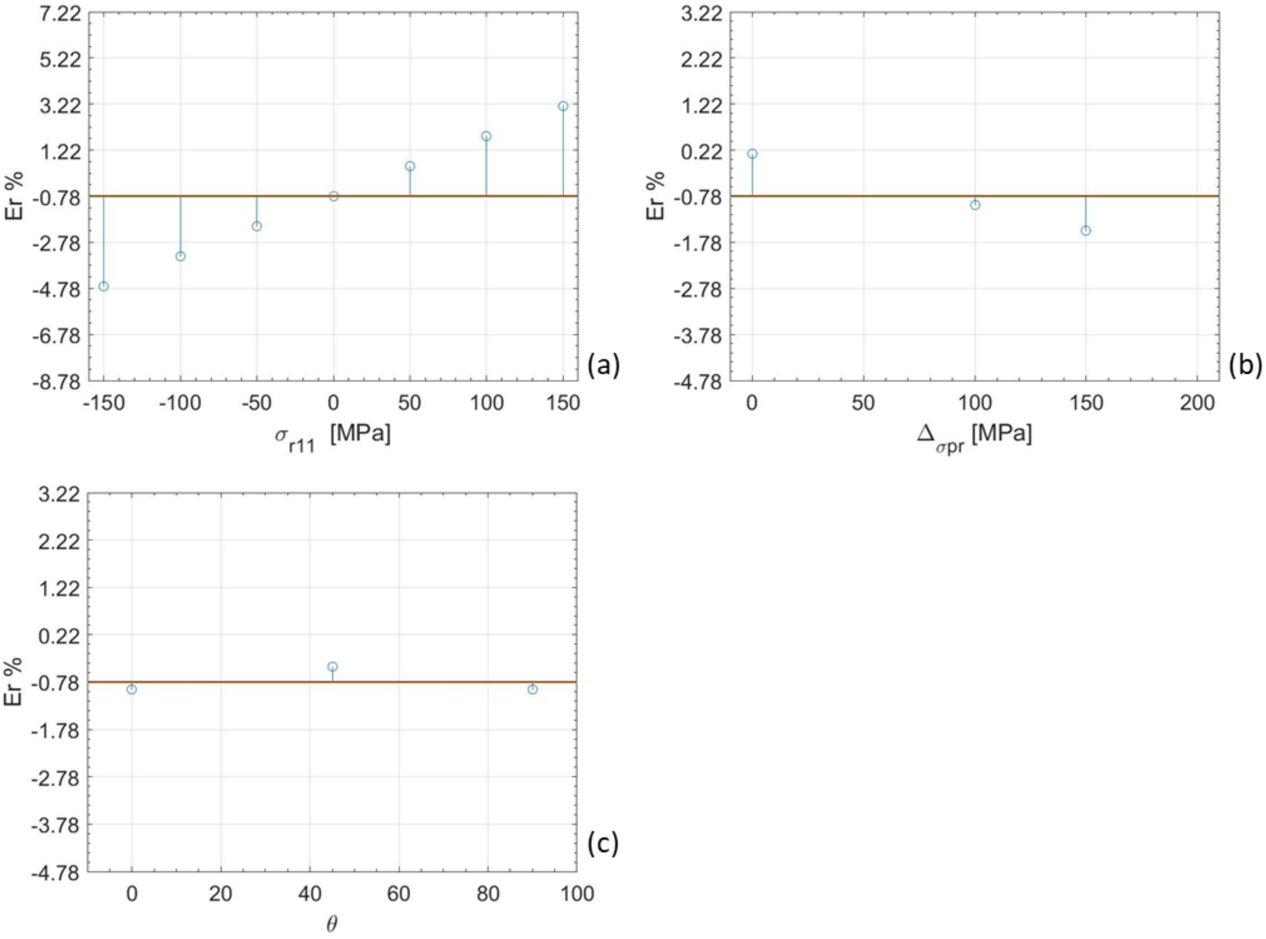

Figure 52 ANOM results for the tensile case. The Means (blue circles) and the UDL (orange line) and LDL (yellow line) are plotted for the different levels of the residual stress characteristics (a) σ_{r11}, (b) $\Delta\sigma_{rp}$ and (c) θ.

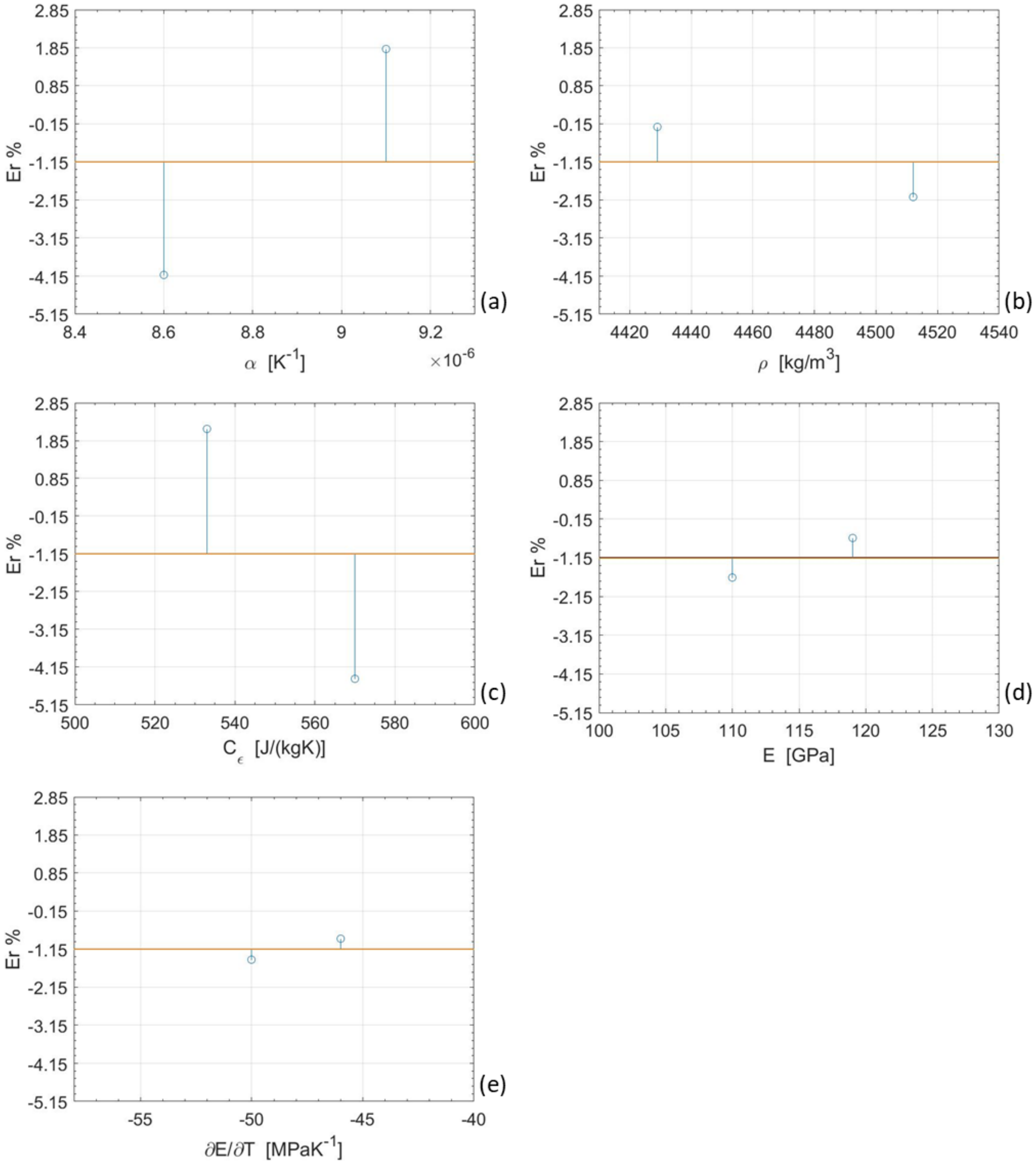

Figure 53 ANOM results for the compression case. The Means (blue circles) and the UDL (orange line) and LDL (yellow line) are plotted for the different levels of the material characteristics (a) α, (b) ρ, (c) Cε, (d) E and (e) ∂E\∂T.

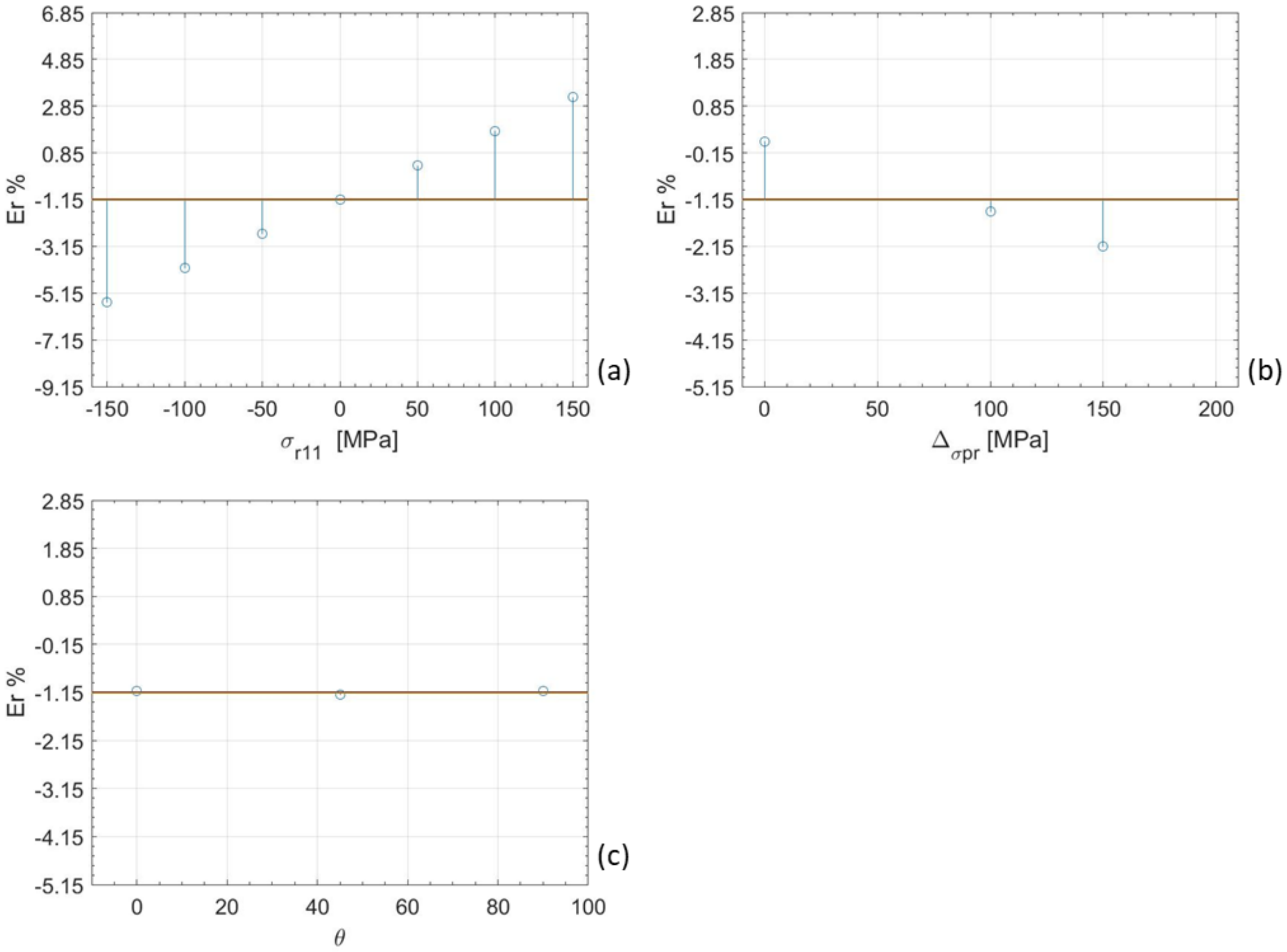

Figure 54 ANOM results for the compression case. The Means (blue circles) and the UDL (orange line) and LDL (yellow line) are plotted for the different levels of the residual stress characteristics (a) σr11, (b) Δσrp and (c) θ.

5.2.7. Robust Design application: sum of stresses measurements methodology

The first study was focused on the problem of TSA application in stress measurement. The aim was to identify the loading characteristics which ensure the more accurate and robust measurement of stresses by applying the classical TSA equation and comparing three different calibration methods:

1) Evaluation of the thermoelastic constant by using the nominal values for the material characteristics.
2) Evaluation of the thermoelastic constant by simulating an experimental calibration with relaxed dog-bone samples of the same material.
3) Evaluation of the thermoelastic constant by simulating an experimental calibration with a dog-bone samples of the same material, in the same residual stress condition but with a variable orientation for the residual stress principal system.

The calibration methods studied in this work are all based on the proportional relation between the thermoelastic response and the sum of the principal stress variation. Despite the availability of calibration procedures based on the second order effect, they cannot be compered because limited to cases of monoaxial loading and monoaxial residual stress.

5.2.8. Sum of stresses measurements: Problem Definition and workflow

Figure 55 shows the block diagram representation of the system. In the case of TSA application in stress measurement the control factor are the loading characteristics while the noise factors are the material characteristics variation, the residual stress system characteristics, and the IR camera noise.

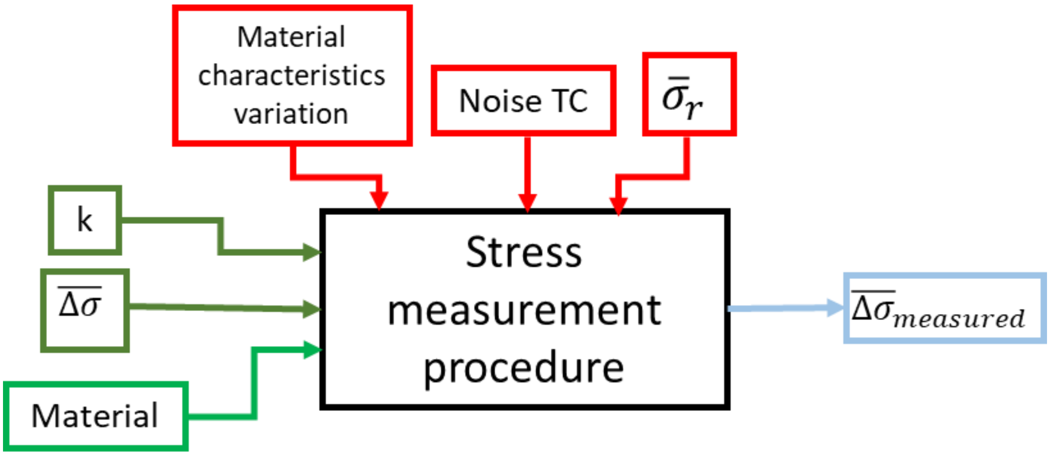

Figure 55 Block diagram of the TSA stress measurement system

The study was carried out by implementing the Taguchi method: a control factors matrix was built by considering 3 different values for each control factor and an external matrix was built considering 2 values for the material characteristics and 3 values for the residual stress system characteristics and 3 values for the IR camera Noise.

The IR camera noise values considered are [141]:

$$\mu_{Noise} - \sqrt{3/2} \cdot \boldsymbol{\sigma}_{Noise}, \qquad \mu_{Noise} \text{ and } \mu_{Noise} + \sqrt{3/2} \cdot \boldsymbol{\sigma}_{Noise} \qquad \text{Eq 122}$$

Where $\mu_{Noise}$and $\cdot \boldsymbol{\sigma}_{Noise}$ are respectively the mean value and the variance of the Noise affecting the amplitude of the thermal response measurement obtained by simulating an high number of repetition of the ΔT measurement with the lock-in analysis.

The values assumed for the control factor and the remaining noise factors are listed in Table 14, Table 15 and Table 16.

Due to the absence of a limit on the number of simulations, both the control factor matrix and the external matrix were full factorial plan.

The steps of the processing of the simulation results are described in Figure 56. The thermoelastic response $\Delta T_{measured}$ was used to evaluate the sum of the principal stress by applying the classical approach.

The first calibration method was applied calculating the thermoelastic constant as:

$$K_0 = -\frac{\alpha_0}{\rho_0 \cdot C_{p0}} \qquad \text{Eq 123}$$

The second and third calibration method were applied simulating experimental calibration. For each control factor combination and for each error factor combination the calibration constant K_0 was evaluate simulating the calibration procedure on a dog-bone sample keeping the same values of k and $\Delta\sigma$.

The first calibration was simulated with free-residual stress samples, the second calibration was simulated considering a sample of the same material and the same residual stress conditions but with variable orientation for the residual stress principal system.

For all cases, the sum of principal stresses was then evaluated as:

$$(\Delta\sigma_{11} + \Delta\sigma_{22})_{measured} = {K_0}^{-1} \frac{\Delta T_{measured}}{T_0} \qquad \text{Eq 124}$$

The stress measurement obtained by using Eq 124 was then compared with the value imposed as input and the relative error was evaluated as:

$$Er = \frac{(\Delta\sigma_{11} + \Delta\sigma_{22})_{imposed} - (\Delta\sigma_{11} + \Delta\sigma_{22})_{measured}}{(\Delta\sigma_{11} + \Delta\sigma_{22})_{imposed}} \cdot 100 \qquad \text{Eq 125}$$

The value calculated with Eq 125 represents the performance of the measurement and the optimization problem aims to minimize that value and its variance.

The problem type is smaller the batter and the signal to noise ratio and the quality loss function were calculated for each value j of each control factor as [141]:

$$SN_{ij} = -10 \cdot \log\left(\frac{1}{N_{ij}} \sum_{n=1}^{N_{ij}} {y_n}^2\right) \qquad \text{Eq 126}$$

$$\frac{Q_{ij}}{K} = {X_{ij}}^2 + {S_{ij}}^2 \qquad \text{Eq 127}$$

Where the subscript ij indicates the value j of the i-esim control factor. Nij is the number of combinations of control factors with control factor i having value j and yn is the mean of all the values of Er for the nth control factor combination.

X_{ij} and ${S_{ij}}^2$ are the mean and the variance estimated from the Nij measurements yn.

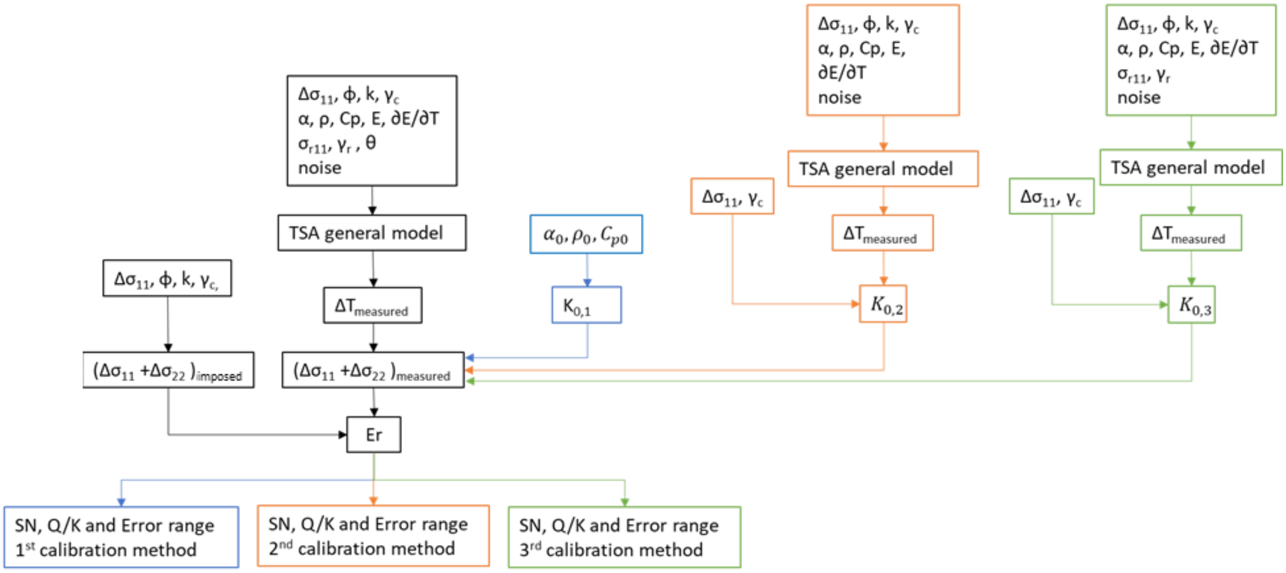

Figure 56 Workflo of the TSA stress measurement system Robust Design

In order to give information about the stress measurement performance on real components it is important to underline that the only parameter that can be tuned by the operator is the ratio k, which is equal to the ratio between the mean and the amplitude of the load, constant for every pixel of the IR camera. In the case of complex geometry, the stress distribution can be very complex, and the tension tensor cannot be considered as a control factor.

The statistical analysis allowed to evaluate the SN and Q/K for each value of k in the plan. Once the optimal value of k was identified, the effect of the loading characteristics on the measurement error was investigated by evaluating the same indicators for each of their values, considering only the tests of the plan with the optimal k.

Finally, for each calibration technique the overall error range has been evaluated as $\mu \pm 3S$, where μ and S are the mean and standard deviation of the relative errors of the optimal-k simulation plan.

5.2.9. Sum of stresses measurements: Results and discussions

For each calibration method, the results are reported in terms of the error statistics associated to each value of the factor k both for the manly tensile (Table 19) and manly compression (Table 20) loading conditions.

All the calibration methods present comparable values of standard deviation of the relative error, however in every condition the third calibration method show Means of the relative error lower than the others.

In the tensile loading case, the plots of the SN (Figure 57) and the Q/K (Figure 58) show consistent trends for the parameter k, identifying the same optimal values. The quality of the measurement increases with the mean load only with the first calibration, while for the two experimental calibration the mean load reduces the effect of the source of error due to residual stress. This latter effect is higher with the second calibration, when the calibration sample is relaxed end residual stress is completely neglected.

Also, in the compression case all the three calibration methods show a similar trend for the Q/K (Figure 58): a decrease of the quality of the measurement with the mean load.

Table 19 Tensile case. Means and Means of the Standard Deviations of the relative error for each value of the control factor k and each calibration method

		calib.1		calib.2		calib.3	
		Mean Error %	StDev	Mean Error %	StDev	Mean Error %	StDev
k	0	-0.921	6.454	-1.041	4.498	0.154	3.797
	1	8.317	6.741	-0.956	4.024	0.108	3.251
	1,5	12.937	6.988	-0.921	3.836	0.093	3.044

Table 20 Compression case. Means and Means of the Standard Deviations of the relative error for each value of the control factor k and each calibration method

		calib.1		calib.2		calib.3	
		Mean Error %	StDev	Mean Error %	StDev	Mean Error %	StDev
k	0	-1.125	5.456	-1.246	3.148	0.002	0.551
	1	-9.159	5.453	-1.360	3.444	0.003	0.611
	1,5	-13.176	5.554	-1.428	3.622	0.003	0.649

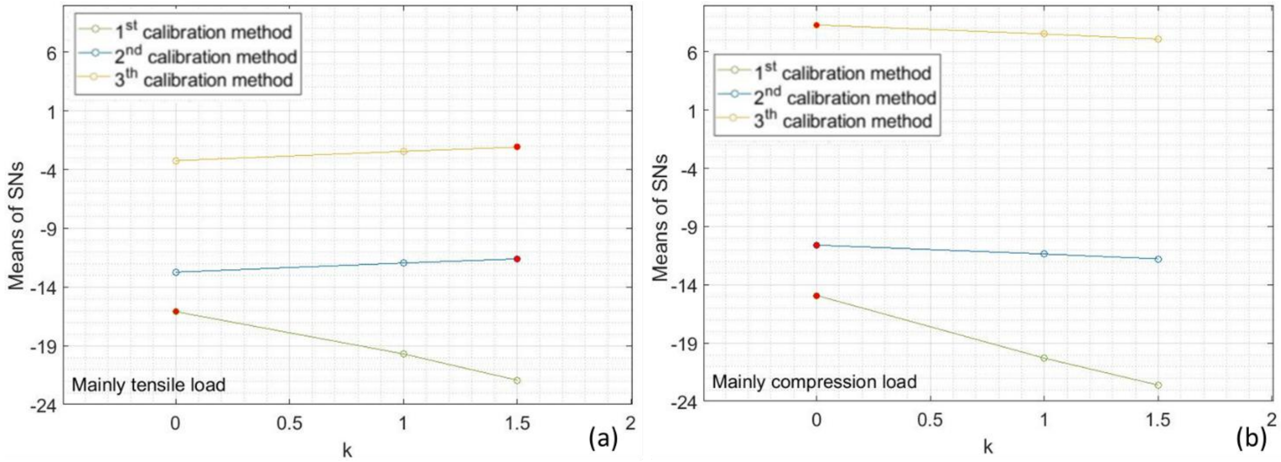

Figure 57 Means of SNs of the relative error for each value of the control factor k and each calibration method for (a) the mainly tensile and (b) the mainly compression loading case.

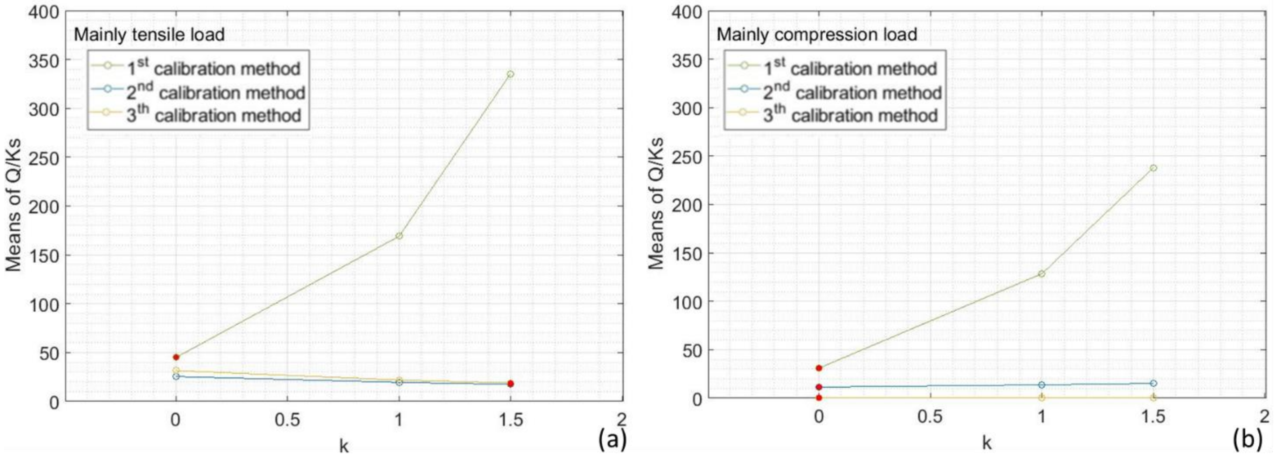

Figure 58 Means of Q/Ks of the relative error for each value of the control factor k and each calibration method for (a) the mainly tensile and (b) the mainly compression loading case.

The measurements with a mainly compressive load reported better measurement performance, however this result is influenced by the choice of an unbalanced simulation plane.

Under real stress measurement conditions, it is not possible to control the direction of the load, therefore it is important to provide only one optimal k value for a given calibration, regardless of the direction of the load.

For the first calibration method the optimal value is k=0, which corresponds to a better SN and a lower Q/K for each load condition. For the second and third calibration methods the best operating solution is to adopt the highest possible k value, since in the case of tensile this leads to a more significant improvement in performance than the increase that would occur with a null mean load in compression.

Consequently, the effect of the loading characteristics on the measurement error was investigated by evaluating the Means of SNs and Q/Ks for each of their values, considering all the tests of the plan with k=0 for the first calibration method and with k=1.5 for the second and third calibration methods.

The estimate statistical parameter for the relative error are reported in Table 21 (tensile case) and Table 22 (compression case). In Figure 59 and Figure 60 the Means of the SNs and Q/Ks are respectively plotted for each loading characteristic for both the considered cases.

The main variable affecting the measurement is the calibration method, whenever possible, the best option is always that of an experimental calibration on the same sample.

All three calibration methods do not show a strong variation in measurement performance with varying Δσ. In general, an increase of the amplitude of the load implies a higher signal and reduction of the relative error, however the direct interaction between Δσ and the source of errors leads to an inversion of the trend of the Means of SNs in the compression case for the second calibration method. Only the third calibration method shows an inversion in the trend of the SN (Figure 60) with respect to the Q/K with varying Δσ11. In this case, although the average error decreases with the Δσ11 modulus, improving the accuracy of the measurement, the standard deviation increases faster causing a reduction in precision.

All the calibration methods present an increase both in terms of SN and quality of the measurement in the case of equally biaxial condition. The factor γl affect both the second amplitude and mean load principal components and the resulting effect is a combination of the two. The third calibration method proves to be more sensitive to angle variations.

It appears that the measurement performance is improved in the case of monoaxial load tilted of 45°, but this is a consequence of the relative position respect to the residual stress system which varies between 0 and 90 °, thus the results show that the error is minimized how much the two systems are aligned.

Table 21 Tensile case. Means and Means of the Standard Deviations of the relative error for each value of the factors Δσ11, ϒl, φ and each calibration method when the optimal value of k is imposed.

		calib.1		calib.2		calib.3	
		Mean Error %	StDev	Mean Error %	StDev	Mean Error %	StDev
$\Delta\sigma_{11}$ [MPa]	-200	-0.921	6.460	-0.955	4.036	0.108	3.286
	-150	-0.921	6.452	-0.920	3.824	0.091	3.025
	-100	-0.921	6.449	-0.888	3.648	0.079	2.823
Υ_l	1	-0.697	8.120	-0.622	5.196	0.240	6.425
	1,5	-0.966	5.807	-0.996	3.400	0.038	2.538
	2	-1.101	5.434	-1.145	2.912	0.000	0.169
φ [°]	0	-1.101	6.896	-1.062	4.245	0.132	3.921
	45	-0.562	5.568	-0.639	3.016	0.014	1.292
	90	-1.101	6.896	-1.062	4.245	0.132	3.921

Table 22 Compression case. Means and Means of the Standard Deviations of the relative error for each value of the factors Δσ11, ϒl, φ and each calibration method when the optimal value of k is imposed.

		calib.1		calib.2		calib.3	
		Mean Error %	StDev	Mean Error %	StDev	Mean Error %	StDev
$\Delta\sigma_{11}$ [MPa]	-200	-1.125	5.455	-1.533	3.895	0.004	0.674
	-150	-1.125	5.455	-1.422	3.606	0.003	0.632
	-100	-1.125	5.457	-1.327	3.364	0.003	0.641
Υ_l	1	-1.101	5.433	-1.344	3.429	0.000	0.165
	1,5	-1.128	5.452	-1.423	3.592	0.003	0.655
	2	-1.146	5.482	-1.516	3.844	0.008	1.126
φ [°]	0	-1.101	5.462	-1.404	3.643	0.005	0.826
	45	-1.173	5.444	-1.476	3.578	0.001	0.293
	90	-1.101	5.462	-1.404	3.643	0.005	0.826

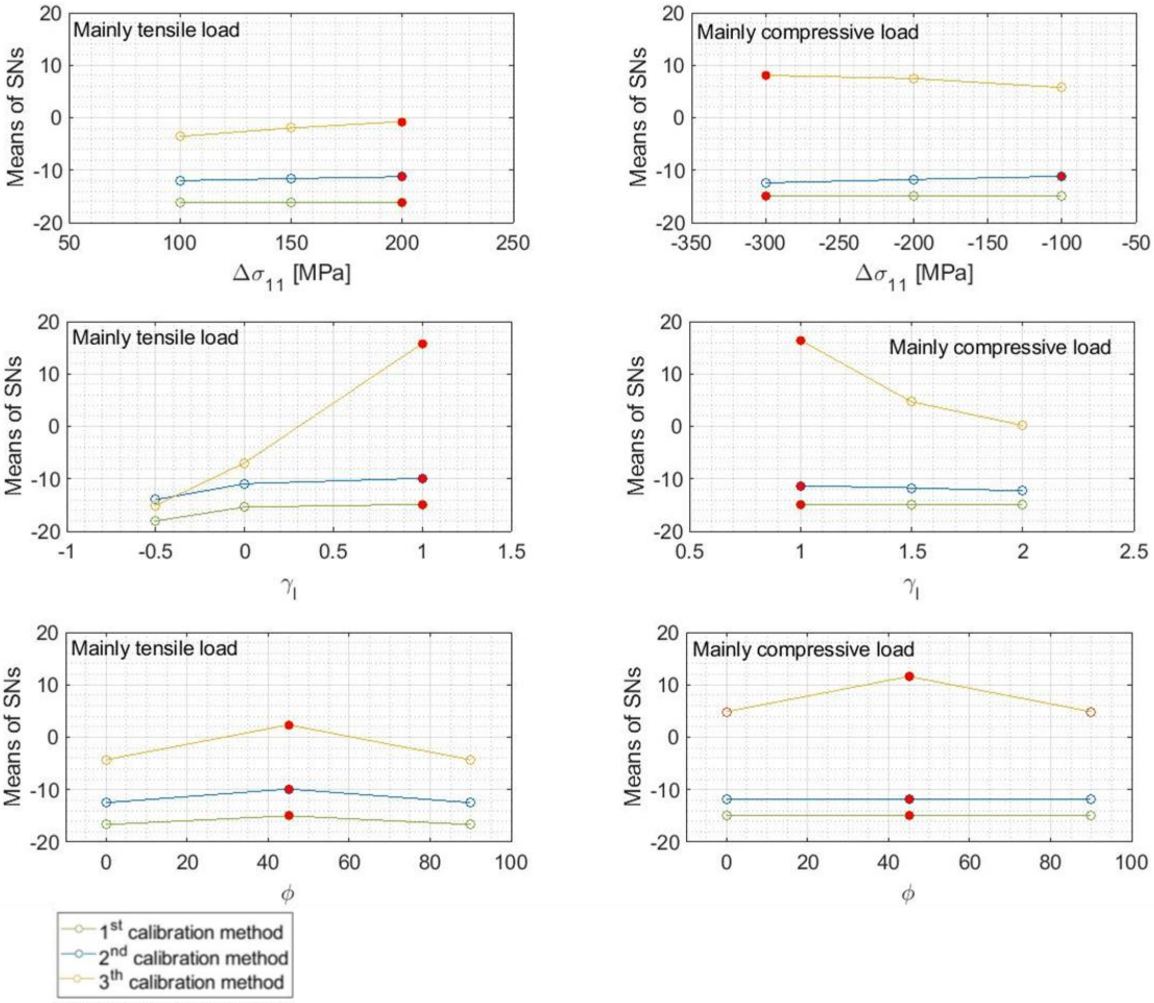

Figure 59 Means of SNs of the relative error for each value of the factors Δσ11, γl, φ and each calibration method when the optimal value of k is imposed.

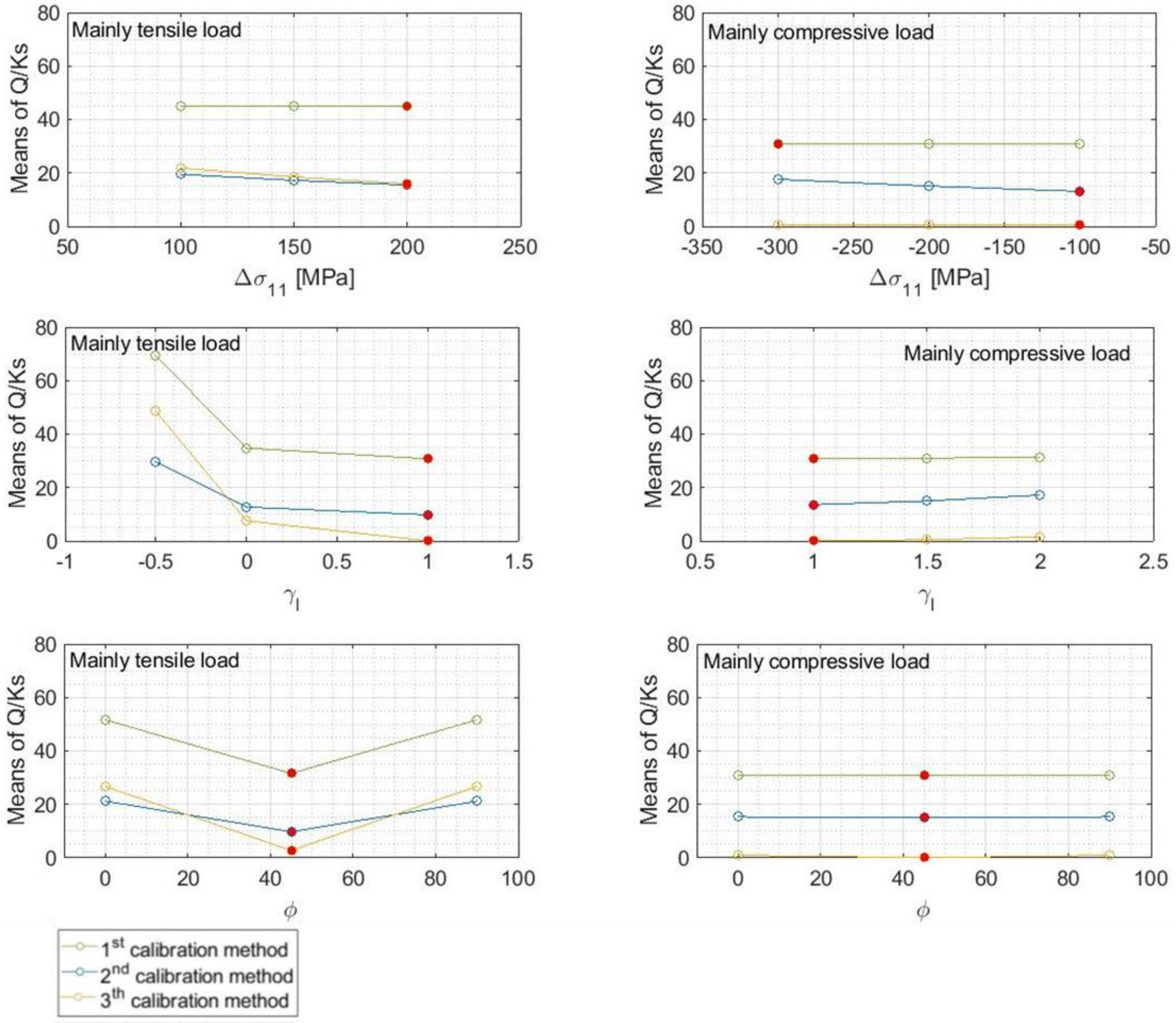

Figure 60 Means of Q/Ks of the relative error for each value of the the factors Δσ11, γl, φ and each calibration method when the optimal value of k is imposed.

The estimate statistical parameter for the relative error are reported first considering the full factorial plan (Table 23) and then considering only the tests with the value of k which showed better results from the previous analysis (Table 24).

The results give operative directions for TSA application.

It is always to avoid the use of a calibration constant evaluated with nominal values for the material characteristics; in this case the error has a mean of +6,78% ranging from -28,4% to +41,9% when the load is mainly tensile, and of -7,820% ranging from -33,2% to +17,5%. The measurement performances improve if a null mean load is adopted (k=0), bringing these ranges to -20.8% - +19% and -17,5 - +15,2% respectively.

In the case of tensile load, the second calibration method can guarantee an average error of -0,97%, ranging from -14.3% to 12,4%; in the same case, the third calibration method showed a Mean of error of +0,12% with a range from -14,6% to +14,8%. In compression the

Means of error for the two calibration methods became -1,3% and 0,003%, ranging respectively from -11,6% to 8,9% and from -2,3% to +2,3%.

If the best value of k is imposed, the performance improvement is less effective than it is in the first method, and the errors Means became respectively -0.9% (ranging from -13,1% to +11,3%) and -0,01% (ranging from -12,9% to +13,1%) in tensile load conditions and respectively -1,25% (ranging from -10,7% to +8,2%) and -0,003% (-2,1% and +2,1%) in compression.

It could seem that using the first and third method there is a strong difference in performance between the traction and compression case. However, it is due to the unbalance of the load's representation. In these two cases the main sources of error are more sensitive to the load direction. The choice to implement such a plan is related to the typical operative conditions; the results reflect these conditions and must be accordingly interpreted.

Table 23 Overall relative error statistics

	Mainly tensile load				Mainly compression load			
	Mean	**Std.Dev**	**Lower error**	**Higher error**	**Mean**	**Std.Dev**	**Lower error**	**Higher error**
$K_{0,1}$	6.778	11.713	-28.363	41,918	-6.146	7.003	-27.155	14.863
$K_{0,2}$	-0.973	4.449	-14.319	12,373	-1.316	3.337	-11.328	8.696
$K_{0,3}$	0.118	4.899	-14.580	14,816	0.003	0.745	-2.234	2.239

Table 24 best k - relative error statistics

	Mainly tensile load				Mainly compression load			
	Mean	**Std.Dev**	**Lower error**	**Higher error**	**Mean**	**Std.Dev**	**Lower error**	**Higher error**
$K_{0,1}$	-0.921	6.642	-20.847	19.004	-1.125	5.456	-17.494	15.244
$K_{0,2}$	-0.921	4.067	-13.123	11.281	-1.246	3.149	-10.694	8.203
$K_{0,3}$	0.093	4.329	-12.894	13.079	0.002	0.693	-2.077	2.082

5.2.10. Conclusions

In this work a statistical approach was applied to study the TSA measurement performance by implementing an analytical model.

The ANOVA and ANOM showed the effect that the various sources of error induce on the relations between the thermal signal and the parameters and their interactions.

The influence of each parameter is strictly connected to the ranges selected for the source of error and for the parameter itself. The study involved the implementation of ranges which reflect real operative conditions, and the results where the following:

- All the parameters induce a significative variation in the thermal response.
- The analytical model gives the exact relation between the parameters and the thermoelastic response but cannot give information about their effect on the measured signal which depends on all the noise factors.
- The error mean and the influence of the amplitude of residual stresses is higher in the compression case, characterized by more critical loading conditions and residual stress slightly unbalanced towards the same sign.
- The effect of the residual stress system orientation is lower in the compression case.

The Robust Design applied to the TSA stress measurement system lead the following results:

- The tests conditions which can guarantee the smallest error range (from -2,07% to +2,07%) includes:
- An experimental calibration with the sample in the same residual stress condition of the component/structure; this implies that the best practice is to use calibration samples extracted from the same component or to calibrate with the use of strain gauges on the component itself.
- A null mean load (R=-1) if the calibration is performed with the first method.
- A mean load as high as possible if the calibration is performed with the second or third method.
- The adoption of a calibration constant estimated with nominal values for the material characteristics implies an error that can range from the -28,4% to +41,9%, lowering at the interval -20.8% - +19% when the mean load effect is compensated

by adopting k=0. Thus, the general indication is to prefer an experimental calibration.

5.3. A Robust Design approach to develop a TSA residual stress measurement procedure on Ti6Al4V alloy

5.3.1. Introduction

In this work a novel TSA procedure to measure residual stresses is proposed.

The novel procedure is based on the realization of three measurements characterized by three different configurations for the set up. These conditions allow to write three equations using the TSA general model in three unknown values defining the residual stress system.

Aim of this work is to perform a Robust Design of the TSA measurement system by applying statistic on an analytical model also simulating the various types of errors that can be made on the process. The main result is the identification of the triad of loading characteristics which ensure the best performance in terms of quality and variance of the residual stress measurement.

5.3.2. Novel TSA procedure to measure residual stresses

The residual stress vector in the plane can be defined through three parameters, which are the principal components σ_{r11} and σ_{r22} and the angle θ between the reference system and the principal system. Residual stresses are identified once all these three characteristics are known.

The proposed procedure is based on the realization of three distinct measurements characterized by three different configurations for the loading system.

If the stress distribution and the material proprieties are known, it is possible to write three equations using the general model in three unknown values, defining the residual stress system.

The procedure can be summarized in the following steps:

1. Determination of the thermo-physical properties of the material and determination of the stiffness matrix.
2. Selection of three different load conditions for which the distribution of surface stresses in the component is known.

3. Carrying out TSA tests with the selected loads and acquisition of the thermoelastic signal with an IR camera.

4. Lock-in analysis and assessment of the three values of first harmonic amplitude ΔT and reference temperature T_0.

5. Solution of the system of three equations in three unknowns obtained by writing Eq. 10 in the three tasted cases.

5.3.3. residual stresses measurements: Problem Definition and workflow

The block diagram in Figure 61 describes the system of residual stress measurement with TSA based on the procedure described in the paragraph 5.3.2.

The control factor is the triad of setups, defined by the characteristics that identify the applied stress.

To represent and compact all the data, it is convenient to express both the applied stress vector and the residual stress vector in their principal components; in this case Eq 103 can be written as:

$$\begin{aligned}
&\rho c_{\varepsilon} {T_0}^{-1} \Delta T \\
&= \left[\left(\begin{pmatrix} C_{1111} & C_{1122} & C_{1112} \\ C_{2211} & C_{2222} & C_{2212} \\ C_{1211} & C_{1221} & C_{1212} \end{pmatrix}^{-1} \left(k \begin{bmatrix} cos^2\phi & sin^2\phi & 2cos\phi sin\phi \\ sin^2\phi & cos^2\phi & -2cos\phi sin\phi \\ -cos\phi sin\phi & cos\phi sin\phi & cos^2\phi - sin^2\phi \end{bmatrix} \begin{pmatrix} \Delta\sigma_{11} \\ \Delta\sigma_{22} \\ 0 \end{pmatrix} \right.\right.\right. \\
&\left.\left. + \begin{bmatrix} cos^2\theta & sin^2\theta & 2cos\theta sin\theta \\ sin^2\theta & cos^2\theta & -2cos\theta sin\theta \\ -cos\theta sin\theta & cos\theta sin\theta & cos^2\theta - sin^2\theta \end{bmatrix} \begin{pmatrix} \sigma_{r11} \\ \sigma_{r22} \\ 0 \end{pmatrix} \right)\right)^{T} \begin{pmatrix} \frac{\partial C_{1111}}{\partial T} & \frac{\partial C_{1122}}{\partial T} & \frac{\partial C_{1112}}{\partial T} \\ \frac{\partial C_{2211}}{\partial T} & \frac{\partial C_{2222}}{\partial T} & \frac{\partial C_{2212}}{\partial T} \\ \frac{\partial C_{1211}}{\partial T} & \frac{\partial C_{1221}}{\partial T} & \frac{\partial C_{1212}}{\partial T} \end{pmatrix}^{T} \qquad \text{Eq 128} \\
&\left. - \begin{pmatrix} \alpha_{xx} \\ \alpha_{yy} \\ \alpha_{yx} \end{pmatrix}^{T} \begin{pmatrix} C_{1111} & C_{1122} & C_{1112} \\ C_{2211} & C_{2222} & C_{2212} \\ C_{1211} & C_{1221} & C_{1212} \end{pmatrix}^{T} \right] \begin{pmatrix} C_{1111} & C_{1122} & C_{1112} \\ C_{2211} & C_{2222} & C_{2212} \\ C_{1211} & C_{1221} & C_{1212} \end{pmatrix}^{-1} \begin{bmatrix} cos^2\phi & sin^2\phi & 2cos\phi sin\phi \\ sin^2\phi & cos^2\phi & -2cos\phi sin\phi \\ -cos\phi sin\phi & cos\phi sin\phi & cos^2\phi - sin^2\phi \end{bmatrix} \begin{pmatrix} \Delta\sigma_{11} \\ \Delta\sigma_{22} \\ 0 \end{pmatrix}
\end{aligned}$$

Where $\Delta\sigma_{11}$ and $\Delta\sigma_{22}$ are the principal components of the amplitude of the load, $k = \frac{\sigma_{m11}}{\Delta\sigma_{11}} = \frac{\sigma_{m22}}{\Delta\sigma_{22}}$ is the ratio between the mean load and the and amplitude components, here considered constant in every direction of the amplitude tensor and φ is the angle between the principal loading system and the reference system.

The material characteristics have been considered known and fixed assuming their nominal values, so they are a signal factor.

The only noise factor considered is the IR camera noise. To simulate the IR camera noise, a white gaussian noise of 0.01 K (experimentally determined on a typical Camera with an integration time of 2500µs [18]) was added to the response evaluated with Eq 128.

For the classification of the residual surfactant vector, great attention must be paid. First, we need to distinguish the vector of the simulated residual stresses (i.e., the value introduced in Eq 128 in the system to be solved) from the vector obtained as the solution of the system. The first can be classified as signal factor, since it is a variable affecting the output that cannot be controlled; the second is the output of the system.

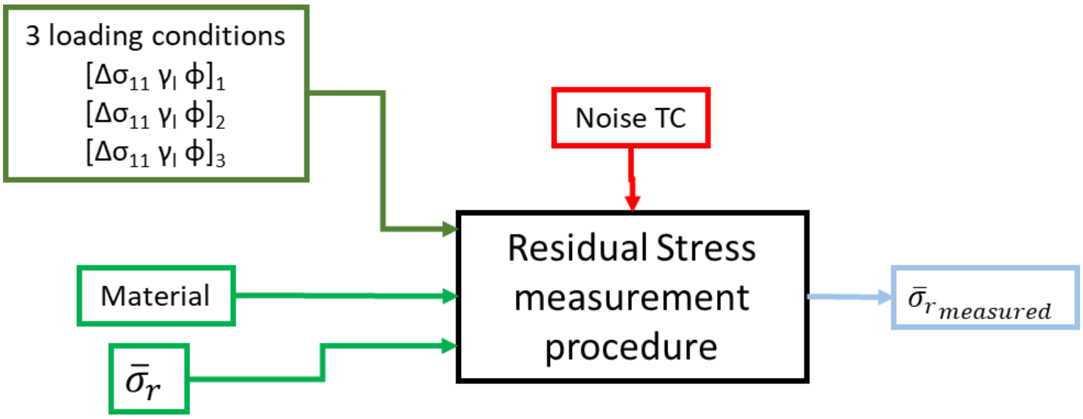

Figure 61 Block diagram of the TSA stress measurement system

In order to investigate the procedure performance in different residual stress conditions the analysis was repeated in 3 cases, identified by the ratio $\boldsymbol{\gamma_r} = \frac{\sigma_{r11}}{\sigma_{r22}}$: traction-traction, traction-compression and compression-compression. For each case every combination of 3 values of σ_{r11} and 3 values of θ were studied (Table 25, Table 26 and Table 27):

Table 25 Simulated residual stress characteristics for the tractio-traction case

TRACTION-TRACTION, γ_r=0.5			
σ_{r11} [MPa]	100	-	300
θ	0	45	90

Table 26 Simulated residual stress characteristics for the tractio-compression case

TRACTION-COMPRESSION, γ_r=-1.5			
σ_{r11} [MPa]	100	-	300
θ	0	45	90

Table 27 Simulated residual stress characteristics for the compression-compression case

COMPRESSION-COMPRESSION, γ_r=1.5			
σ_{r11} [MPa]	-100	-	-300
θ	0	45	90

The study was conducted considering the physical and mechanical characteristics of the alloy Ti6Al4V, whose thermoelastic behaviour is affected by the second order effect.
The material characteristics and their variability range were set based on literature values .
The amplitude and the mean load were selected considering the mechanical characteristics of material and the yield strength in order to ensure the linear elastic conditions.
The residual stress vectors were selected considering both literature typical values and preliminary results from the analytical study of the thermoelastic behaviour of the Ti6Al4V alloy.

The first simulation plan was built considering 6 different setups, each setup is described by a triad of parameters defining the loading conditions. The selection of the values for the loading characteristics is based on the following considerations:

- The ANOVA results show that main parameters affecting the thermal response are $\Delta\sigma_{11}$, φ and K (paragraph 5.2);
- The mono-axial loading can be easily reproduced with loading machines and standard dog bone sample.
- To avoid buckling it must be applied a sinusoidal load whit $\sigma m > \Delta\sigma_{11}$

In Table 28 the configurations of the 6 setups are reported.

Table 28 Configurations of the 6 setups of the first simulation plan

setup	$\Delta\sigma_{11}$ [MPa]	φ
1	100	45
	200	45
	300	45
2	200	0
	100	0
	200	45
3	200	0
	200	45
	200	90
4	100	0
	200	0
	300	45
5	100	0
	100	45
	300	90
6	100	0
	200	45
	300	90

The simulation steps are shown in Figure 62; for each residual stress condition and for each triad of setup configuration 3 value of $\Delta T_{measured}$ were obtained following the steps described in paragraph 5.3.2.

The $\Delta T_{measured,i}$ are used as input to the system of 3 equations (Eq 128) where the unknow values are the 3 characteristics of the residual stress system. Once solved the system gives the $[\sigma_{r11}, \gamma_r, \theta]_{measured}$, the results were then compared with the [σr11, γr, θ]imposed. The problem is nominal the best type and the signal to noise ratio and the quality loss function were calculated for each residual stress condition and each of the 6 setups as:

$$SN_{kj} = 10 \cdot log \frac{\mu_{kj}{}^2}{\boldsymbol{S}_{kj}{}^2} \qquad \text{Eq 129}$$

$$\frac{Q_{kj}}{K} = \left(\mu_{kj} - y_{k,nominal}\right)^2 + \boldsymbol{S}_{kj}{}^2 \qquad \text{Eq 130}$$

Where the subscript *k* and *j* indicates respectively the residual stress characteristic (σ_{r11}, γ_r and θ) and the *j-esim* triad defining the setup and. $y_{k,nominal}$ is the nominal value for the *k*- residual stress characteristic.

μ_{kj} and $\boldsymbol{S}_{kj}{}^2$ are the estimated mean and variance of the 5 repetitions.

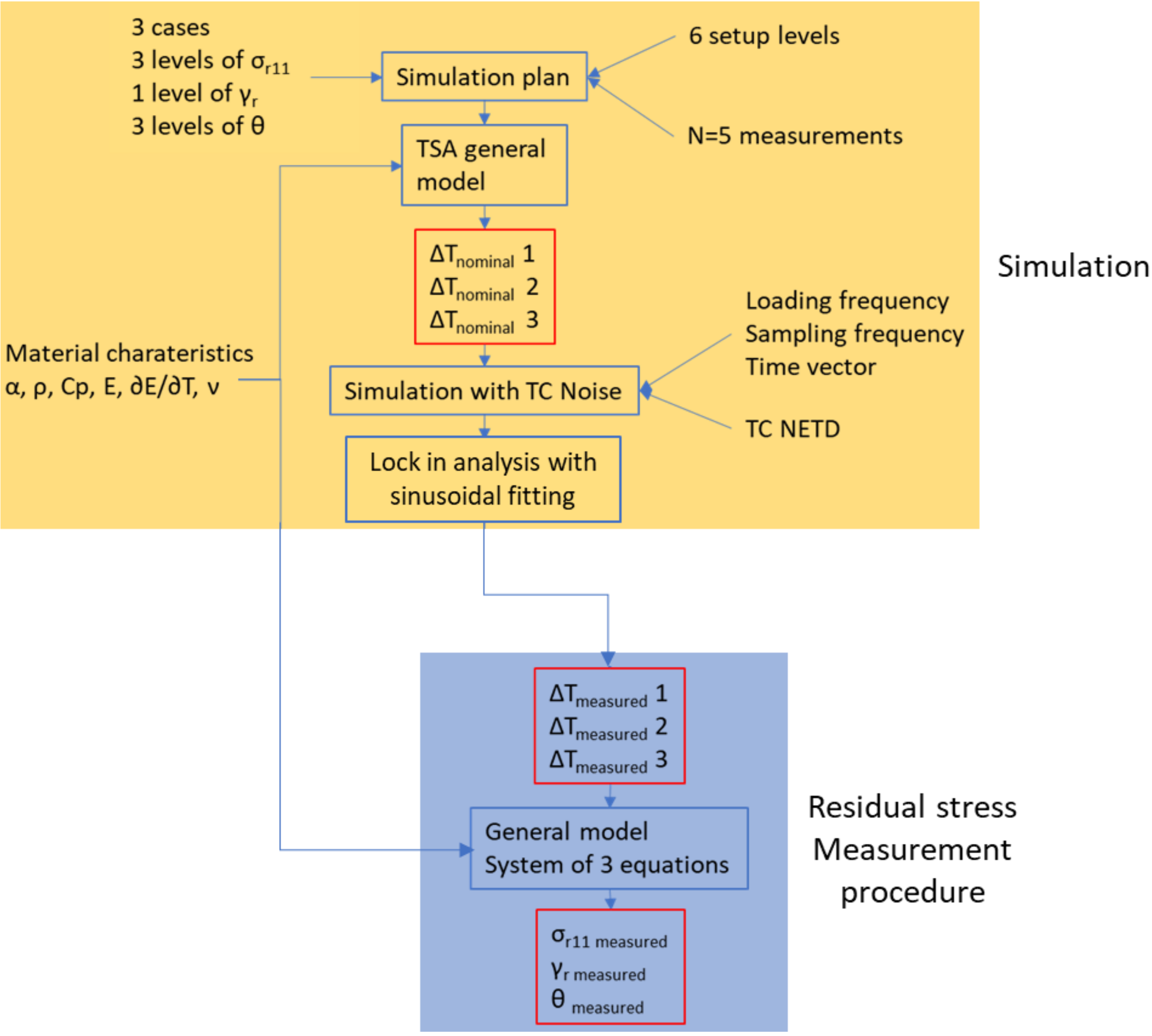

Figure 62 Simulation and residual stress measurement steps

The first simulation plan results gave a base to identify which are the triads of setup for which the system can be solved. A second simulation plan was then designed and simulated considering only the most promising triads and by varying just the amplitude of the load.

5.3.4. Residual stresses measurements: results and discussion

The results from the first simulation plane demonstrated the same trend for all the residual stress conditions.

From Figure 63 to Figure 65 the results are reported for each measured characteristic in term of the mean, the standard deviation, the signal to noise ratio, and the quality loss function. All figures show both the case with high residual stress module ($|\sigma_{r11}|$=300 MPa) and the case with low high residual stress module ($|\sigma_{r11}|$=100 MPa).

The main result is that the system of 3 equations can be solved only if the 3 triads are characterized by 3 different angles φ.

The simulation showed how the variation of the residual stress system orientation affects the quality of the measurement, but the effect differs for each of the 3 residual stress characteristics. Thus, an angle θ=45° implies a better measurement of θ but a worse evaluation of the ratio Υ_r.

The best results are obtained when the residual stresses components are opposite in sign (traction-compression case)

To further investigate the influence of the triad of set up on the measurement performances, a second analysis was carried out, comparing only triads with different angles and by varying the amplitude of the stress imposed. The simplifying hypotheses of the application of mono-axial tensile stress and unitary k ratio were maintained in this case also.

The stress amplitude triples have been made to vary considering three different levels (100, 180 and 225 MPa) and all the possible combinations, obtaining 9 different configurations (Table 29).

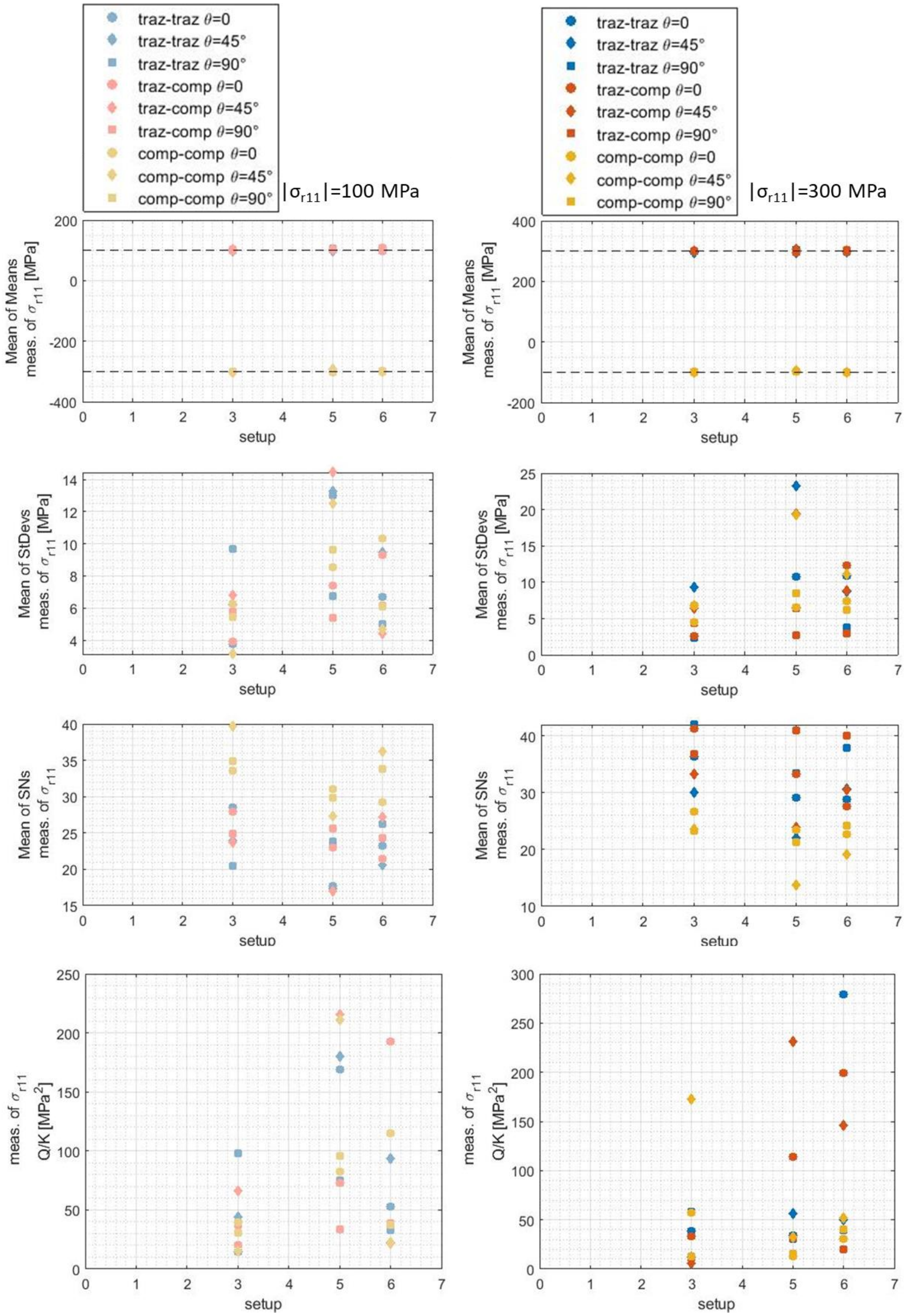

Figure 63 First simulation plan results for σ_{r11} measurement in term of mean, standard deviation, signal to noise ratio, and quality loss function.

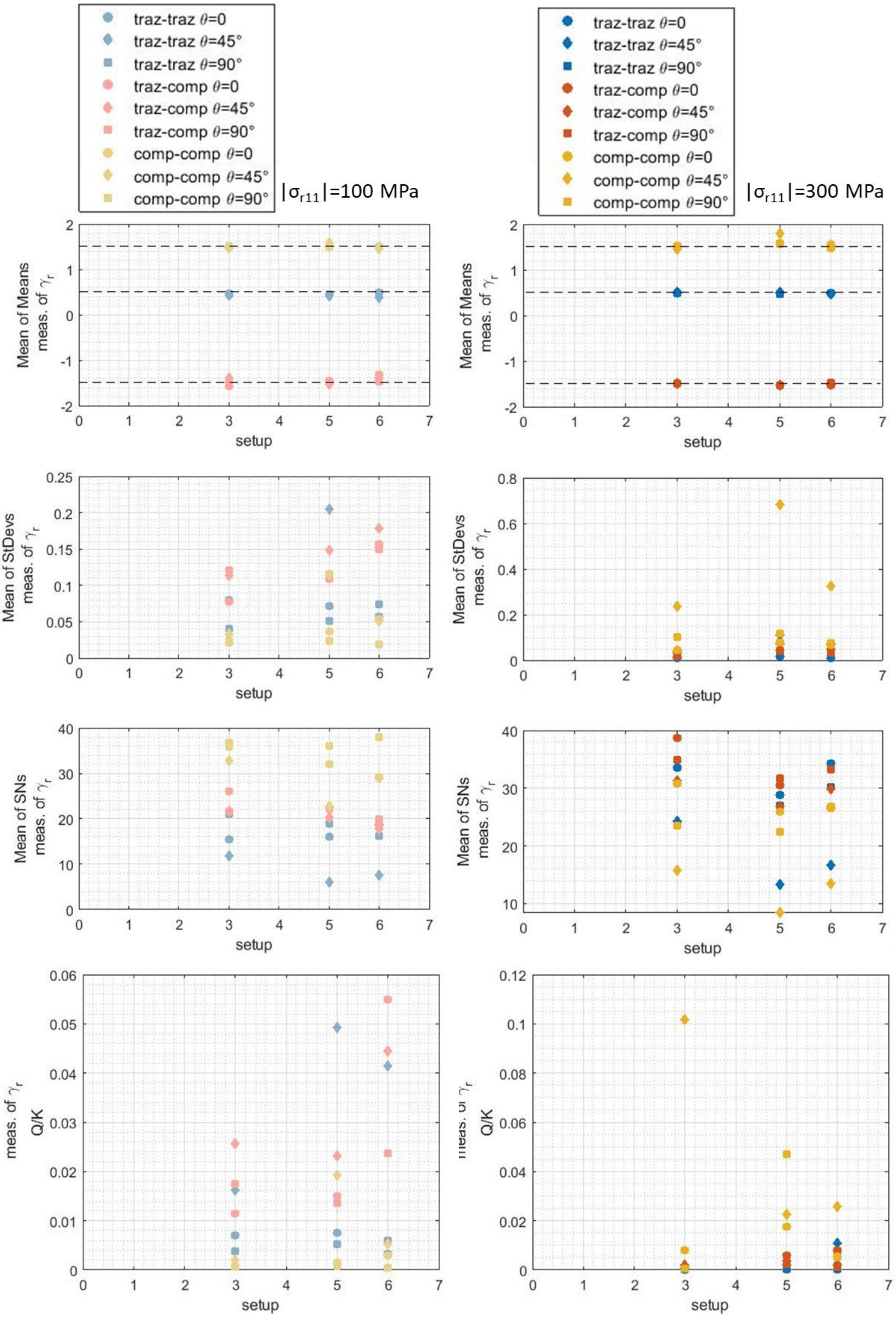

Figure 64 First simulation plan results for γ_r measurement in term of mean, standard deviation, signal to noise ratio, and quality loss function.

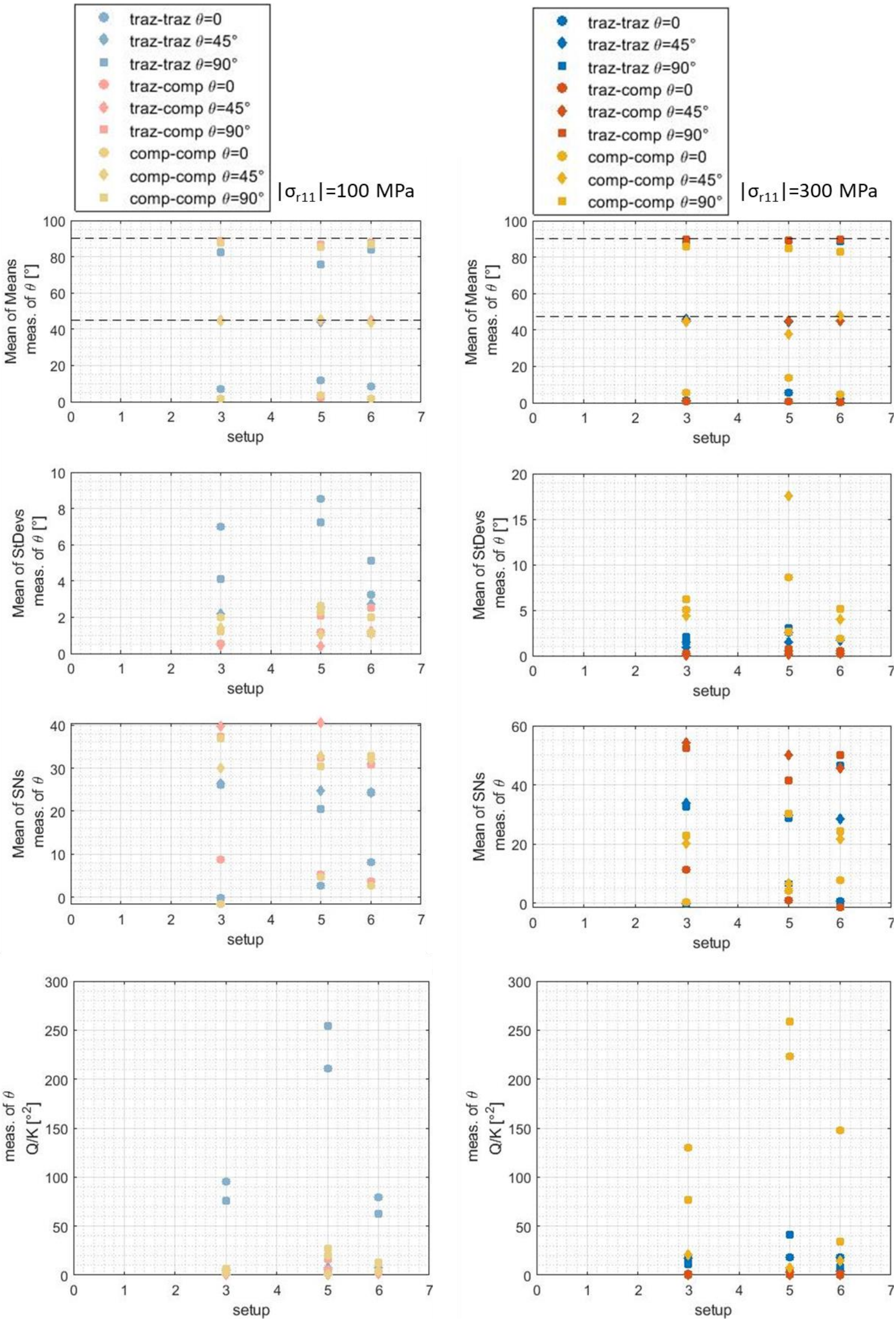

Figure 65 First simulation plan results for θ measurement in term of mean, standard deviation, signal to noise ratio, and quality loss function.

Table 29 second simulation plan. All the triad of set up variables are characterized by a monoaxial amplitude of the stress, a constant ratio between mean stress and amplitude of the stress, and three distinct values of the angle.

setup	$\Delta\sigma_{11}$ [MPa]	φ
1	100	0
	100	45
	100	90
2	100	0
	100	45
	180	90
3	100	0
	180	45
	180	90
4	100	0
	100	45
	125	90
5	100	0
	225	45
	225	90
6	180	0
	180	45
	180	90
7	180	0
	180	45
	225	90
8	180	0
	225	45
	225	90
9	225	0
	225	45
	225	90

From Figure 66 to Figure 68 the results obtained from the second simulation plan are reported.

For all the configurations of residual stresses and set-up triples, as the applied stress increases, the standard deviation is reduced, the SN ratio increases, and the Q decreases.

The sensitivity to this effect differs with which of the three vector characteristics and residual stresses is measured (σ_{r11}, γ_r and θ).

In the traction-traction and traction -compression cases the measurement of σ_{r11} shows better precision (high SN values) when its absolute value is higher, while in the compression-compression residual stress condition the trend is opposite Figure 66. This effect is more pronounced in the low residual stress case.

The measurement of the ratio γ_r shows a similar behaviour Figure 67. In this case the Q also demonstrates a greater sensitivity to the characteristics of residual stresses: at low stresses imposed greater accuracy (lower Q) is obtained in the case of compression-compression, while at high stresses imposed the best results are obtained in the other two cases.

The angle θ measurement is the one that provides the least compact data Figure 68. In any configuration, the worst measure is in the case of $\theta = 0$. The case of traction-compression always gives the best results, and the measurement is not affected by the set-up triplet or by the entity of the residual stresses.

On the contrary, in the traction-traction case the increase of the residual stress modulus improves the SN ratio and higher modulus of the imposed stresses improve the Q; this is more evident in the case of low residual stresses.

The compression-compression case presents a completely opposite trend: high residual stresses determine a worsening of SN and, always confirming the improvement trend of the Q as the imposed stress increases, this is more marked in the case of high residual stress.

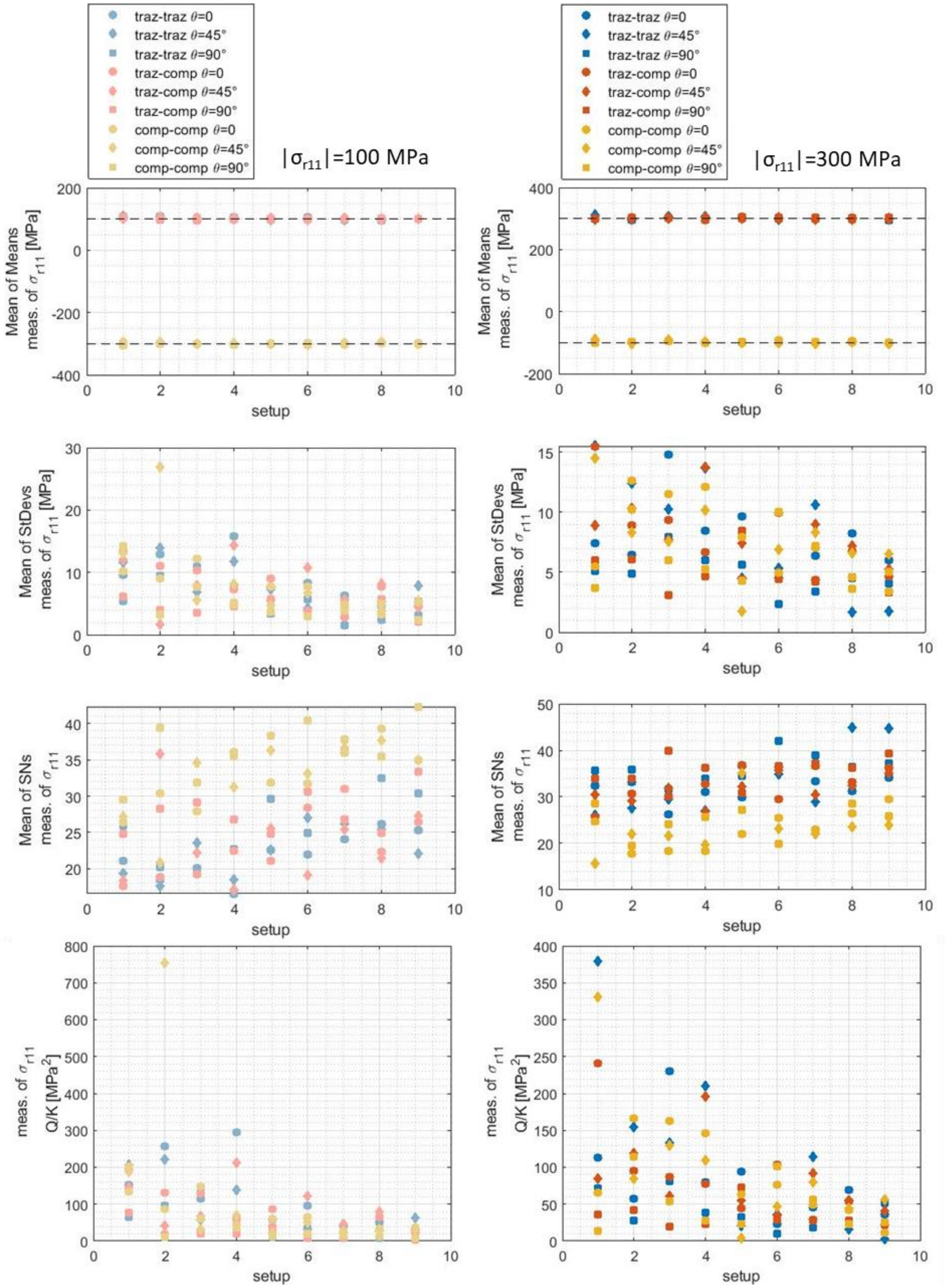

Figure 66 Second simulation plan results for σr11 measurement in term of mean, standard deviation, signal to noise ratio, and quality loss function.

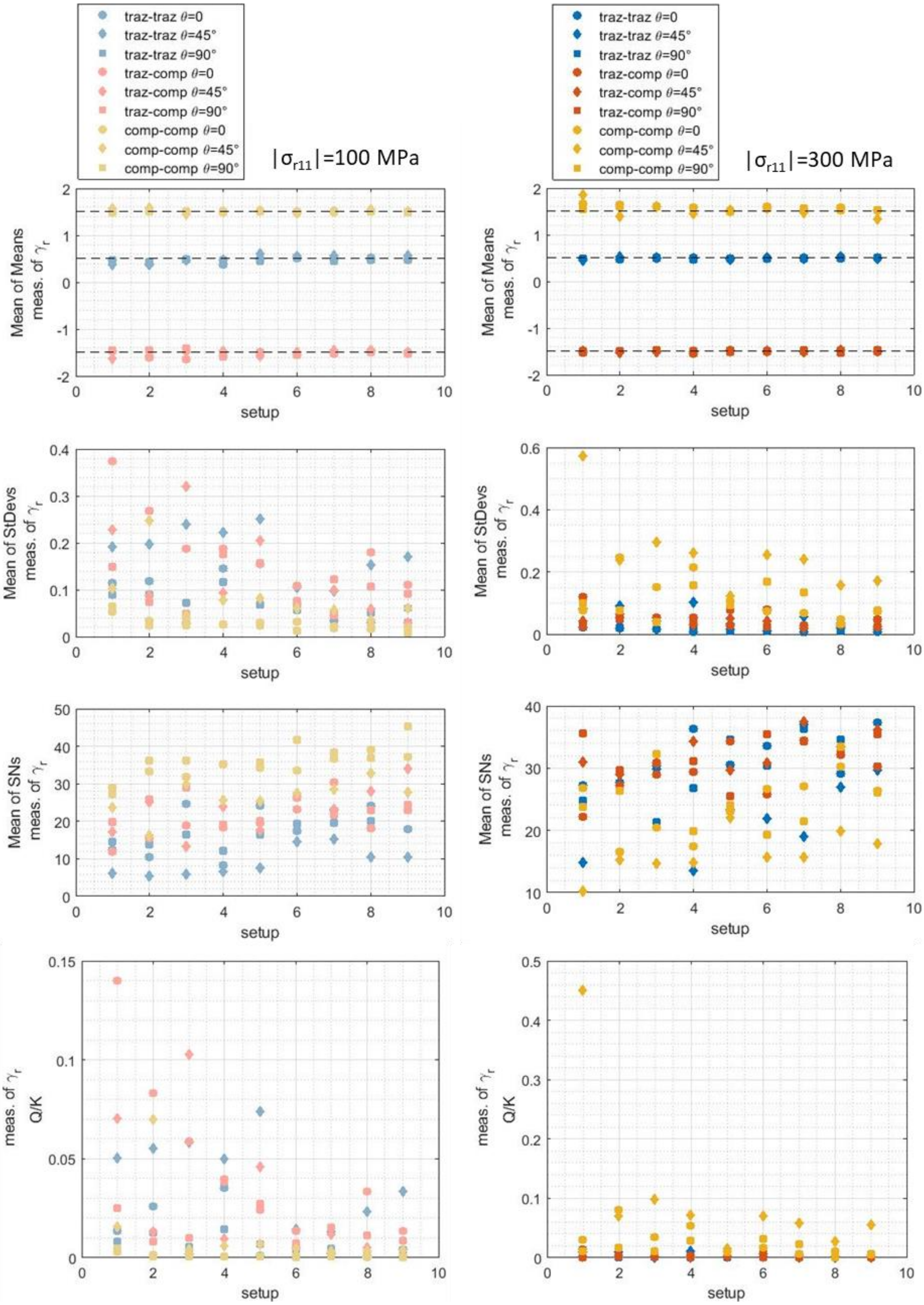

Figure 67 Second simulation plan results for γ_r measurement in term of mean, standard deviation, signal to noise ratio, and quality loss function.

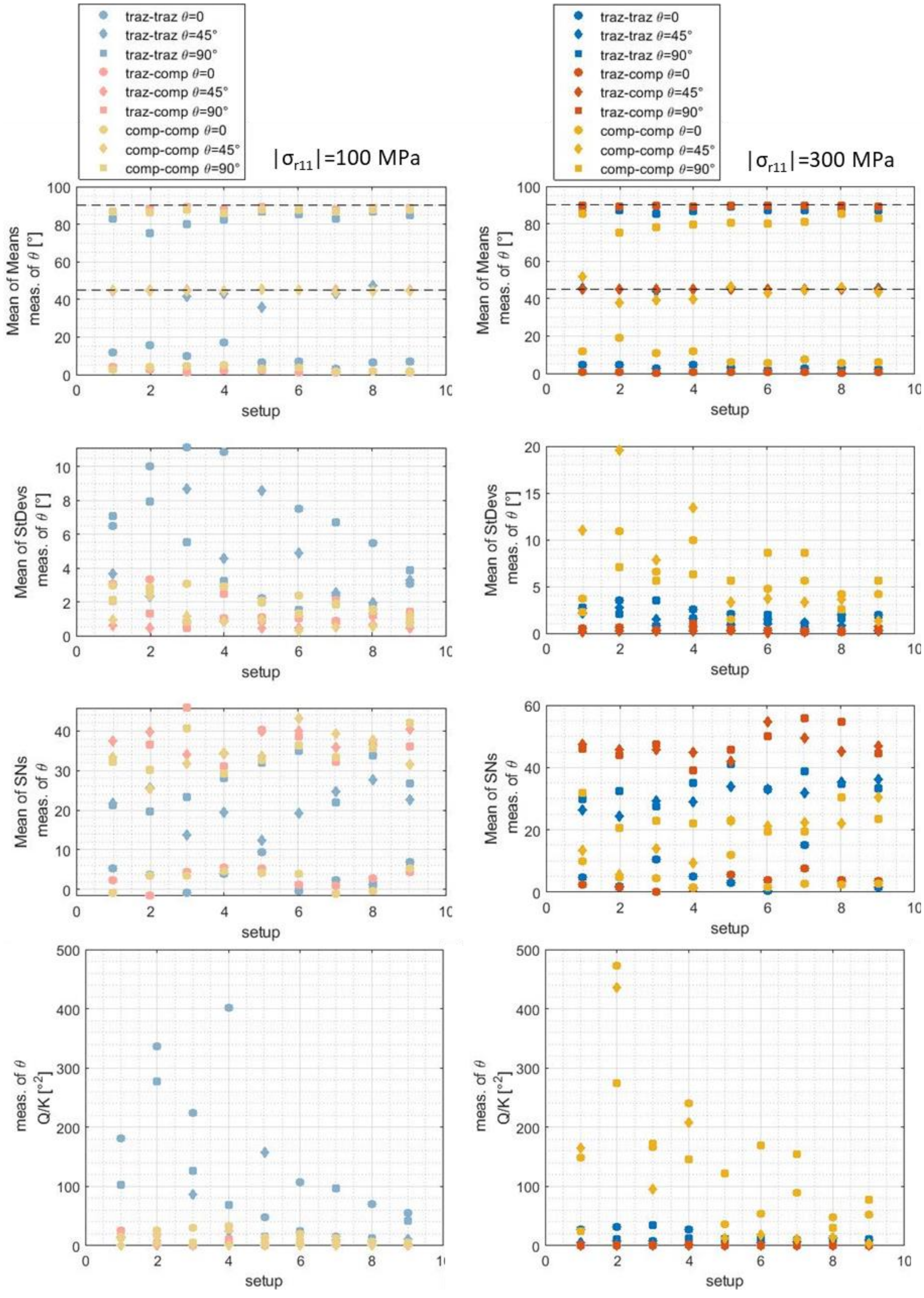

Figure 68 Second simulation plan results for θ measurement in term of mean, standard deviation, signal to noise ratio, and quality loss function.

5.3.5. Conclusions and future work

In this work a novel procedure to measure residual stress by means of TSA was proposed.

The procedure is based on TSA general equation and for the first time it presents the capability to measure generally oriented and bi-axial residual stress by means of TSA.

The residual stress vector in the plan can be identified by three characteristics, which are the first principal component, the ratio between the two principal component and the angle between the residual stress principal system and the reference system.

The proposed method is based on the TSA measurement in three distinct loading conditions. If the material proprieties and the stress distribution are known a system of three TSA general equations and three variables can be written and solved, obtaining the three characteristics of the residual stress vector.

The study presented is an application of statistic to the analytical modelling of the system. The process of TSA measurement was simulated also considering the TC Noise in such a way to perform a robust design-like study aiming at the residual stress measurement procedure optimization.

The following results were obtained:

- The system of three equations can be solved only if the three loading conditions are characterized by three different angles between the applied stress and the sample reference system.
- The measurement accuracy and precision are affected both by the loading conditions and the residual stress being measured.
- With the same residual stress, an increase in the modules of the applied stress determines an improvement in performance.
- High residual stress improves the measurement in the cases of residual stress principal components of traction-traction and traction-compression.
- Low residual stress improves the measurement in the cases of residual stress principal components of compression-compression.

The work here presented demonstrates the potential of TSA in residual stress assessment. The optimization study allowed to define the best practice in order to obtain a measurement that is as precise and accurate as possible.

The present research is an on-going activity, and the work is continuing with the experimental application of what has been simulated to obtain validation of the results obtained.

CHAPTER 6.

EXPERIMENTAL STUDY OF NOVEL FRACTURE MECHANICS CHARACTERIZATION PROCEDURES

This chapter collects the research activity conducted on the application of thermal method in the field of method fracture mechanics. All the activities were carried out with the collaboration of the Departamento de Ingeniería Mecánica y Minera of the Universidad de Jaén.

In paragraph 2.3.6 state of the art and potential of the TSA in the materials fracture characterization were described. Starting from those assumptions, the research activity was articulated according to two different strands, which are the determination of the SIF and the identification of the plastic zone around the crack tip.

In particular, the work described in paragraph 6.1 proposes and experimentally validate a new formulation for evaluating the SIF, mode I, by using TSA on components in materials characterized by a not-negligible second order effect, such as Titanium and Aluminium.

Paragraph 6.2 reports the experimental study carried out on the parameters which characterize the thermal response of a cracked Titanium CT samples under a cyclic load at different frequencies. The analysis of the dissipation phenomena involved in the material plasticization in the area ahead the crack tip allowed to relate these parameters to the plastic zone extension.

6.1. Influence of the Second order effects on the Thermoelastic behaviour in proximity of crack tips on Titanium

6.1.1. Introduction

The aim of this work is to identify the plastic zone around the crack tip by means full-field experimental methods such as DIC and Thermal Signal Analysis. In particular the thermal footprint was compared with shape and size of the plastic zone predicted through the application of DIC in combination with two theoretical models: Westergaard's model for the stress distribution around the crack tip and the more recent Christopher-James-Patterson (CJP) model.

Starting from the revised TSA theory, the TSA equation has been developed by describing the stress state, in terms of principal stresses, at the crack tip by means of different theoretical model: Westergaard equation, Williams series expansion truncated at the second term and Williams series expansion truncated at the third term. The equations obtained are valid only in the SIF-dominance zone and express the distribution of the first harmonic amplitude ΔT1 around the crack tip as a function of the SIF and the polar coordinates of the point respect to the crack tip. Such the equations where employed to fit experimental data from TSA dynamical test on Titanium CT samples for two different value of the loading ratio R (0.1 and 0.5).The fitting was performed by applying the Over deterministic method on a mesh of point around the crack tip, and the optimized variable were the specific model parameters and the crack tip position.

6.1.2. The proposed approach: a new formulation for describing the thermoelastic effect in proximity of crack tip

In this section, a new equation will be obtained to describe the thermoelastic behaviour of materials in the presence of a crack.

In a similar way to the works of Patterson et al. [47], Palumbo et al. [25] and Di Carolo et al. [18], two material constants can be defined as reported in Eq 57.

By considering the plane stress conditions, substituting Eq 57 in Eq 54 and neglecting the variations of the Poisson's ratio with the temperature [51][150], we obtain:

$$\frac{\dot{T}}{T} = -[a + \upsilon b(\Delta\sigma_1 + \Delta\sigma_2)](\sigma_1 \dot{+} \sigma_2) + (b + \upsilon b)\left(\Delta\sigma_1 \Delta\dot{\sigma_1} + \Delta\sigma_2 \Delta\dot{\sigma_2}\right) \qquad \text{Eq 131}$$

Under a generic sinusoidal loading in which the load changes between its maximum and minimum values, P_{min} and P_{max}, the loading ratio R can be defined as:

$$R = \frac{P_{min}}{P_{max}} = \frac{\sigma_{i,min}}{\sigma_{i,max}}, \qquad \sigma_{mi} = \Delta\sigma_i \frac{1+R}{1-R} = \Delta\sigma_i R_f \qquad \text{with } i = 1{,}2 \qquad \text{Eq 132}$$

Thus, under a generic sinusoidal loading, the principal stresses and their rate of change are:

$$\sigma_1 = \Delta\sigma_1(R_f + \sin\omega t), \qquad \sigma_2 = \Delta\sigma_2(R_f + \sin\omega t) \qquad \text{Eq 133}$$

$$\dot{\sigma_1} = \Delta\sigma_1\omega\cos\omega t, \qquad \dot{\sigma_2} = \Delta\sigma_2\omega\cos\omega t \qquad \text{Eq 134}$$

Substituting Eq 132, Eq 133 and Eq 134 into Eq 131 gives:

$$\begin{aligned}\frac{\dot{T}}{T} = -\big[a + vb(\Delta\sigma_1 + \Delta\sigma_2)(R_f + \sin\omega t)\big](\Delta\sigma_1 + \Delta\sigma_2)\omega\cos\omega t \\ + (b + vb)\big(\Delta{\sigma_1}^2 + \Delta{\sigma_2}^2\big)(R_f + \sin\omega t)\omega\cos\omega t\end{aligned} \qquad \text{Eq 135}$$

After few simple mathematical steps, Eq 135 can be written as:

$$\begin{aligned}\frac{\dot{T}}{T} = \big[-a(\Delta\sigma_1 + \Delta\sigma_2) + bR_f\big(-2v\Delta\sigma_1\Delta\sigma_2 + \Delta{\sigma_1}^2 + \Delta{\sigma_2}^2\big)\big]\omega\, cos\,\omega t \\ + \big[b(1+2v)\big(\Delta{\sigma_1}^2 + \Delta{\sigma_2}^2\big) + +2vb\Delta\sigma_1\Delta\sigma_2\big]\omega\, sin\,\omega t\, cos\,\omega t\end{aligned} \qquad \text{Eq 136}$$

Integrating Eq 136, considering $\Delta T << T_0$ and neglecting the static components, the general expression of the thermoelastic signal in proximity of the crack is:

$$\frac{\Delta T\ (t)}{T_0} = g_1\sin\omega t + g_2\cos 2\omega t \qquad \text{Eq 137}$$

where:

$$g_1 = \big[-a(\Delta\sigma_1 + \Delta\sigma_2) + bR_f\big(-2v\Delta\sigma_1\Delta\sigma_2 + \Delta{\sigma_1}^2 + \Delta{\sigma_2}^2\big)\big] \qquad \text{Eq 138}$$

$$g_2 = -\frac{1}{2}\big[b(1+2v)\big(\Delta{\sigma_1}^2 + \Delta{\sigma_2}^2\big) + 2vb\Delta\sigma_1\Delta\sigma_2\big] \qquad \text{Eq 139}$$

It is important to highlight that the mean stresses in Eq 131 could include the presence of residual stresses. As it is shown in the work [18], residual stresses affect the thermoelastic signal and then can significantly affect the SIF evaluation. In this work, residual stress-free samples were employed, therefore residual stress was not included in the model.

Another important issue is represented by the plastic zone at the crack tip. It is well known that the stress values are limited by the yield stress of the material and then by the plastic behaviour that generates a stress redistribution around the crack tip. However, it is important to highlight that the aim of this work is to investigate the effect of the mean stress and how second-order terms change the thermoelastic equation in the proximity of the crack in the new formulation. The effect of the plastic zone in TSA application has been extensively treated in literature by several authors in many works [24][63][151][152][153] and, in this regard, methods and procedures based on the classical TSA equation (and its validity hypothesis), used for describing the stress state at the crack tip in presence of the plastic area, can be extended in the same way to the new proposed formulation. In the present research it is not in the aim of the authors to make any speculation on plastic zone and its extension.

In presence of a crack in a flat plate, the state of the stress is characterized by two SIFs values, mode I and mode II, respectively, K_I and K_{II}. In this regard several theoretical models have been developed and they can be employed to describe the state of stress around the crack. In this work two models where considered: Westergaard equations [154] and Williams series expansion [59] truncated at the third term.

6.1.3. Derivation of TSA temperature variation using Westergaard solution

Westergaard equations [154] can be used to describe the state of stress around the crack in polar coordinates, as it is shown in Figure 69 and Eq 140.

It is important to highlight that Equation (17) includes the *T-stress* [63] for the stress σ_x. Its omission can lead to an error in SIF evaluation that can be difficult to quantify since the T-stress may vary significantly with varying structure geometries and loadings [62], [63].

$$\begin{pmatrix}\sigma_x\\ \sigma_y\\ \tau_{xy}\end{pmatrix}=\frac{K_I}{\sqrt{2\pi r}}\cos\frac{\theta}{2}\begin{bmatrix}1-\sin\frac{\theta}{2}\sin\frac{3\theta}{2}\\ 1+\sin\frac{\theta}{2}\sin\frac{3\theta}{2}\\ \sin\frac{\theta}{2}\cos\frac{3\theta}{2}\end{bmatrix}+\frac{K_{II}}{\sqrt{2\pi r}}\begin{bmatrix}-\sin\frac{\theta}{2}\left(2+\cos\frac{\theta}{2}\cos\frac{3\theta}{2}\right)\\ \sin\frac{\theta}{2}\cos\frac{\theta}{2}\cos\frac{3\theta}{2}\\ \cos\frac{\theta}{2}\left(1-\sin\frac{\theta}{2}\sin\frac{3\theta}{2}\right)\end{bmatrix}+\begin{bmatrix}\sigma_{0x}\\ 0\\ 0\end{bmatrix} \qquad \text{Eq 140}$$

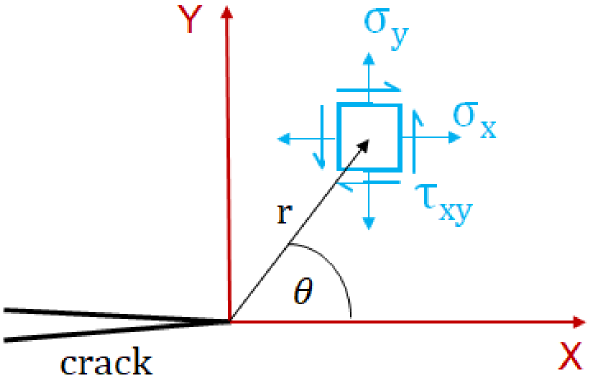

Figure 69 Polar coordinates used to describe the stress state around the crack tip.

The principal stresses σ_1 and σ_2, can be obtained by applying Eq 141:

$$\sigma_1,\sigma_2=\frac{\sigma_x+\sigma_y}{2}\pm\sqrt{\left(\frac{\sigma_x-\sigma_y}{2}\right)^2+\tau_{xy}^2} \qquad \text{Eq 141}$$

Considering the only mode I of loading, and expressing the stress component into Eq 138 and Eq 139 by Westergaard Equations (Eq 140) after few mathematical steps gives:

$$\begin{aligned}g_1=&-a\left(\frac{2K_{Ia}}{\sqrt{2\pi r}}\cos\frac{\theta}{2}+\sigma_{0x}\right)\\ &+bR_f\left\{\frac{K_{Ia}^2}{4\pi r}\left[2(1-v)(\cos\theta+1)+(1+v)\sin^2\theta\right]\right.\\ &\left.+\frac{\sigma_{0x}K_{Ia}}{2\sqrt{2\pi r}}\left[(3-5v)cos\frac{\theta}{2}+(1+v)cos\frac{5\theta}{2}\right]+{\sigma_{0x}}^2\right\}\end{aligned} \qquad \text{Eq 142}$$

and

$$\begin{aligned} g_2 = -\frac{1}{2} b \Bigg\{ & \frac{{K_{Ia}}^2}{2\pi r}\left[(1+3\nu)\,cos\,\theta - \frac{(1+\nu)}{4} cos(2\theta) + \frac{1}{4}(5+13\nu)\right] \\ & + \frac{K_{Ia}\sqrt{2}}{\sqrt{\pi}}\frac{T_s}{4\sqrt{r}}\left(\left((3+11\nu)\,cos\left(\frac{\theta}{2}\right) + (1+\nu)\,cos\left(\frac{5}{2}\cdot\theta\right)\right)\right) \\ & + {\sigma_{0x}}^2(2\nu+1)\Bigg\} \end{aligned} \qquad \text{Eq 143}$$

Eq 142 and Eq 143 show as the thermoelastic signal also presents terms in which the order of singularity is 1 induced by the presence of the mean stress, as already noted by Jones et al. [155].

By setting *b=0*, from Eq 137 and Eq 142 it can obtain the classical solution used for relating the thermoelastic signal and K_{Ia}:

$$\Delta T_{nc}(t) = -T_0\left(\frac{2aK_{Ia}}{\sqrt{2\pi r}}\cos\frac{\theta}{2} + \sigma_{0x}\right)\sin\omega t \qquad \text{Eq 144}$$

where ΔT_{nc} stands for the non-correct value of ΔT.

Comparing Eq 137 and Eq 142 with Eq 144, it is worth to notice that the thermoelastic temperature variation ΔT depends also on the stress ratio *R* and on the material constants *b* and υ. This means that an error in ΔT evaluation and then in SIF evaluation can be made in using Eq 144 instead of Eq 142.

6.1.4. Derivation of TSA temperature variation by using Williams series expansion

In this subsection the Williams series expansion truncated to the third term was combined with the TSA second order equation to obtain the new formulation.

Considering a polar coordinates system with its centre at the crack tip, the first three terms of the Williams' series expansion describing the elastic stress field surrounding the crack for mode I are:

$$\sigma_x = \frac{K_I}{\sqrt{2\pi r}} cos\frac{\theta}{2}\left(1 - sin\frac{\theta}{2} sin\frac{3\theta}{2}\right) + T_s + A_{I3}\sqrt{r}\cos\frac{\theta}{2}\left(1+\sin^2\frac{\theta}{2}\right) + O(r) \qquad \text{Eq 145}$$

$$\sigma_y = \frac{K_I}{\sqrt{2\pi r}} cos\frac{\theta}{2}\left(1 + sin\frac{\theta}{2} sin\frac{3\theta}{2}\right) + A_{I3}\sqrt{r}\cos\frac{\theta}{2}\left(1 - \sin^2\frac{\theta}{2}\right) + O\left(r^{3/2}\right) \qquad \text{Eq 146}$$

$$\tau_{xy} = \frac{K_I}{\sqrt{2\pi r}} cos\frac{\theta}{2} sin\frac{\theta}{2} cos\frac{3\theta}{2} - A_{I3}\sqrt{r}\sin\frac{\theta}{2}\cos^2\frac{\theta}{2} + O(r) \qquad \text{Eq 147}$$

where T_s is the T-stress and A_{I3} the third term coefficient.

Expressing the stress component into Eq 142 and Eq 143 by Williams series truncated to the third term (Eq 145, Eq 146 and Eq 147), after few mathematical steps gives:

$$\begin{aligned} g_1 = a&\left[-\cos\left(\frac{\theta}{2}\right)\left(2A_{I3}\sqrt{r} + \frac{K_{Ia}\sqrt{2}}{\sqrt{\pi}}\right) - T_s\right] \\ &+ bRf\left\{\left(\frac{{K_{Ia}}^2}{2\pi r} + {A_{I3}}^2 r\right)\left[(1-\nu)\cos\theta - \frac{(1+\nu)}{4}\cos(2\theta)\right.\right. \\ &\left.+ + \frac{1}{4}(5-3\nu)\right] \\ &+ \frac{K_{Ia}\sqrt{2}}{\sqrt{\pi}}\left[A_{I3}\left(\frac{1}{8}\big((7-9\nu)\cos(\theta) + (1+\nu)\cos(3\theta)\big) + (1-\nu)\right)\right. \\ &\left.+ \frac{T_s}{4\sqrt{r}}\left(\left((3++5\nu)\cos\left(\frac{\theta}{2}\right) + (1+\nu)\cos\left(\frac{5}{2}\theta\right)\right) + (1-\nu)\right)\right] \\ &\left.+ \frac{A_{I3}T_s\sqrt{r}}{2}\left[(5-3\nu)\cos\left(\frac{\theta}{2}\right) - (1+\nu)\cos\left(\frac{3}{2}\theta\right)\right] + T_s^2\right\} \end{aligned} \qquad \text{Eq 148}$$

and

$$\begin{aligned} g_2 = -\frac{1}{2} b \Bigg\{ & \left(\frac{{K_{Ia}}^2}{2\pi r} + {A_{I3}}^2 r \right) \left[(1+3\nu)\, cos\,\theta - \frac{(1+\nu)}{4} cos(2\theta) + \frac{1}{4}(5+13\nu) \right] \\ & + \frac{K_{Ia}\sqrt{2}}{\sqrt{\pi}} \Bigg[A_{I3} \Bigg(\frac{1}{8} \big((7 + +23\nu)\, cos(\theta) + (1+\nu)\, cos(3\theta) \big) \\ & + (1+3\nu) \Bigg) + \frac{T_s}{4\sqrt{r}} \Bigg(\Bigg((3+11\nu)\, cos\left(\frac{\theta}{2}\right) + (1+\nu)\, cos\left(\frac{5}{2}\cdot\theta\right) \Bigg) \Bigg) \Bigg] \\ & + + \frac{A_{I3} T_s \sqrt{r}}{2} \left[(5+13\nu)\, cos\left(\frac{\theta}{2}\right) - (1+\nu)\, cos\left(\frac{3}{2}\theta\right) \right] + T_s^2(2\nu+1) \Bigg\} \end{aligned} \qquad \text{Eq 149}$$

For b=0, we can find the classical solution for the thermoelastic expression combined with Williams equations:

$$\frac{\Delta T_{nc,}(t)}{T_0} = a \left[- cos\left(\frac{\theta}{2}\right) \left(2A_{I3}\sqrt{r} + \frac{KI_a\sqrt{2}}{\sqrt{\pi}} \right) - T_s \right] sin\ \omega t \qquad \text{Eq 150}$$

where ΔT_{nc} stands for non-corrected value of ΔT.

Again, comparing Eq 137 and Eq 148 with Eq 150, we find that the thermoelastic temperature variation at the angular velocity ω depends also on the stress ratio R and on the material constants b and υ while, the thermoelastic variation at the twice of the angular velocity depends only on the material constants.

6.1.5. Methods: Experimental implications in SIF evaluation

In the present section, the methods used for applying the proposed formulations will be shown. In particular, the proposed formulations will be verified and compared with the classical theory both for the Williams and Westergaard approaches. Moreover, experimental tests were carried out on the Titanium grade 2 at two different stress ratios and the SIF value has been assessed via the overdeterministic method [21][62]. The results will be compared with the synthetic data to show the statistical significance of including in the TSA formulation the second-order effects.

6.1.5.1. TSA analysis with synthetic data

Eq 137 combined with Eq 142 and Eq 143 and Eq 148 and Eq 149 can be employed to obtain synthetic thermoelastic data derived from the two considered models, if the mechanical and thermo-physical constants of material are known.

In the proposed equations the thermoelastic temperature variation now consists of two harmonic components at ω and 2ω. Generally, experimental thermographic data are processed via hardware or software [24] [156], to extract, separately, the amplitude and phase images related to the first and second harmonic of the thermoelastic signal. In this regard, the temperature variation, ΔT_c, obtained by the new formulation can be represented as:

Eq 142, Eq 143, Eq 148 and Eq 149 can be rewritten as a function of K_{Imax} and the stress ratio R. In this case, we can write:

and then, by using Westergaard equations the components are:

$$\begin{aligned}\Delta T_{c1,west}(r,\theta) = T_0\Bigg\{&-a\left(\frac{K_{Imax}}{\sqrt{2\pi r}}(1-R)\cos\frac{\theta}{2}+\sigma_{0x}\right)\\&+bR_f\Bigg[\frac{K_{Imax}^2}{16\pi r}(1-R)^2(2(1-\upsilon)(\cos\theta+1)+(1+\upsilon)\sin^2\theta)\\&+\frac{\sigma_{0x}K_{Imax}}{4\sqrt{2\pi r}}(1-R)\left((3-5\upsilon)cos\frac{\theta}{2}+(1+\upsilon)cos\frac{5\theta}{2}\right)+{\sigma_{0x}}^2\Bigg]\Bigg\}\end{aligned} \qquad \text{Eq 151}$$

$$\begin{aligned}\Delta T_{c2.west}(r,\theta) = -\frac{1}{2}T_0 b\Bigg\{&\frac{{K_{Imax}}^2(1-R)^2}{8\pi r}\Bigg[(1+3\nu)\,cos\,\theta-\frac{(1+\nu)}{4}cos(2\theta)\\&+\frac{1}{4}(5+13\nu)\Bigg]\\&+\frac{K_{Imax}(1-R)}{\sqrt{2}\sqrt{\pi}}\frac{T_S}{4\sqrt{r}}\left(\left((3+11\nu)\,cos\left(\frac{\theta}{2}\right)+(1+\nu)\,cos\left(\frac{5}{2}\theta\right)\right)\right)\\&+{T_S}^2(2\nu+1)\Bigg\}\end{aligned} \qquad \text{Eq 152}$$

In the same way, the thermoelastic components for Williams series are:

$$\begin{aligned}
\Delta T_{c1,will}(r,\theta) = T_0\Bigg\{ & a\left[-\cos\left(\frac{\theta}{2}\right)\left(2A_{I3}\sqrt{r}+\frac{K_{Imax}\sqrt{2}}{2\sqrt{\pi}}(1-R)\right)-T_S\right] \\
& + bRf\Bigg\{\left(\frac{{K_{Imax}}^2}{8\pi r}(1-R)^2+{A_{I3}}^2 r\right)\Bigg[(1-\nu)\cos\theta-\frac{(1+\nu)}{4}\cos(2\theta) \\
& +\frac{1}{4}(5-3\nu)\Bigg] \\
& +\frac{K_{Imax}}{\sqrt{2}\sqrt{\pi}}(1 \\
& -R)\Bigg[A_{I3}\Bigg(\frac{1}{8}\big((7-9\nu)\cos(\theta)+(1+\nu)\cos(3\theta)\big)+(1-\nu)\Bigg) \\
& +\frac{T_S}{4\sqrt{r}}\Bigg(\Bigg((3-5\nu)\cos\left(\frac{\theta}{2}\right)+(1+\nu)\cos\left(\frac{5}{2}\theta\right)\Bigg)+(1-\nu)\Bigg)\Bigg] \\
& +\frac{A_{I3}T_S\sqrt{r}}{2}\left[(5-3\nu)\cos\left(\frac{\theta}{2}\right)-(1+\nu)\cos\left(\frac{3}{2}\theta\right)\right]+{T_S}^2\Bigg\}\Bigg\}
\end{aligned}$$

Eq 153

$$\begin{aligned}
\Delta T_{c2,will}(r,\theta) = -\frac{1}{2}T_0 b\Bigg\{ & \left(\frac{{K_{Imax}}^2(1-R)^2}{8\pi r}+{A_{I3}}^2 r\right)\Bigg[(1+3\nu)\,cos\,\theta \\
& -\frac{(1+\nu)}{4}cos(2\theta)+\frac{1}{4}(5+13\nu)\Bigg] \\
& +\frac{K_{Imax}(1-R)}{\sqrt{2}\sqrt{\pi}}\Bigg[A_{I3}\Bigg(\frac{1}{8}\big((7+23\nu)\,cos(\theta)+(1+\nu)\,cos(3\theta)\big) \\
& +(1+3\nu)\Bigg)+\frac{T_S}{4\sqrt{r}}\Bigg(\Bigg((3+11\nu)\,cos\left(\frac{\theta}{2}\right)+(1+\nu)\,cos\left(\frac{5}{2}\theta\right)\Bigg)\Bigg)\Bigg] \\
& +\frac{A_{I3}T_S\sqrt{r}}{2}\left[(5+13\nu)\,cos\left(\frac{\theta}{2}\right)-(1+\nu)\,cos\left(\frac{3}{2}\theta\right)\right]+{T_S}^2(2\nu+1)\Bigg\}
\end{aligned}$$

Eq 154

Eq 151, Eq 152, Eq 153 and Eq 154 can be used for obtaining the synthetic corrected and non-corrected thermoelastic temperature variations that will be compared with measured thermoelastic data, as it will be explained in the following sections, in order to study the second-order effects for each model.

6.1.5.2. *Experimental TSA data analysis*

In this work experimental data were acquired to compare the ability of the two considered thermoelastic models (with and without second order correction) to describe the elastic stress field around the crack tip, and thus to characterize the fracture behaviour of the material.

Experimental data were collected recording with a cooled IR camera the cracked samples thermal response to a dynamical load. The thermal data were then processed by using the IRTA [38] software, which performed the lock-in analysis to obtain the first harmonic amplitude ΔT_1 and phase ϕ_1 maps.

The data processing involved the application of the Last Square Overdetherministic method [66] to obtain the value of the unknowns of the two systems, that are the respective ΔK_I and T-stress and, only for Williams, the third term coefficient A_{I3}.

The crack tip coordinates are also optimized. The algorithm is based on crack tip search in an area close to the initial guess, choosing the solution which minimize the sum of deviations.

The phase data were employed to identify the crack tip initial value for the optimization and the minimum mesh radius; following the approach proposed by several authors [24][151][152], the crack tip was guessed at the point of sign inversion of an horizontal profile passing for the minimum (Figure 70). The plastic zone can be approximated to the area with negative phase, which at most can overestimate its size due to dissipative phenomena depending on the load frequency. Thus, the minimum mesh radius can be selected as the point where the phase return to zero (Figure 70).

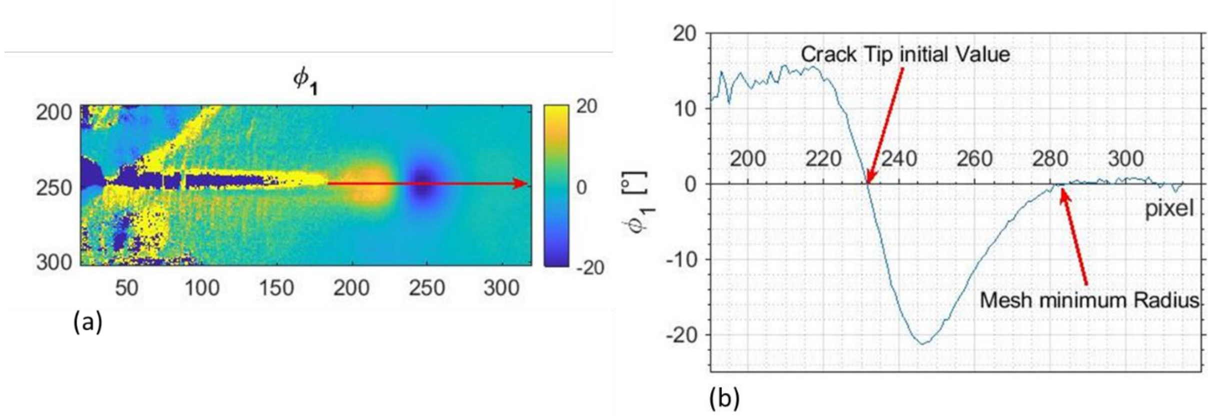

Figure 70 Phase (φ_1) map (a) and data along the profile passing through the minimum (b).

The data processing workflow is shown in Figure 71 and it can be summarized by the following steps:

1. Experimental data were acquired with a cooled IR camera during dynamical tests on CT Titanium samples.
2. A lock-in Analysis was performed: the acquired signal was decomposed into harmonics for each pixel and the first amplitude ΔT_1 and its phase ϕ_1 maps were obtained.
3. The $\phi 1$ map was employed to identify the crack tip initial value and the elastic stress field boundaries.
4. A semi annular mesh of points was created in the elastic zone around the crack tip (Figure 70).
5. The experimental calibration was performed on Titanium dog bone sample and the thermoelastic parameters *a* and *b* were evaluated.
6. For each considered thermoelastic model an Overdeterministic System of equation was written by substituting the ΔT_1 values of the mesh, together with the calibration parameters *a* and *b*, the loading conditions, and the polar coordinates in Eq 151 and Eq 153 respectively. The unknowns of this system are the parameters that describe the two models (ΔK_I in Westergaard equations and ΔK_I, T_s and A_{I3} in Williams' series expansion).
7. The crack tip was located with a trial and error procedure, by assuming the initial guess as coordinates for the crack tip and searching the optimum in a close area. The Overdeterministic System was solved for each point and the solution was obtained by minimizing deviations.

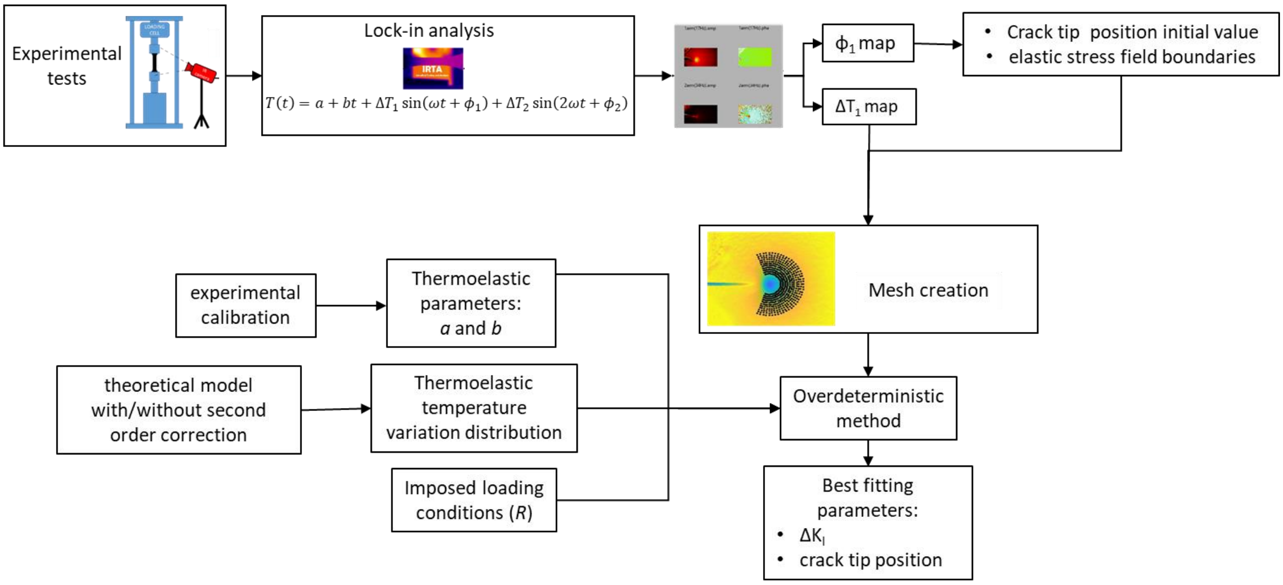

Figure 71 Workflow of the data processing.

6.1.6. Material and experimental set-up

A calibration procedure was performed following the procedure suggested by Palumbo et al. [25] in order to find the thermoelastic parameters *a* and *b*.

In this regard TSA dynamical uniaxial tensile test with different level of mean load were performed on a dog-bone sample in pure Titanium grade 2 material, with a useful section of 14.55 mm^2. The dynamical tensile tests were performed by using a loading frame MTS model 370 with a 25 kN of capacity (Setup and equipment: loading frame, infrared camera.Figure 73). Table 30 shows the test plan performed for calibration: the tests were carried out with a loading frequency of 15Hz applying three different levels of loading amplitudes P_a=*700, 1000 and 1200 N*, and three levels of mean stress P_m=*1400, 1600 and 1800 N*. Three sequences of 1000 frames each were recorded for each load condition.

Table 30 Calibration load conditions

P_a [N]	P_m [N]
700	1400
700	1600
700	1800
1000	1400
1000	1600
1000	1800
1200	1400
1200	1600
1200	1800

TSA was performed on pure Titanium grade 2 Compact Tensile (CT) specimens whose geometry is reported in Figure 4. In

Table 31 the mechanical characteristics of the material are reported.

All the samples were prepared by panting the with a black mat spray in order to enhance and uniform the surface emissivity (Figure **72**).

.

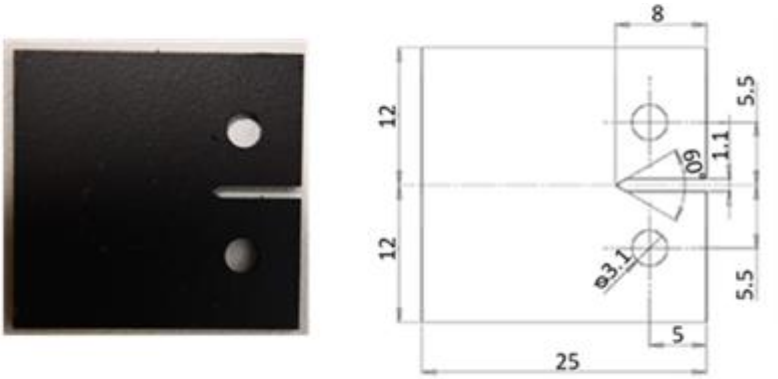

Figure 72 Samples geometry

Table 31 Pure Titanium grade 2 mechanical characteristics

Young modulus E [GPa]	Yield strength Rp0.2 [MPa]	Ultimate tensile strength Rm [MPa]
105	390	448

Table 32 shows the loading conditions applied to the Titanium CT samples during the dynamical test. In particular, two loading ratios were investigated R=0.1 and R=0.5, keeping the maximum load (750 N) and the loading frequency (17 Hz) constant.

Thermal sequences of 300 frames each where acquired at different number of cycles following the crack growth with a pitch of about 0.5 mm. The thermal acquisitions were realized by using a FLIR X6581 IR camera with the acquisition parameters set as reported in Table 33.

Table 32. Tests parameters used for CT specimens

Specimen	Pmin [N]	Pmax [N]	Pmed [N]	ΔP [N]	R	f [Hz]
CT1	75	750	412.5	337.5	0.1,	17
CT2	375	750	562.5	187.5	0.5	17

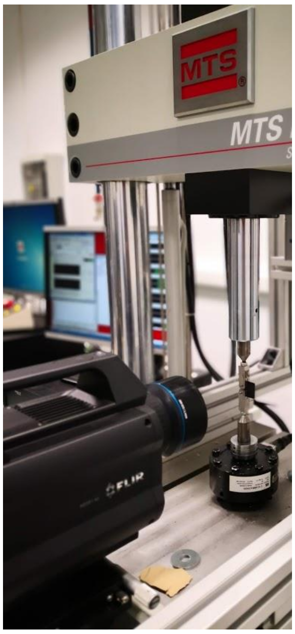

Figure 73 Setup and equipment: loading frame, infrared camera.

Table 33 IR camera acquisition parameters

Window	640x356
Temperature range [°C]	5-35
Integration Time	2500
Resolution [mm/pixel]	0.033
Frequency [Hz]	200
Number of frames	1500

6.1.7. Results and discussion

In present section, the assessment of the thermoelastic constants from thermoelastic data is presented. The effect of the correction of Westergaard Eq 151 and Williams models Eq 153 is shown in terms of thermoelastic maps comparing synthetic and experimental data and in terms of evaluated SIFs ($\Delta KI_{\_c,west}$ and $\Delta KI_{\_c,will}$) for the tests carried out at R=0.1 and R=0.5.

6.1.7.1. Assessing of thermoelastic constants

In a 'dog-bone' shaped sample, the stress distribution is known, thus the parameters a and b were found by equating intercept and slope of the experimental curve $\Delta T_1/T_0$ versus the mean load; in fact, by focusing on the semi-amplitude of the temperature running at the same loading frequency ΔT_1 and for an uniaxial loading condition, one can describe the temperature variations as Eq 61.

The results were obtained applying the linear regression of data as are reported in Figure 74:

a = (3.59e-6±1.47e-8) [1/MPa]

b = (-2.825e-9± 1.36e-10) [1/MPa2]

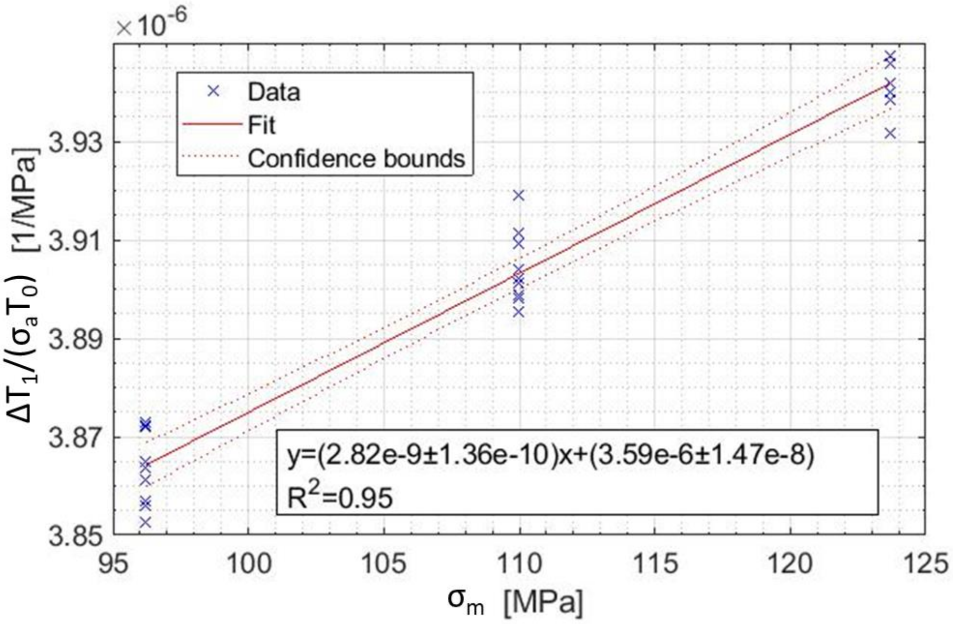

Figure 74 Thermoelastic data as function of mean stress and linear fitting. The temperature amplitude is here reported with positive sign.

6.1.7.2. *Effect of correction on thermoelastic data and SIFs values*

A first qualitative demonstration of the importance of considering second order effects of thermoelastic signal in proximity of the crack-tip in two loading conditions at *R=0.1* and *R=0.5* can be seen by observing the TSA maps in Figure 75 (a)-(d). In the maps are compared the contour lines of experimental thermoelastic temperature data ΔT_1 divided by T_0 and the synthetic $\Delta T_1 / T_0$ data obtained by considering the model equations.

Westergaard data (contour lines reported in Figure 75 (a)), show that the synthetic ‘corrected’ data are closer to the experimental data than ‘non-corrected’ ones, and the difference (‘corrected’/‘non-corrected’) is marked. This consideration is also valid for the data of the test at *R=0.5*, Figure 75 (b). It is worth noting that there is a difference in the shape of contour lines between experimental and synthetic data especially far away from the plastic area ($\Delta T_1 / T_0$ less than 6 10^{-4} at R=0.1 and 5 10^{-4} at R=0.5). This effect in general depends on the model adopted for representing the stress distribution around crack tip.

The synthetic maps obtained by using corrected Williams' solution, Figure 75 (c)-(d), are very close to the experimental data both at $R=0.1$ and $R=0.5$ near the plastic area. The difference in the shape of contour lines between corrected (solid black line) and non-corrected data (dotted red line) is more marked in the case of the data at $R=0.5$.

Far away from the plastic area, especially at $R=0.5$, for $\Delta T_1 / T_0$ less than 5 10^{-4} both the corrected model and non-corrected contours fail in approximating the experimental data.

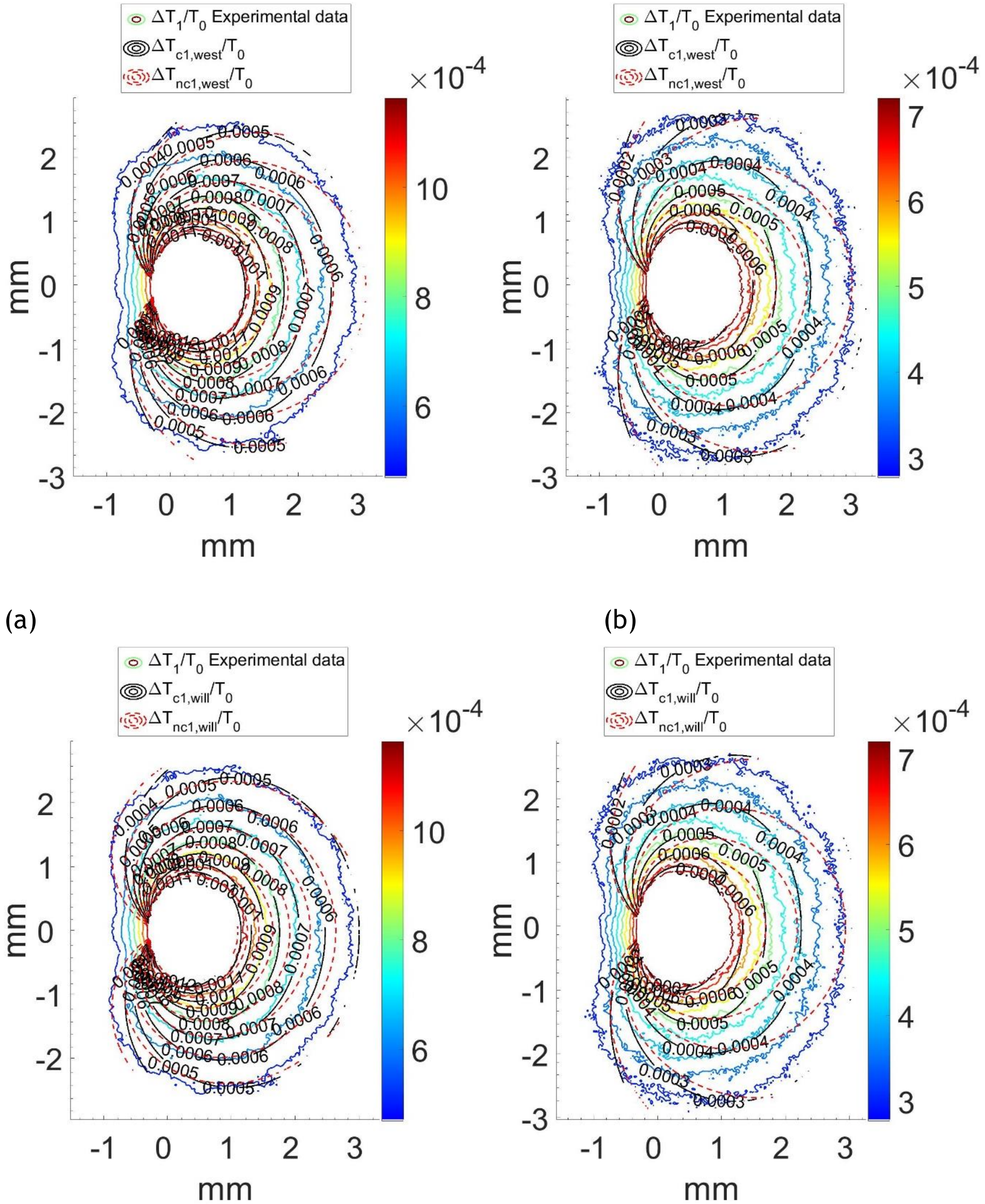

(a) (b)

(c) (d)

Figure 75 Thermoelastic temperature ΔT1 divided by T0 experimentally assessed (coloured contours) ,and synthetic data with (black solid contour) and without (red dotted contour) second order, correction for Westergaard (a) R=0.1 -(b)R=0.5 and Williams (c) R=0.1 and (d) R=0.5.

The effect of the correction on the SIF evaluation can be easily obtained by observing Table 4a-b in which $\Delta K_{I\_c,west}$ and $\Delta K_{I\_c,will}$ are compared to the corresponding value without correction, respectively $\Delta K_{I\_nc,west}$ and $\Delta K_{I\_nc,will}$. These values represent the best fitting parameters of a regression analysis based on the least squares method that is a standard approach to approximate the solution of overdetermined systems, as explained in previous section.

By observing Table34(a), the difference between $\Delta K_{I\_c,west}$ and $\Delta K_{I\_nc,west}$ appears qualitatively significant for both stress ratios. Clearly, as the ΔK_I value depends on the stress amplitude, the SIF values are higher for $R=0.1$ value than the $R=0.5$ one.
The statistical significance of the difference between $\Delta K_{I\_c,west}$ and $\Delta K_{I\_nc,west}$ has been quantitatively assessed by calculating the percent difference $\Delta\%$ (Table34), according the following formula:

$$\Delta_{\%} = \frac{\Delta K_{I\ c} - \Delta K_{I\ nc}}{\Delta K_{I\ c}} * 100 \qquad \text{Eq 155}$$

Table 34. Evaluation of corrected and non-corrected SIFs and related statistics parameters by using Westergaard (a) and Williams solutions (b)

R	*Loading cycles*	*$\Delta K_{I\_c,west}$ [MPa(m)$^{1/2}$]*	*$\Delta K_{I\_nc,west}$ [MPa(m)$^{1/2}$]*	*Δ%*	*Res_{c_west} [MPa(m)$^{1/2}$]*	*Res_{nc_west} [MPa(m)$^{1/2}$]*	*$R^2_{c,west}$*	*$R^2_{nc,west}$*
	9200	20.87	25.89	-24.05	2.41E-07	3.10E-07	0.99	0.98
	12200	23.24	28.7	-23.54	4.30E-07	8.56E-07	0.99	0.98
0.1	15200	29.08	33.86	-16.44	1.06E-06	2.61E-06	0.99	0.97
	17200	34.09	41.19	-20.85	3.06E-06	5.87E-06	0.98	0.96
	18200	39.42	49.62	-25.86	5.01E-06	8.98E-06	0.98	0.96
	51200	10.47	12.7	-21.3	1.98E-07	2.97E-07	0.98	0.97
	61200	12.15	16.05	-21.3	2.39E-07	4.44E-07	0.98	0.97
0.5	67200	12.18	15.14	-32.11	2.19E-07	3.45E-07	0.98	0.97
	74200	13.91	18.03	-24.3	2.95E-07	5.76E-07	0.98	0.97
	79200	15.24	19.04	-29.65	4.45E-07	1.04E-06	0.98	0.96

(a)

R	*Loading cycles*	*ΔKI_c,will [MPa(m)1/2]*	*ΔKI_nc,will [MPa(m)1/2]*	*Δ%*	*Resc_will [MPa(m)1/2]*	*Resnc_will [MPa(m)1/2]*	*R2c,will*	*R2nc,will*
	9200	*21.59*	*26.51*	*-22.78*	*2.39E-07*	*3.21E-07*	*0.99*	*0.98*
	12200	*24.06*	*27.90*	*-15.96*	*4.31E-07*	*7.64E-07*	*0.99*	*0.98*
0.1	*15200*	*29.75*	*27.31*	*+8.23*	*1.21E-06*	*7.20E-07*	*0.98*	*0.99*
	17200	*33.25*	*34.91*	*-4.99*	*3.04E-06*	*3.28E-06*	*0.98*	*0.98*
	18200	*39.60*	*49.85*	*-25.86*	*5.45E-06*	*9.02E-06*	*0.97*	*0.96*
	51200	*10.71*	*12.56*	*-17.24*	*1.96E-07*	*3.04E-07*	*0.98*	*0.97*
	61200	*12.21*	*16.05*	*-17.24*	*2.38E-07*	*4.46E-07*	*0.98*	*0.97*
0.5	*67200*	*12.12*	*14.75*	*-31.46*	*2.18E-07*	*3.41E-07*	*0.98*	*0.97*
	74200	*13.52*	*17.91*	*-21.68*	*2.97E-07*	*5.87E-07*	*0.98*	*0.97*
	79200	*15.33*	*19.00*	*-32.43*	*4.66E-07*	*1.20E-06*	*0.98*	*0.96*

(b)

The estimated difference is roughly of 20% at $R=0.1$ while it increases from *21%* to *29%* at $R=0.5$.The $\Delta K_{I\_nc,west}$ is always higher in value than $\Delta K_{I\_c,west}$, both at $R=0.1$ and $R=0.5$.

In Table 34 (a) are also reported the residuals (Res_{c_west}, Res_{nc_west}) a quantitative measurement of the goodness of the adopted model (lower values mean for a good fit). In any case, $R=0.1$ and $R=0.5$, the residuals of the Westergaard model corrected are lower than the related non-corrected values. This means that the correction is necessary as it improves the data analysis.

As a further confirmation of the necessity to consider second order effect there is the latter statistics parameter reported in Table 34(a): the coefficient of determination R^2. The $R^2_{c,west}$ for the two stress ratios are higher than $R^2_{nc,west}$.

As for Westergaard model, there is a marked difference between $\Delta K_{I\_c,will}$ and $\Delta K_{I\_nc,will}$ of all the test conditions ($R=0.1$ and $R=0.5$). In general, the second-order effects produce lower SIF values with respect to those obtained with the non-corrected Williams model.

In this case, the percent difference *Δ%* changes significantly between corrected and corrected SIFs. Between corrected and noncorrected data at $R=0.1$, *Δ %* varies in the range 5-26% while for the test at $R=0.5$ it varies between 17-32%.

The Res_{c_will} values are smaller than the corresponding Res_{nc_will}, meaning that the corrected model is capable of a better ΔK_I estimation. As for the coefficients of determination, both $R^2_{c,will}$ and $R^2_{nc,will}$ are close to 1, in particular $R^2_{c,will}$ is always higher than $R^2_{nc,will}$.

Summarising, the quantitative analyses focused on investigating the effect of the second order effects correction on Westergaard and Williams' models with T-stress lead to draw the following considerations:

- $\Delta K_{I\_c,will}$ are similar to $\Delta K_{I\_c,west}$, specifically the effect of the correction involves lower values of SIF;
- The evaluated residuals and R^2 coefficients demonstrate the improvement in the analysis when adopting a 'corrected' model fitting both by using Westergaard and Williams models.

In order to make more consistent considerations, in following graphs of Figure 76 (a)-(d), the SIF values at different crack lengths are compared to the values obtained by using the formula proposed by the Standard ASTM [61], considered as a reference curve.

Figure 76 reports the ΔK_I measured by ASTM (black solid line) and the ΔK_I corrected and non-corrected at $R=0.1$ (Figure 76 (a)) and $R=0.5$ (Figure 76 (b)). The little difference in crack length between corrected ($\Delta K_{I\_c,west}$, $\Delta K_{I\_c,will}$) and non-corrected ($\Delta K_{I\_nc,west}$, $\Delta K_{I\_nc,will}$) data points, Figure 76, can be explained by considering that the crack length depends on the crack tip found by implementing the fitting procedure described in previous section, that in turns depends on the adopted model.

As previously shown in Table 34, for Westergaard data, the difference between corrected and non-corrected data (Figure 76 (a)-(b)) is almost constant, in effect $\Delta K_{I\_nc,west}$ seems like shifted upwards to the reference curve. $\Delta K_{I\_c,west}$ data fit very well the ASTM reference curve.

Figure 76 (c)-(d) reports the data of $\Delta K_{I\_c,will}$ and $\Delta K_{I\_nc,will}$ for the two tests at different stress ratios ($R=0.1$ and $R=0.5$), each one compared to the ΔK_I provided by the Standard. In this case, the proposed correction is in total agreement with the reference curve for both the tests at $R=0.1$ and 0.5 while, as results from Table 34, $\Delta K_{I\_nc,will}$ are higher than the reference curve and very scattered.

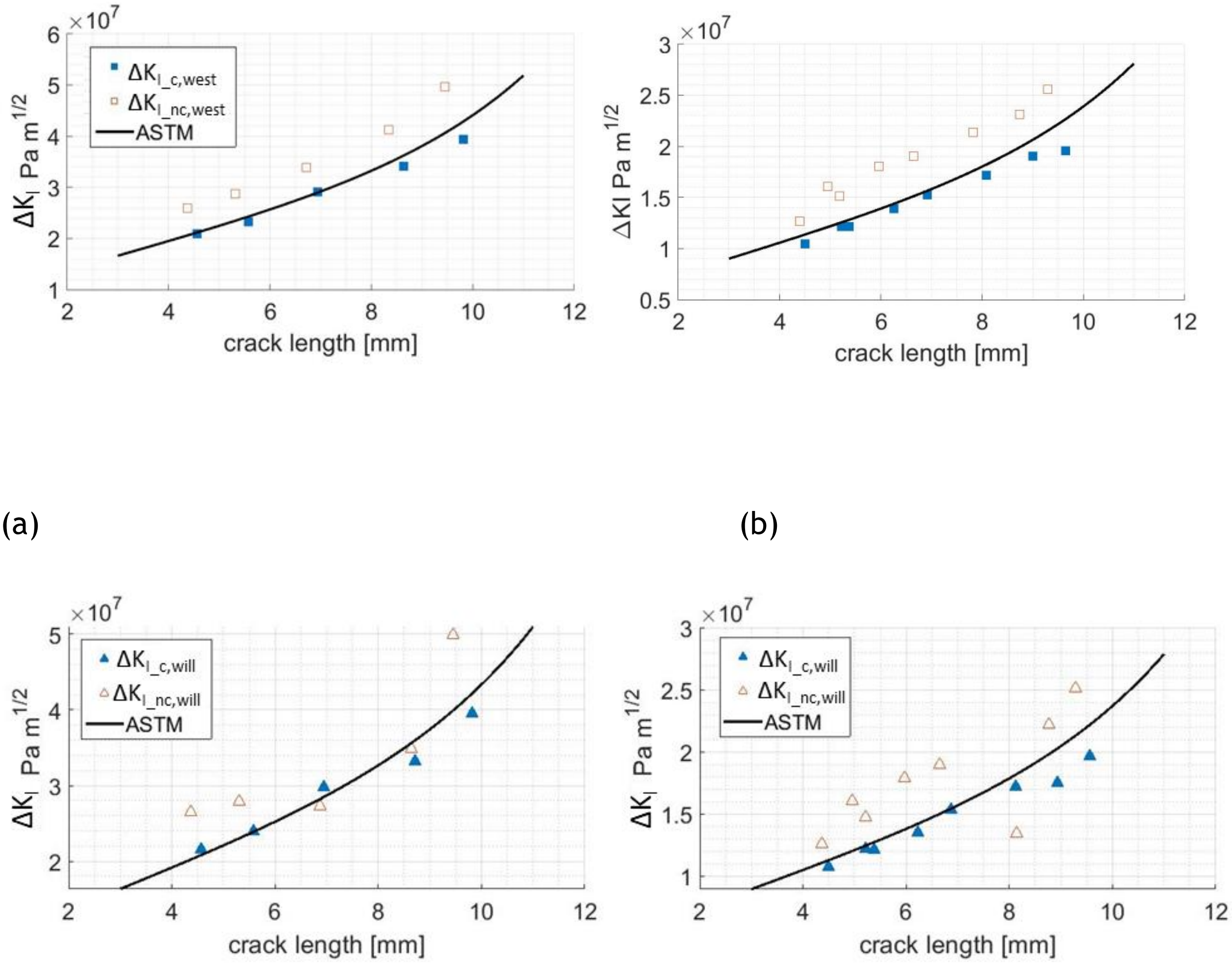

(a) (b)

(c) (d)

Figure 76. ΔKI assessed by using Westergaard solution for the test at R=0.1 (a) and R=0.5 (b), and Williams solution for the test at R=0.1 (c) and R=0.5 (d) compared to ΔKI assessed by using the Standard ASTM [61].

6.1.8. Conclusions

In this work, a new formulation has been proposed for describing the TSA signal in proximity of the crack tip on titanium and aluminium. The proposed approach starts from the revised theory of the TSA where the effect of the mean stress on the thermoelastic signal is considered.

The thermoelastic equation has been rewritten for describing the stress distribution around a crack by using Westergaard and Williams solutions with T-stress. The main results can be summarized as follows:

A part of the thermoelastic equation occurs at twice of the loading frequency. This component depends on the square of the SIF and the stress ratio for both Westergaard and Williams' solutions.

The component of the thermoelastic signal that occurs at the load frequency depends on the material properties and the stress ratio.

The effects the proposed formulation have been investigated experimentally by performing tests on small CT samples of Pure Titanium in two loading conditions: R=0.1 and R=0.5. The experimental results have been compared with synthetic thermoelastic data. The major outcome from this analysis is a more capability in the describing the stress distribution in proximity of the crack tip by the proposed formulation. The effect of the correction is pronounced in both Williams' and Westergaard models.

Furthermore, the possible implications in the SIF evaluation by using classical thermoelastic equation have been investigated. The SIFs obtained as the output of an algorithm based on an over-deterministic approach were compared to the those assessed by following the ASTM Standard procedure.

In general, the second order effects are significant above all for titanium since it presents a high sensitivity to the mean stress and higher mechanical properties than aluminium.

The proposed equations can be a useful tool to understand the limits of applicability of classical theory and well-known solutions and the error made in neglecting the second order effects.

6.2. Evaluation of the plastic zone around the crack tip in Titanium by using thermal signal analysis

6.2.1. Introduction

The process of crack growth is affected by the energy dissipated at the notch/crack tip.

In this experimental work the parameters T2 Φ_1 and Φ_2 which characterize the thermal response and are capable of describing the plastic work at the crack tip, were used for studying fracture mechanics of pure titanium small scale samples. Moreover, the influence of loading frequency was investigated too.

6.2.2. Experimental campaign and Signal processing

In this work, small scale compact tension specimens made of pure grade 2 Titanium were tested. The sample geometry is reported in Figure 77, while the material characteristics are reported in table 1

Table 35. Pure Titanium mechanical characteristics

Young modulus, E	105 GPa
Yield strength, σ_y	390 MPa
Ultimate tensile strength, σ_u	448 MPa

The tests were carried out by using a loading frame MTS model 370 with a 25 kN of capacity Figure 77. According to ASTM E 647, the test procedure involved constant-force-amplitude load at stress ratio R=0.1. The sample was pre-cracked by applying loading cycles with the frequency of 17 Hz, a maximum load of 750 N and R=0.1 until the crack did not reached a length of about 3 mm (after 21000 cycles). The thermographic acquisitions were performed every 2000 cycles with a maximum load of 400 N, R=0.1 and different loading frequencies, ranging between 8 and 23 Hz. The experimental campaign characteristics are reported in Table 36.

Thermographic sequences were acquired during tests by adopting the cooled detector of FLIR IR X6540 SC IR camera at a frequency of 200 Hz. A geometrical resolution of 0.0352 mm/pixel was adopted for the crack monitoring. Figure 77 shows the setup and equipment.

Referring to equation 1, a mathematical algorithm implemented in IRTA® software was used to extract pixel by pixel, the phase angle and the amplitude of the first and second

Fourier harmonics of the thermoelastic signal. Data are calibrated in temperature, assuming for the black painted surface an emissivity of 0.95.

Table 36. Experimental campaign

N° of cycles	F_{max} [N]	R	frequency [Hz]	N° of acquisitions
23000	400	0.1	17	3
25000			8	3
27000			10	3
29000			13	3
31000			15	3
33000			17	3
35000			19	3
37000			21	3
39000			23	3
41000			8	3
43000			10	3
45000			13	3
47000			15	3
49000			17	3
51000			19	3
53000			21	3
55000			23	3

To compare the minimum Φ_1 and the maximum T_2, the 2° percentile and the 98° percentile were respectively evaluated in an area extracted around the crack tip.

In order to reduce the noise, T_2 and Φ_2 maps where filtered using a Gaussian filter, while the data used to plot T_2 and Φ_2 horizontal profiles have been smoothed by applying a moving-average filter with a radius of 5 pixels.

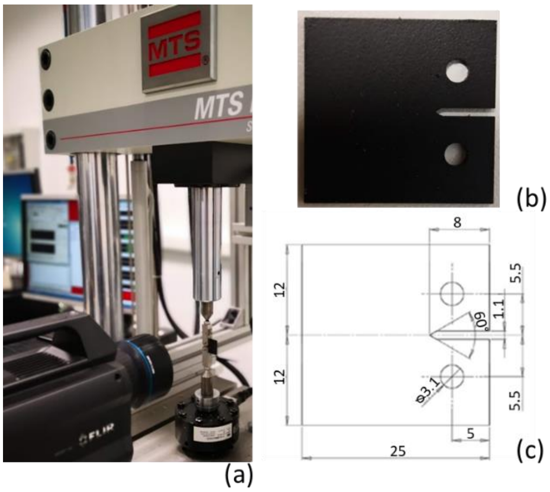

Figure 77 (a) Setup and equipment. The sample face used for the TSA acquisitions was painted with a black mat spray (b). The measures are reported in mm (c)

6.2.3. Results and discussion

Figure 78 shows the results in terms of maps of Φ1, T2 and Φ2 at the crack tip for the loading frequency of 8 Hz, 17 Hz and 23 Hz of the area around the crack tip considered in this analysis.

The Φ_1 and Φ_2 data have been re-phased by subtracting the mean value evaluated in an area of the sample whose stress field is not affected by the crack during the loading.

For the two phases, the areas and the absolute value at the crack tip interested by the heat source due to the plasticity decrease when the frequency increases. The area and the absolute value of the amplitude T_2, instead is lower at 17 Hz.

These trends are confirmed in Figure 79, where the 2° percentile of the phase signal and the 98° percentile of the thermal signal are reported; while the former increases monotonically the latter stabilizes, being highly affected by the noise at around 15 Hz.

In Figure 80, Figure 81 and Figure 82 are plotted the values of Φ_1, T_2 and Φ_2 along a horizontal profile parallel to the crack and passing for the crack tip for all the frequencies.

The comparison between the horizontal profiles gives information about the potential of the TSA in describing the area around the crack tip which is locally plasticizing. The Φ_1 horizontal profiles show how the phase area affected by the non-adiabatic conditions (which imply a non-null phase value) decreases with the frequency but it seems to stabilize at roughly 17 Hz.

From Figure 78, considering only the frequencies 17, 19, 21 and 23 Hz it is possible to infer the crack tip position between the pixels 520 and 521 (range of 1 pixel, corresponding to 0.0352 mm), which is the point of sign-inversion of Φ_1. At 8 Hz the point of sign inversion is shifted of 4 pixels (0.14 mm) on the right.

The point at which the first phase returns to zero can be related to the plastic zone extent but it is also influenced by conduction effects, which imply its variation with the loading frequency. In effect, the length of the negative section varies from 37 pixels (1,3 mm) at 23 Hz to 46 pixels (1,62 mm) at 15 Hz and to 65 pixels (2.29 mm) at 8 Hz.

The comparison among the T_2 horizontal profiles (Figure 79) and the Φ_1. horizontal profiles (Figure 78), shows how the pixels characterized by a negative Φ_1 present an increase of the amplitude T_2, which is higher than the average value measured in the elastic area.

The section on the right of the crack tip is interested by a maximum signal value, that the authors attribute to the crack closure [105], a dissipative phenomenon where the opposing faces of a crack remain in contact during the loading, occurring at twice of the loading frequency.

The crack closure effect is also evident in the Φ_2 horizontal profiles on the right side of the red dashed line indicating the crack tip position in Figure *82*. All the frequencies show a higher value at the crack interface.

The area ahead the crack tip is instead characterized by Φ_2 negative values, however the phase variation is not high enough to be distinguished from noise.

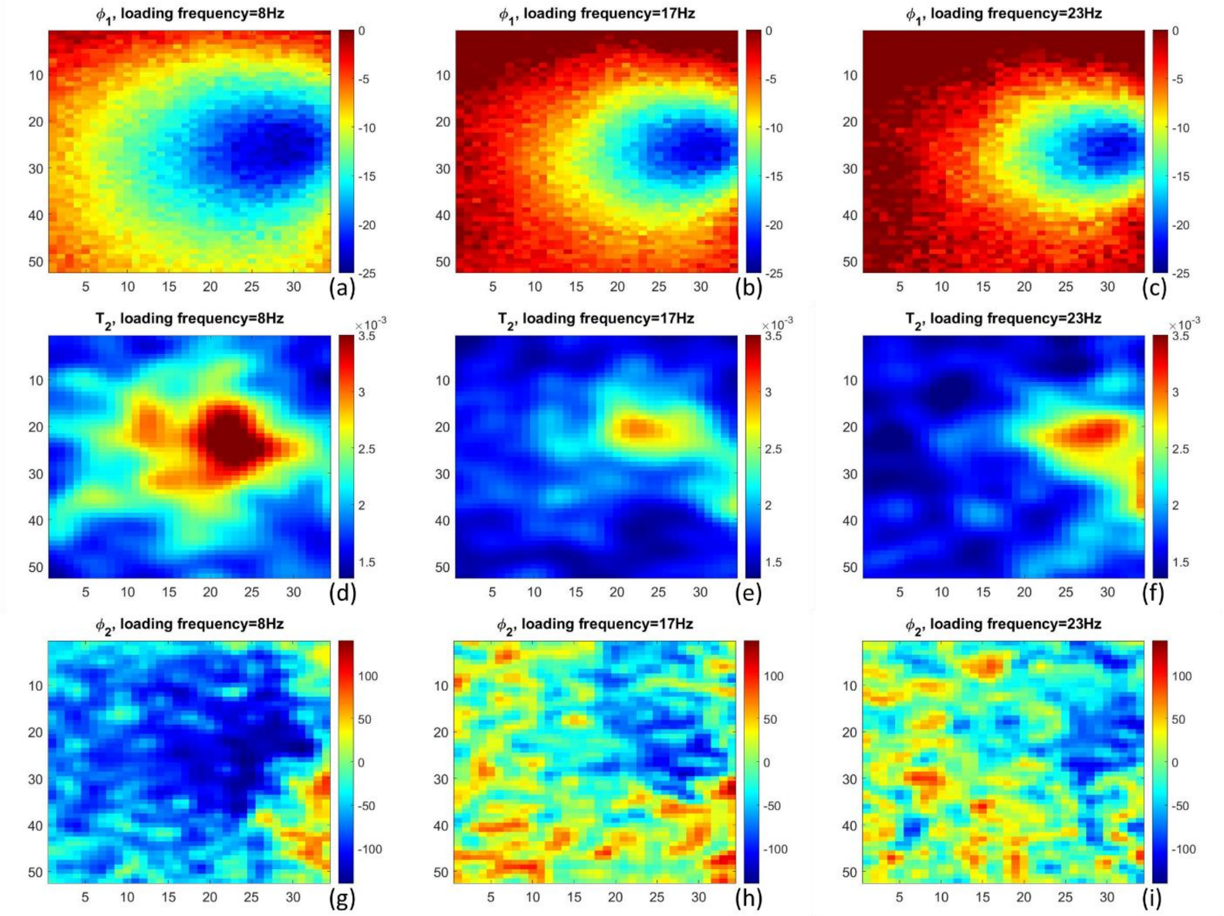

Figure 78 . Φ_1 at the crack tip for the loading frequency of 8 Hz (a), 17 Hz (b) and 23 Hz (c), T_2 at the crack tip for the loading frequency of 8 Hz (d), 17 Hz (e) and 23 Hz (f) and Φ_2 at the crack tip for the loading frequency of 8 Hz (g), 17 Hz (h) and 23 Hz (i)

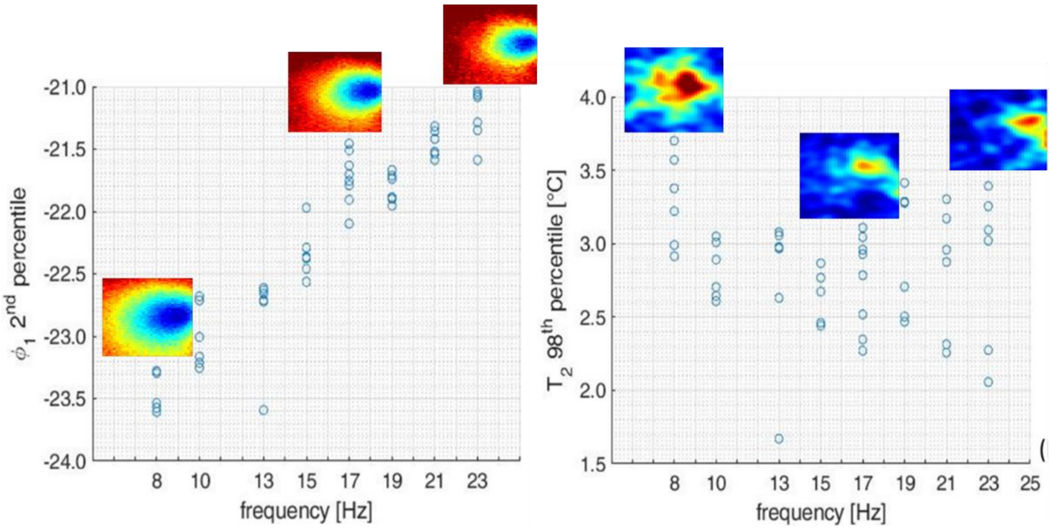

Figure 79 *a) 2nd percentile of the phase signal and b) 98th percentile of the T_2 as function of the loading frequency*

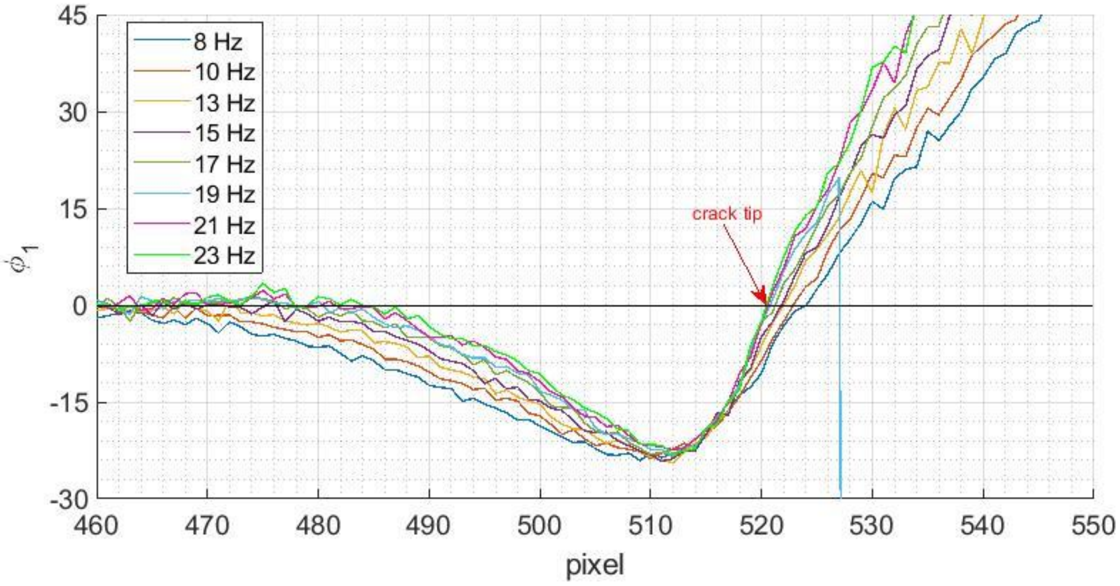

Figure 80 Φ_1 along a horizontal profile parallel to the crack and passing for the crack tip for all the tested loading frequencies

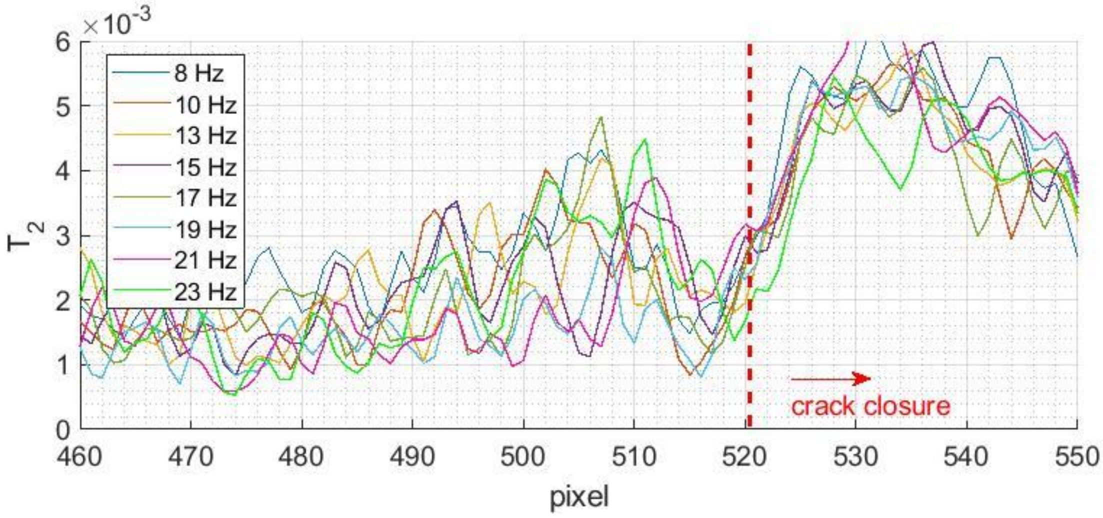

Figure 81 *. T_2 along a horizontal profile parallel to the crack and passing for the crack tip for all the tested loading frequencies. The maximum reached at the left of the red dashed line is due to the crack closure effect.*

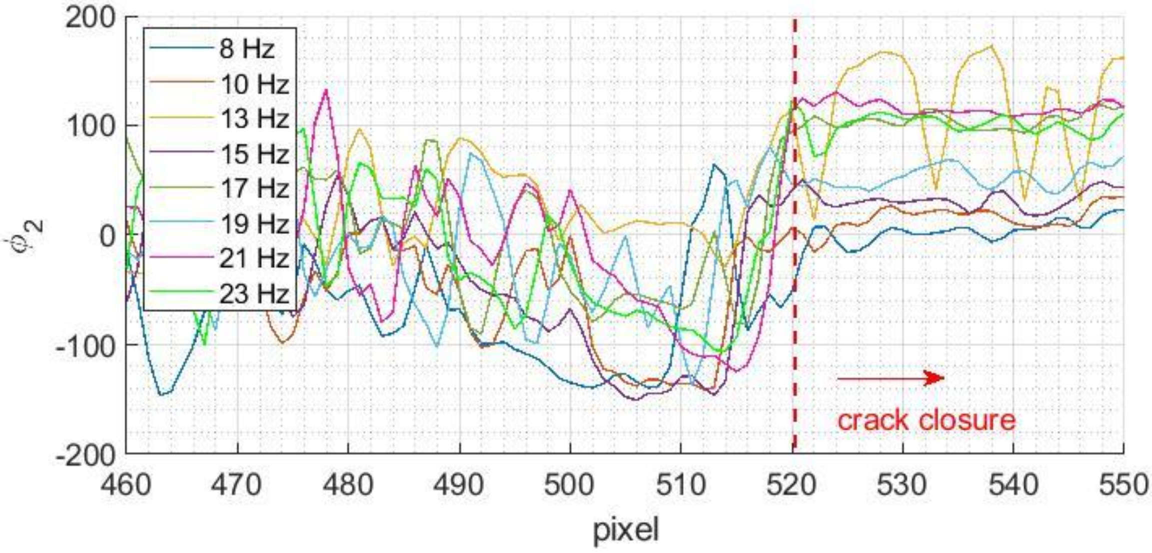

Figure 82. Φ_2 along a horizontal profile parallel to the crack and passing for the crack tip for all the tested loading frequencies. The maximum reached at the left of the red dashed line is due to the crack closure effect.

6.2.4. Plastic zone identification

The study leads to a first attempt to employ the two thermal parameters φ_1 and T_2 to identify the plastic zone shape and size.

Figure 83 shows the overlap of the two areas. The binarized maps of φ_1 and T_2 are reported in yellow and orange, respectively. In both cases the threshold was the average value measured in an area not affected by the effects of plastic deformation.

The results are consistent:

- The thermal parameter φ_1 can overestimate the plastic area due to diffusivity effect;
- The thermal parameter T_2 can underestimate the plastic zone extension because the contribute to the second harmonic due to the monotonic zone is drown in the IR camera Noise.

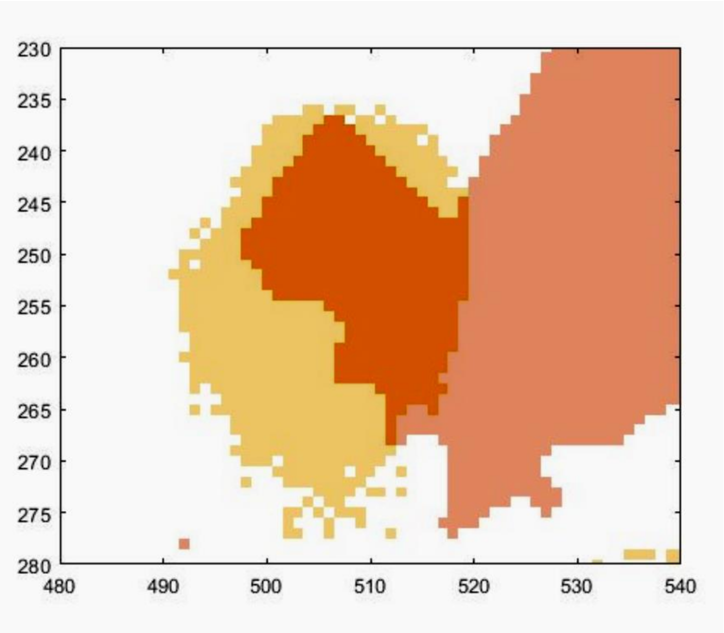

Figure 83 binarized maps of T_2 (orange) and Φ_1 (yellow) identifying the zone affected by of plastic deformation.

6.2.5. Conclusions and Future work

In this work the parameters T_2 Φ_1 and Φ_2 which characterize the thermal response of a cracked Titanium CT samples under a cyclic load at different frequencies were studied in order to relate them to the plastic area ahead the crack tip.

The experimental tests showed the following results for the three parameters:

The parameter Φ_1 presents absolute values and an area of sign inversion which decrease with the frequency; However, the difference is smaller at the higher frequencies. In the frequency range 17-23 Hz, the point of sign inversion localizes the same crack tip position, while at 8 Hz the point is shifted of 0.14 mm.

Considering the horizontal profile passing for the crack tip and parallel to the direction of the crack propagation, the extent of the sign inversion zone passes from 1,30 to 2,9 mm.

The parameter T_2 presents absolute values and the area with values above the elastic zone average signal which decrease with the frequency up to 15 Hz. From 15 to 23 Hz the trend reverses and both the absolute values and the area increase with the frequency, but the trend is not clear due to the high noise value.

The data obtained for the parameter Φ_2 are difficult to interpreter due to the noise. However, it is possible to estimate a common trend which is characterized by a sign inversion ahead the crack tip.

Both the T_2 and Φ_2 curves prove the presence of the crack closure which appears as an increase of both the parameters.

The strong dependence of the results on the frequency could indicate that conductive phenomena interfere with dissipative phenomena which are more important at low frequency. To relate the thermal parameters to the dimensions of the plastic zone around the crack tip, the material thermal-physic characteristics and all the heat sources should be considered, including the crack closure contribution.

Further work will imply the comparison of the experimental results with the study of the thermal behaviour of the Titanium cracked CT sample through a FEM analysis, by simulating all the heat sources involved.

6.3. Investigation of the plastic zone around the crack tip in small-scale pure Titanium specimens by means of Thermal Signal Analysis and Digital Image Correlation

6.3.1. Introduction

In this work two experimental techniques (DIC and Thermal Signal Analysis) for the quantitative plastic zone assessment are compared.

The experiments were performed on pure grade 2 Ti, testing 5 small scale CT with different values of loading ratio (0,1, 0,2, 0,3, 0,4 and 0,5 respectively).

The derivation of the horizontal and vertical displacements experimentally measured with DIC were used to get the strain field (εxx, εyy and τxy); the stress field was then calculated by applying the constitutive law (with E=105 GPa and v=0.33). To identify the plastic zone, the Von Mises equivalent stress criteria has therefore been applied, knowing the yield strength of the material (390 MPa).

The thermographic signal has been analyzed in the time domain: the phase of the first harmonic and the amplitude of the second harmonic were considered in order to identify the plastic zone through the lock-in Thermal Signal Analysis. For both the thermal parameters the comparison has been realized by subtracting the mean level evaluated in a zone far from the crack.

6.3.2. Experimental campaign

The activity was carried out using five Compact-Tensile specimens extracted from a 1 mm thick sheet of pure Titanium grade 2. The samples geometry is reported in Figure 84.

All the samples were prepared by panting both faces. On the side used for the DIC work a speckle pattern has been realized spraying black painting on a white background. The other face used for the Thermal acquisitions was painted with a black mat spray in order to enhance the surface emissivity (Figure 84).

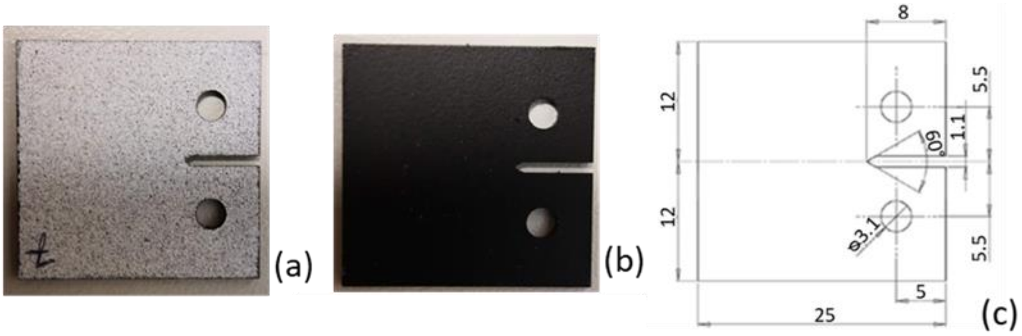

Figure 84 Samples geometry. The speckle pattern (a) was painted on the side used for DIC work while the other face used for the Thermal acquisitions was painted with a black mat spray (b). In (c) the dimensions are in mm.

One dog-bone sample extracted from the same sheet was also employed to perform the Thermoelastic Stress calibration in order to evaluate the constant *A*.

In Table 37 the mechanical properties of this commercially pure titanium alloy are given.

Table 37 Mechanical characteristics for the commercially pure Titanium employed in this work.

PURE TITANIUM GRADE 2 MECHANICAL CHARACTERISTICS

Young's modulus [GPa]	Yield stress [MPa]	Ultimate stress [Mpa]	Elongation %	Poisson's ratio
105	390	448	20	0.33

6.3.3. Test procedure and data acquisition

The tests were carried out by using a loading frame MTS model 370 with a 25 kN of capacity (Figure 85). According to ASTM E 647, the test procedure involved constant-force-amplitude load, fixed R ratio and fixed loading frequency. All the samples were tested with the same maximum load (750 N) and frequency (17 Hz) but with different R ratio. Table 38 shows the test parameter adopted for each sample.

DIC data were acquired by using a Marlin F146B CCD camera 1280X960 fitted with a CF zoom lens 13-130mm and a 9.7 μm/pixel ratio. The images were captured statically: after a defined number of cycles the fatigue cycling was paused, and a stepwise loading was applied. Three images were captured at the three different load level 0, P_{min} and P_{max}.

Thermal data were acquired by means of a FLIR X6581 cooled IR camera with a window of 640X356 pixels and a μm/pixel ratio of about 30.2. Sequences of 1500 were recorded with a sampling frequency of 200Hz and an integration time of 2287.4 μs.

Table 38 Load characteristics for the five samples

Loading conditions						
specimen	**P_{min} [N]**	**P_{max} [N]**	**P_{med} [N]**	**ΔP [N]**	**R**	**f [Hz]**
CT1	**75**	**750**	**412.5**	**337.5**	**0.1**	**17**
CT2	**150**	**750**	**450**	**300**	**0.2**	
CT3	**225**	**750**	**487**	**262.5**	**0.3**	**17**
CT4	**300**	**750**	**525**	**225**	**0.4**	**17**
CT5	**375**	**750**	**562.5**	**187.5**	**0.5**	**17**

Figure 85 Experimental set-up

6.3.4. Methods of data processing

The data processing workflow is showed in Figure 86. DIC data were employed to provide Von Mises equivalent stress maps both with the direct method and the indirect method based on the application of theoretical analytical predictions.

Thermal data were employed to provide T_1, T_2, Φ_1 and Φ_2 maps.

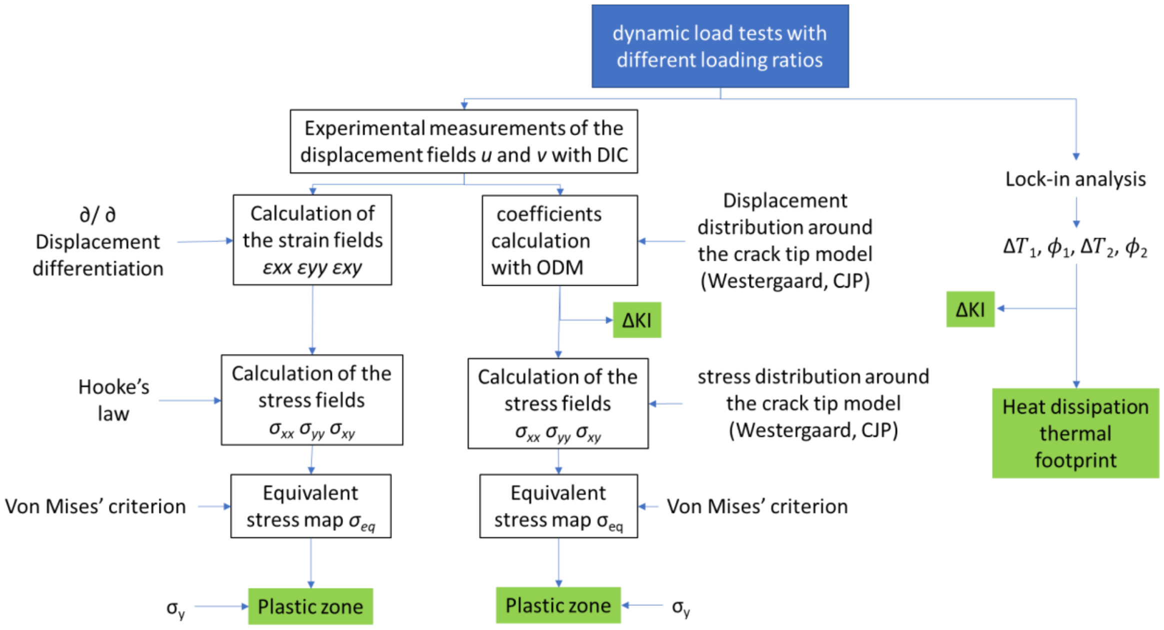

Figure 86 Activity workflow

6.3.4.1. DIC data processing

DIC data were analyzed with the software Ncorr which provided the maps of vertical and horizontal displacements *u* and *v*.

Direct method. The direct method for the estimation of the stress field and thus the determination of the plastic zone shape and size, consisted in the following steps:

- Assessment of the vertical and horizontal displacements *u* and *v* (Ncorr). The determination of the plastic zone was carried out considering the unloaded and the maximum load conditions respectively as reference and current images, while for the evaluation of the ΔK_I, the minimum and the maximum loading conditions were compared.
- Determination of the strain fields at the crack tip by differentiation of the displacement fields. In this regard, the Green-Lagrange strain tensor was employed in order to consider second-order terms.
- Determination of the stress fields using Hooke's law.
- Calculation of the equivalent stress map by applying Von-Mises' criterion (Figure 87)
- Individuation of the plastic zone size and shape by connecting all points where the yield criterion is met, that is, where the equivalent stress is equal to the yield stress.

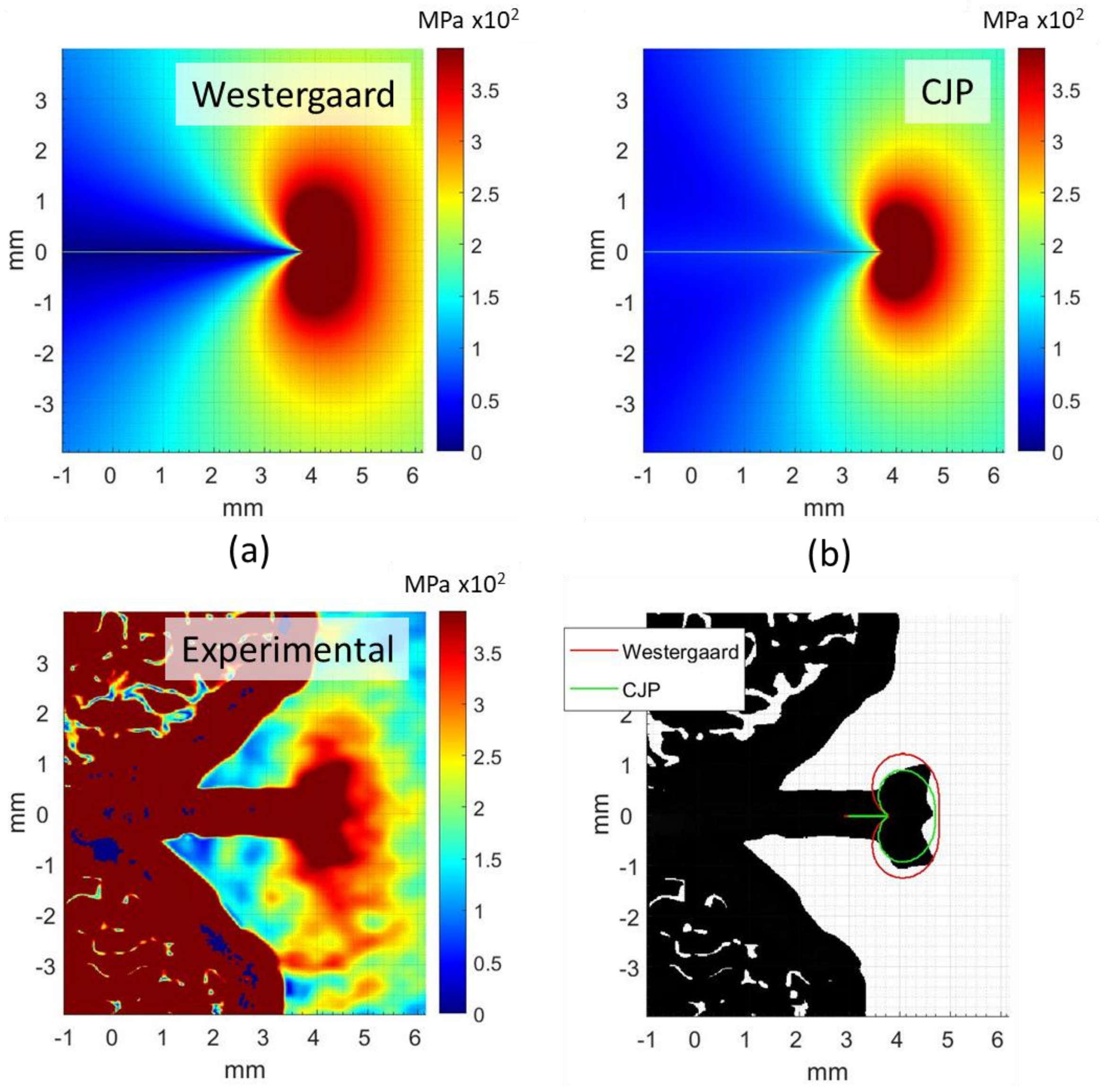

(a) (b)

(c) (d)

Figure 87 Von Mises' Equivalent stress maps obtained for the CT5 from the combination of DIC data with the Westergaard's model (a) and the CJP model (b) and from the direct experimental displacements derivation (c). The plastic zone shape and size were identified putting the Yield strength as limit. In (d) the plastic zone profiles predicted by the theoretical models are overlapped to the binarized experimental map.

Indirect method. The plastic zone shape and size evaluated with the direct method was compared with the theoretical analytical predictions provided by the two models described in paragraph 2.3.1 (Westergaard and CJP). In this paper the multi-point over-deterministic method [92] was implemented in order to determine from analysis of the experimental displacements the coefficients which describe the two crack tip stress models.

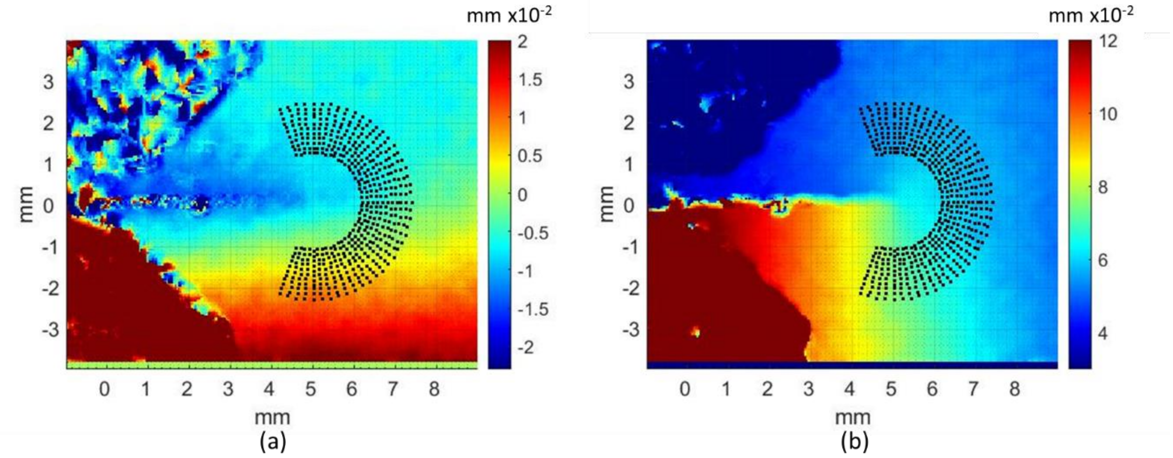

Figure 88 DIC (a) Horizontal and (b) vertical displacement fields the crack tip for CT5 and the annular mesh of data points used for the evaluation of stress intensity factors.

The application of the indirect method was carried out as follow:

- Assessment of the vertical and horizontal displacements u and v (Ncorr)
- Definition of an annular mesh (Figure 88). The selection of the inner and outer radii was made in such a way to avoid including plastic deformation and to be in the singularity-dominated zone. For the same reason, the mesh does not encompass the crack flanks.
- Iterative selection of the crack tip position and fitting of experimental displacements with the models equation. The solution (in terms of stress intensity factor) was found using the best fit identified by the lowest residuals.
- Prediction of the stress fields using the theoretical models
- Calculation of the equivalent stress map by applying Von-Mises' criterion (Figure 87)
- Individuation of the plastic zone size and shape by connecting all points where the yield criterion is met, that is, where the equivalent stress is equal to the yield stress.

6.3.4.2. Thermal Signal processing

The thermal sequences acquired where processed by using the software IRTA®. For the evaluation of the heat dissipation thermal footprint (Figure 89), the procedure for the data processing involved the following steps:

- Lock-in analysis and pixel by pixel evaluation of the calibrated Fourier harmonic components: T_1 and T_2 and their phases Φ_1 and Φ_2
- Pixel by pixel subtraction of the mean value evaluated in an area not affected by the singularity of the crack.
- Application of a Gaussian 2-D smoothing in order to obtain noise reduction.
- Flipping and resizing of the image in order to compare the map with the DIC images.
- The evaluation of ΔKI by means of the Stanley method required the following steps:
- Lock-in analysis and pixel by pixel evaluation of the uncalibrated first Fourier harmonic S
- Extraction of the analysis area around the maximum value of the signal S
- Application of the Stanley method (paragraph 2.3.5) and evaluation of ΔK_I. The constant A was experimentally evaluated following the classical calibration procedure (paragraph 2.1.4) on a dog-bone sample.

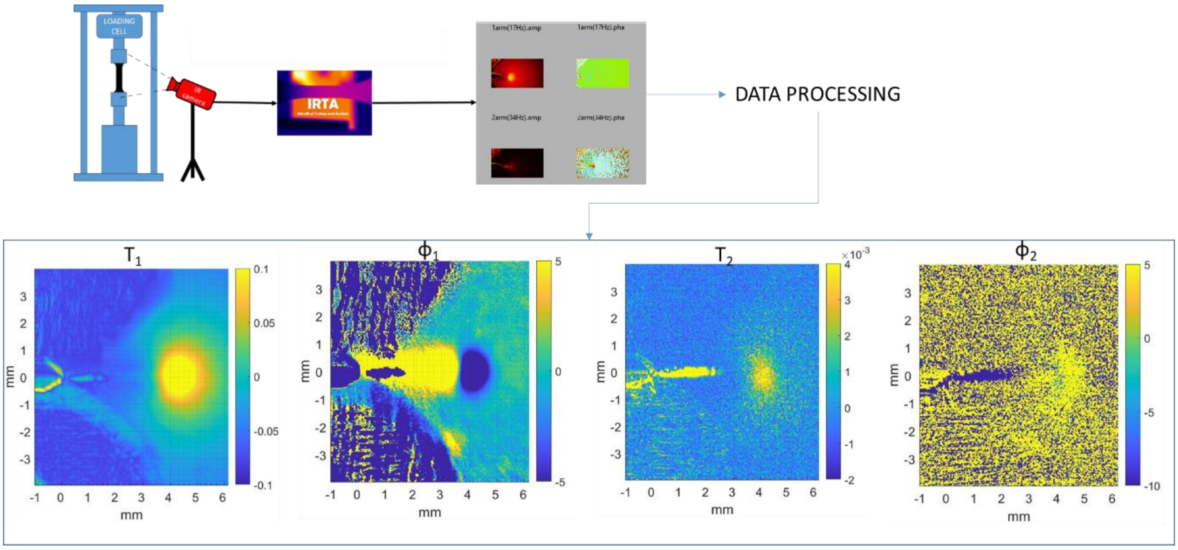

Figure 89 Data acquisition and processing workflow to obtain the map of amplitude and phase of the first and second Fourier harmonic of the thermal signal.

6.3.5. Results and discussion

6.3.5.1. Plastic zone from DIC direct and indirect method and thermal maps comparison

The plastic zone shapes and sizes identified with the direct and indirect methods have been compared with the thermal maps obtained from the thermal signal processing.

The thermal parameters affected by the presence of localized plasticization are Φ_1 and T_2. Variations in the second harmonic phase are also related to dissipative phenomena due to plasticization, but it is hard to identify the boundary of the area due to the high noise level (Figure 89).

Figure 8 shows the superposition of the plastic zone boundaries on the phase maps for two different load ratios (R=0.1 and R=0.5) and a comparable crack length (4.1 mm and 3.8 mm respectively). Among the three boundaries (DIC direct method, Westergaard and CJP), the one that best approximates the thermal parameter footprint is the one predicted by the CJP model.

In Figure 90 it is shown the Φ_1 profiles along the crack line; in the same plot the Von Mises' equivalent stress profiles are also reported. Between the two tests (R=0.1 and R=0.5) there is no significative difference in Φ_1 and in both cases the crack tip determinate by theoretical models fitting is closer to the minimum phase signal rather than the sign inversion.

Figure 91 shows the same maps and profile plots for the thermal parameter T_2. In this case the lower load ratio determines a higher and less noisy signal (being T_2 proportional to ΔP) but in both cases the area interested from an above average increase in T_2 falls within the three predictions and also in this case it is better approximated by the CJP model.

In any case, due to the influence of some test parameters (such as R on T_2 and frequency on Φ_1), it is not possible to establish a single threshold for the thermal parameters that identify the plastic zone.

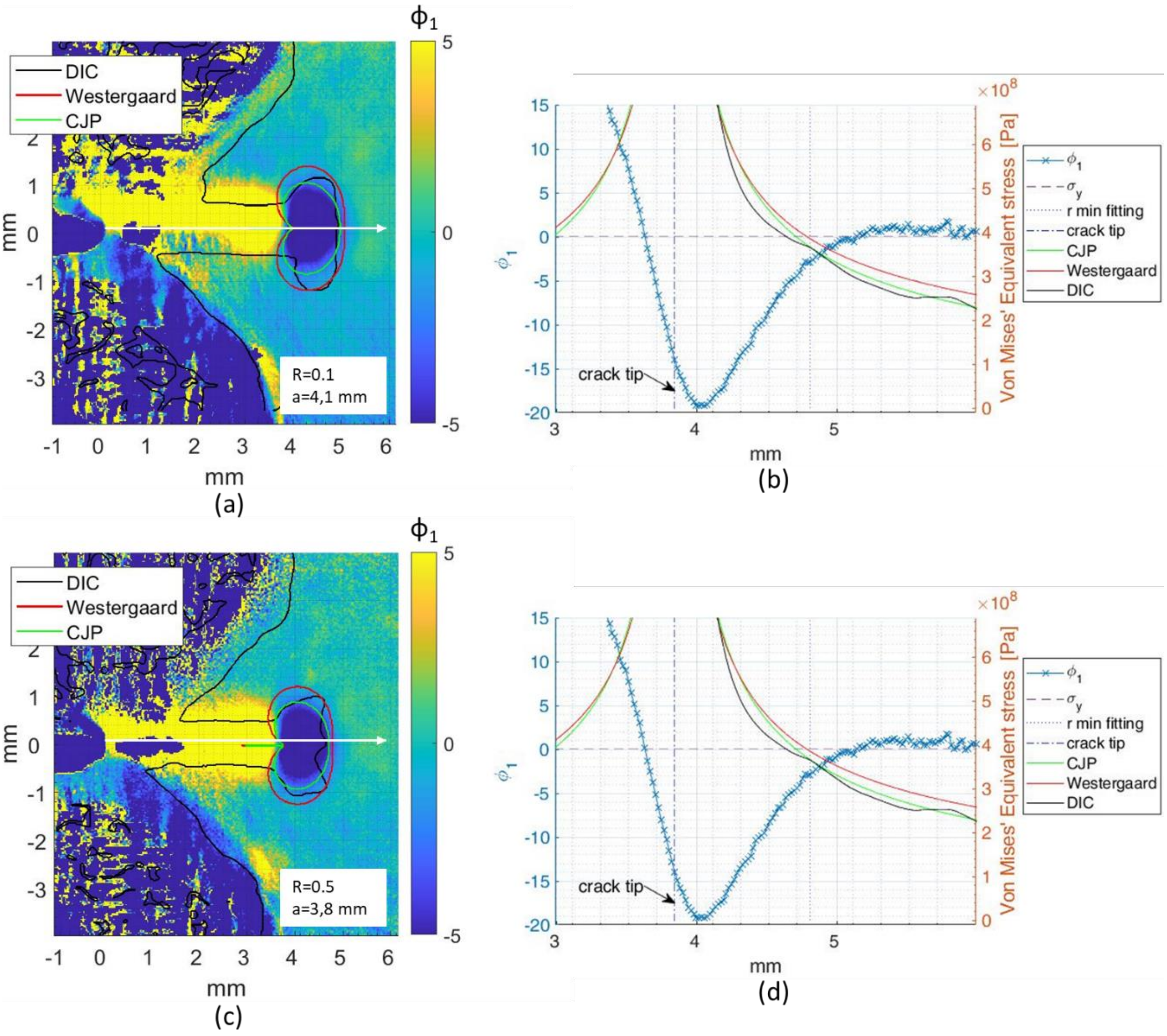

Figure 90 Phase of the first Fourier Harmonic for (a) CT1 (R=0.1) at the crack length of 4.1 mm and (c) CT5 (R=0.5) at the crack length of 3.8 mm. The plastic zone profiles predicted by direct experimental displacements derivation and the theoretical models are overlapped. The Φ1 profiles along the crack line and the Von Mises' equivalent stress profiles are also reported (b and d)

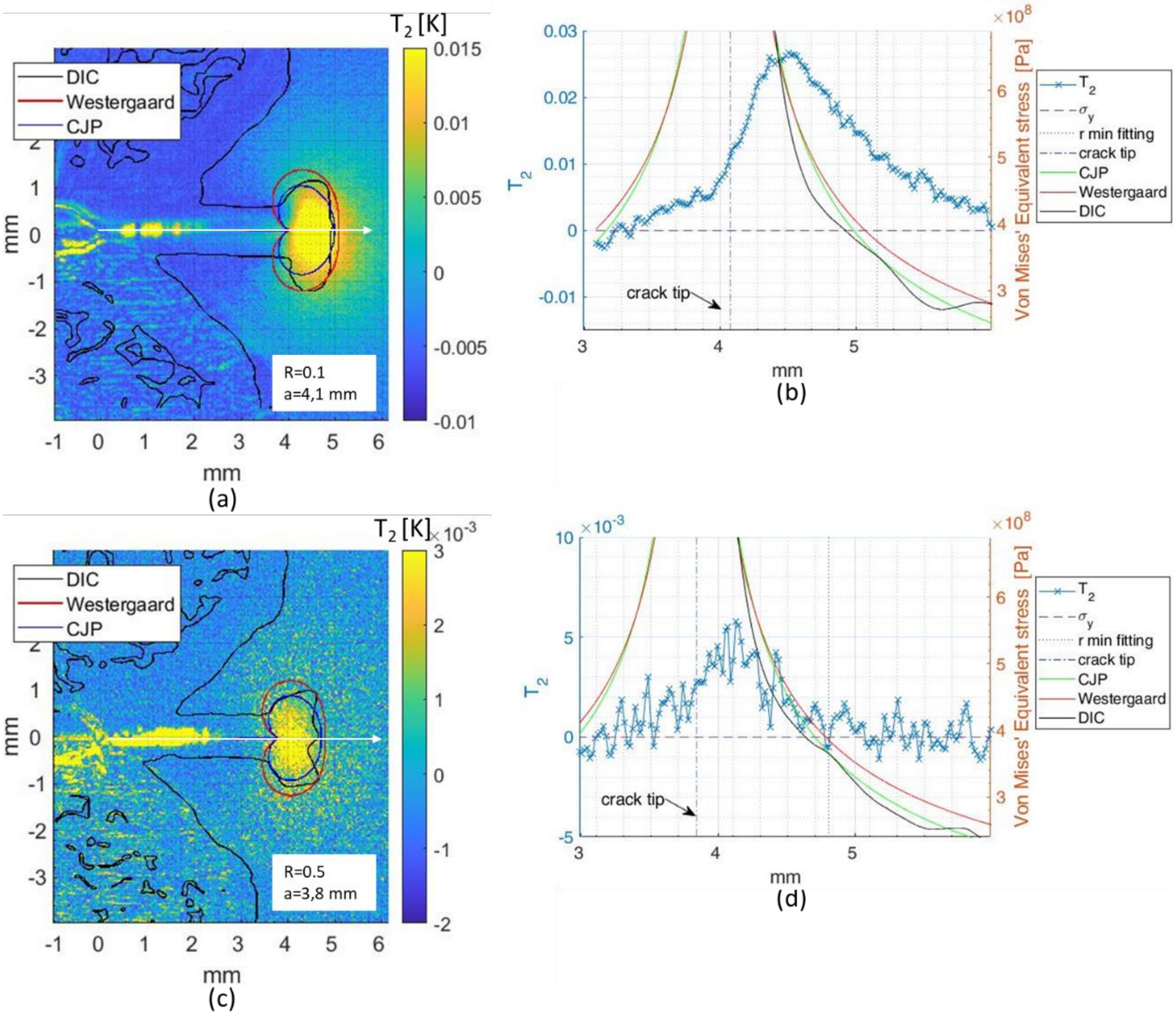

Figure 91 Amplitude of the second Fourier Harmonic for (a) CT1 (R=0.1) at the crack length of 4.1 mm and (c) CT5 (R=0.5) at the crack length of 3.8 mm. The plastic zone profiles predicted by direct experimental displacements derivation and the theoretical models are overlapped. The T2 profiles along the crack line and the Von Mises' equivalent stress profiles are also reported (b and d)

6.3.5.2. ΔKI from and Stanley's method comparison

Table 39 reports the results obtained from the evaluation of the ΔK_I by using the DIC indirect method with the two theoretical models (Westergaard and CJP) and applying the Stanley's method.

In Table 39 are also reported the ΔK_I nominal values, evaluated as prescribed in ASTM E 647.

The % errors evaluated with respect to this nominal value are shown in Table 40.

In all tests the CJP model provides a ΔK_I value closer to the nominal one, with an error ranging from 1.5 to 19.6 %.

This result could be expected since, contrary to the CJP model, both Stanley and Westergaard do not consider the boundary interactions between the elastic stress field and plastic zone surrounding the crack tip.

Furthermore, the Stanley's method does not consider the presence second order effects which, in metals such as Titanium, are not negligible.

Table 39 ΔKI obtained by using the DIC indirect method with the two theoretical models (Westrgaard and CJP) and applying the Stanley's method. The nominal value evaluated as prescribed in ASTM E 647 is also reported

R	Nc_{TSA}	Nc_{DIC}	crack length [mm]	ΔK_F [MPa·m$^{1/2}$]	ΔK_{West} [MPa·m$^{1/2}$]	ΔK_{St} [MPa·m$^{1/2}$]	ΔK_{ASME} [MPa·m$^{1/2}$]
0,1	20900	21500	5,0	34,5	33,2	34,5	42,9
0,2	23400	24000	5,0	39,7	30,3	36,8	40,3
0,3	25200	26000	5,2	33,1	28,6	24,9	36,1
0,4	47400	48000	4,9	31,7	23,5	20,6	29,9
0,5	84200	85000	5,0	26,1	23,1	22,4	25,5

Table 40 Percentage error in the determination of the ΔKI with respect to the nominal value evaluated as prescribed in ASTM E 647

R	Nc_{TSA}	Nc_{DIC}	crack length [mm]	CJP % er	Wester. % er	Stan. % er
0,1	20900	21500	5,0	19,6	22,6	19,6
0,2	23400	24000	5,0	1,5	24,8	8,7
0,3	25200	26000	5,2	8,3	20,8	31,0
0,4	47400	48000	4,9	6,0	21,4	31,1
0,5	84200	85000	5,0	2,4	9,4	12,2

6.3.6. Conclusion and future work

In this work two experimental full-field techniques were employed to assess the shape and size of the plasticized area around the tip of a growing crack.

The thermal footprint obtained from the Thermal Signal Analysis was compared with shape and size of the plastic zone predicted through the application of DIC both by using the direct derivation of strains/stress field and in combination with two theoretical models: Westergaard’s and CJP.

The study led the following results:

- The maps of the thermal parameters show an agreement with the results obtained from the DIC analysis in combination with the theoretical models; however, effects that vary with the test parameters (such as R and the loading frequency) are not negligible and make it difficult to establish a limit for the identification of the plastic zone.

- The theoretical model which showed a better agreement both with the plastic zone predicted by using the direct method and the thermal footprint of both the considered parameters is the CJP model. It is confirmed that the model gives an improved description of the elastic stress field surrounding the crack enclave.

- Furthermore, the CJP model proved, for each R, to provide a ΔK for the opening mode closer to what was calculated with the ASTM standard.

- The Stanley’s method for the evaluation of ΔK_I resulted in values affected by an error of up to 31% compared to the ASTM standard. This result should consider that the method does not incorporate the boundary interactions between the elastic stress field and plastic zone (since it is based on Westergaard’s equations) and does not consider the presence of second order effects which, in metals such as Titanium and Aluminium, are not negligible.

The present research work continues with the aim of identifying all the effects that affect the thermal signal characterizing the plastic area around the crack.

In particular, the study is continuing with:

- An analysis at different test frequencies aimed at isolating secondary effects on the thermal footprint.

- A FEM modelling of all the heat sources affecting the system, including the crack closure phenomenon, aimed to validate experimental data and to develop a procedure for the quantitative assessment of the plastic zone shape and size based on thermal parameters.

- The development of a new method for the evaluation of ΔK_I that considers the presence of T-stress and the effects of the second order (when not negligible), based on the Thermoelastic Stress Analysis general model and Williams' equations.

CHAPTER 7.

DUAL COLOR TECHNIQUE APPLICABILITY INVESTIGATION

The work reported in this chapter arises from the collaboration between the Polytechnic of Bari and the laboratory of Methods and Technologies for Observations and Measurements of the Italian Aerospace Research Center of Capua (CE).

The laboratory monitors the experimental activities carried out in the large CIRA plants, and in particular the tests in the Plasma Wind Tunnel (PWT) which simulates the thermo-fluid dynamic conditions to which the spacecraft are subjected during re-entry into the atmosphere. The criticality that characterizes these tests requires the development and refinement of *ad hoc* temperature detection techniques, which are able to guarantee accurate measurements in extended temperature ranges ranging from 200 ° C to 2500 ° C and are able to follow strong thermal gradients to which the test articles are subjected, all in a hostile and difficult to access environment.

The research activity is a study of the thermographic dual color technique applicability at high temperatures. It is an analytical study carried out by using a mathematical model based on Planck's Law integration, convoluted with the real response curves of sensors, optics, filters and attenuators. The presented model has been validated at high temperature and used to optimize the hardware set up for dual color measurements both in terms of operative spectral band and also for choosing the best pair of filters. Furthermore, spectral emissivity trend curves for different materials, available in literature, and at different temperatures have been used in the theoretical model in order to simulate and replicate experimental results. The experimental simulations obtained with dual color technique have been compared with those obtained through classical techniques based on the a priori knowledge and setting of the emissivity average values.

The aim is to establish in which conditions and for which class of Thermal Protection System (TPS) materials used to protect the inner cold structure of hypersonic space vehicles made of aluminium or metallic alloys, the dual color technique can be used for a more accurate and precise temperature measurement compared to the classical techniques. The applicability study was carried out up to high temperature (2000 °C) which are reached by the TPS surfaces during the re-entry phase from Earth orbit or from interplanetary trajectories due to the high heat flux loads produced by the strong shock wave during the deceleration phase.

7.1. Determination of a suitable couple of filters for the IR camera

Savino et al [126] demonstrated how an IR camera operating in MW is needed to obtain sufficiently accurate temperature measurements. Furthermore, to avoid the influence of environment radiation reflected by filter when it is supported by an external wheel [126], the camera has to be equipped with an integrated filter wheel. Moreover, the rotation of this filter wheel has to be as fast as possible to switch in such a short time to consider the thermal state of the object unchanged.

The multispectral camera FLIR ORION SC 7600 meets these requirements [157]. The standard calibration interval is from 5°C to 300°C and it can be extended up to 3000°C with the interposition of filter and attenuator.

The validated model has been used to detect a suitable couple of filters to make the FLIR ORION SC 7600 operative in the experimental applications of dual color technique. A virtual IR camera has been mathematically developed using technical data provided by the developer, including the response curve of the sensor and the transmittance curve for the optic. These curves are plotted in Fig.1 together with the transmittance curves for the filter and the attenuator applied in standard application to reach temperature higher than 300 °C, indicated respectively as F_{std} and A_{std}.

The optimization process began with the modelling of filters transmittance curves through the Gaussian functions (Eq 156) which gives the transmittance value for an ideal filter, normalised respect to 1.

$$F_{\text{gauss}}(\lambda) = e^{-\left(\frac{\lambda - W}{\sqrt{2} \cdot \frac{A}{2}}\right)^2} \qquad \text{Eq 156}$$

The optimization parameters have been:

- Central wavelength of the two filters (W_1 e W_2)
- Spectral bandwidth of the two filters (A_1 e A_2)
- Distance between the central wavelength of the two filters ($W2$ - $W1$)

In Figure 93, Figure 94 and Figure 95 the signal ratio (SR) for a blackbody is plotted as function of the temperature for different couples of Gaussian filters varying the optimization parameters; the couples with the highest sensitivity are those that show the greater slope.

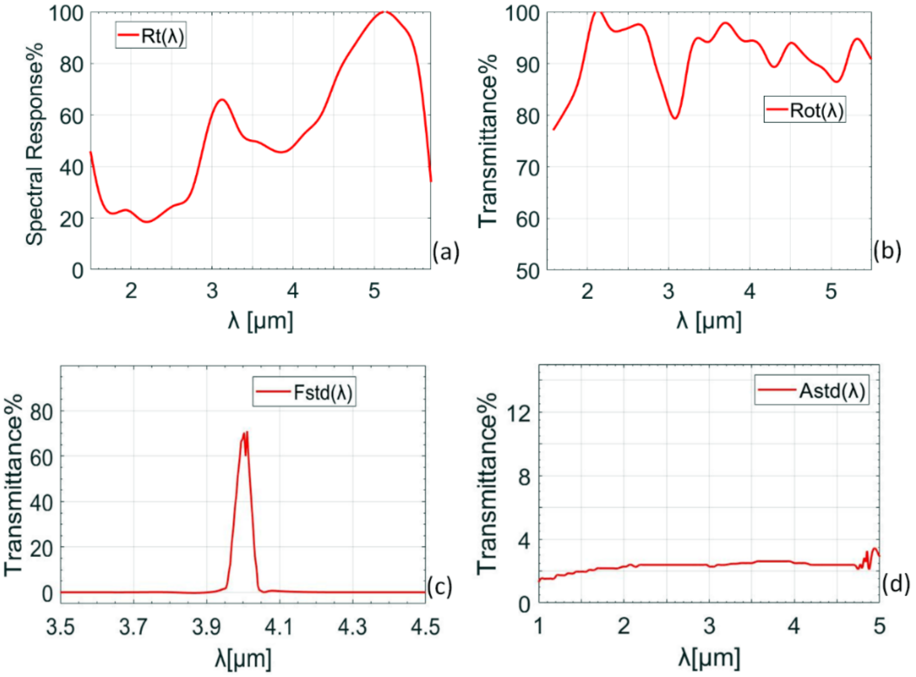

Figure 92 (a) Spectral response of sensor and transmittance curves for each element of the optic chain of the FLIR ORION SC7600 [20]:, (b) optic lens, (c) filter used in standard application for the range 300°C-1500°C, (d) attenuator added to the filter in standard application for the range up to 3000°C.

A greater sensitivity in *SR* trend in function of temperature has been found for couples of filters with W_1 e W_2 between 1.6 µm and 2.3 µm (*Figure 93*), and the result is in agreement with what found by Mölleman et al. [125], Savino et al. [126] and Musto et al. [127]. The spectral bandwidths showed less influence on the measurements sensitivity even if better results are obtained with narrower filters (A_1=A_2= 50 nm, *Figure 94*). The sensitivity increases with the distance W_1-W_2, but choosing high value for this parameter means moving away from the local grey body hypothesis. On the contrary, two wavelengths excessively close to each other lead to a moderate *SR* sensitive curve in function of the temperature (*Figure 95*). As a good compromise, it was taken W_1-W_2= 100 nm.

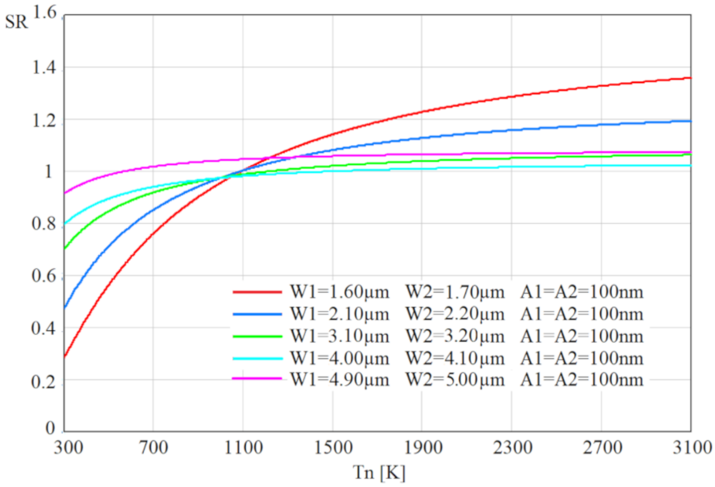

Figure 93 The SR vs Temperature for a blackbody is shown. The curves refer to different couples of Gaussian filters varying the central wavelength but keeping constant the spectral bandwidths and the distance between the central wavelengths.

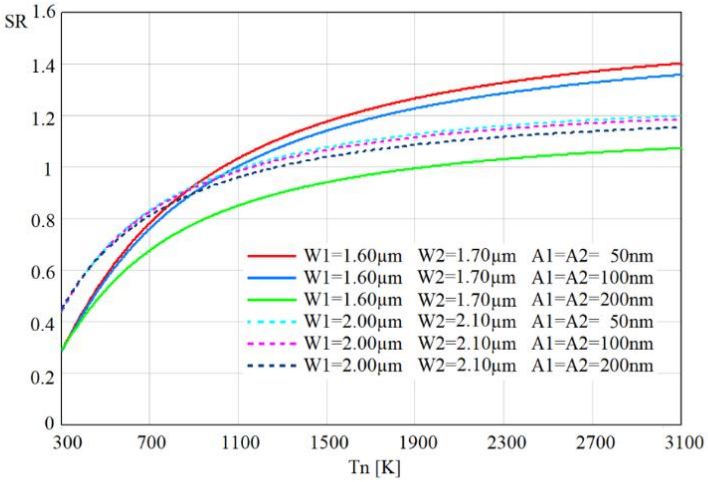

Figure 94 The SR vs Temperature for a blackbody is shown. The curves refer to different couples of Gaussian filters varying the spectral bandwidths of the two filters and keeping constant the central wavelengths and distance between them.

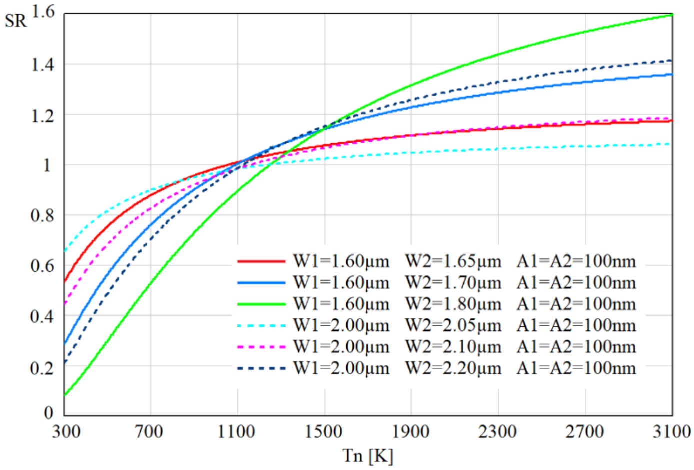

Figure 95 The SR vs Temperature for a blackbody is shown. The curves refer to different couples of Gaussian filters varying the distance between the central wavelengths of the two filters and keeping constant the spectral bandwidths and the central wavelengths.

The following commercially available filters have been selected [157]:

- Spectrogon NB-2097-055-nm (*f1*)
- Spectrogon NB-2210-047-nm (*f2*)
- Spectrogon NB-2310-050-nm (*f3*)

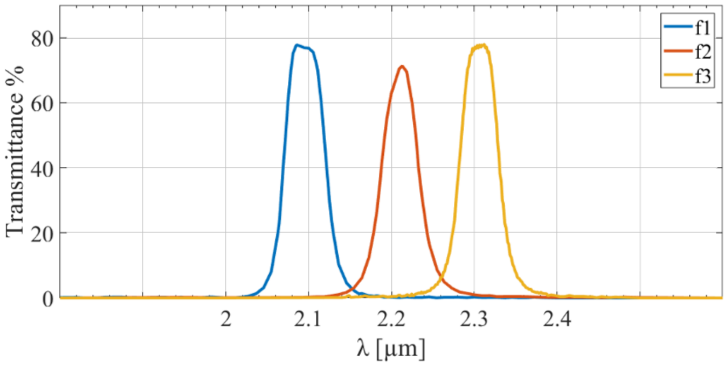

Figure 96 Transmittance curves for the selected filters provided by the producer[157]: Spectrogon NB-2097-055-nm (f1), Spectrogon NB-2210-047-nm (f2) and Spectrogon NB-2310-050-nm (f3).

Figure 96 shows the transmittance curves for the selected filters.

A check has been performed on the SR verifying that it is not influenced by the uncertainty due to the single filter measurement fluctuations, in terms of *DL* (Digital Level) [126]. This means that considering an uncertainty for the FLIR ORION 7600 thermal camera (*ΔDL*) of

1/1000 [157] for the output value of the *DL* and assuming also $DL_1 \approx DL_2 \approx DL$ and $\Delta DL_1 \approx \Delta DL_2 \approx \Delta DL$, the *SR* uncertainty due to *ΔDL* can be expressed as:

$$\Delta SR(T) = \sqrt{\left(\frac{\partial SR}{\partial DL_2} \cdot \Delta DL_2\right)^2 + \left(\frac{\partial SR}{\partial DL_1} \cdot \Delta DL_1\right)^2}$$

$$= \sqrt{\left(\frac{\partial(\frac{DL_1}{DL_2})}{\partial DL_2} \cdot \Delta DL_2\right)^2 + \left(\frac{\partial(\frac{DL_1}{DL_2})}{\partial DL_1} \cdot \Delta DL_1\right)^2} = \qquad \text{Eq 157}$$

$$= \sqrt{\left(-\frac{DL_1}{{DL_2}^2} \cdot \Delta DL_2\right)^2 + \left(\frac{1}{DL_2} \cdot \Delta DL_1\right)^2} \approx \frac{\Delta DL}{DL} \cdot \sqrt{2} = 0{,}001 \cdot \sqrt{2} \approx 0{,}001$$

Imposing a minimum accuracy of *τ%* on temperature measurement (i.e. $\Delta T \leq \tau\%\ T$), approximating $\Delta S(T) \cong \partial SR$ and $\Delta T \cong \partial T$, the following relation must be satisfied:

$$\frac{\partial SR(T)}{\partial T} \geq \frac{0{,}001}{\tau\% T} \qquad \text{Eq 158}$$

Graphically, this corresponds to consider acceptable curves *∂SR (T) / ∂T* that remain above the curve representing the accuracy limit of 0.001 / (*τ% T*). The threshold has been selected considering the accuracy on the measured temperature value, of 2%, as stated by the IR camera developer [157]. As shown in *Figure 97*, this condition is verified for all the operative configurations considered when a relative accuracy of 2% is imposed.

To extend the temperature measurements range an attenuator was also chosen for pre-filtering:

- Spectrogon ND-IR-OD-1.0-Ø25.4x1.0 mm (*$A_{10\%}$*)

Considering the actual response curves of sensor, optics and filters (*Figure 92* and *Figure 96*) and attenuators [157][157], it was possible to estimate the temperature range that can be measured in different configurations.

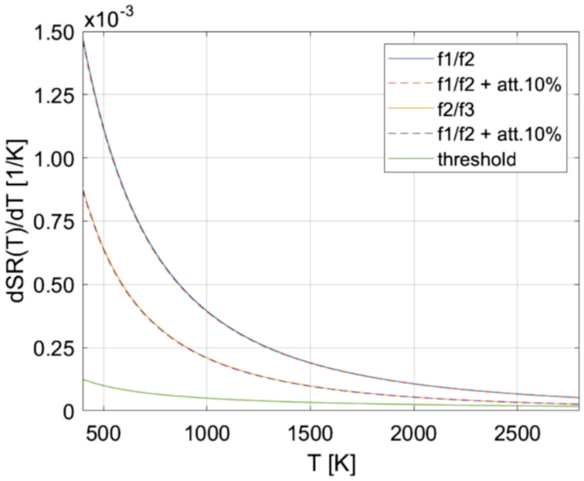

Figure 97 The derivative of SR respect to the temperature for different couples of filters (including also the condition with attenuator) is shown. The dSR(T)/dT curves have been obtained by implementing the real transmittance curves of filters and attenuators.

The sensitivity and saturation limits for each configuration reported in Table 41 and plotted in *Figure 98* were estimated by evaluating the radiation detected by the sensor at the temperature limit values in the absence of filters.

Table 41 Temperature ranges for each filters configuration

Filter	**Temperature ranges (°C)**		
	No Attenuation	***A_{std}***	***$A_{10\%}$***
F_{std}	179.9 - 1516.4	569.7-OVER 3000	-
f1	374.6 - 1239.7	-	552.5 - 2652.5
f2	368.3 - 1318.9	-	554.0 - 3064.8
f3	346.3 - 1277.2	-	526.2 - 3278.9

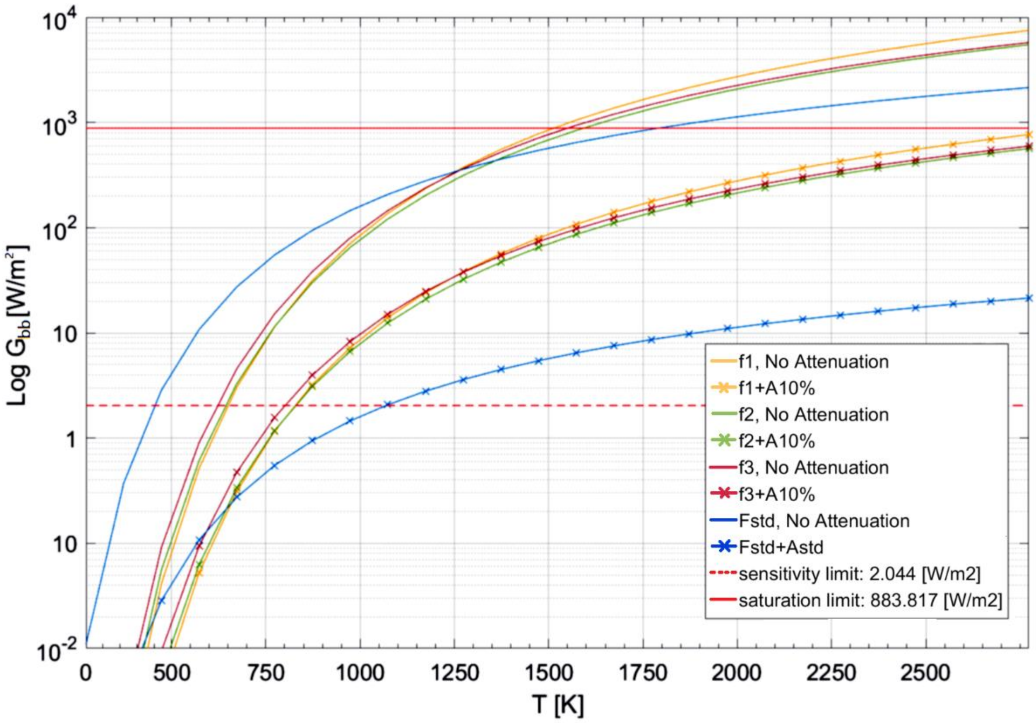

Figure 98 The thermosignal for a black body detected by the IR camera sensor in different filters-attenuator configuration (in logarithmic scale) vs temperature. All the configurations have been simulated considering the actual response curves for filters and attenuators. The sensitivity limit and the saturation limit are also reported.

7.2. Analytical simulation

In such a way to evaluate the applicability of the Dual Color technique to high temperature, like those reached during PWT tests, and the use of such technique for any kind of TPS materials (meaning any kind of emissivity), several materials at different temperature have been selected among the limited amount listed in the literature in the IR camera spectral range ([158][159][160][161][162][163]).

In the present work the materials have been divided into the following classes:

- Low Emissivity Materials, $\varepsilon < 0.4$ in the spectral operating band of the IR camera;
- Mid Emissivity Materials, $0.4 < \varepsilon < 0.8$ in the spectral band of operation of the IR camera;
- High Emissivity Materials, $\varepsilon > 0.8$ in the spectral operating band of the IR camera.

Using Eq 83, the virtual built-in IR camera was used to evaluate the values of the radiation detected by the IR camera sensor when the materials (with their emissivity curve, plotted in *Figure 99*, *Figure 100* and *Figure 101*) are at specific temperatures.

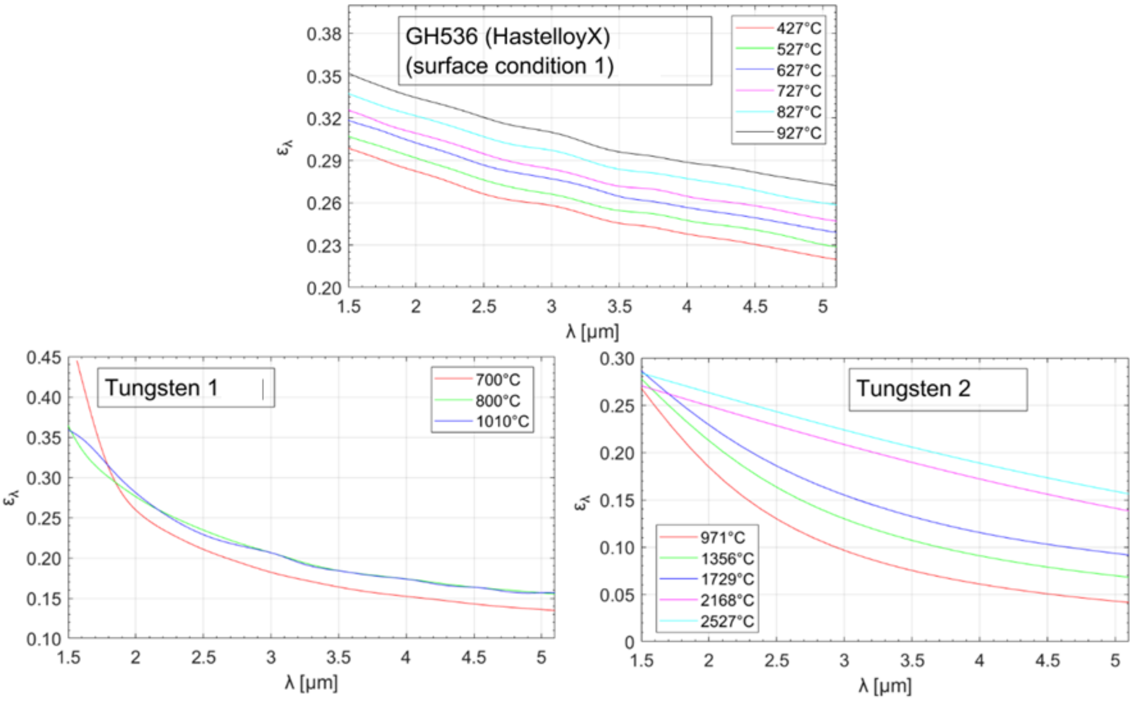

Figure 99 Spectral Emissivity curves of the low emissivity materials selected for the numerical simulation. The curves have been obtained using data available in literature[158][159][160].

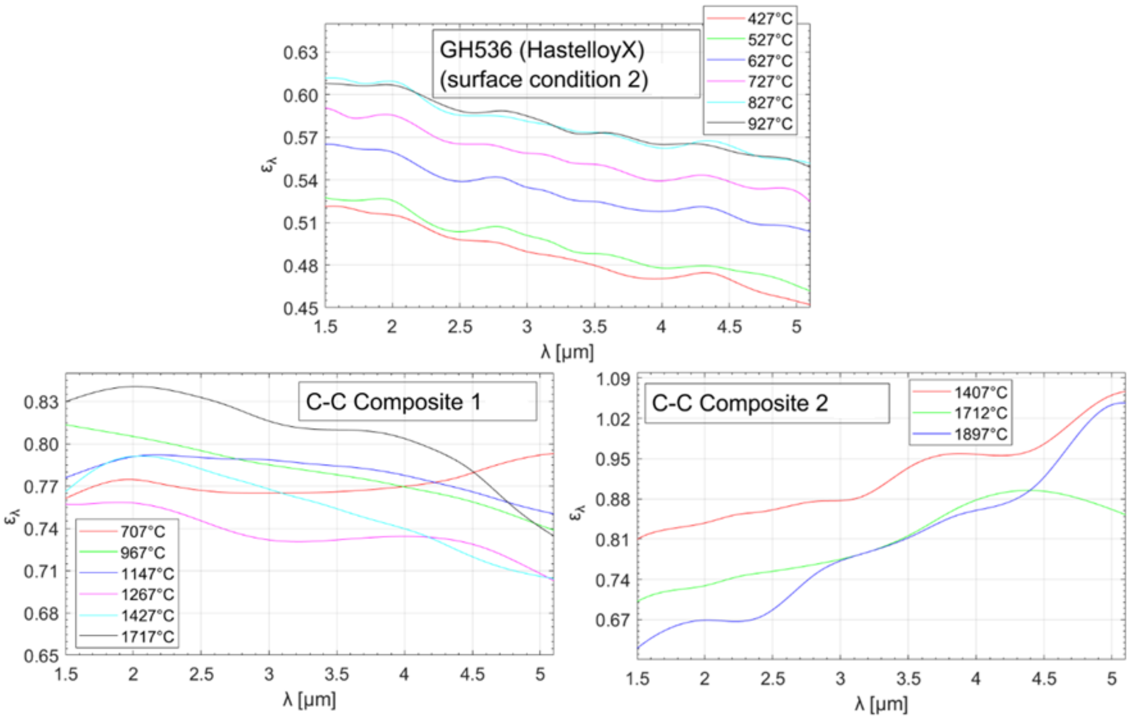

Figure 100 Spectral Emissivity curves of the mid emissivity materials selected for the numerical simulation. The curves have been obtained using data available in literature[158][161][162].

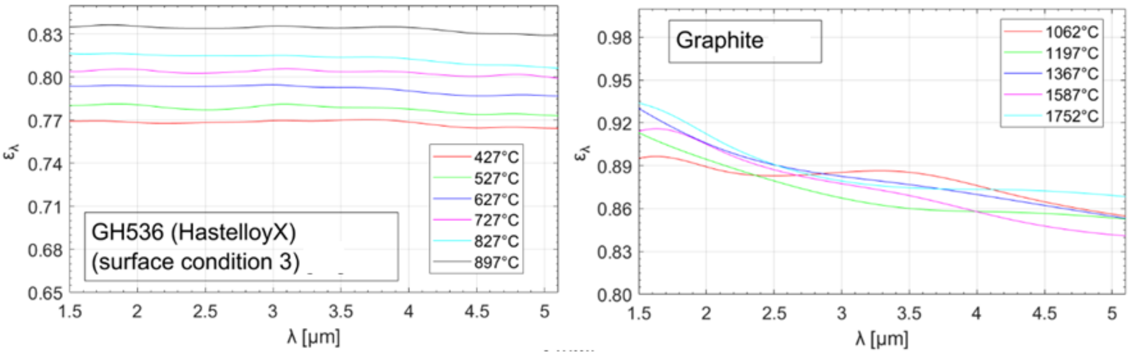

Figure 101 Spectral Emissivity curves of the high emissivity materials selected for the numerical simulation. The curves have been obtained using data available in literature[158][163].

An analysis of accuracy has been performed in such a way to compare three different approaches:

- Classical Technique (with a standard set up)
- Single color
- Dual color

The selected materials are listed in Table 42, together with the temperatures at which the emissivity curves are known in the operating range of the IR camera. The configuration of the filters used for the simulation is also shown.

Table 42 Selected materials are listed with the temperatures at which the emissivity curves are known in the operating range of the camera. The configuration of the filters used for the simulation is also shown.

MATERIAL	Temperature [°C]	Dual color filter configuration	Single Color filter configuration and local average emissivity	Classical technique filter configuration and average emissivity
GH536 (HastelloyX) (surface condition 1) [20]	427 527 627 727 827 927	Couple of filters *f1/f2*	Filter *f1* ε_{medf1}=0.30	standard filter ε_{med}=0.26
		Couple of filters *f2/f3*	Filter *f2* ε_{medf2}=0.30	
			Filter *f3* ε_{medf3}=0.30	
Tungsten 1 [21]	700 800 1010	Couple of filters *f1/f2* with 10% attenuator	Filter *f1* with 10% attenuator ε_{medf1}=0.27	standard filter and attenuator ε_{med}=0.17
		Couple of filters *f2/f3* with 10% attenuator	Filter *f2* with 10% attenuator ε_{medf2}=0.25	
			Filter f3 with 10% attenuator ε_{medf3}=0.25	
Tungsten 2 [22]	971 1356 1729 2168 2527	Couple of filters *f1/f2* with 10% attenuator	Filter f1 with 10% attenuator ε_{medf1}=0.22	standard filter and attenuator ε_{med}=0.12
		Couple of filters *f2/f3* with 10% attenuator	Filter f2 with 10% attenuator ε_{medf2}=0.21	
			Filter f3 with 10% attenuator ε_{medf3}=0.20	
GGH536 (HastelloyX) (surface condition 2) [20]	427 527 627 727 827 927	Couple of filters *f1/f2*	Filter f1 ε_{medf1}=0.57	standard filter ε_{med}=0.52
		Couple of filters *f2/f3*	Filter f2 ε_{medf2}=0.56	
			Filter f3 ε_{medf3}=0.55	
C-C composite 1 [23]	707 967 1147 1267 1427 1717	Couple of filters *f1/f2* with 10% attenuator	Filter f1 with 10% attenuator ε_{medf1}=0.80	standard filter and attenuator ε_{med}=0.76
		Couple of filters *f2/f3* with 10% attenuator	Filter f2 with 10% attenuator ε_{medf2}=0.80	
			Filter f3 with 10% attenuator ε_{medf3}=0.80	
C-C composite 2 [24]	1407 1712 1897	Couple of filters *f1/f2* with 10% attenuator	Filter f1 with 10% attenuator ε_{medf1}=0.76	standard filter and attenuator ε_{med}=0.9
		Couple of filters *f2/f3* with 10% attenuator	Filter f2 with 10% attenuator ε_{medf2}=0.77	
			Filter f3 with 10% attenuator ε_{medf3}=0.78	
GH536 (HastelloyX) (surface condition 1) [20]	427 527 627 727 827 927	Couple of filters *f1/f2*	Filter f1 ε_{medf1}=0.80	standard filter ε_{med}=0.80
		Couple of filters *f2/f3*	Filter f2 ε_{medf2}=0.80	
			Filter f3 ε_{medf3}=0.80	
Graphite [25]	1062 1197 1367 1587 1752	Couple of filters *f1/f2* with 10% attenuator	Filter *f1* with 10% attenuator ε_{medf1}=0.90	standard filter ε_{med}=0.86
		Couple of filters *f2/f3* with 10% attenuator	Filter *f2* with 10% attenuator ε_{medf2}=0.89	
			Filter *f3* with 10% attenuator ε_{medf3}=0.89	

7.3. Temperature measurement with Standard (Classic - Single Color) and Dual Color Techniques

The classical thermographic measurements with the standard set up are based on the local grey body hypothesis, which consists in the assumption of constant values for emissivity throughout the applied filter transmittance spectral band. Therefore, for each selected material, a local average emissivity ε_{med} has been considered, calculated as an average of the mean values of different temperatures curves in the transmittance spectral band of the applied filter.

The simulation has been carried out evaluating $G_{real}(T_{real})$, the thermosignal of the material at temperature T_{real}, with the IR camera in a standard operative configuration, i.e. equipped with the standard filter and, when necessary, the standard attenuator provided by the producer, in order to reach high temperatures. To get $G_{real}(T_{real})$ Eq 83 has been used considering: the spectral range of the FLIR Orion Sc7600 as integration interval; the spectral response of the sensor and the transmittance curves for the optics, filter and - when necessary – attenuator (*Figure* 92); the known emissivity curve for each material at T_{real}.

The temperature T_{CT} revealed through the classical technique is such as to satisfy the following:

$$G_{real}(T_{real}) = \varepsilon_{med} \cdot G_{bb}(T_{CT}) \qquad \text{Eq 159}$$

Using Eq 159, the temperature value with the standard set up (T_{CT}) has been found for several values of T_{real} (Table 42).

As regard the single color technique, the measurements of $G_{real}(T_{real})$ with Eq 83 were simulated by equipping the IR Camera with each of the filters and - when necessary - the attenuator selected in paragraph 7.1.

$G_{real}(T_{real})$ was then matched to the radiation detected by the virtual IR camera, in the same previous configuration, for a black body at temperature T_{SC} (G_{bF}) multiplied for the local average emissivity value (ε_{med})

$$G_{realF}(T_{real}) = \varepsilon_{med} \cdot G_{bF}(T_{SC}) \qquad \text{Eq 160}$$

The temperature evaluated with the single color technique T_{SC} has been found for each selected material for the values of T_{real} at which the emissivity curves are known (Table 42).

A simple graphical representation of the evaluation process of T_{SC} is shown in Figure 102: the fixed temperature value T_{real} is used to enter the curve $G_{realF}(T_{real})$, the corresponding value of the thermal signal is then used to go into the curve $G_{sc}(T) = \varepsilon_{medF} \cdot G_{bF}(T_{SC})$ and then find the temperature T_{SC}.

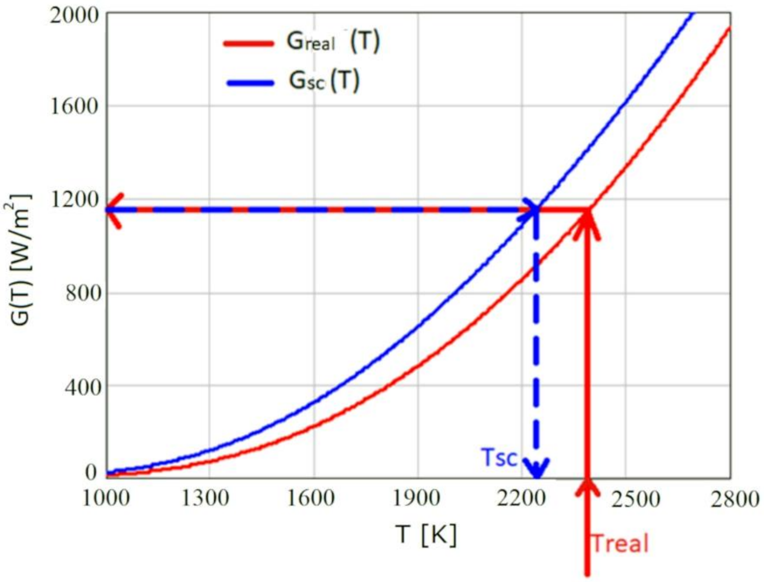

Figure 102 Graphical representation of the evaluation process of TSC. Tungsten 2 [160] was used.

Regarding the dual color technique the analysis has been carried out putting $SR_{realF1\_F2}(T_{real})$, that is the signals ratio detected by the virtual IR camera equipped with the filter *F1* and *F2* (where radiation associated to *F1* and *F2* is obtained from Eq 83 that includes emissivity trend), equal to the signal ratio $SR_{bF1\_F2}(T_{DC})$ (obtained from the ratio between Eq 86 and Eq 87) (Eq 161).

$$SR_{realF1\_F2}(T_{real}) = SR_{bF1\_F2}(T_{DC}) \qquad \text{Eq 161}$$

Using Eq 161 the temperature value estimated with the dual color technique (T_{DC}) has been found for several values of T_{real} and for two different couples of filters defined in paragraph 7.1. (Table 42).

A simple graphical representation of the evaluation process of T_{DC} is shown in Figure 103: the fixed temperature value T_{real} is used to go into the curve of the signals ratio for a real surface $SR_{realF1\_F2}(T)$, the corresponding value is then used to enter the curve of the signals ratio for a black body $SR_{bF1\_F2}(T)$ and find its correspondent temperature value T_{DC}.

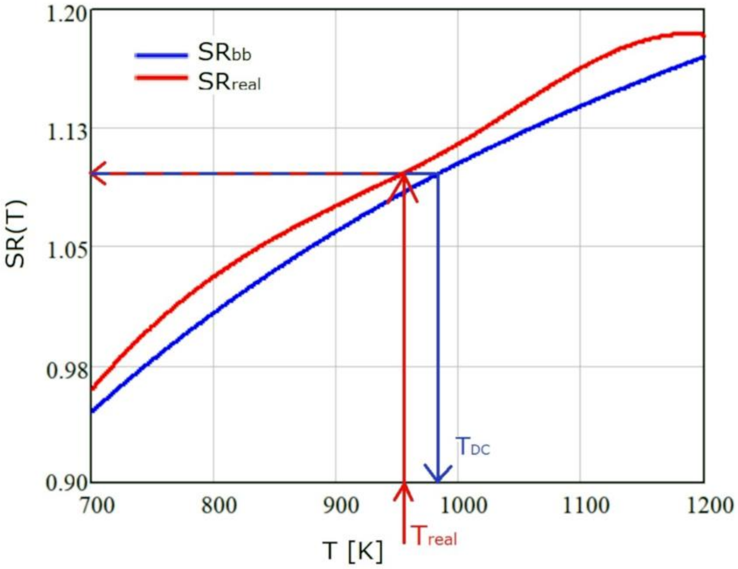

Figure 103 Graphical representation of the evaluation process of TDC. GH536 (HastelloyX) (surface condition 2) [158] was used.

Indicating with T_{meas} the temperature value obtained using the simulation techniques measuring an imposed T_{real}, the accuracy in temperature was evaluated as:

$$er\% = \frac{|T_{real} - T_{meas}|}{T_{real}} \quad \text{Eq 162}$$

This will allow to compare dual color technique and standard technique in order to evaluate the benefit of the dual color when a degree of uncertainty is associated to the emissivity knowledge.

7.4. Analysis of accuracy

The accuracy can be analytically described as a function of the main process variables.

The spectral density of radiation can be written as:

$$E_\lambda(T) = \varepsilon_\lambda \cdot \frac{C_1}{\lambda^5 \cdot \left(e^{\frac{C_2}{\lambda \cdot T}} - 1\right)} \left[\frac{W}{m^2 \cdot sr\ nm}\right] \qquad \text{Eq 163}$$

The exponent of exponential function in Eq 163 is given by the ratio between C_2, which is of the order of 10^4 μm · K, and the product λ · T which instead, in reference to Wien's law, is of the order of 10^3 μm · K in the spectral and thermal range of our interest (λ~ 2 μm and T ~ 2000 K), therefore it is possible to assume $e^{[C_2/(\lambda T)]} \approx e^{10} >> 1$ and consider the following approximation valid:

$$e^{\frac{C_2}{T \cdot \lambda}} - 1 \approx e^{\frac{C_2}{T \cdot \lambda}} \qquad \text{Eq 164}$$

Substituting in Eq 163 and applying logarithms:

$$ln\, E_\lambda\,(T) = ln\, \varepsilon_\lambda + ln\, C_1 - 5 \cdot ln\, \lambda - \frac{C_2}{T \cdot \lambda} \qquad \text{Eq 165}$$

Eq 165 can be written both as function of T_{real} and as a function of T_{CT}:

$$ln\, E_\lambda\,(T_{real}) = ln\, \varepsilon_\lambda + ln\, C_1 - 5 \cdot ln\, \lambda - \frac{C_2}{T_{real} \cdot \lambda} \qquad \text{Eq 166}$$

$$ln\, E_\lambda\,(T_{CT}) = ln\, \varepsilon_{med} + ln\, C_1 - 5 \cdot ln\, \lambda - \frac{C_2}{T_{CT} \cdot \lambda} \qquad \text{Eq 167}$$

Indicating the absolute value of the difference between the $lnE_\lambda(T_{real})$ and $lnE_\lambda(T_{CT})$ as "Res", or residual, from Eq 166 and Eq 167 derives:

$$\frac{|T_{real} - T_{CT}|}{T_{real}} = T_{CT} \cdot \frac{\lambda}{C_2} \cdot \left(ln \frac{\varepsilon_{med}}{\varepsilon_\lambda} + Re\, s\right) \qquad \text{Eq 168}$$

The term on the left in Eq 168 is the analytical expression of the relative accuracy on measurements using a standard set up.

Appling the same analysis, the analytical expression of the accuracy on measurements using the single color technique can be found:

$$\frac{|T_{real} - T_{SC}|}{T_{real}} = T_{SC} \cdot \frac{\lambda}{C_2} \cdot \left(ln \frac{\varepsilon_{med}}{\varepsilon_{\lambda}} + Re\,s \right) \qquad \text{Eq 169}$$

In a similar way to the other two techniques, also for the dual color it is possible to find an analytical expression of the accuracy.

Considering Eq 164, eq. 4 can be written in the form:

$$IRR(T_{obj}) = \frac{\varepsilon_{obj1}}{\varepsilon_{obj2}} \left(\frac{\lambda_2}{\lambda_1} \right)^5 e^{\frac{C_2}{T_{obj}} \left(\frac{1}{\lambda_1} - \frac{1}{\lambda_2} \right)} \qquad \text{Eq 170}$$

With logarithms application, Eq 170 becomes:

$$ln\left(IRR(T_{obj}) \right) = ln \left(\frac{\varepsilon_{obj1}}{\varepsilon_{obj2}} \right) + 5\, ln \left(\frac{\lambda_2}{\lambda_1} \right) + \frac{C_2}{T_{obj}} \left(\frac{1}{\lambda_1} - \frac{1}{\lambda_2} \right) \qquad \text{Eq 171}$$

Eq 171 can be written both as function of T_{real} and as a function of T_{DC}:

$$ln\left(IRR(T_{real}) \right) = ln \left(\frac{\varepsilon_{obj1}}{\varepsilon_{obj2}} \right) + 5\, ln \left(\frac{\lambda_2}{\lambda_1} \right) + \frac{C_2}{T_{real}} \left(\frac{1}{\lambda_1} - \frac{1}{\lambda_2} \right) \qquad \text{Eq 172}$$

$$ln\left(IRR(T_{DC}) \right) = ln(1) + 5\, ln \left(\frac{\lambda_2}{\lambda_1} \right) + \frac{C_2}{T_{DC}} \left(\frac{1}{\lambda_1} - \frac{1}{\lambda_2} \right) = 5\, ln \left(\frac{\lambda_2}{\lambda_1} \right) + \frac{C_2}{T_{DC}} \left(\frac{1}{\lambda_1} - \frac{1}{\lambda_2} \right) \qquad \text{Eq 173}$$

Indicating the absolute value of the difference between the ln(IRR(T_{real})) and ln(IRR(T_{CT})) as "Res", or residual, from Eq 172 and Eq 173 derives:

$$\frac{|T_{real} - T_{DC}|}{T_{real}} = \frac{T_{DC}}{C_2} \cdot \frac{\lambda_1 \lambda_2}{|\lambda_2 - \lambda_1|} \cdot \left(ln \frac{\varepsilon_{obj1}}{\varepsilon_{obj2}} + Re\,s \right) \qquad \text{Eq 174}$$

The terms on the left of the Eq 168, Eq 169 and Eq 174 represents the analytical expression of the relative accuracy on measurements using the classical, the single color and the dual color techniques respectively.

Eq 168 and Eq 169 show analytically how the accuracy decreases linearly by increasing the revealed temperature T_{SC} (T_{CT} in Eq 169) and wavelength λ and with natural logarithm of average emissivity.

Eq 174 shows how the uncertainty on the temperature measurement using the dual color technique grows linearly with T_{DC}, with the product $\lambda_1\lambda_2$ and with the natural logarithm of the ratio $\varepsilon_{obj1}/\varepsilon_{obj2}$ (which is as much higher as the gray body hypothesis does not approximate real behavior), while it linearly decreases with the increasing of the distance between the central wavelengths of the applied filters.

7.5. Model experimental validation

The analytical model used for analysis has been already validate from 100°C to 650°C by Savino et al. [126]. In this work, to extend the analysis to temperature values compatible with those experienced in PWT and used in this work, the model validation has been extended up to 2000°C.

It is important to underline as the proposed model can be used to replicate the response of any IR camera of which spectral response and transmittance curves are known.

Therefore, the experimental data have been obtained by using a micro-bolometric IR detector operating between 7.5 and 14 μm (IR camera FLIR A655, whose response curve of the detector and the optic are reported in Figure 104) and three different black bodies: MIKRON M310, MIKRON M305 and MIKRON M390. Each black body operates in a different temperature range, in order to cover the considered temperature range (from 50°C up to 2000°C).

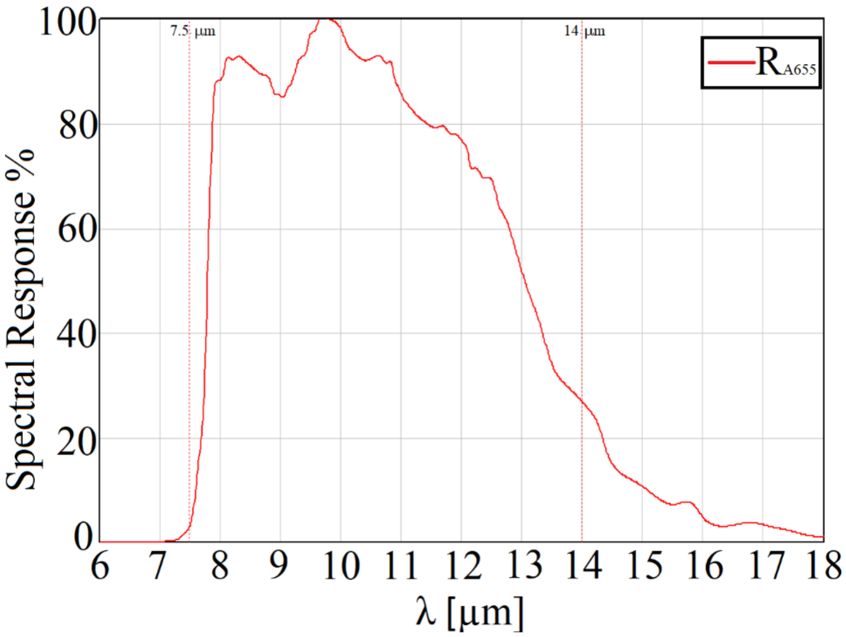

Figure 104 Response curve of the detector of the IR camera FLIR A655 is shown. The curve includes the response of the optics in front of the camera.

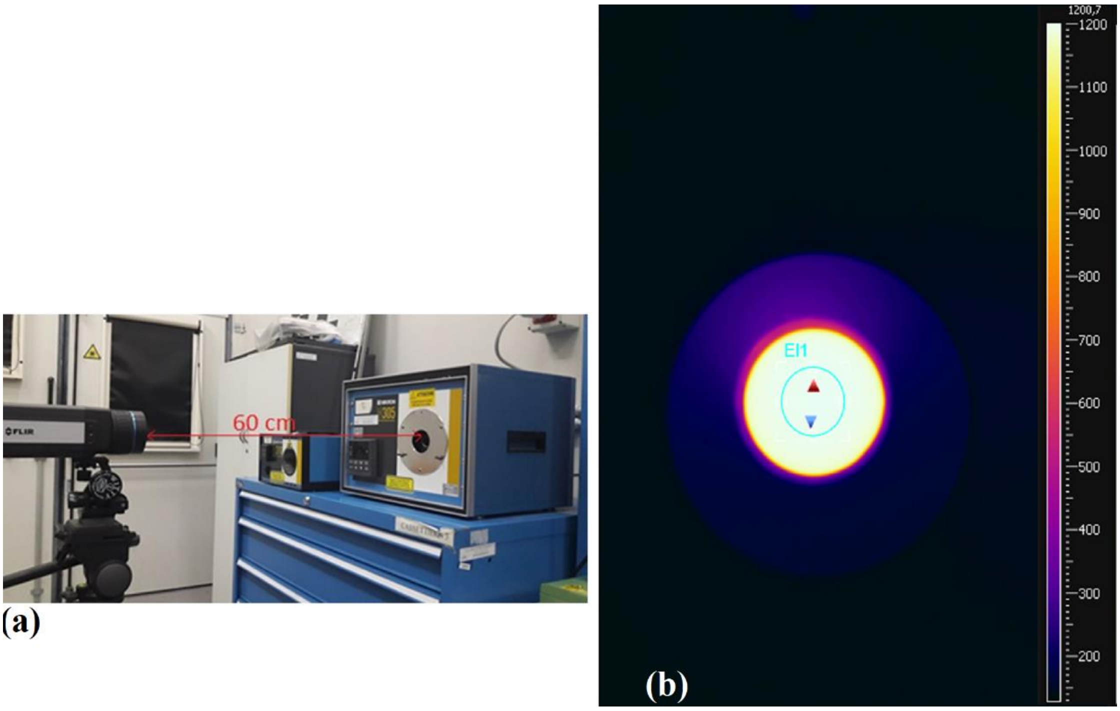

Figure 105 (a) Experimental set-up. (b) Screen capture from the software FLIR Researcher Max during temperature acquisition from the black body MIKRON M310. The circular blue line borders the area considered for the evaluation of the average signal, while the red and blue triangles point to the hottest and coldest spot respectively; the coloured bar indicates the object signal values.

To analytically simulate the same measurements, the model has been implemented in MATHCAD code using the real transmittance curves provided by the producer for sensors and optics[157].

In Table 43 and Table 44 temperature ranges and object parameters are reported.

Table 43 Temperature ranges of experimental measurements are shown.

BLACK BODY	**TEMPERATURE RANGE [°C]**
MIKRON M310	50-300
MIKRON M305	200-900
MIKRON M390	900-2000

Table 44 Object parameters are shown.

EMISSIVITY	0.995
ENVIRONMENTAL TEMPERATURE	20.0 °C
RELATIVE HUMIDITY	0.5
ATMOSPHERIC TRASMITTANCE COEFFICIENT	0.99
CAMERA-BLACK BODY DISTANCE	60 cm

ACQUISITION FREQUENCY	6.25 fps (frame per second)
ACQUISITION TIME	160 ms

Thermographic data have been collected and processed by the software Researcher Max (FLIR). Average value of the signal has been considered in a circular area in the central cavity of each black body (Figure *105*).

7.6. Results

7.6.1. Model validation

In order to validate the proposed model, the experimental campaign was carried out using IR camera FLIR A655 with a micro-bolometric IR detector operating between 7.5 and 14 μm (whose detector response curve and the optics are reported in Figure 104).The black bodies employed, and the relative temperature ranges are reported in Table 43.

In Figure 106, Figure 107 and Figure 108, results are plotted in terms of the analytical radiance and the experimentally detected object signal. $G_a(T)$ is obtained from Eq 83 considering that no filter or attenuator is applied in front of the camera (i.e. F(λ)=1 and A(λ)=1), while spectral curve of the detector is reported in Figure *104* that includes the response of the optics in front of the camera. Experimental data (blue circles) refers to middle values on the observed area, while analytical results (red curves) are plotted with upper and lower limits which indicates a theoretical uncertainty of ±2% on temperature measurements stated by the hardware developer.

Results fit very well with the experimental measurements and few differences could be due to the sensor thermal drift that occurs over time and to a not exactly match between the transmittance curve provided and the actual one.

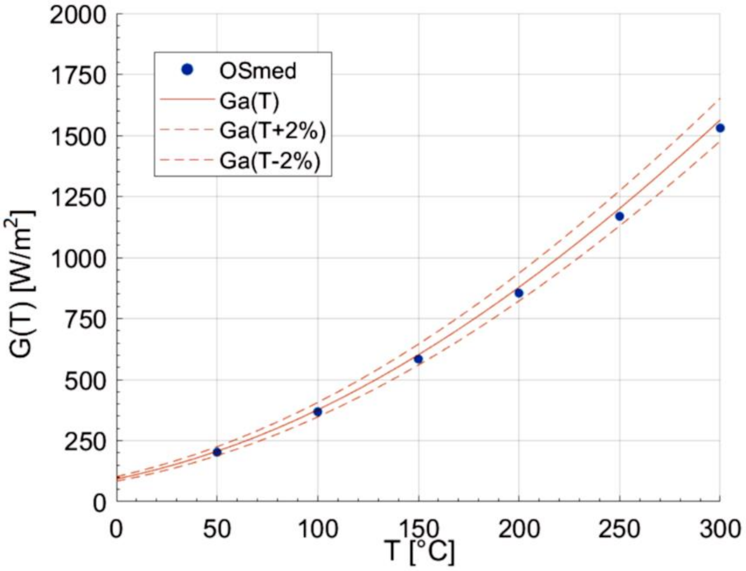

Figure 106 Comparison of the mean value of the experimentally detected radiance (indicated as object signal OSmed) measured with black body M310 for the FLIR A655 thermal camera and the analytically evaluated thermosignal in the same temperature range.

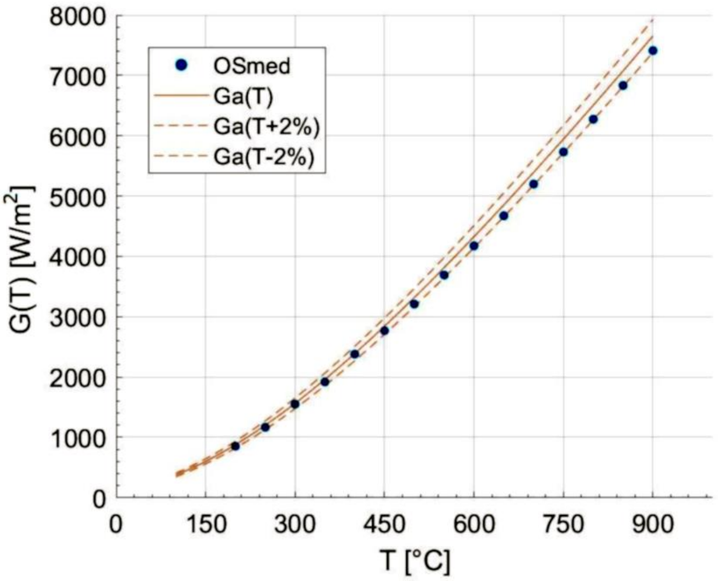

Figure 107 Comparison of the mean value of the experimentally detected radiance (indicated as object signal OSmed) measured with black body M305 for the FLIR A655 thermal camera and the analytically evaluated thermosignal in the same temperature range.

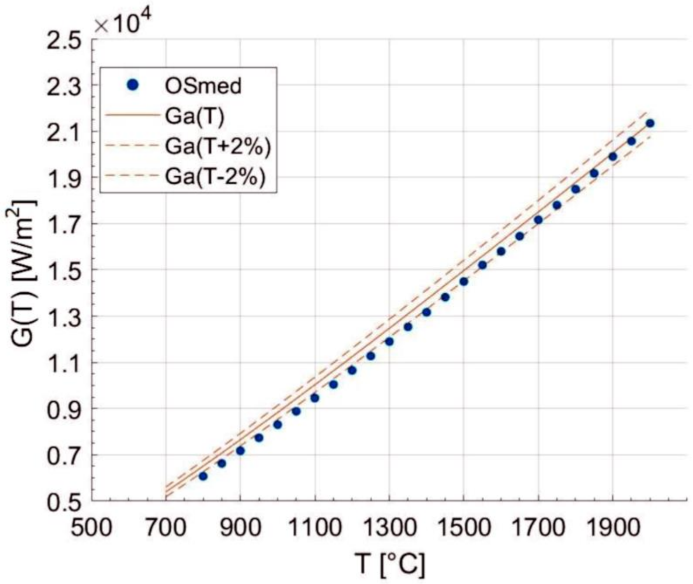

Figure 108 Comparison of the mean value of the experimentally detected radiance (indicated as object signal OSmed) measured with black body M390 for the FLIR A655 thermal camera and the analytically evaluated thermosignal in the same temperature range.

7.6.2. Results from numerical analysis

The analytical simulation was carried out building a virtual camera with the thermal response of the multispectral camera FLIR ORION SC 7600 (whose detector response curve and the optics are reported in Figure 92) equipped with filters and, if necessary, with attenuator as reported in Table 42.

The results obtained from numerical simulations show how the dual color thermographic technique is characterized by an accuracy of few % for almost all the considered materials. In the third and fourth column of Table 45 the accuracies in the dual color temperature measurements obtained for the two-different couple of filters considered are reported and calculated considering temperature in °C.

The GH536 (HastelloyX) (surf. cond. 2 and 3) shows accuracy values that are most often lower than 5% with values in the range of 0,01 to 1,58 % for the surface condition 3. This result is most likely due to the higher roughness which leads to a higher and less variable emissivity with wavelength. The high and mid emissivity materials like Graphite and C-C composite (1 and 2) present low values, ranging respectively from 0,21 to 4,16 %, from 0,32 to 2,56 % and from 2.92 to 12,70 %. The worst results are those of Tungsten, for both curves considered, where a maximum uncertainty of about 49 % has been found.

In Table 46 the accuracy values obtained with the classical technique ($er_{CT}\%$, Eq 162) are reported, while in Table 47, Table 48 and Table 49 are reported the accuracy values obtained with the single color technique ($er_{SC}\%$, Eq 162) for each filter considered. Results are relative to simulations where the average emissivity is known with an uncertainty of -60, -40, -20, 0, +20, +40 and +60 %. Better accuracy in dual color temperature measurements occurs for almost all medium-high emissivity materials when the average emissivity differs for values higher than 15-20% from the effective one. For low emissivity class, results depend on the kind of material. Therefore, for tungsten dual color temperature measurements give, in most of the cases, worst results than single color technique while for classical one, better results are obtained when the average emissivity differs for values higher than 50-60%. Concerning the GH536 (HastelloyX) (surf. cond.1) better results using dual color technique respect to the standard ones can be revealed when the average emissivity differs for values higher than 20-25%.

The analytical accuracy values found are in accordance with Eq 168, Eq 169 and Eq 174. In dual color measurements the accuracy is highly influenced by the emissivity behaviour in the spectrum, shown from the dependency in the $\log(\varepsilon_{obj1}/ \varepsilon_{obj2})$ parameter of the Eq 174. For single color and classical techniques, instead, is the $\log(\varepsilon_{med}/ \varepsilon_{obj})$ (Eq 168, Eq 169) to govern the measurements accuracy value which is strictly linked to the accuracy on the average emissivity value.

In Figure 109 it is shown a comparison of the three different approaches. For each material are reported the “temperature from technique vs the real temperatures” relative to values at which emissivity curves are known. The results have been obtained using the dual color technique (red indicator) and the classical (blue indicator) as well as single color (green indicator) techniques using the 40% accuracy on the average emissivity value. The continuous black line represents the real temperature. The ±5% precision band is also reported to graphically quantify the goodness of the measurements.

Table 45 Simulations results. In the first and second column the material and the simulation temperatures are respectively indicated; in the third and fourth column, are reported the accuracy in the dual color measurements obtained for the two-different couple of filters selected (and when necessary attenuator).

Material	T_{real} [°C]	er_{dc}%	
		$f1/f2$	$f2/f3$
GH536 (HastelloyX) (surf. Cond. 1)	427	2.59	3.23
	527	0.69	3.99
	627	2.61	1.73
	727	3.87	3.28
	827	3.89	3.34
	927	2.86	4.08
Tungsten 1	700	21.28	24.16
	800	13.72	10.88
	1010	23.79	24.3
Tungsten 2	971	40.05	42.69
	1356	44.13	47.95
	1729	48.17	48.98
	2168	40.63	47.68
	2527	48.35	46.65
GH536 (HastelloyX) (surf. Cond. 2)	427	2.95	3.01
	527	5.26	3.03
	627	3.93	3.17
	727	3.25	4.2
	827	6.96	5.28
	927	4.14	3.23
C-C Composite 1	707	0.81	0.64
	967	0.91	1.1
	1147	0.32	0.41
	1267	1.63	2.16
	1427	1.74	2.56
	1717	1.35	0.52
C-C composite 2	1407	8.36	3.92
	1712	12.7	2.92
	1897	8.53	9.81
GH536 (HastelloyX) (surf. Cond. 3)	427	0.01	0.32
	527	0.6	0.27
	627	0.07	0.12
	727	1.58	0.69
	827	0.66	0.06
	927	0.04	0.12
Graphite	1062	1.53	1.14
	1197	1.9	2.01
	1367	2.39	0.21
	1587	3.86	3.62
	1752	4.16	4.12

Table 46 Simulations results. In the first and second column the material and the simulation temperatures are respectively indicated; in the columns from the third to the ninth are reported the accuracy values obtained with the classical technique with the standard filter (and, when necessary, attenuator) relative to simulations where the average emissivity is known with a systematic error of -60, -40, -20,0, +20, +40 and +60%.

f_{std}								
Material	T_{real} [°C]	$er_{ct}\%$						
		$\Delta\varepsilon$						
		-60%	-40%	-20%	0	20%	40%	60%
GH536 (HastelloyX) (surf. Cond. 1)	427	18.9	8.8	2.59	1.76	5.06	7.68	9.83
	527	23.11	11.04	3.78	1.25	5.02	7.99	10.43
	627	27.96	13.73	5.33	0.41	4.68	8.01	10.72
	727	32.36	16	6.5	0.09	4.63	8.3	11.27
	827	38.81	19.82	8.98	1.75	3.52	7.6	10.87
	927	45.06	23.41	11.25	3.22	2.59	7.05	10.62
Tungsten 1	700	26.03	11.31	2.69	3.16	7.49	10.87	13.62
	800	35.42	17.52	7.24	0.36	4.68	8.58	11.72
	1010	42.5	20.57	8.32	0.26	5.56	10.01	13.56
Tungsten 2	971	9.54	4.3	12.29	17.68	21.64	24.71	27.2
	1356	34.78	11.69	0.96	9.17	15.02	19.47	23
	1729	61.05	27.84	10.23	0.91	8.7	14.52	19.07
	2168	101.81	53.4	28.39	12.89	2.23	5.62	11.67
	2527	132.96	72.74	41.97	23.09	10.22	0.82	6.38
GH536 (HastelloyX) (surf. Cond. 2)	427	18.57	8.52	2.35	1.99	5.27	7.88	10.02
	527	22.02	10.15	2.99	1.96	5.68	8.61	11.01
	627	28.27	13.97	5.54	0.22	4.5	7.85	10.57
	727	33.66	17.01	7.37	0.86	3.93	7.65	10.66
	827	39.6	20.42	9.49	2.2	3.12	7.22	10.52
	927	43.71	22.39	10.4	2.48	3.26	7.66	11.18
C-C Composite 1	707	31.92	15.89	6.56	0.25	4.4		
	967	41.05	19.94	8.08	0.26	5.4		
	1147	47.85	23.15	9.55	0.7	5.63		
	1267	47.27	21.6	7.57	1.51	7.98		
	1427	52.45	23.98	8.62	1.23	8.2		
	1717	67.97	32.81	14.22	2.48	5.71		
C-C composite 2	1407	59.92	29.53	13.19	2.73	4.66		
	1712	61.17	28.04	10.47	0.65	8.44		
	1897	63.81	28.67	10.17	1.47	9.58		
GH536 (HastelloyX) (surf. Cond. 3)	427	20.47	10.12	3.77	0.68	4.05		
	527	24.23	11.96	4.58	0.52	4.34		
	627	28.32	14.02	5.58	0.19	4.47		
	727	32.46	16.07	6.57	0.15	4.58		
	827	36.87	18.32	7.72	0.64	4.53		
	927	41.86	20.99	9.24	1.46	4.17		
Graphite	1062	44.71	21.68	8.89	0.51			
	1197	47.61	22.49	8.71	0.24			
	1367	53.82	25.48	10.15	0.3			
	1587	58.75	27.23	10.41	0.28			
	1752	64.7	30.25	12.04	0.54			

Table 47 Simulations results. In the first and second column the material and the simulation temperatures are respectively indicated; in the columns from the third to the ninth are reported the accuracy values obtained with the single color with the filter f1 (and when necessary attenuator) technique relative to simulations where the average emissivity is known with a systematic error of -60, -40, -20,0, +20, +40 and +60 %.

f_1								
Material	T_{real} [°C]	er_{sc}%						
		$\Delta\varepsilon$						
		-60%	-40%	-20%	0	20%	40%	60%
GH536 (HastelloyX) (surf. Cond. 1)	427	9.32	4.59	1.48	0.81	2.61	4.08	5.32
	527	11.16	5.61	2	0.64	2.69	4.36	5.77
	627	13.38	6.94	2.8	0.21	2.53	4.41	5.99
	727	15.61	8.24	3.55	0.18	2.42	4.51	6.25
	827	18.24	9.84	4.56	0.8	2.08	4.39	6.3
	927	21.16	11.65	5.74	1.57	1.6	4.14	6.23
Tungsten 1	700	14.15	7.14	2.66	0.57	3.06	5.07	6.75
	800	16.66	8.66	3.61	0	2.77	4.99	6.84
	1010	20.79	10.75	4.57	0.22	3.07	5.7	7.86
Tungsten 2	971	13.81	5.08	0.36	4.2	7.13	9.48	11.41
	1356	23.94	11.07	3.39	1.9	5.84	8.95	11.48
	1729	34.34	16.97	6.97	0.25	4.68	8.5	11.57
	2168	47.51	24.39	11.51	3.06	3.03	7.68	11.39
	2527	59.42	31.19	15.81	5.87	1.19	6.54	10.77
GH536 (HastelloyX) (surf. Cond. 2)	427	9.15	4.43	1.32	0.96	2.75	4.22	5.45
	527	10.78	5.27	1.68	0.94	2.98	4.64	6.04
	627	13.35	6.91	2.77	0.23	2.55	4.44	6.01
	727	15.92	8.51	3.79	0.41	2.2	4.3	6.05
	827	18.77	10.3	4.98	1.19	1.71	4.04	5.97
	927	20.64	11.2	5.34	1.2	1.95	4.47	6.55
C-C Composite 1	707	14.38	7.29	2.77	0.49	3		
	967	19.81	10.22	4.28	0.09	3.09		
	1147	22.74	11.45	4.6	0.18	3.78		
	1267	23.42	11.22	3.89	1.19	4.99		
	1427	27.87	13.78	5.45	0.24	4.48		
	1717	35.96	18.31	8.15	1.33	3.67		
C-C composite 2	1407	32.49	17.62	8.85	2.87	1.57		
	1712	32.16	15.38	5.69	0.84	5.63		
	1897	31.13	13.5	3.41	3.34	8.27		
GH536 (HastelloyX) (surf. Cond. 3)	427	9.81	5.04	1.9	0.41	2.22		
	527	11.61	6.02	2.38	0.28	2.35		
	627	13.53	7.07	2.92	0.09	2.42		
	727	15.54	8.18	3.49	0.13	2.47		
	827	17.6	9.29	4.06	0.34	2.52		
	927	20.02	10.68	4.87	0.76	2.36		
Graphite	1062	21.06	10.63	4.23	0.25			
	1197	23.7	11.91	4.79	0.16			
	1367	27.29	13.71	5.64	0.1			
	1587	31.39	15.55	6.33	0.08			
	1752	34.83	17.21	7.08	0.29			

Table 48 Simulations results. In the first and second column the material and the simulation temperatures are respectively indicated; in the columns from the third to the ninth are reported the accuracy values obtained with the single color with the filter f2 (and when necessary attenuator) technique relative to simulations where the average emissivity is known with a systematic error of -60, -40, -20,0, +20, +40 and +60 %.

f2								
Material	T_{real} [°C]	er_{sc}%						
		$\Delta\varepsilon$						
		-60%	-40%	-20%	0	20%	40%	60%
GH536 (HastelloyX) (surf. Cond. 1)	427	9.85	4.82	1.52	0.9	2.79	4.34	5.63
	527	11.95	6.03	2.19	0.6	2.76	4.53	6
	627	14.21	7.34	2.94	0.23	2.68	4.66	6.31
	727	16.52	8.65	3.68	0.13	2.6	4.8	6.62
	827	19.35	10.37	4.77	0.8	2.23	4.66	6.66
	927	22.57	12.38	6.1	1.68	1.67	4.33	6.53
Tungsten 1	700	14.66	7.22	2.5	0.89	3.5	5.6	7.34
	800	17.84	9.27	3.9	0.08	2.84	5.18	7.12
	1010	21.91	11.22	4.67	0.09	3.36	6.11	8.36
Tungsten 2	971	13.86	4.7	0.97	4.97	8.01	10.43	12.42
	1356	24.89	11.27	3.2	2.33	6.43	9.65	12.27
	1729	36.25	17.78	7.22	0.17	4.97	8.95	12.15
	2168	51.09	26.29	12.59	3.66	2.75	7.63	11.51
	2527	63.88	33.62	17.26	6.76	0.69	6.3	10.73
GH536 (HastelloyX) (surf. Cond. 2)	427	9.73	4.71	1.42	0.99	2.88	4.42	5.72
	527	11.36	5.5	1.71	1.06	3.21	4.95	6.41
	627	14.22	7.35	2.95	0.22	2.67	4.65	6.3
	727	17.05	9.12	4.1	0.52	2.23	4.44	6.28
	827	19.89	10.83	5.19	1.18	1.87	4.31	6.33
	927	22.12	12	5.76	1.37	1.96	4.61	6.79
C-C Composite 1	707	15.28	7.72	2.92	0.52	3.16		
	967	21.08	10.82	4.52	0.1	3.25		
	1147	24.24	12.17	4.89	0.15	3.93		
	1267	24.85	11.83	4.07	1.27	5.26		
	1427	29.57	14.53	5.72	0.28	4.71		
	1717	38.17	19.33	8.58	1.41	3.83		
C-C composite 2	1407	34.31	18.43	9.16	2.86	1.8		
	1712	34.07	16.2	5.97	0.89	5.9		
	1897	31.02	12.75	2.36	4.55	9.59		
GH536 (HastelloyX) (surf. Cond. 3)	427	10.45	5.36	2.03	0.41	2.32		
	527	12.32	6.37	2.51	0.3	2.48		
	627	14.41	7.52	3.11	0.07	2.53		
	727	16.46	8.6	3.63	0.08	2.65		
	827	18.74	9.85	4.29	0.36	2.65		
	927	21.37	11.36	5.19	0.85	2.45		
Graphite	1062	22.44	11.28	4.5	0.24			
	1197	25.24	12.63	5.07	0.15			
	1367	29.02	14.51	5.95	0.11			
	1587	33.25	16.37	6.61	0.04			
	1752	36.85	18.1	7.4	0.27			

Table 49 Simulations results. In the first and second column the material and the simulation temperatures are respectively indicated; in the columns from the third to the ninth are reported the accuracy values obtained with the single color with the filter f3 (and when necessary attenuator) technique relative to simulations where the average emissivity is known with a systematic error of -60, -40, -20, 0, +20, +40 and +60 %.

f3								
Material	T_{real} [°C]	$er_{sc}\%$						
		$\Delta\varepsilon$						
		-60%	-40%	-20%	0	20%	40%	60%
GH536 (HastelloyX) (surf. Cond. 1)	427	10.27	5	1.56	0.98	2.94	4.55	5.89
	527	12.46	6.25	2.25	0.65	2.91	4.73	6.26
	627	14.97	7.74	3.14	0.17	2.72	4.78	6.49
	727	17.35	9.07	3.87	0.16	2.69	4.97	6.86
	827	20.35	10.89	5.02	0.87	2.29	4.8	6.88
	927	23.72	12.97	6.39	1.78	1.71	4.48	6.75
Tungsten 1	700	14.97	7.21	2.3	1.21	3.9	6.07	7.87
	800	18.92	9.87	4.23	0.24	2.8	5.24	7.25
	1010	22.81	11.58	4.75	0.01	3.6	6.44	8.77
Tungsten 2	971	14.05	4.52	1.34	5.46	8.59	11.08	13.12
	1356	25.76	11.52	3.13	2.52	6.76	10.08	12.78
	1729	38.04	18.62	7.6	0.27	5.06	9.17	12.47
	2168	54.13	27.79	13.44	4.13	2.53	7.59	11.6
	2527	67.97	35.94	18.73	7.6	0.16	5.99	10.58
GH536 (HastelloyX) (surf. Cond. 2)	427	10.18	4.92	1.48	1.05	3.01	4.61	5.96
	527	11.91	5.76	1.8	1.08	3.32	5.13	6.64
	627	14.93	7.71	3.11	0.2	2.75	4.8	6.51
	727	17.89	9.54	4.29	0.55	2.31	4.61	6.52
	827	20.84	11.31	5.39	1.22	1.96	4.49	6.59
	927	23.33	12.64	6.09	1.51	1.96	4.71	6.98
C-C Composite 1	707	16.03	8.07	3.06	0.53	3.28		
	967	22.11	11.31	4.72	0.11	3.37		
	1147	25.37	12.75	5.14	0.12	4.04		
	1267	25.89	12.23	4.21	1.34	5.47		
	1427	30.91	15.12	5.92	0.31	4.84		
	1717	40.02	20.21	8.98	1.52	3.91		
C-C composite 2	1407	35.61	18.96	9.29	2.76	2.06		
	1712	35.67	16.92	6.24	0.88	6.06		
	1897	31.71	12.76	2.05	5.05	10.21		
GH536 (HastelloyX) (surf. Cond. 3)	427	10.97	5.64	2.16	0.41	2.4		
	527	12.89	6.64	2.61	0.32	2.59		
	627	15.11	7.87	3.25	0.06	2.62		
	727	17.22	8.96	3.77	0.06	2.77		
	827	19.65	10.3	4.49	0.38	2.74		
	927	22.43	11.89	5.42	0.89	2.53		
Graphite	1062	23.5	11.83	4.73	0.21			
	1197	26.37	13.12	5.3	0.14			
	1367	30.42	15.15	6.21	0.21			
	1587	34.76	17.03	6.86	0.03			
	1752	38.48	18.81	7.67	0.26			

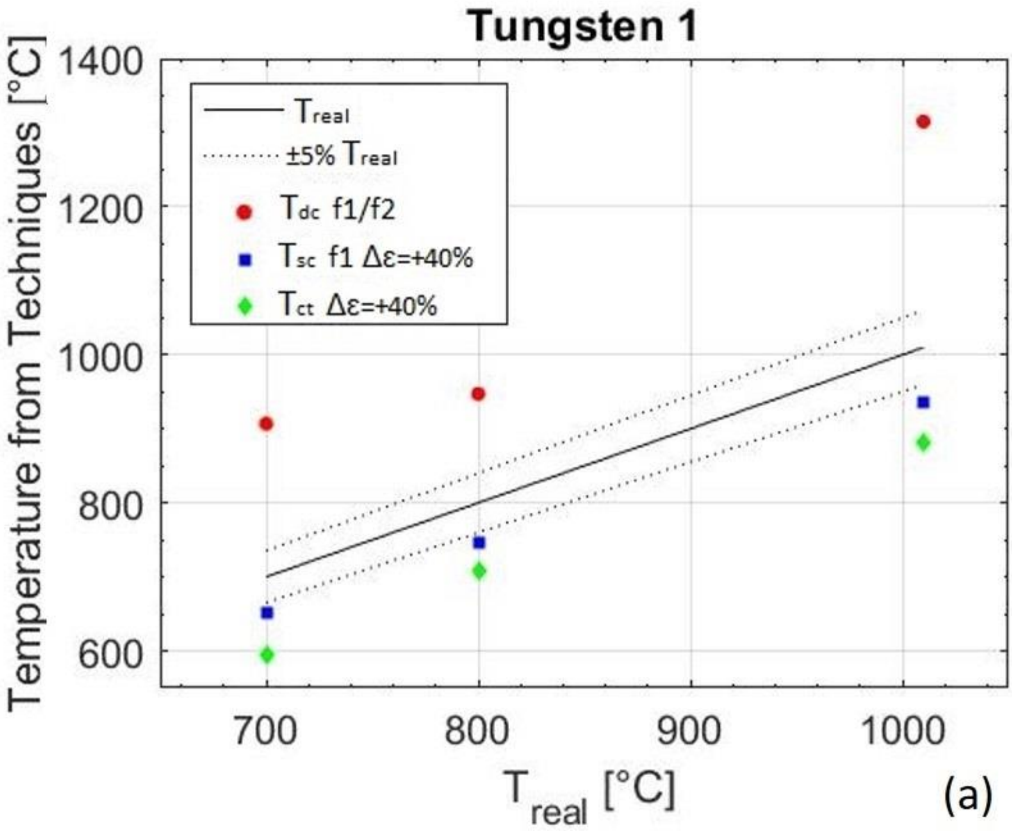
Tungsten 1
Temperature from Techniques [°C]
1400
1200
1000
800
600
700
800
900
1000
T real [°C]
T real
±5% T real
T dc f1/f2
T sc f1 Δε=+40%
T ct Δε=+40%

(a)

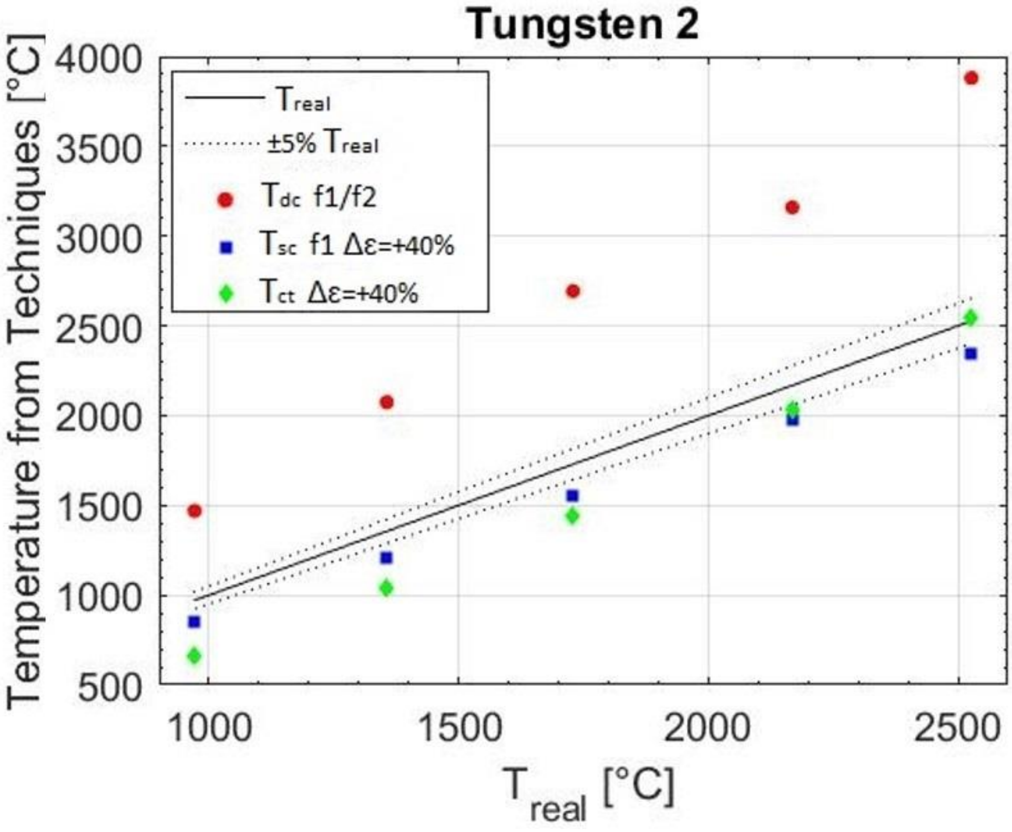
Tungsten 2
Temperature from Techniques [°C]
4000
3500
3000
2500
2000
1500
1000
500
1000
1500
2000
2500
T real [°C]
T real
±5% T real
T dc f1/f2
T sc f1 Δε=+40%
T ct Δε=+40%

(b)

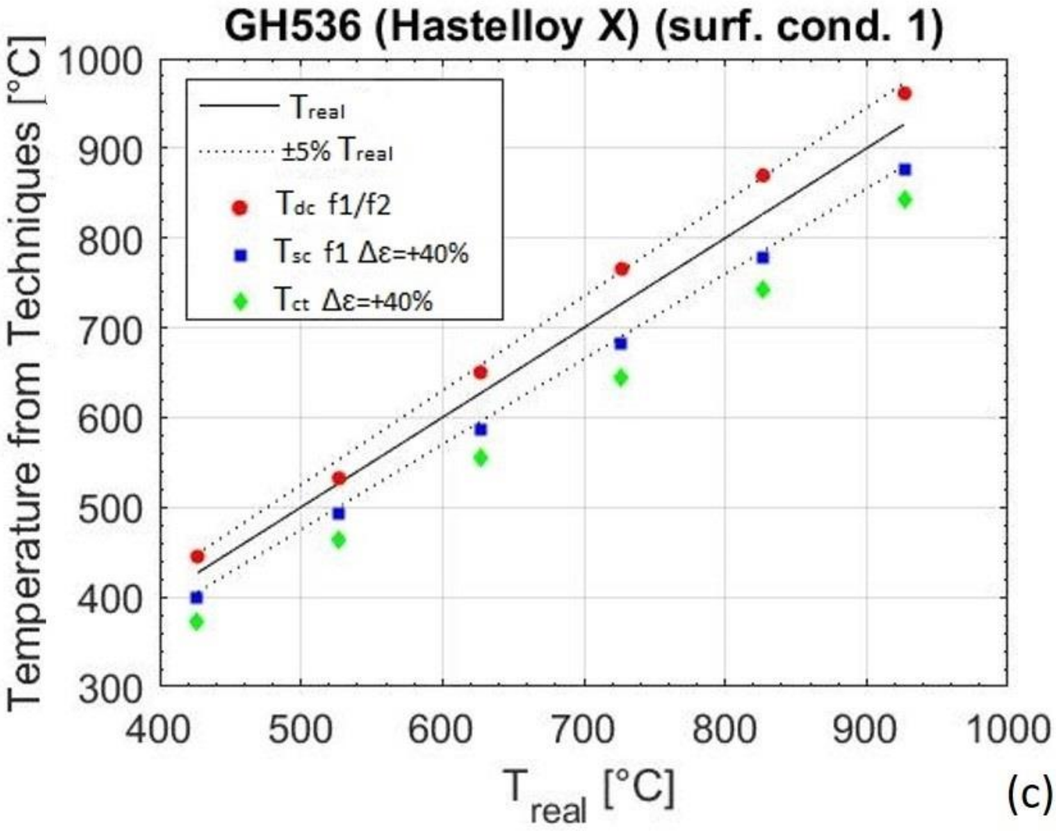
GH536 (Hastelloy X) (surf. cond. 1)
Temperature from Techniques [°C]
1000
900
800
700
600
500
400
300
400
500
600
700
800
900
1000
T real [°C]
T real
±5% T real
T dc f1/f2
T sc f1 Δε=+40%
T ct Δε=+40%

(c)

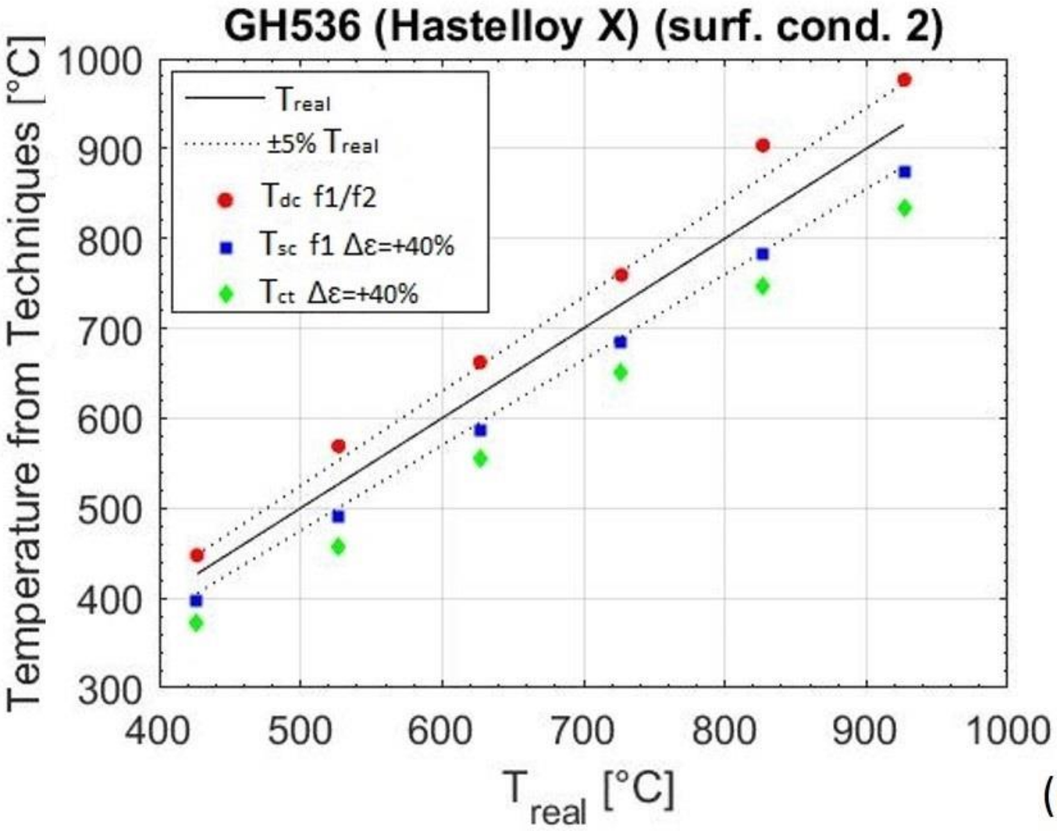
GH536 (Hastelloy X) (surf. cond. 2)
Temperature from Techniques [°C]
1000
900
800
700
600
500
400
300
400
500
600
700
800
900
1000
T real [°C]
T real
±5% T real
T dc f1/f2
T sc f1 Δε=+40%
T ct Δε=+40%

(d)

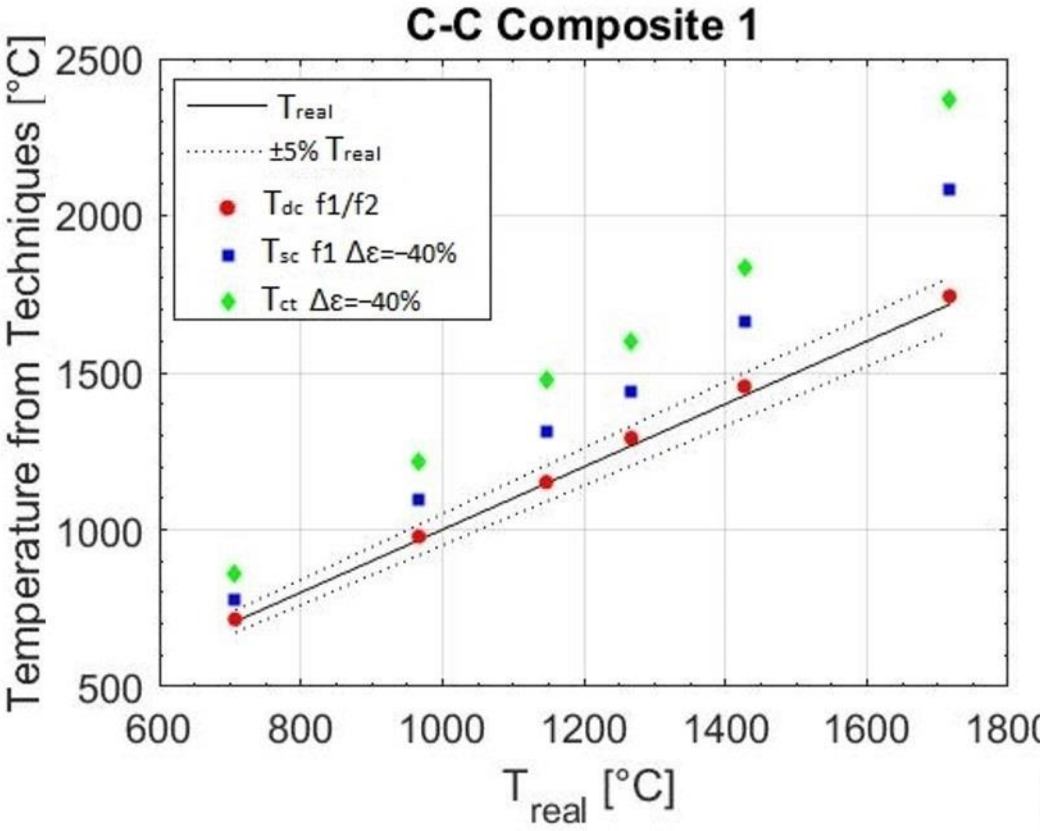
C-C Composite 1
Temperature from Techniques [°C]
2500
2000
1500
1000
500
600
800
1000
1200
1400
1600
1800
T real [°C]
T real
±5% T real
T dc f1/f2
T sc f1 Δε=−40%
T ct Δε=−40%

(e)

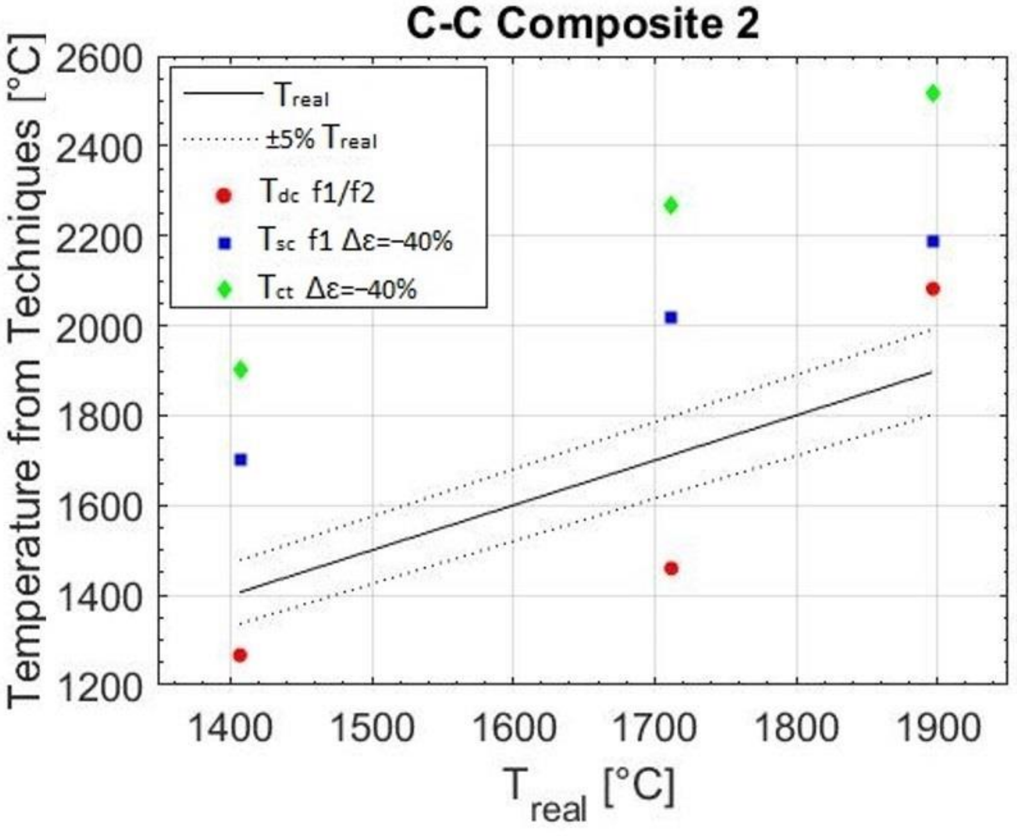
C-C Composite 2
Temperature from Techniques [°C]
2600
2400
2200
2000
1800
1600
1400
1200
1400
1500
1600
1700
1800
1900
T real [°C]
T real
±5% T real
T dc f1/f2
T sc f1 Δε=−40%
T ct Δε=−40%

(f)

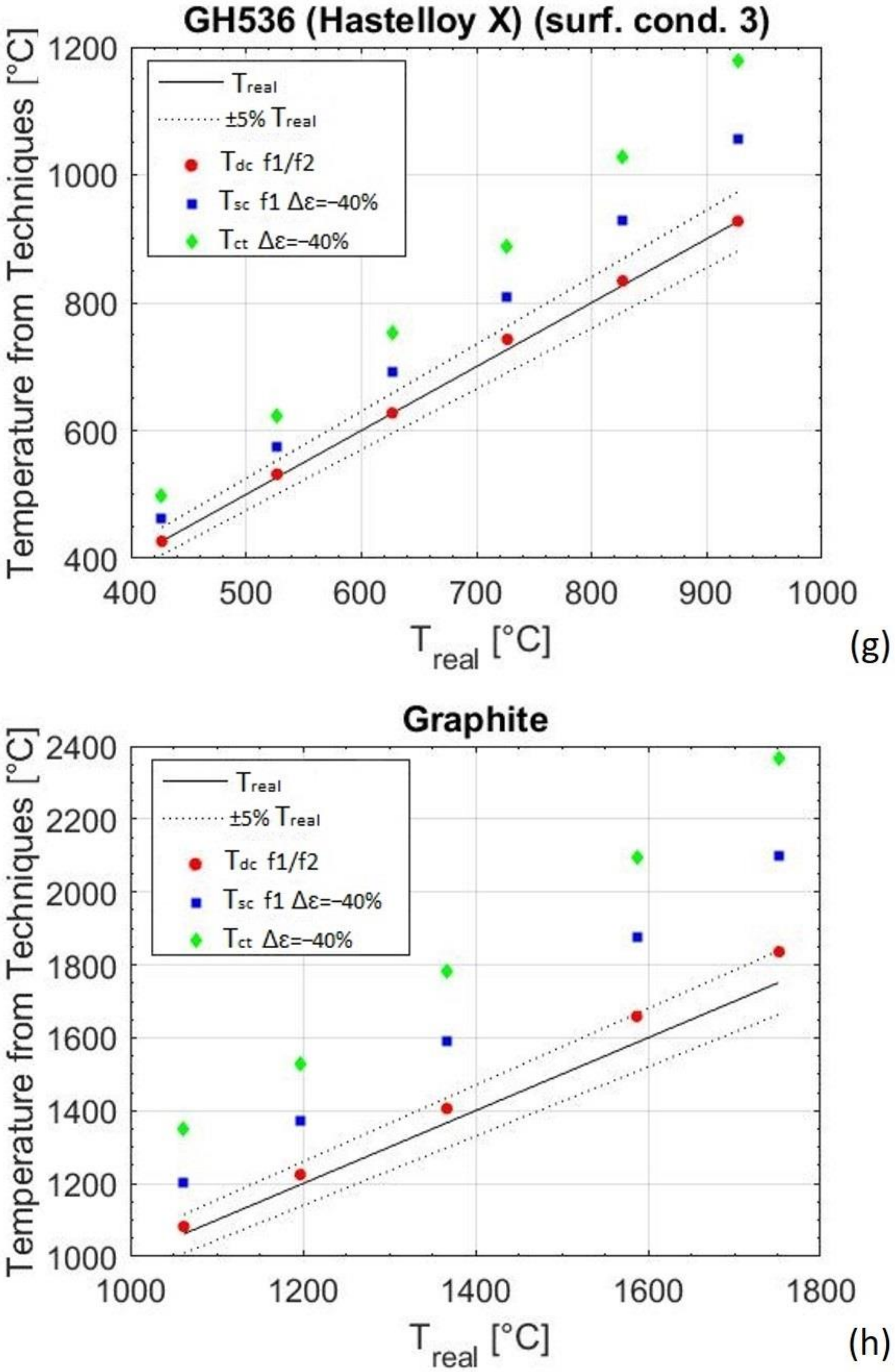

Figure 109 Comparison between the three different approaches for:(a) Tungsten1, (b) Tungsten 2, (c) GH536 (HastelloyX) (surf. Cond. 1), (d) GH536 (HastelloyX) (surf. Cond. 2), (e) C-C composite 1, (f) C-C composite 2, (g) GH536 (HastelloyX) (surf. Cond. 3), (h) Graphite. For each analytical result the ±5% precision bar is also reported.

7.7. Conclusions and outlook

In this work, the capability of the dual color technique in measuring high temperature of materials has been investigated. In particular, an analytical model capable to simulate and replicate the response of the IR camera has been developed and validated up to 2500°C. Moreover, the following main results have been obtained:

- The analytical study conducted shows that the optimum operating conditions for dual color technique is to use a multi-spectrophotometric IR camera operating in near-medium infrared range (2.0 - 2.3 μm) equipped with a pair of narrowband filters (with a full width of 50 ÷ 100 nm) and with a distance between filter central wavelengths of about 0.1μm;
- The results of the numerical simulation show a good applicability of the dual color technique for materials with medium-high emissivity ($\varepsilon>0.4$) for which it is possible to guarantee a relative temperature accuracy lower than 5%. Moreover better accuracy in dual color temperature measurements respect to the standard technique occurs when the average emissivity differs for values higher than about 15% from the effective one.
- The results obtained with dual color technique applied on low emissivity materials ($\varepsilon< 0.4$) show how, for tungsten, a better accuracy than standard technique is obtained when the average emissivity differs for values higher than about 40% from the effective one. Concerning the GH536 (HastelloyX) (surf. cond.1), better accuracy results using dual color technique respect to the standard ones can be revealed when the average emissivity differs for values higher than about 20%.

Components tested in PWT are generally made of materials that belong to a medium-high emissivity class, therefore during the tests, although the emissivity value may vary instantaneously (making difficult to find an average value to be used for the techniques single color and classical), the local grey body hypothesis is always sufficiently verified. For these reasons, the dual color technique can be a valid tool for the monitoring of the thermal fields that characterize the specimens tested in PWT.

CONCLUSIONS

In this thesis the investigation and development of thermographic techniques for stress analysis and materials characterization is presented.

The research activity was characterized by an analytical and experimental approach. All the problems were addressed with a clear strategy: the system under study is carefully characterized, trying to classify all the variables and phenomena involved and described through the physical laws that regulate it. This analysis allowed not only a targeted selection of test conditions and experimental tests, but also a more conscientious analysis and interpretation of the results.

The study carried out on the Thermoelastic Stress Analysis led to innovative contributions that in this thesis have been described step by step, guiding the reader through the research development.

A new equation for describing the thermoelastic behaviour of materials was presented. In particular, the proposed equation allows to study the behaviour of homogeneous and non-isotropic materials undergoing any loading conditions and residual stresses. The equation is valid for any material, however, its usefulness with respect to the classical TSA equation lies in the variation of the mechanical characteristics with temperature. The TSA general model is of practical interest only for those materials for which this second order effect is not negligible. By using this TSA general model, a preliminary analytical study was conducted in the simplified conditions of isotropic material and uniaxial loads to determine the sensitivity of the TSA to the variation of the mechanical and physical characteristics and to the presence of residual stresses.

The simulation results demonstrated how the main parameters affecting the thermoelastic signal of materials are their thermo physical properties (α, ρ and $C\varepsilon$), while small variations of E and $\partial E/\partial T$ do not involve a variation of the experimentally detectable.

As for the residual stresses, the simulation showed that their effect on the thermoelastic signal highly depends on each of the three characteristics that define the vector. On one side, if neglected, this effect leads to an error in the measurement, on the other side it could be exploited, by applying appropriate procedures for residual stresses estimation.

To explore this potential, all the source of error in the TSA measurement were considered and a statistical approach was implemented simulating also random variables, such as the TC noise.

The statistical analysis allowed to evaluate the minimum value of residual stresses which lead to significant and measurable variations of the thermoelastic signal for aluminium and titanium alloys.

The ANOVA and ANOM demonstrated how the influence of each parameter is strictly connected to the ranges selected for the source of error and for the parameter itself.

With the application of a robust design-like approach applied to simulation, it was also possible to establish best practice guidelines for the application of the TSA technique to minimize the effect of various sources of error and thus optimize measurement.

The study demonstrated which are the tests conditions that guarantee the smallest error range (from -2,07% to +2,07%). These includes an experimental calibration with the sample in the same residual stress condition of the component/structure, otherwise a null mean load must be adopted.

The TSA general model was also employed in the development of a novel procedure to measure residual stress.

In this case also the robust design applied to simulation has demonstrated its usefulness in the feasibility study of the proposed procedure and in its optimization, leading to the identification of the best operating conditions that make a measurement as accurate and precise as possible.

The further application of TSA is the characterization of the fracture behaviour of materials and components. In particular, three characteristics of the thermal signal in dynamic test were investigated. These are the first and second harmonic of the amplitude of the signal (T_1 and T_2) and their phase (φ_1 and φ_2).

The T_1 analytical expression obtained from the TSA general model was rewritten for describing the stress distribution around a crack by using Westergaard and Williams solutions and a novel procedure for the SIF evaluation was proposed. The experimental application of the procedure demonstrated how for a material affected by the second order effect it guarantees a more capability in the describing the stress distribution in proximity of the crack tip. The effect of the correction is pronounced in both Williams' and Westergaard models.

The parameters T_2, φ_1 and φ_2 are sentinel of dissipation and they can be related to the plastic area ahead the crack tip.

The experimental tests proved a strong dependence of the thermal footprint on the frequency of the applied load. This could indicate that conductive phenomena interfere with dissipative phenomena which are more important at low frequency.

A first raw estimation of the plastic zone shape and size was obtained from the maps of T_2 and φ_1. Nevertheless, to relate the thermal parameters to the dimensions of the plastic zone around the crack tip, the material thermal-physic characteristics and all the heat sources should be considered, including the crack closure contribution.

The thermal footprint obtained from the Thermal Signal Analysis was also compared with the plastic zone predicted through the application of DIC both by using the direct derivation of strains/stress field and in combination with two theoretical models: the Westergaard's equation and the CJP model. The comparison confirmed the influence on the thermal signal of the test parameters (such as R and the loading frequency) that make it difficult to establish a limit for the identification of the plastic zone.

The dual color was the further thermographic technique object of this work. Its application is the free-emissivity temperature measurement for the characterization of the spaceships Thermal Protection System. The study involved the development of an analytical model capable to simulate and replicate the response of the IR camera. The model was validated up to 2500°C. The work demonstrates that the dual color technique is the best thermographic approach for materials characterized by low emissivity gradient through the IR camera operational spectrum, and in general it has to be preferred in all those applications where the emissivity can change considerably over time while retaining less variability in the spectral range. This feature has been revealed more evident in materials with medium-high emissivity. This latter is the condition which characterize the test carried out in the PWT on TPSs.

This thesis is the result of an in-depth work that is part of the articulated activity of a research group dedicated to the study, development, and validation of non-destructive techniques for structural diagnostics and materials characterization. The ultimate goal is to establish standard test procedures and methods that can be applied both in the academic and industrial fields.

REFERNCES

[1] *Maldague XPV, Theory and Practice of Infrared Technology for Nondestructive Testing (2001), New York: Wiley-Interscience*

[2] *Hudson R, Infrared System Engneering, (1969), New York: Wiley-Interscience*

[3] *M. Planck, The theory of heat radiation, second ed., P. Blakiston's Son & Co., Philadelphia, 1906.*

[4] *Vollmer M, Mollman KP, Infrared Thermal Imaging. Fundamentals, Research and Applications, 2018, Wiley-*

[5] *Budzier H, Gerlach G, Thermal Infrared Sensors. Theory, Optimization and Practice, (2011), John Wiley & Sons, Ltd*

[6] *Minkina W and Dudzik S, Infrared Thermography Errors and Uncertaineties, 2009 John Wiley & Sons, Ltd*

[7] *The Ultimate Infrered Handbook for R&D Professionals, FLIR AB.*

[8] *Michael A. Kinch, State of art INfared Detector Technology, 2014,SPIE Press (USA)*

[9] *M. A. Biot, Thermoelasticity and Irreversible Thermodynamics, J. Appl. Phys. 27, 240 (1956).*

[10] *Harwood N and Cummings WM, Thermoelastic Stress Analysis, 1991, Adam Hilger, Bristol Philadelphia and New York*

[11] *N. Rajic, D. McSwiggen, M. McDonald, D. Whiteley, In situ thermoelastic stress analysis—An improved approach to airframe structural model validation, QIRT J. 2018, 16, 8–34.*

[12] *G. Allevi, M. Cibeca, R. Fioretti, R. Marsili, R. Montanini, G. Rossi, Qualification of additively manufactured aerospace brackets: A comparison between thermoelastic stress analysis and theoretical results, Measurement 2018, 126, 252–258.*

[13] *N. R. Kolanu, S. K. Tripathy, G. Raju, M. Ramji, Linear Least Square Approach for the Estimation of Crack Tip Fracture Parameters Using Isopachic Data from Thermoelastic Stress Analysis, Trans Indian Inst Met (2019) 72(11):2933–2945.*

[14] *G. Pitarresi, E.A. Patterson, A review of the general theory of thermoelastic stress analysis, J. Strain Anal. Eng. Des. 2003, 38, 405–417.*

[15] *P. Stanley, W. K. Chan, Quantitative stress analysis by means of the thermoelastic effect, Journal of Strain Analysis Vol 20 No 3 1985.*

[16] *A.K. Wong, S.A. Dunn, J.G. Sparrow, Residual stress measurement by means of the thermoelastic effect, Nature 1988, 332, 613–615.*

[17] *U. Galietti, D. Palumbo, Thermoelastic Stress Analysis of Titanium Components and Simultaneous Assessment of Residual Stress, Proceeding of EPJ Web of Conferences, ICEM 14—14th International Conference on Experimental Mechanics, Poitiers, France, 4–9 July 2010; p. 38012.*

[18] *F. Di Carolo, R. De Finis, D. Palumbo, U. Galietti, A Thermoelastic Stress Analysis General Model: Study of the Influence of Biaxial Residual Stress on Aluminium and Titanium, Metals 2019, 9, 671.*

[19] *F. Ancona, R. De Finis, G. P. Demelio, U. Galietti, D. Palumbo, Study of the plastic behavior around the crack tip by means of thermal methods, Procidia Structural Integrity 2 (2016) 2113-2122.*

[20] *D. Palumbo, F. Ancona, R. De Finis, U. Galietti, Experimental study of the crack growth in stainless steels using thermal methods, Procedia Engineering 109 (2015) 338 – 345.*

[21] *F.A.Díaz, J M.Vasco-Olmo, E.López-Alba, L.Felipe-Sesé, A.J.Molina-Viedma, D.Nowell, Experimental evaluation of effective stress intensity factor using thermoelastic stress analysis and digital image correlation, International Journal of Fatigue, Volume 135, June 2020, 105567.*

[22] *A.E. Morabito, V. Dattoma, U. Galietti, Energy analysis of fatigue damage by thermographic technique, Thermosense XXIV 4710, 456-463.*

[23] *R. De Finis, D. Palumbo, U. Galietti, A multianalysis thermography-based approach for fatigue and damage investigations of ASTM A182 F6NM steel at two stress ratios, Fatigue and Fracture of Engineering Materials and Structures42(1), pp. 267-283.*

[24] *R. De Finis, D. Palumbo, U. Galietti, Mechanical behaviour of stainless steels under dynamic loading: An investigation with thermal methods, Journal of Imaging2(4),32.*

[25] *D. Palumbo, U. Galietti, Data correction for thermoelastic stress analysis on titanium components, Exp. Mech. 2016, 56, 451–462.*

[26] G. Gamot, T. Lasserre, L. Richard, J. Neggers, N. Swiergiel, F. HildCalibrating, *Thermoelastic stress analysis with integrated digital image correlation: Application to fatigue cracks, J Strain Analysis 2019, Vol. 54(5-6) 320–330.*

[27] *BR Boyce, Steps to modern thermoelastic stress analysis*

[28] *P. Stanley, Beginnings and Early Development of Thermoelastic Stress Analysis,*

[29] *Gough, J. (1805) A description of a property of caoutchouc or Indian rubber; with some reflections on the cause of the elasticity of this substance in a letter to Dr. Holme. Manchester Phil. Mem., Second Series, 1, 288–295.*

[30] *Weber, W. (1830) Ueber die specifische Wa¨rme fester Ko¨rper, insbesondere der Metalle. Annalen der Physik und Chemie, Band XX, 177–213. (An alternative version of this reference is: Poggendorffs Annalen, 1830, Band XX, 177–213, J.C. Poggendorff, Berlin.)*

[31] *Thomson, W. (1853) On the dynamical theory of heat. Trans. R. Soc. Edin., 20, 261-283. (The paper was 'read' in March 1851 and there is a note on p. 280 dated April 1851.*

[32] *Thomson, W. (1857) On the thermoelastic and thermomagnetic properties of matter. Q. J. Math., 1, 57–77. (This paper is dated 1855 in Refs [11] and [19]; the above date is from Todhunter, Vol II, Pt II [1631], 359-360.)*

[33] *Joule, J. P. (1857) On the thermoelasticity of ferruginous metals, and on the thermal effects of stretching solid bodies. Proc. R. Soc., VIII, 355–356.*

[34] *Joule, J. P. (1857) On the thermal effects of the longitudinal compression of solids. Proc. R. Soc., VIII, 564–566.*

[35] *Joule, J. P. (1859) On some thermodynamic properties of solids. Phil. Trans., CXLIX, 91–131.*

[36] *Compton, K. T. and Webster, D. B. (1915) Temperature changes accompanying the adiabatic compression of steel. Phys. Rev., V, 159–166.*

[37] *Belgen, M. H. (1967) Structural stress measurements with an infrared radiometer. ISA Trans., 6, 49–53.*

[38] *http://www.desinnovation.com/soluzioni/software/*

[39] *S Baron and EA Patterson, The development of simultaneous thermo- and photo-elasticity for principal stress analysis, Strain Vol.35, N.2, May 1999.*

[40] *S.M. Duelieu-Smith, Alternative calibration techniques for quantitative thermoelastic stress analysis. Strain 31 (1995) 9-16*

[41] *J.M. Duelieu, P. Stanley, Accuracy and precision in the thermoelastic stress analysis technique, Appliede Stress Analysis, Springer Netherlands. (1990) 627-638*

[42] *Belgen, M.H. Infrared Radiometric Stress Instrumentation application range study. NASA contractor report, NASA CR-1067, 1968.*

[43] *Machin A.S.; Sparrow, J.G.; Stimson M.G. Mean stress dependence of the thermoelastic constant. Strain 1987, 23(1), 27-30.*

[44] *Dunn S.A.; Lombardo D.; Sparrow, J.G. The Means Stress effect in Metallic Alloys and Composites. Proc. SPIE 1084, Stress and Vibration: Recent Developments in Industrial Measurement and Analysis, (31 July 1989); https://doi.org/10.1117/12.952913.*

[45] *Wong, A.K.; Jones, R.; Sparrow, J.G. Thermoelastic constant or thermoelastic parameter? J. Phys. Chem. Solids 1987, 48, 749-753.*

[46] *Wong, A.K.; Sparrow, J.G.; Dunn, S.A. On the revised theory of the thermoelastic effect. J. Phys. Chem. Solids 1988, 48, 395–400.*

[47] *Patterson, E.A. The Potential for Quantifying Residual Stress Using Thermoelastic Stress Analysis. In Proceedings of the SEM Annual Conference and Exposition on Experimental and Applied Mechanics 2007, Springfield, MA; USA, 3–6 June 2007; pp. 664–669.*

[48] *Du, Y.; Backman, D.; Patterson, E.A. A New Approach to Measuring Surface Residual Stress Using Thermoelasticity. In Proceedings of the SEM Annual Conference and Exposition on Experimental and Applied Mechanics 2008, Orlando, FL; USA, 2–5 June 2008; Volume 2; pp. 673–680.*

[49] *Quinn, S.; Dulieu-Barton, J.M.; Langlands, J.M. Progress in thermoelastic residual stress measurements. Strain 2004, 40, 127–133.*

[50] *Structural Alloys Handbook, 1996 edition, John M. (Tim) Holt, Technical Ed; C. Y. Ho, Ed., CINDAS/Purdue University, West Lafayette, IN, 1996.*

[51] M. Fukuhara, A. Sanpei, Elastic moduli and internal frictions of Inconel 718 and Ti-6Al-4V as a function of temperature, J Mater Sci Lett 12: 1122, 1993

[52] F A Kandil, J D Lord, A T Fry and P V Grant, A Review of Residual Stress Measurement Methods-A Guide to Technique Selection, National Physical Laboratory, Teddington Middlesex, TWll OL W , UK

[53] Gyekenyesi, A.L.; Baaklini, G.Y. Thermoelastic Stress Analysis: The Mean Stress Effect in Metallic Alloys. In Proceeding of SPIE 3585, Nondestructive Evaluation of Aging Materials and Composites III, Newport Beach, CA, USA, 8 February 1999.

[54] Gyekenyesi, A.L.; Baaklini, G.Y. Quantifying Residual Stresses by Means of Thermoelastic Stress Analysis. In Proceeding of SPIE 3993, Nondestructive Evaluation of Aging Materials and Composites IV, Newport Beach, CA, USA, 13 May 2000.

[55] Robinson A.F.; Dulieu-Barton, J.M.; Quinn, S.; Burguete, L. The potential for assessing residual stress using thermoelastic stress analysis: A study of cold expanded holes. Exp. Mech. 2013, 53, 299–317.

[56] Westergaard, H.M., “Bearing Pressures and Cracks.” Journal of Applied Mechanics, Vol. 6, 1939,

[57] Irwin, G.R., “Analysis of Stresses and Strains near the End of a Crack Traversing a Plate.” Journal of Applied Mechanics, Vol. 24, 1957, pp. 361–364.

[58] Sneddon, I.N., “The Distribution of Stress in the Neighbourhood of a Crack in an Elastic Solid.” Proceedings, Royal Society of London, Vol. A-187, 1946, pp. 229–260.

[59] Williams, M.L., “On the Stress Distribution at the Base of a Stationary Crack.” Journal of Applied Mechanics, Vol. 24, 1957, pp. 109–114.

[60] T.L. Anderson, FRACTURE MECHANICS Fundamentals and Applications, 2005 by Taylor & Francis Group, LLC

[61] ASTM E 647–00. Standard test method for measurement of fatigue crack growth rates; 2004.

[62] M Zanganeh, R A Tomlinson*,andJ R Yates, T-stress determination using thermoelastic stressanalysis, The Journal of Strain Analysis for Engineering Design · June 2008

[63] Giuseppe Pitarresi, Mauro Ricotta, Giovanni Meneghetti, Investigation of the crack

tip stress field in a stainless steel SENT specimen by means of Thermoelastic Stress Analysis, 25th International Conference on Fracture and Structural Integrity

[64] C. J. Christopher · M. N. James ·E. A. Patterson · K. F. Tee, Towards a new model of crack tip stress fields

[65] Muskhelishvili, N. I. (1977) Some Basic Problems of the Mathematical Theory of Elasticity, Noordhoff International Publishing: Groningen.

[66] J.M Vasco-Olmo, M. N. James, C. J. Christopher, E. A. Patterson and F. A. Díaz, Assessment of crack tip plastic zone size and shape and its influence on crack tip shielding, Fatigue Fract Engng Mater Struct, 2016, 39, 969–981 (2016)

[67] M.N. James, C:J. Christopher, Yanwei Lu, E.A. Patterson, Local crack plasticity and its influences on the global elastic stress field, International Journal of Fatigue 46 (2013) 4–15

[68] Irwin, G.R., "Plastic Zone Near a Crack and Fracture Toughness." Sagamore Research Conference Proceedings, Vol. 4, 1961 Syracuse University Research Institute, Syracuse NY pp. 63–78.

[69] Dugdale, D.S., "Yielding in Steel Sheets Containing Slits." Journal of the Mechanics and Physics of Solids, Vol. 8, 1960, pp. 100–104.

[70] Barenblatt, G.I., "The Mathematical Theory of Equilibrium Cracks in Brittle Fracture." Advances in Applied Mechanics, Vol. VII, Academic Press, 1962, NY pp. 55–129.

[71] RA Tomlinson, EJ Olden, Thermoelasticity for the analysis of crack tip stress fields—a review, Strain 35 (2), 49-55 (1999),

[72] Patterson, E.A. and Olden, E.J. (2004), Optical analysis of crack tip stress fields: a comparative study. Fatigue & Fracture of Engineering Materials & Structures, 27: 623-635. doi:10.1111/j.1460-2695.2004.00774.x

[73] Palumbo Davide, De Finis Rosa, Galietti Umberto, Evaluation of the heat dissipated around the crack tip of AISI 422 and CF3M steels by means of thermography, Procedia Structural Integrity, Volume 18, 2019, Pages 875-885

[74] A. Fedorova, M.V. Bannikov, O.A. Plekhov, Infrared thermography study of the fatigue crack propagation, Fract Struct Integr, 21 (2012), pp. 46-53J. Bär(2014),

[75] G. Meneghetti, M. Ricotta, Evaluating the heat energy dissipated in a small volume surrounding the tip of a fatigue crack, International Journal of Fatigue, Volume 92, Part 2, 2016, Pages 605-615

[76] Uğuz, A. andMartin, J. W. (1996) Plastic zone size measurement techniques for metallic materials. Mater. Charact., 37, 105–118

[77] Diaz F.A., Patterson E.A.,Yates R.A. "Some improvements in the analysis of fatigue cracks using thermoelasticity". Int J. of Fatigue 26(4), pp. 365–376, 2004.

[78] Diaz, F.A., Patterson E.A., Yates, J.R, Assessment of effective stress intensity factors using thermoelastic stress analysis Journal of Strain Analysis for Engineering Design Volume 44, Issue 7, 1 October 2009, Pages 621-631

[79] Díaz, F.A., Patterson, E.A., Tomlinson, R.A., Yates, J.R., Measuring stress intensity factors during fatigue crack growth using thermoelasticity, Fatigue and Fracture of Engineering Materials and StructuresVolume 27, Issue 7, July 2004, Pages 571-583

[80] Stanley P, Chan WK. The determination of stress intensity factors and crack tip velocities from thermoelastic infrared emissions. Proc. of International conference of fatigue of engineering materials and structures, c262, IMechE, Sheffield, UK, 1986: 105–114.

[81] Paris P, Erdogan F. A critical analysis of crack propagation laws. J Basic Eng, Transact Am Soc Mech Eng 1963;D85(4):528–37. 10.1115/1.3656900.

[82] Yates JR et al. "Quantifying crack tip displacement fields with DIC". Eng Fract Mech, 77, pp. 2063-14, 2010.

[83] Réthore J, Limodin N, Buffière JY, Roux S, Hild F. Three-dimensional analysis of fatigue crack propagation using X-ray tomography, digital volume correlation and extended finite element simulations. Procedia IUTAM 2012;4(4):151–8.

[84] Saka M, Sato I, Abè H. NDE of a 3-D surface crack using magnetic field induced by DC current flow. NDT&E Int 1998;5:325–8.

[85] Williams JJ, Yazzie KE, Padilla E, Chawla N, Xiao X, De Carlo F. Understanding fatigue crack growth in aluminium alloys by in situ X-ray synchrotron tomography. Int J Fatigue 2013;57:79–85.

[86] Kainuma S, Ahn JH, Jeong YS, Takahashi H. Evaluation on estimation in

characteristics of fatigue crack using micro-encapsulated dye mixing paint. Engng Fail Anal 2015;25:1–12.

[87] Tanabe H, Kida K, Takamatsu T, Itoh N, Santos EC. Observation of magnetic flux density distribution around fatigue crack and application to nondestructive evaluation of stress intensity factor. Proced Eng 2011;10:881–7.

[88] Cui ZQ, Yang HW, Wang WX, Yan ZF, Ma ZZ, Xu BS, et al. Research on fatigue crack growth behavior of AZ31B magnesium alloy electron beam welded joints based on temperature distribution around the crack tip. Engng Fract Mech 2015;133:14–23.

[89] F. Ancona, D. Palumbo, R. De Finis, G.P. Demelio, U. Galietti, Automatic procedure for evaluating the Paris Law of martensitic and austenitic stainless steels by means of thermal methods Engineering Fracture Mechanics 163 (2016) 206–219

[90] M A Sutton, W J Walters, W H Peters, W F Ranson and S R McNeil1, “Determination of displacements using an improved digital correlation method”, Image Vis Comput. 1983;1(3):133-139. https://doi.org/10.1016/0262-8856 (83)90064-1.

[91] J. Tong, “Full-field characterisation of crack tip deformation and fatigue crack growth using digital image correlation—a review”, Fatigue Fract Eng Mater Struct. 2018;41:1855–1869.

[92] J.M. Vasco-Olmo, F.A. Díaz, F.V. Antunes, M.N. James, “Characterisation of fatigue crack growth using digital image correlation measurements of plastic CTOD”, Theoretical and Applied Fracture Mechanics 101 (2019) 332–341

[93] Arun Mohan, Sumathi Poobal, “Crack detection using image processing: A critical review and analysis”, Alexandria Engineering Journal (2018) 57, 787–798.

[94] J.R. Yates, M. Zanganeh, Y.H. Tai, “Quantifying crack tip displacement fields with DIC”, Engineering Fracture Mechanics 77 (2010) 2063–2076.

[95] W. J. Wang, J. M. Dulieu-Barton, Q. Li, Assessment of non-adiabatic behaviour in thermoelastic stress analysis of small-scale components. Experimental Mechanics 50 (2010) 449-61.

[96] Enke, NF., Sandor, BI., 1988. Cyclic plasticity analysis by differential infrared thermography. Proceeding of the VII International Congress on Experimental Mechanics, 830-835.

[97] *Sakagami, T., Kubo, S., Tamura, E., Nishimura, T., 2005. Identification of plastic-zone based on double frequency lock-in thermographic temperature measurement. International Conference of Fracture ICF 11*

[98] *Connesson, N., Maquin, F., Pierron, F., 2011. Experimental Energy Balance During the First Cycles of Cyclically Loaded Specimens Under the Conventional Yield Stress. Experimental Mechanics, 51, 23-45.*

[99] *Pukas SR. Theoretical considerations for determining stress intensity factors via thermoelastic stress analysis. Stress analysis by Thermoelastic Technique. Proc. SPIE 1987;731:88–101.*

[100] *Dulieu-Barton JM, Fulton MC, Stanley P. The analysis of thermoelastic isopachic data from crack tip stress fields. Fatigue Fract Eng Mater Struct 2000;23:303–13.*

[101] *Lesniak JR, Bazile DJ, Boyce BR, Zickel MJ, Cramer KE, Welch CS. Stress intensity measurement via infrared focal plane array. Non-traditional Methods of Sensing Stress, Strain, and Damage in Materials and Structures, ASTM STP 1318, Philadelphia 1997*

[102] *Weertman J. "Theory of fatigue crack growth based on a BCS crack theory with work hardening". Int J. of Fatigue 9, 125-155, 1973.*

[103] *Klingbeil N.W. "A total dissipated energy theory of fatigue crack growth in ductile solids". Int J. of Fatigue 25(2), pp. 117-128, 2003.*

[104] *Mazari M., Bouchouicha B., Zemri M., Benguediab M., Ranganathan N. "Fatigue crack propagation analyses based on plastic energy approach", 2008. Computational Materials Science 41, 344-349, 2003).*

[105] *Palumbo D., De Finis R., Ancona F., Galietti U. "Damage monitoring in fracture mechanics by evaluation of the heat dissipated in the cyclic plastic zone ahead of the crack tip with thermal measurements". Eng Fract Mech 181, pp. 65-75, 2017.*

[106] *Carrascal I., Casado J.A., Diego S., Lacalle R., Cicero S., Álvarez J.A. "Determination of the Paris' law constants by means of infrared thermographic techniques". Polymer Testing 40, pp. 39-45, 2014.*

[107] *Meneghetti G., Ricotta M."Evaluating the heat energy dissipated in a small volume surrounding the tip of a fatigue crack", Int J. of Fatigue 92 (2), pp. 605-615, 2016.*

[108]E. Marble, “Measuring the Spectral Emissivity of Thermal Protection Materials During Atmospheric Reentry simulation”, NASA/ASEE Summer Faculty Fellowship Program-1995, Johnson Space Center.

[109]Y. Le Sant, M. Marchand, P. Millan, J. Fontaine, “Infrared thermography on large facilities”, 3rd ONERA-DLR Aerospace Symposium Paris (France), June 20-22, 2001

[110]M. De Cesare, L. Savino, G. Ceglia, D. Alfano, F. Di Carolo, A.D. French, D. Rapagnani, A. Cipullo, A. Del Vecchio, A. Di Leva, A. D'Onofrio, U. Galietti, L. Gialanella, F. Terrasi, Applied radiation physics techniques for diagnostic evaluation of the plasma wind and thermal protection system critical parameters in aerospace re-entry

[111]F. De Filippis, C. Toscano, D. Gallo, P. Caruso, L.Savino, Influence of Mirrors utilization on the Radiation Emitted by Models Subjected to Hypersonic Flow for Surface Temperature Determination, 11th International Conference on Quantitative InfraRed Thermography (QIRT) Naples, Italy, June 11 – June 14, 2012.

[112]G. Machin, K. Anhalt, M. Battuello, F. Bourson, P. Dekker, A. Diril, F. Edler,C.J. Elliott, F. Girard, A. Greenen, L. Knˇazovická, D. Lowe, P. Pavlásek, J.V. Pearce, M. Sadli, R. Strnad, M. Seifert, E.M. Vuelban, The European project on high temperature measurement solutions in industry (HiTeMS) – A summary of achievements, Measurement 78 (2016) 168-179.

[113]B. Müller, U. Renz, S. Hoppe, F. Klocke, Radiation thermometry at a high-speed turning process, Journal of Manufacturing Science and Engineering 126 (2004) 488-495.

[114]P. M. Reynolds, A review of multicolour pyrometry for temperatures below 1500 °C, British Journal of Applied Physics 15 (1964) 579-589.

[115]K. Chrzanowski, Problem of determination of effective emissivity of some materials in MIR range, Infrared Physics & Technology 36 (1995) 679-684.

[116]O. Riou, V. Guiheneuf, F. Delaleux, P.-O. Logerais, J.-F. Durastanti, Accurate methods for single-band apparent emissivity measurement of opaque materials, Measurement 89 (2016) 239-251.

[117]O. Riou, P.-O. Logerais, J.-F. Durastanti, Quantitative study of the temperature dependence of normal LWIR apparent emissivity, Infrared Physics & Technology 60 (2013) 244–250.

[118]P. B. Coates, Multi-wavelength pyrometry, Metrologia 17 (1981) 103-109.

[119]B. Müller, U. Renz, Development of a fast fiber-optic two-color pyrometer for the temperature measurement of surfaces with varying emissivities, Review of Scientific Instruments 72 (2001) 3366-3374.

[120]T. Ueda, M. Huda, K. Yamada, K. Nakayama, Temperature measurement of CBN tool in turning of high hardness steel, Annals of the CIRP C48/1 (1999) 63-66.

[121]G. Hunter, C. D. Allemand, T. W. Eagar, Multiwavelength pyrometry: an improved method, Optical Engineering 24(6) (1985) 1081-1085.

[122]B. Bouvry, G. Cheymol, L. Ramiandrisoa, B. Javaudin, C. Gallou, H. Maskrot, N. Horny, T. Duvaut, C. Destouches, L. Ferry, C. Gonnier, Multispectral pyrometry for surface temperature measurement of oxidized Zircaloy claddings, Infrared Physics & Technology 83 (2017) 78-87.

[123]C. Zhang, E. Gauthier, C. Pocheau, C. Balorin, J.Y. Pascal, M. Jouve, M.H. Aumeunier, X. Courtois, Th. Loarer, M. Houry, Surface temperature measurement of the plasma facing components with the Multi-Spectral Infrared thermography diagnostics in Tokamaks, Infrared Physics & Technology 81 (2017) 215-222.

[124]F.Meraudea, Real time multispectral high temperature measurement: Application to control in the industry, Image and Vision Computing 25 (2007) 1124-1133.

[125]K.-P. Möllmann, F. Pinno, M. Vollmer, Two-color or ratio thermal imaging – potentials and limits, InfraMation 2010 Proceedings.

[126]L. Savino, M. De Cesare, M. Musto, G. Rotondo, F, De Filippis, A. Del Vecchio, F. Russo, Free emissivity temperature investigations by dual color applied physics methodology in the mid- and long- infrared ranges, International Journal of Thermal Sciences 117 (2017) 328-341.

[127]M. Musto, G. Rotondo, M. De Cesare, A.D. Vecchio, L. Savino, F. De Filippis, Error analysis on measurement temperature by means Dual-Color Thermography Technique, Measurement

[128]W.G. Fahrenholtz, E.J. Wuchina, W.E. Lee, Y. Zhou, Ultra-High Temperature Ceramics: Materials for Extreme Environment Applications, Wiley - The American Ceramic Society, 2014, pp. 1–441.

[129] T. Laux, T. Ullmann, M. Auweter-Kurtz, H. Hald, A. Kurz, Investigation of thermal protection materials along an X-38 re-entry trajectory by plasma wind tunnel simulations, 2nd International Symposium on Atmospheric Reentry Vehicles and Systems - Proceedings of the Association Aronautique et Astronautique de France, 2001, pp. 1–9.

[130] D.E. Glass, Ceramic matrix composite (CMC) thermal protection systems (TPS) and hot structures for hypersonic vehicles, 15nd AIAA Space Planes and Hypersonic Systems and Technologies Conference, 2008, pp. 1–36 AIAA-2008-2682.

[131] D. Alfano, Spectroscopic properties of carbon fibre reinforced silicon carbide composites for aerospace applications,, Properties and Applications of Silicon Carbide Chapter 10 (2011) 231–250.

[132] G. Tumino, S. Mancuso, J.-M. Gallego, S. Dussy, J.-P. Preaud, G. Di Vita, P. Brunner, Acta Astronaut. 124 (2016) 2–17.

[133] W. Krenkel, Ceramic Matrix Composites: Fiber Reinforced Ceramics and Their Applications, Wiley - The American Ceramic Society, 2008, pp. 1–418.

[134]S.D. Williams, D.M. Curry, Assessing the orbiter thermal environment using flight data, J. Spacecr. Rocket. 21 (1984) 534–541.

[135]W.G. Fahrenholtz, G.E. Hilmas, I.G. Talmy, J.A. Zaykoski, Refractory diborides of zirconium and hafnium, J. Am. Ceram. Soc. 90 (2007) 1347–1364.

[136]A. Chamberlain, W. Fahrenholtz, G. Hilmas, D. Ellerby, Oxidation of ZrB2-SiC ceramic under atmospheric and reentry conditions, Refractories Applications Transactions 1 (2005) 1–8.

[137]J. Marschall, D.A. Pejakovic, W.G. Fahrenholtz, G.E. Hilmas, F. Panerai, O. Chazot, Temperature jump phenomenon during Plasmatron testing of ZrB2-SiC ultrahigh-temperature ceramics, J. Thermophys. Heat Transf. 26 (2012) 559–572.

[138]I. Şakraker, B. Helber, O. Chazot, Experimental characterization of cork based thermal protection material P50. 8th European Symposium on Aerothermodynamics for Space Vehicles, March 2015, Lisbon, Portugal.

[139]F.S. Milos, D.J. Rasky, Review of numerical procedures for computational surface thermochemistry, J. Thermophys. Heat Transf. 8 (1) (1994) 24–34.

[140]G. Taguchi, Introduction to Quality Engineering , Asian Productivity Organization (Distributed by American Supplier Institute Inc., Dearborn, MI) , 1986.

[141]S. M. Phadke, Quality Engineering Using Robust Design, Prentice Hall, Englewood Cliffs, N.J. , 1989

[142]D. Montgomery, Design and Analysis of Experiments, 8th ed., John Wiley & Sons Inc, 2012.Materials Technology Conference and Exhibition, 2014, pp. 1–4.

[143]R. T. Potter, L. J. Graves, The application of thermoelastic stress analysis techniques to fibre composites, SPIE Vol. 817 Optomechanical Systems Engineering, 1987

[144]R. Boyer, G. Welsch, and E. W. Collings, Materials Properties Handbook: Titanium Alloys , eds. ASM International, Materials Park, OH, 1994.

[145]Metals Handbook, Vol.2 - Properties and Selection: Nonferrous Alloys and Special-Purpose Materials, ASM International 10th Ed. 1990.

[146]Metals Handbook, Vol. 3, Properties and Selection: Stainless Steels, Tool Materials and Special-Purpose Metals, Ninth Edition, ASM Handbook Committee., American Society for Metals, Materials Park, OH, 1980.

[147]Robinson A.F.; Dulieu-Barton, J.M.; Quinn, S.; Burguete, L. A Review of Residual Stress Analysis using Thermoelastic Techniques. In Proceeding of 7th International Conference on Modern Practice in Stress and Vibration Analysis, Murray Edwards College, Cambridge, UK, 8–10 September 2009; p. 012029.

[148]Standard Test Method for Determining Residual Stresses by the Hole-Drilling Strain-Gage Method, ASTM E837-13a.

[149]L. S. Nelson, Exact Critical Values for Use with the Analysis of Means, Journal of Quality Technology, 15(1), 1983

[150]E.R. Naimon, M.H. Ledbetter, W.F. Weston, Low-temperature elastic properties of four wrought and annealed aluminium alloys, J. Mater. Sci. 10 (1975), 1309–1316.

[151]F.A. Diaz, E.A. Patterson, J.R. Yates, Differential Thermography Reveals Crack Tip Behaviour ?, in Proceedings 2005 SEM Annual Conference on Experimental Applied

Mechanics, Society for Experimental Mechanics, 2005, Portland, OR, USA, 6–9 June 2005, pp. 1413–1419.

[152]R.A. Tomlinson, E.A. Patterson, Examination of Crack Tip Plasticity Using Thermoelastic Stress analysis, Thermomechanics and Infra-Red Imaging, in: Proceedings of the Society for Experimental Mechanics Series 2011, Volume 7, Springer, New York, NY.

[153]F. Di Carolo, R. De Finisi D.Palumbo J. M. Vasco-Olmo ,F. A. Díaz, U. Galietti, Study of the plasticity effect at the crack tip in Titanium by using thermal signal analysis, 15th Quantitative InfraRed Thermography Conference, Porto (Portogal), 21-30 September 2020.

[154]Janssen, M., Zuidema, J. and Wanhill, R. J. H. (2006) Fracture Mechanics, 2nd ed, Spon Press: Abingdon.

[155]R. Jones, S. Pitt, An experimental evaluation of crack face energy dissipation. Int J Fatigue 28 (2006) 1716-1724. doi:10.1016/j.ijfatigue.2006.01.009.

[156]P. Stanley, Applications and potential of thermoelastic stress analysis, J Mater Process Tech 64 (1997), 359-370.

[157]https://www.flir.it/..

[158]B. Kong, T. Li, Q. Eri, Normal spectral emissivity of GH536 (HastelloyX) in three surface conditions, Applied Thermal Engineering 133 (2016) 20-26.

[159]C. Cagran, G. Pottlacher, M. Rink, W. Bauer, Spectral Emissivities and Emissivity X-Points of Pure Molybdenum and Tungsten, International Journal of Thermophysics 26 (2005) 1001-1015.

[160]V. D. Dmitriev, G. K. Kholopov, Integral radiant emissivity of tungsten in the 1200-2800 K temperature range, Zhurnal Prikladnoi Spektroskopii 3 (1965) 72-75.

[161]L. S. Slobodkin, M. Ya. Flyaks, Emissivity measurement for a carbon-carbon composite and a phenolic carbon plastic, Lykov Institute of Heat and Mass Transfer, Belorussian Academy of Sciences, Minsk.Translated from Inzhenerno-Fizicheskii Zhurnal 57 (1989) 308-313.

[162]R. M. Wakefield, Surface emissivity of a reinforced carbon composite material with an oxidation inhibiting coating, NASA TM X-62, 315, 1973.

[163]G. Neuer, Spectral and Total Emissivity Measurements of Highly Emitting Materials, International Journal of Thermophysics 16 (1995) 257-265.

Ringraziamenti

A conclusione del mio percorso di studi e ricerca desidero ringraziare tutte le persone che mi hanno guidata, aiutata e sostenuta rendendo possibile la realizzazione di questo lavoro e la mia crescita professionale e personale.

Vorrei innanzi tutto ringraziare il mio tutor, il prof. Umberto Galietti per la fiducia che ha riposto in me, per avermi dato la possibilità di intraprendere il mio percorso come ricercatrice, per il tempo dedicato a discutere e costruire questo lavoro e per tutti i preziosi insegnamenti che giorno dopo giorno hanno reso possibile la stesura della mia tesi.

Un ringraziamento speciale va a Rossella e Davide, il cui prezioso contributo è stato fondamentale per la mia ricerca. Entrambi sono stati per me un modello, un riferimento e una guida attraverso gli alti e bassi del mio percorso.

Ringrazio Mario De Cesare e Luigi Savino del Centro Italiano di Ricerca Aerospaziale per avermi da sempre seguita, incoraggiata e coinvolta nel loro lavoro.

Desidero ringraziare il prof. Francisco Diaz del Departamento de Ingeniería Mecánica y Minera dell'università di Jaèn che mi ha accolto nel mio periodo di studio in Spagna e mi ha dato la possibilità di fare meccanica seprimentale, ed avermi aperto le porte del suo laboratorio facendomi sentire a casa. Grazie anche ai prof. Josè Vasco-Olmo, Luis Felipe, Elias Lopez ed Angel Molina per avermi dedicato il loro tempo e avermi dato tutto il supporto di cui ho avuto bisogno.

Ringrazio i miei colleghi e compagni di avventura Ester e Giuseppe per aver condiviso con me i migliori e peggiori momenti che in questi anni di dottorato abbaimo dovuto affrontare.

Desidero ringraziare tutta la mia famiglia che sempre mi ha sostenuta in ogni mia scelta.

Infine desidero ringraziare Ezio, il mio coraggio e la mia forza.